Using a Sliding Plate Rheometer to Obtain Material Parameters for Simulating Long Fiber Orientation in Injection Molded Composites

Mark J. Cieslinski

Dissertation submitted to the faculty of the Virginia Polytechnic Institute and State University in partial fulfillment of the requirements for the degree of

Doctor of Philosophy

In

Chemical Engineering

Donald G. Baird, Chair

Stephen M. Martin

Richey M. Davis

Peter Wapperom

August 26th, 2015

Blacksburg, VA

Keywords: Sliding Plate Rheometer, Fiber Suspension Rheology, Fiber Orientation

Using a Sliding Plate Rheometer to Obtain Material Parameters for Simulating Long Fiber Orientation in Injection Molded Composites

Mark J. Cieslinski

Abstract

This work is concerned with determining empirical parameters in stress and fiber orientation models required to accurately simulate the fiber orientation in injection molded composites. An independent approach aims to obtain the material parameters using a sliding plate rheometer to measure the rheology of fiber suspensions at increased fiber lengths subjected to transient shear flow. Fiber orientation was measured in conjunction with shear stress to determine the relationship between stress and fiber orientation. Using a compression molding sample preparation procedure, the transient shear stress response was measured for glass and carbon fiber suspensions up to a number average fiber aspect ratio (length/diameter) of 100. Increases in concentration or fiber aspect ratio caused the magnitude of the stress response to increase by as much as an order of magnitude when compared to the suspending matrix. The degree of shear thinning at low shear rates also increased with increases in aspect ratio and concentration. The compression molding sample preparation procedure provided poor control of the initial fiber orientation which led to the investigation of samples subjected to flow reversal and samples generated through injection molding. The samples prepared through injection molding provided improved repeatability in the measured shear stress response and fiber orientation evolution during the startup of flow compared to compression molded samples and samples subjected to flow reversal. From repeatable stress and orientation evolution data, models for stress and fiber orientation were assessed independently. Current theories for stress were unable to reflect the overshoot in the measured stress response and could at best capture the steady state. The transient behavior of the fiber orientation models were found to be highly dependent on the initial fiber orientation. The repeatable orientation data obtained from the injection molding sample preparation procedure provided material parameters in the strain reduction factor and reduced

strain closure models. The injection molded samples provided evolution data from different initial fiber orientations to provide further scrutiny or validation of the material parameters. Orientation model parameters that provided reasonable agreement to multiple sets of fiber evolution data in simple shear flow should allow for a better assessment of the orientation models in complex flow simulations.

Original Contributions

The following are considered to be original contributions to this research:

- Demonstrated the ability of the sliding plate rheometer to measure the transient viscosity of concentrated fiber suspensions at different concentrations and fiber lengths of glass and carbon fibers in a polypropylene matrix. In addition, unexpected sample deformation was observed and reported which may be considered an experimental limitation until further studied.

- Identified that previous sample preparation procedures provided poor repeatability in the initial fiber orientation used for transient rheological measurements. Proposed preparation methods of generating an initial fiber orientation through flow reversal and injection molding were evaluated based on the repeatability of the measured stress response and measured evolution of fiber orientation.

- Assessed predictions of shear stress using experimental measurements of fiber orientation to calculate the fourth order orientation tensor in the current stress theories. This method allows for the stress theory to be evaluated independently of an orientation evolution equation or closure approximation, which may induce additional errors.

- Revealed through simulations in simple shear flow that the initial fiber orientation can significantly impact the predicted orientation evolution and stress response. Obtaining repeatable initial fiber orientation data allowed for orientation model parameters to be determined which were then evaluated using evolution data with different initial fiber orientations.

Format of Dissertation

This dissertation is written in manuscript format. Chapters 3 – 6 are self-contained papers intended for publication in peer-reviewed journals, with Chapter 3 currently in print. Each paper contains the relevant background information, experimental procedures, results and conclusions pertaining to the primary motivation of the paper. With the exception of Chapters 1 and 2, the tables and figures are presented at the end of each chapter.

Acknowledgements

I would first like to thank my advisor, Dr. Donald G. Baird, for allowing me the opportunity to conduct the research that culminated in this dissertation. His support, guidance and constructive criticism contributed greatly in my development as an individual and researcher. I would like to thank Dr. Peter Wapperom for being a member of my advisory committee and providing fresh insight and critique to many aspects of this research. Additional gratitude is given to committee members Dr. Stephen Martin and Dr. Richey Davis for their thoughtful comments and suggestions throughout this research project.

Many individuals at Virginia Tech allowed for my time in graduate school to be such a positive experience. I am appreciative to Dr. Richey Davis, Dr. Mike Ellis and Dr. Carlos Suchicital for allowing me access to their laboratories and equipment for this research. I would like to acknowledge the chemical engineering department staff for their kind assistance: Tina Russell, Diane Cannaday, Nora Bentley, Jane Price, Melanie Darden, Michael Vaught, Kevin Holshouser and Riley Chan. I would also like to thank current and past members of the polymer processing laboratory for many fruitful discussions. In particular, I would like to thank Kevin Herrington, Gregorio Vélez-García, John Hofmann, Kevin Meyer, Chen Qian and Hongyu Chen. It was a pleasure to work in such a supportive environment.

Lastly, I would like to thank my friends and family for their many words of encouragement. I owe a debt of gratitude to my parents, for their unwavering love and support that has shaped me into the person I am today.

Table of Contents

List of Figures

List of Tables

Chapter 1 Introduction

Chapter 1 Introduction

The addition of discontinuous fibers to a polymer matrix provides a means to increase a part's strength to weight ratio while retaining the ability to use traditional melt processing techniques [1]. It has been shown that increased mechanical enhancement can be obtained by increasing fiber length [2]. As an example, glass fibers can improve the tensile and flexural properties of a part, but long glass fibers (lengths > 1 mm) provide additional enhancement to creep and impact properties when compared to short glass fibers (lengths < 1 mm) [3, 4].

It has been observed for long fiber composites that the orientation distribution within an injection molded part will determine the bulk mechanical performance [5]. A high degree of fiber alignment in a particular direction will coincide with anisotropic mechanical properties [5, 6]. For long fiber composites formed in basic injection molding geometries, measurements of Young's modulus have been shown to vary by up to a factor of two throughout the part depending on the fiber orientation distribution [7, 8].

In order to optimize a part's mechanical properties, it is of interest to simulate the fiber orientation developed during the molding process. From these simulations, mold design and processing conditions can be tailored to impart a desired fiber microstructure.

Current theories relating fiber orientation to the bulk flow of the suspension use models that account for fiber orientation and the extra stress due to the fibers. The extra stress tensor is dependent on fiber orientation and couples orientation to the equations of momentum. In order for fiber orientation models to accurately predict the fiber microstructure within a composite, material specific parameters must be determined.

A rheological approach to obtain material parameters provides many benefits. First, the testing conditions, such as temperature and shear rate, can be controlled. Second, orientation and stress models often simplify due to the well-defined flow field. Third, the use of an accurate stress

tensor can allow for material parameters to be determined without experimentally measuring fiber orientation. Finally, the material parameters are obtained independently of the molding process.

A brief description of the approaches used to model fiber orientation is provided in §1.1. In §1.2, the theories accounting for the extra stress in fiber suspensions are discussed. Next, §1.3 provides brief comments on the methods used for rheological testing of fiber suspensions. In §1.4, an overview of simulations using material parameters obtained from rheology is provided. In closing, §1.5 provides the objectives of this research.

1.1 Orientation Theory

Continuum orientation models are highly desired for their computational efficiency in complex flow simulations. Many of the works regarding the orientation of particles with an aspect ratio stem from the pioneering work of Jeffery [9], who derived the governing equations to describe the rotation of an ellipsoid in the presence of flow. This approach had been expanded for use with concentrated fiber suspensions of industrial interest by adding a phenomenological term to account for the effect on orientation due to interactions between fibers [10]. This term is referred to as isotropic rotary diffusion. In recent years, improvements to this model have taken into account slowed orientation kinetics [11, 12], fiber-fiber interactions [13], anisotropic rotary diffusion [14] and fiber flexibility [15-17]. Some models include dependencies on concentration, fiber length and fiber flexibility, while other models account for changes in these characteristics through phenomenological parameters. An orientation model by Férec et al. [13] accounts for fiber-fiber interactions of rigid fibers which scales linearly with concentration. A semi-flexible fiber orientation model from Strautins and Latz [15] includes terms dependent on fiber length and the rigidity of a fiber. Physically the fibers are represented according to Figure 1.1, where the orientation of a semi-flexible fiber is represented by an end-to-end vector. A majority of the orientation models have been exposed to limited evaluation and their ability to reflect a variety of concentrations, fiber lengths and fiber types is largely unknown.

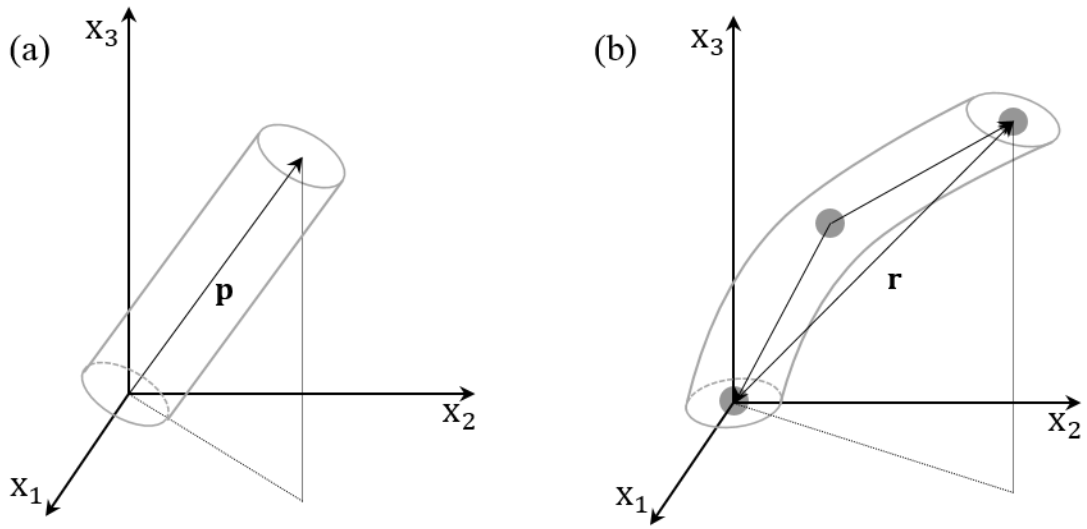

Figure 1.1: General representations of (a) rigid and (b) semi-flexible fibers

An alternative approach to continuum models is to perform numerical simulations on individual fibers subject to specified forces and torques. These simulations can be formulated to encompass a variety of complex fiber dynamics like fiber networks [18], fiber-fiber interactions [19] and fiber flexibility [20]. Flexible fibers are often modeled as linked rigid segments with their movement to describe bending related to the physical properties of the fiber [21]. Results are able to predict phenomena not always included in continuum models such as the formation of flocculations [22] and particle migration [23]. The limit on numerical simulations is the computation time required to solve the particle dynamics. This has largely restricted these works to a small population of fibers in simple flows. However, information gathered on the orientation and interactions of semi-flexible fibers could be used to focus research efforts toward the improvement of continuum models and experimental methods.

1.2 Stress Theory

The extra stress in a fiber suspension involves additive contributions from the matrix and the fibers. The fiber contributions may include terms accounting for the tension imposed on an inextensible fiber [24, 25], fiber-fiber interactions [13, 26] and the bending of semi-flexible fibers

[16, 17]. Currently, theories have only been developed for the dilute and semi-dilute concentration regimes where fiber interactions are mostly hydrodynamic. As fiber lengths increase, fiber-fiber interactions and fiber flexibility become more pronounced. A thermodynamically derived theory has been proposed to account for fiber-fiber interactions and semi-flexible fibers [16, 27]. This model relies on parameters that cannot be directly measured. Often for concentrated suspensions, the contributions of the fibers are scaled empirically due to lack of an available stress equation [17, 28]. Recently developed stress theories have largely been untested outside of the authors' original work. The evaluation of a stress tensor must coincide with an orientation model because stress and orientation are a highly coupled set of equations. A reliable stress tensor would provide the means to determine orientation model parameters from stress measurements taken from a rheometer.

1.3 Rheology

The stresses measured during rheological experiments are a reflection of the fiber orientation. It has been the focus of many researchers to perform rheological measurements during the startup of shear flow in order to observe the changes in stress with changes in fiber orientation [17, 29-31]. As fibers orient with the flow a shear stress growth overshoot is observed. Additionally, fiber suspensions will also exhibit a first normal stress difference that will also overshoot even when no normal stresses are observed in the matrix. For steady shear flow, the greatest differences between suspensions are observed at low deformation rates. Furthermore, the fiber suspensions will exhibit a shear thinning behavior at low shear rates which is not evident in the matrix and has yet to be fully understood.

A variety of techniques have been used to measure the rheological behavior of fiber suspensions, each with their own set of limitations. A cone-and-plate rheometer is prone to gap effects near the cone apex and the parallel disk rheometer imposes an inhomogeneous shear rate [32]. In addition, rotational rheometers impose curvilinear streamlines which may be problematic

because the orientation of straight fiber may be influenced by a flow that is always curved. The use of a sliding plate rheometer will impose a rectilinear flow field and has shown the ability to capture shear stresses in fiber suspensions [17, 33]. Ortman et al. [17] investigated the effect of initial orientation on the shear stress growth. The stress growth overshoot appears to broaden as the fibers increase in length. Orientation was measured at different times during flow so that a semi-flexible orientation model and a modified stress model that included flexibility could be evaluated. This allowed for orientation model parameters to be determined with the intent of applying the parameters to simulations of injection molded composites.

1.4 Rheology and Complex Flow Simulations

A primary focus in investigating a material under well-defined conditions within a rheometer is to apply the findings to processing flows. For rigid fibers, Mazahir and coworkers [34] determined model parameters from orientation data obtained at different shear strains from the work of Eberle et al. [31] during the startup of shear flow. Orientation models could then be evaluated in an injection molded center-gated disk using parameters that were obtained independently of the processing flow. A representation of a center-gated disk mold geometry is provided in Figure 1.2(a). For semi-flexible fibers, Mazahir [35] and Meyer et al. [36] performed orientation simulations on a center-gated disk using a semi-flexible orientation model and parameters obtained from the rheological work of Ortman et al. [17]. Improved predictions of fiber orientation were observed when compared to a Hele-Shaw approximation and the use of a rigid fiber model.

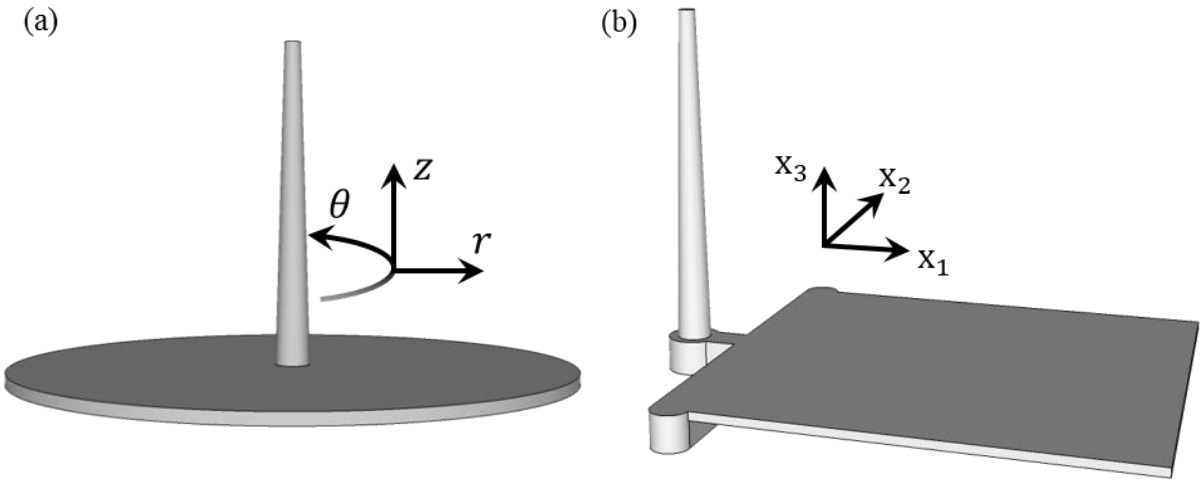

Figure 1.2: Representation of a (a) center-gated disk and (b) end-gated plaque injection molding geometries

Meyer [37] applied the parameters that were used in center-gated disk calculations to an end-gated plaque [Figure 1.2(b)] where the simulations poorly predicted fiber orientation. In order for simulations to reflect fiber orientation data in the end-gated plaque, the model parameters were fit to data at one location while the orientation models were evaluated at other locations within the plaque. Results showed that a semi-flexible orientation model was able to provide improved predictions when compared to a rigid fiber model along and away from the plaque's plane of symmetry. However, these parameters were at least an order of magnitude different than what were used for the center-gated disk simulations using the same material. An orientation model should be valid for all flows and model parameters should only be dependent on the fiber suspension. Simulations were performed only under a single set of conditions and the additional stress due to the fibers was not included. Meyer [37] briefly noted that the parameters prescribing flexibility and fiber interactions were dependent on each other. Current methods must be revised to accurately determine these parameters such that they are valid for all possible flows.

1.5 Research Objectives

The primary focus of this research is to investigate the rheology of semi-flexible fiber suspensions in simple shear flow as it relates to fiber orientation kinetics. In doing so, this approach may provide an independent method for obtaining material parameters used in predicting fiber orientation in complex processing flows. Three objectives have been formulated pertaining to this goal:

1. Assess the ability of the sliding plate rheometer to measure changes in the transient response of semi-flexible fiber suspensions with changes in concentration, fiber length and fiber flexibility.

2. Use the stress growth response along with measured fiber orientation data from simple shear flow to evaluate current fiber suspension theories and quantify material parameters' sensitivity to changes in concentration, fiber length and fiber flexibility.

3. Develop a self-consistent method to obtain material parameters in the semi-flexible fiber orientation model that are representative of a broad distribution of fiber lengths and fiber flexibilities.

1.6 References

[1] Advani SG, Sozer EM. Process Modeling in Composites Manufacturing. New York: Marcel Dekker, Inc.; 2003.

[2] Chin W-K, Liu H-T, Lee Y-D. Effects of fiber length and orientation distribution on the elastic modulus of short fiber reinforced thermoplastics. Polym Compos. 1988;9:27-35.

[3] Truckenmüller F, Fritz HG. Injection molding of long fiber-reinforced thermoplastics: a comparison of extruded and pultruded materials with direct addition of roving strands. Polym Eng Sci. 1991;31:1316-29.

[4] Silverman EM. Effect of glass fiber length on the creep and impact resistance of reinforced thermoplastics. Polym Compos. 1987;8:8-15.

[5] Nguyen BN, Bapanapalli SK, Holbery JD, Smith MT, Kunc V, Frame BJ, et al. Fiber length and orientation in long-fiber injection-molded thermoplastics - part I: modeling of microstructure and elastic properties. J Compos Mater. 2008;42:1003-29.
[6] Gupta M, Wang KK. Fiber orientation and mechanical properties of short-fiber-reinforced injection molded composites: simulated and experimental results. Polym Compos. 1993;14:367-82.
[7] Hofmann JT. Extension of the Method of Ellipses to Determining the Orientation of Long, Semi-Flexible Fibers in Model 2- and 3-Dimensional Geometries. PhD Thesis: Virginia Polytechnic Institute and State University; 2013.
[8] Hine PJ, Davidson NC, Duckett RA, Ward IM. Measuring the fibre orientation and modelling the elastic properties of injection-moulded long-glass-fibre-reinforced nylon. Compos Sci Technol. 1995;53:125-31.
[9] Jeffery GB. The motion of ellipsoidal particles immersed in a viscous fluid. Proc R Soc London, Ser A. 1922;102:161-79.
[10] Folgar F, Tucker CL. Orientation behavior of fibers in concentrated suspensions. J Reinf Plast Compos. 1984;3:98-119.
[11] Huynh HM. Improved Fiber Orientation Predictions for Injection-Molded Composites. Master's Thesis: University of Illinois Urbana-Champaign; 2001.
[12] Wang J, O'Gara JF, Tucker CL. An objective model for slow orientation kinetics in concentrated fiber suspensions: theory and rheological evidence. J Rheol. 2008;52:1179-200.
[13] Férec J, Ausias G, Heuzey MC, Carreau PJ. Modeling fiber interactions in semiconcentrated fiber suspensions. J Rheol. 2009;53:49-72.
[14] Phelps JH, Tucker CL. An anisotropic rotary diffusion model for fiber orientation in short- and long-fiber thermoplastics. J Non-Newton Fluid Mech. 2009;156:165-76.
[15] Strautins U, Latz A. Flow-driven orientation dynamics of semiflexible fiber systems. Rheol Acta. 2007;46:1057-64.
[16] Rajabian M, Dubois C, Grmela M. Suspensions of semiflexible fibers in polymeric fluids: rheology and thermodynamics. Rheol Acta. 2005;44:521-35.
[17] Ortman K, Baird D, Wapperom P, Whittington A. Using startup of steady shear flow in a sliding plate rheometer to determine material parameters for the purpose of predicting long fiber orientation. J Rheol. 2012;56:955-81.
[18] Le Corre S, Caillerie D, Orgéas L, Favier D. Behavior of a net of fibers linked by viscous interactions: theory and mechanical properties. J Mech Phys Solids. 2004;52:395-421.
[19] Tang W, Advani SG. Dynamic simulation of long flexible fibers in shear flow. CMES-Comp Model Eng. 2005;8:165-76.
[20] Hinch EJ. The distortion of a flexible inextensible thread in a shearing flow. J Fluid Mech. 1976;72:317-33.
[21] Wang G, Yu W, Zhou C. Optimization of the rod chain model to simulate the motions of a long flexible fiber in simple shear flows. Eur J Mech B-Fluid. 2006;25:337-47.
[22] Switzer LH, Klingenberg DJ. Flocculation in simulations of sheared fiber suspensions. Int J Multiphase Flow. 2004;30:67-87.
[23] Wang J, Tozzi EJ, Graham MD, Klingenberg DJ. Flipping, scooping, and spinning: drift of rigid curved nonchiral fibers in simple shear flow. Phys Fluids. 2012;24:123304.
[24] Lipscomb GG, Denn MM, Hur DU, Boger DV. The flow of fiber suspensions in complex geometries. J Non-Newton Fluid Mech. 1988;26:297-325.
[25] Dinh SM, Armstrong RC. A rheological equation of state for semiconcentrated fiber suspensions. J Rheol. 1984;28:207-27.
[26] Djalili-Moghaddam M, Toll S. A model for short-range interactions in fibre suspensions. J Non-Newton Fluid Mech. 2005;132:73-83.
[27] Keshtkar M, Heuzey MC, Carreau PJ, Rajabian M, Dubois C. Rheological properties and microstructural evolution of semi-flexible fiber suspensions under shear flow. J Rheol. 2010;54:197-222.

[28] Sepehr M, Ausias G, Carreau PJ. Rheological properties of short fiber filled polypropylene in transient shear flow. J Non-Newton Fluid Mech. 2004;123:19-32.
[29] Laun HM. Orientation effects and rheology of short glass fiber-reinforced thermoplastics. Colloid Polym Sci. 1984;262:257-69.
[30] Sepehr M, Carreau PJ, Moan M, Ausias G. Rheological properties of short fiber model suspensions. J Rheol. 2004;48:1023-48.
[31] Eberle APR, Baird DG, Wapperom P, Vélez-García GM. Using transient shear rheology to determine material parameters in fiber suspension theory. J Rheol. 2009;53:685-705.
[32] Eberle APR, Baird DG, Wapperom P, Vélez-García GM. Obtaining reliable transient rheological data on concentrated short fiber suspensions using a rotational rheometer. J Rheol. 2009;53:1049-68.
[33] Ericsson KA, Toll S, Månson J-AE. Sliding plate rheometry of planar oriented concentrated fiber suspension. Rheol Acta. 1997;36:397-405.
[34] Mazahir SM, Vélez-García GM, Wapperom P, Baird D. Evolution of fibre orientation in radial direction in a center-gated disk: experiments and simulation. Composites Part A. 2013;51:108-17.
[35] Mazahir S. Improvement in Orientation Predictions of High-Aspect Ratio Particles in Injection Mold Filling Simulations. PhD Thesis: Virginia Polytechnic Institute and State University; 2013.
[36] Meyer KJ, Hofmann JT, Baird DG. Initial conditions for simulating glass fiber orientation in the filling of center-gated disks. Composites Part A. 2013;49:192-202.
[37] Meyer KJ. Improved Prediction of Glass Fiber Orientation in Basic Injection Molding Geometries. PhD Thesis: Virginia Polytechnic Institute and State University; 2013.

Chapter 2 Review of Literature

Chapter 2 Review of Literature

This chapter is devoted to reviewing experimental and theoretical works pertaining to the rheology of fiber suspensions. The first section provides general information on fiber composites. Classifications of fiber suspensions are given in §2.2. In §2.3 a brief review is provided on the methods for experimentally determining fiber orientation. In §2.4 the rheological behavior of fiber suspensions is reviewed in addition to the experimental techniques used to gather this data. The current models for fiber orientation are presented in §2.5. Finally, in §2.6 the available theories for the extra stress caused by the presence of fibers is reviewed.

2.1 Fiber Composites

Fiber composites have been used considerably in industrial applications since their first introduction in the 1940s. The demand to increase a part's mechanical properties while improving the strength to weight ratio has driven continued research over the last three decades. Composites can be regarded as using continuous or discontinuous fibers. Continuous fiber composites are often created from a woven fabric impregnated with thermoplastic or thermoset resins. This process can be performed through compression molding or through manual application which is labor intensive. Discontinuous fiber composites often consist of dispersed fibers in a thermoplastic resin which can be molded using traditional melt processing techniques [1]. Composite pellets used for in industrial processes can be formed in multiple ways. Fibers can be directly added to pure resin during melt compounding to create pellets containing relatively short fibers. Pellets containing longer fibers are generated through a pultrusion process. In this process a bundle of fibers are coated in polymer and then pelletized to a final desired length. The fibers are not well dispersed in this process but the fiber lengths are that of the pellet. Industrial demand for fiber composites has allowed composite pellets to be available from a variety of manufacturers.

The fibers within a composite are chemically different than the surrounding polymer. In order to obtain maximum mechanical benefit, the load must be well distributed from the resin to

the fiber reinforcement. An adhesion promoter or coupling agent is used to improve the interaction between the fibers and the polymer. The coupling agent may be regarded as a finish, sizing, or adhesive depending on thickness [2]. Fibers used in woven fabrics are often given a finish to increase lubrication and protect the fibers from any significant damage before embedded with resin. Glass fibers, for example, can suffer significant mechanical failure due to scratching or defects created during processing. Additional processing is required to apply sizing to the fabric before the resin. Discontinuous fibers are coated with sizing before they are combined with the polymer. Sizing must have desirable mechanical properties to carry the load while the composite is stressed. In addition, sizing should be able to withstand the thermal and mechanical conditions experienced during processing.

Commercial suppliers of fiber composites typically have their own proprietary formulation for coupling agents, often including a lubricant, antistatic, binder and coupling agent [2]. Silane based coupling agents are typically used for glass fibers and other fillers. Natural fibers are hydrophilic and subject to swelling which provides conditions for fungi to degrade the fiber [3]. Silane adhesion promoters and other treatments aim to make fibers less hydrophilic and improve the processing limitations of natural fibers. Some of these processes may reduce the mechanical properties of the fibers, but the composite strength is improved with increased fiber-matrix interaction.

The presence of coupling agents improves mechanical properties but mixed results have been reported on the rheology. Han and coworkers [4] tested glass beads with two silane coupling agents and observed an increase in viscosity for one while the other caused a decrease. They also reported no impact on elasticity due to the coupling agent. Kalaprasad et al. [5, 6] tested untreated glass and sisal fibers in polyethylene along with the effect of sizing on the rheology. An increase in viscosity was attributed to increased interaction between fibers and the suspending fluid.

The significance of Brownian motion in a suspension must be determined before models and experiments can be developed. The term Brownian motion is given to the random motion of a suspended particle in a fluid. The dimensionless rotary Péclet number ($\mathrm{Pé}_r$) is used to determine if a suspension is affected by Brownian motion:

$$\mathrm{Pé}_r = \frac{\dot{\gamma}}{D_r} \tag{2.1}$$

where, $\dot{\gamma}$ is the shear rate and D_r is the rotational diffusion constant. For $\mathrm{Pé}_r < 1$ the randomizing effect of Brownian motion is significant. Ganani and Powell [7] calculate $\mathrm{Pé}_r$ at $\dot{\gamma} = 0.01s^{-1}$ to be on the order of 10^7 for glass fibers with an average diameter of 11 μm and length of 80 μm. The rotary Péclet number will increase with increasing matrix viscosity and fiber length [8]. Brownian motion for fiber suspensions is considered negligible because $\mathrm{Pé}_r \gg 1$ [9-11].

The densities between the fiber and suspending fluid often differ which may result in fiber sedimentation due to gravity. This impact can be diminished by controlling the time scale that a fiber is suspended the fluid under static conditions. Chaouche and Koch [10] proposed an expression for the time scale, t_s, required for a fiber to translate over a distance equal to its length with the fiber parallel to the sedimentation direction as:

$$t_s = \frac{8\eta_m L}{\Delta\rho g d^2[\ln(2a_r) - 0.72]} \tag{2.2}$$

where, η_m is the matrix viscosity, L is the fiber length, $\Delta\rho$ is the difference in densities of fiber and suspending fluid, g is the acceleration due to gravity, d is fiber diameter, and a_r is the fiber aspect ratio defined as the ratio of fiber length to diameter (L/d). For fibers in polymer melts the sedimentation time is significantly large. Fundamental studies of fibers in low viscosity oils must be performed in a timely manner such that sedimentation does not influence the results. The lowest viscosity material that Chaouche and Koch tested still had a sedimentation time scale of about 2

hours. Djalili-Moghaddam and coworkers [12] show that sedimentation can increase the magnitude of the transient shear stress response at short times yet returns to the same steady state as the dispersed suspension.

2.2 Classification of Fiber Suspensions

2.2.1 Classification by Concentration

The concentration regimes for fiber suspensions stem from theories of rod-like molecules given by Doi and Edwards [13]. Concentration regimes are governed by the ability or restriction of a rod to freely rotate. This depends on particle concentration and aspect ratio. These regimes are regarded as dilute, semi-dilute and concentrated. Doi and Edwards discuss these regimes with the following relationship between volume fraction, ϕ_v, and number of fibers per unit volume, n:

$$\phi_v = \frac{\pi n L^3}{4a_r^2}. \tag{2.3}$$

Suspensions are considered to be dilute when a fiber can freely rotate without interaction with other fibers. Fibers are of considerable distance from each other such that any hydrodynamic effects are insignificant. More specifically, the interparticle distance must be greater than the length of a fiber. This imposes the upper bound on the dilute regime as, $n < L^{-3}$. In terms of aspect ratio and concentration the restriction is given as $\phi_v < \pi/4a_r^2$, or approximately $\phi_v < a_r^{-2}$.

The onset of the semi-dilute regime is defined where hydrodynamic interaction between fibers begins to occur. However, direct fiber-fiber contacts are considered limited. Hydrodynamic interactions theoretically occur when rods are within length L of one another or when $n > L^{-3}$. Rotation is considered to be impacted due to these interactions. The properties of the system are not thought to be severely impacted until the mean spacing between fibers is on the order of the fiber diameter. The upper limit on the semi-dilute regime is designated such that the mean spacing is significantly larger than the fiber diameter. The mean spacing between fibers is dependent on

the orientation state. For isotropic orientation the limit is given by $n \ll (dL^2)^{-1}$ and for perfect alignment $n \ll (d^2L)^{-1}$. In terms of aspect ratio these bounds are approximated by $\phi_v \ll a_r^{-1}$ and $\phi_v \ll \pi/4$ for random and aligned orientation, respectively.

The onset of the concentrated regime occurs where $\phi_v \geq a_r^{-1}$. Fiber-fiber interactions are now significant in addition to hydrodynamic interactions. Above a critical concentration, rod-like molecules can exhibit liquid crystalline behavior. Doi and Edwards [13] estimate the critical concentration as $\phi_v \cong 4a_r^{-1}$ and Flory [14] as $\phi_v \cong 12.5a_r^{-1}$. Above the critical concentration rod-like molecules will align on a macroscopic scale at equilibrium. Fiber suspensions may experience analogous behavior by forming clusters of fibers at high concentrations. Suspensions of industrial interest have concentrations of $\phi_v > 0.1$ [1]. As an example, a 30 wt% glass fiber suspension can achieve this critical concentration with an aspect ratio of 30.

2.2.2 Classification by Length

Often a distribution of fiber lengths is observed in processed composites. Fiber length distributions typically exhibit a log-normal or Weibull distribution. It is common to represent the distribution of fibers as number (L_n) and weight (L_w) averages:

$$L_n = \frac{\sum_i n_i L_i}{\sum_i n_i} \tag{2.4}$$

$$L_w = \frac{\sum_i n_i L_i^2}{\sum_i n_i L_i} \tag{2.5}$$

where, n_i is the number of fibers with length L_i in the fiber length distribution. The weight average gives more weight to longer fibers in the distribution than the number average. Huq and Azaiez [15] argue that these averages fail to accurately represent contributions from long and short fibers to the suspension rheology. A modified average fiber length ($L_{mod-avg}$) is derived to be valid for dilute and semi-dilute concentrations:

$$L^2_{mod-avg} = \frac{\sum_i n_i L_i^3}{\sum_i n_i L_i}. \tag{2.6}$$

This average gives more weight to longer fibers than the number or weight averages. Longer fibers were determined to have a greater impact on the viscosity. It should be noted that this average was determined based on the steady shear viscosity and that other material functions were not addressed.

Accurate techniques for measuring fiber length are required to represent a large number of fibers in a composite by a small subset. Fibers must be separated from the suspending matrix either in solvent or from matrix burn off. The fibers are dispersed and imaged on an optical microscope, desktop scanner or other imaging devices. Imaged fibers are counted to create a fiber length distribution. The work of Kunc et al. [16] provides an in-depth analysis of this method. This work also provides a procedure and theoretical corrections to accurately extract a small sample set of fibers from a larger part while accounting for sampling bias.

A fiber can receive the general designation as being short or long. The threshold is based on mechanical properties which is 1 mm in length for glass fibers [17]. However, the terms short and long are often loosely used to designate rigid and semi-flexible fibers, respectively. Short fibers are thought to behave as rigid rods when subjected to flow, while long fibers have the potential for flexibility. Switzer and Klingenberg [18] described the effective stiffness of a cylindrical fiber with the following expression:

$$S^{eff} = \frac{E_Y \pi}{\eta_m \dot{\gamma} a_r^4} \tag{2.7}$$

where, E_Y is the Young's modulus of the fiber, η_m the matrix viscosity and $\dot{\gamma}$ the shear rate. This value characterizes the ratio of a fiber's bending moment with the viscous torque imposed on the fiber from the fluid [19]. As fiber length increases, the effective stiffness of the fiber decreases

significantly with a_r^4. With this dependency on aspect ratio, long fibers may exhibit significantly more bending under flow than short fibers.

2.3 Fiber Orientation Measurements

The anisotropic mechanical properties achieved by fiber composites are determined by the fiber orientation. A variety of approaches have been used to directly measure fiber orientation within a composite. The three-dimensional microstructure can be assessed using confocal laser scanning microscopy [20], scanning acoustic microscopy [21], scanning electron microscopy [22], x-ray tomography [23, 24], microradiography [25], and optical microscopy [26, 27]. Imaging techniques that are able to capture the true three-dimensional structure are often limited to a maximum sample size and may not be universal to all matrix or fiber types or combinations thereof. Techniques that use an imaging plane instead of the three-dimensional volume must make the assumption that fibers are rigid cylinders and have a circular cross section. This method has been widely used for short fiber composites and is often referred to as the method of ellipses [28].

A fiber's intersection with the imaging plane produces an ellipse that can provide a majority of the three-dimensional orientation. The work of Vélez-García and coworkers [27] provides a repeatable procedure and analysis to produce reliable orientation data for short fiber composites. In this method, samples are embedded in mounting compound (thermoplastic resin or epoxy) and polished using modified metallographic techniques. More specifically, it is suggested to remove at least 2 mm of material through coarse polishing with sand paper up to 600 grit. Polishing is completed on an automated polisher using a series of slurries containing particle sizes down to 0.5 μm. A this point the ellipse of a fiber can be seen on the imaging plane, but the contrast between fiber and resin may be small and not enough information may be displayed to perform unambiguous measurements of fiber orientation. Etching of the polished surface with oxygen plasma provides a means to increase the contrast [29, 30] and removes a layer of polymer matrix to reveal the three-dimensional spatial orientation of a fiber [27].

Fiber orientation can be determined by measuring the in-plane angle (ϕ) and the major (M) and minor (m) axes of the ellipse. The out-of-plane angle, θ, can be determined from the ratio of the minor to major axis:

$$\theta = \arccos\left(\frac{m}{M}\right). \tag{2.8}$$

The angles θ and ϕ can be used to describe the orientation of each fiber through a unit vector, **p**, with the following components described in Cartesian coordinates:

$$\mathrm{p}_1 = \sin\theta\cos\phi \tag{2.9}$$

$$\mathrm{p}_2 = \sin\theta\sin\phi \tag{2.10}$$

$$\mathrm{p}_3 = \cos\theta. \tag{2.11}$$

A pictorial representation of the orientation vector is shown in Figure 2.1(a). The intersection of a fiber with the x_1x_2-plane is also shown in Figure 2.1(b). The shaded region indicates the direction of the fiber into the matrix which allows for ϕ to be measured unambiguously.

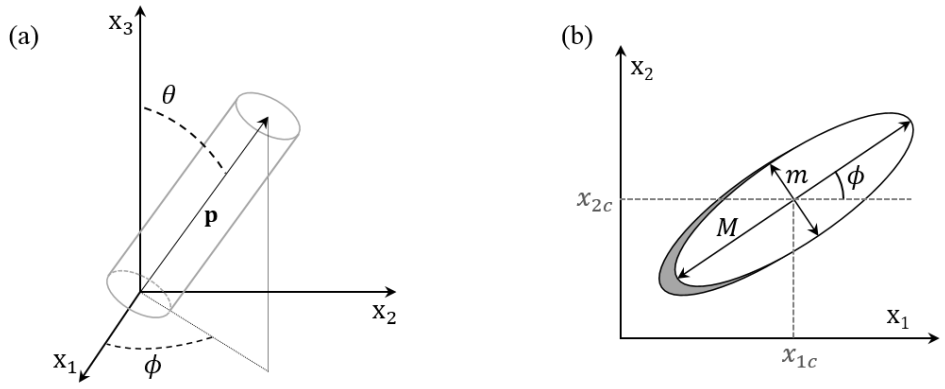

Figure 2.1: (a) A general representation of a rigid high aspect ratio fiber in spherical coordinates and (b) an elliptical projection into the x_1x_2 inspection plane.

A second moment of orientation tensor provides a compact means to represent a population of fibers. The orientation tensor, **A**, describing a population of fibers can be formed by averaging the dyadic products of each **p** vector:

$$\mathbf{A} = \langle \mathbf{pp} \rangle \tag{2.12}$$

Using a two-dimensional inspection plane to measure fiber orientation induces imaging bias that must be taken into account to correctly represent the average orientation of a population of fibers. Fibers perpendicular to the inspection plane have a higher probability to intersect the plane than fibers that are parallel. The following relationship provides an unbiased orientation tensor [31]:

$$\mathbf{A} = \frac{\sum_k (\mathbf{pp})_k L_k F_k}{\sum_k L_k F_k} \tag{2.13}$$

where, $(\mathbf{pp})_k$ is the orientation tensor of the *k-th* fiber, L_k is the length of the fiber, and F_k is a weighting function to account for imaging bias. An additional weighting function was added by Vélez-García et al.[32] to better reflect the distribution of fiber orientation through the sample thickness. Konicek [26] provided an expression for the most general form of the weighting function as:

$$F_k = \frac{1}{L_k \cos\theta_k + d_k \sin\theta_k}. \tag{2.14}$$

This relationship is based on including fiber projections that contain less than half of an ellipse. Orientation cannot be measured accurately for fiber cross sections that are smaller than half of an ellipse. Bay and Tucker [31] account for the experimental limitation that only ellipses larger than half of an ellipse can be measured reliably with the following weighting function:

$$F_k = \begin{cases} \dfrac{1}{L_k \cos\theta_k} & \theta_k \leq \theta_c \\ \dfrac{1}{d_k} & \theta_k > \theta_c \end{cases} \tag{2.15}$$

where the cut-off angle, $\theta_c = \arccos(d/L)$. This cut-off angle is reached as θ approaches $\pi/2$, such that the projection of a fiber on the inspection plane is a rectangle.

Enough fibers must be imaged in order to obtain a representative average fiber orientation for the region of interest in the composite. For short fibers, consistent orientation results were obtained when $\sum F_k = 100 \pm 10$ fibers/mm [32]. This equated to an image analysis width of 700 μm. Hofmann and coworkers [33] determined that the image analysis width must be extended for long fibers because objects extending past the viewing area cannot be measured accurately. This issue arises when fibers longer than the image width are parallel to the inspection plane and that a significant amount of the projection is outside the viewing area. Image analysis width is increased to include highly elongated ellipses within the viewing area. An image analysis width of 5.5 mm produced minimal statistical error in a sample subjected to simple shear flow. Measuring long fibers with the method of ellipses must be done with caution because fibers may no longer be able to be considered as rigid rods. Bay and Tucker [31] state that slight curvature will only have a small effect on measurements as long as the following condition is met:

$$\frac{L}{2r_c} \ll 1 \tag{2.16}$$

where, L is the fiber length and r_c is the radius of curvature. The work of Hofmann [34] evaluated the method of ellipses in two- and three-dimensional flows and observed only a small quantity of bent fibers. This work concluded that the method of ellipses can be used to quantify long glass fibers provided that an enlarged image analysis width is used.

2.4 Rheology of Fiber Suspensions

Understanding the rheology of complex systems under well-defined conditions provides insight to the fluid's behavior in intricate industrial processes. A variety of reviews have been dedicated to the rheology of fiber suspensions [35-41]. In general, the addition of solid particles increases the magnitude of the rheological material functions. Furthermore, particles with aspect ratios will orient based on the flow conditions, thus impacting the material functions. The following literature review will provide an overview of the various methods and results of obtaining rheological data of fiber suspensions. This includes investigations on short and long fiber suspensions because long fiber systems typically contain a wide distribution of fibers of varying lengths. Additionally, the rheology of long fiber systems should correlate with trends observed for short fiber suspensions while the discrepancies should be a result of the increased complexities that arise with longer fiber lengths.

2.4.1 Rheological Behavior

The measurements of the rheological material functions for a fiber suspension are determined by the kinematics of the imposed flow field and the measured stress components. Although flow geometry can significantly affect rheological measurements in fiber suspensions, general trends appear to be relatively universal. A separate analysis is devoted to the methods of obtaining the rheological properties in §2.4.2.

2.4.1.1 Steady Shear

The addition of fibers causes an increase in the steady shear viscosity at all shear rates with the most distinguishable increases occurring at low rates [10, 15, 42-45]. The increase in viscosity is a function of aspect ratio, concentration and fiber curvature. Numerous works report that with increasing aspect ratio and/or concentration a shear thinning behavior occurs at low shear rates [7, 10, 43, 45, 46]. It has not been reported that fluids exhibiting this shear thinning at low rates have a zero shear viscosity. The rates that this may occur are likely below the instrument's measurable

limits and may be of little significance to industrial processes. Chaouche and Koch [10] report no shear thinning to occur in the semi-dilute regime for short fibers where fiber contacts are considered rare. However, in the concentrated regime shear thinning increased with concentration and decreased with increasing matrix viscosity. At higher rates the steady shear viscosity of the suspension parallels that of the suspending medium. For shear thinning matrices, the suspension viscosity typically plateaus before transitioning to the shear thinning regime of the matrix. The magnitude of viscosity is only slightly different for different suspensions at high rates due to aligned fiber orientation.

2.4.1.2 Oscillatory Shear

Oscillatory measurements provide a sufficient representation of the shear viscosity as long as the Cox-Merz [47] relationship remains valid. Some evidence does exist to support the use of the Cox-Merz relationship at low rates [48] and up to a certain concentration [49], but is generally regarded as not acceptable for fiber suspensions [48, 50, 51]. Dynamic material functions are largely unchanged, only increasing in magnitude due to the addition of solid particles [49, 52, 53]. A shear thinning behavior in the complex viscosity at low frequencies can parallel the shear thinning behavior that is observed in steady shear [54-56]. Some researchers observed a slight inflection in the shear storage modulus (G') in the terminal regime [49, 53, 57]. Additionally, this effect was more pronounced with increasing fiber length [53]. However, it is unclear in these works what may be responsible for a measured change in the suspension's storage modulus. A note of caution with oscillatory measurements is that fibers will align with the straining direction under oscillatory flow and the rate of orientation is strain dependent [58]. Large amplitude oscillatory shear has been done to further investigate the composite microstructure [52, 56]. In these works, only slight non-harmonics are observed and attributed to the imperfect reversibility of fiber orientation.

2.4.1.3 Transient Response

The transient response upon the startup or cessation of steady shear is used to give insight into fiber orientation kinetics. During the startup of shear flow, fiber motion causes a stress growth overshoot that will relax to a steady state [7, 48, 52, 59-67]. The magnitude and width of the stress growth overshoot is impacted by the rate of fiber rotation which is a function of aspect ratio and concentration. Laun [59] tested short glass fibers up to 35 wt% and observed that the strain where the maximum stress occurs was independent of concentration. Sample preparation and loading sequence may influence fiber orientation. Some works have elected to subject their samples to shearing prior to rheological measurements [48, 56, 64, 68, 69]. When the startup measurements are performed with shearing in the same direction as the flow history, a small stress growth overshoot is observed due to little fiber rearrangement. When the direction of flow is reversed relative to the direction of initial shearing, the fibers must undergo significant rotation to realign in the flow direction which causes a delay in the stress growth response [52, 60, 65, 67]. Relaxation properties of the composite can be assessed under the cessation of shear flow. The relaxation of the suspension is largely unimpeded by the presence of rigid particles [9, 65] indicating that elasticity is relatively unchanged.

2.4.1.4 Normal Stresses

Normal stresses have resulted from the addition of fibers to the suspending fluid and have been reported for steady, oscillatory and transient measurements. The Weissenberg effect, or rod-climbing, has been reported and may be the first indication of normal stresses in fiber suspensions [70-72]. Most data on the normal stresses in fiber suspensions were obtained from cone-and-plane or parallel disk geometries. A cone-and-plate setup can directly measure the first normal stress difference, N_1, from the normal force transducer. For parallel disks the normal force transducer measures the differences in normal stresses (N_1-N_2). Direct measurements of the secondary normal stress, N_2, are often not made. Available N_2 data for polymer melts show N_1 is greater by

an order of magnitude [73]. Others adopt the Weissenberg hypothesis as a first approximation assuming that N_2 should be exactly zero [56, 74, 75]. Despite the dependence on flow geometry similar overall trends are observed. Normal stresses are observed above a critical concentration and may be the result of fiber-fiber interactions [39]. It has been reported that the normal stresses appear to be more sensitive to concentration than the shear stress [56, 76, 77]. Under steady shear, normal stresses increase proportionally with shear rate [42, 76]. For transient flow, an overshoot is observed which relaxes to a steady state. Normal stresses developed during oscillatory flow are often below the instruments sensitivity for small amplitude oscillatory shear [56]. Increasing the strain amplitude increases the magnitude of the normal forces that are able to be measured by the instrument. For large amplitude oscillatory shear a symmetric response is observed in the stress-strain loops if fiber orientation is symmetric in reference to the flow direction.

2.4.1.5 Extensional Viscosity

Complex fluids in shear free flows can often exhibit interesting behaviors unseen from shear deformation. Such flows are of considerable interest in molding processes at locations where flow can diverge or converge. Early works found that by adding fibers to a suspending fluid the extensional viscosity could increase by an order of magnitude while the shear viscosity might only increase by 10% [72, 78]. This causes the ratio of the steady extensional to the steady shear viscosity, or Trouton ratio, to increase with increases in aspect ratio or concentration [48, 78-81]. Additionally, the substantial increase in extensional viscosity is observable with only a dilute concentration of particles [82]. For more concentrated systems, Kamal and coworkers [83] observed that the suspension would reach a steady extensional viscosity faster than the suspending fluid. They also noted a thinning in extensional viscosity as a function of strain rate. In some cases the transient extension has shown a stress growth overshoot which is dependent on the rate of deformation [84, 85].

Laun [59] investigated the effects of initial orientation of short fibers on the extensional behavior and found that random orientation showed a lower extensional stress than samples with fiber alignment parallel or perpendicular to the straining direction. The rate of stress growth for the random sample is slower than that of the pre-oriented samples, but continues to increase toward the values of the aligned samples prior to sample failure. The addition of fibers causes the maximum Hencky strain of the suspension to decrease when compared to the suspending fluid [59, 83]. An interesting observation by Laun [59] noted that the recoverable strain was greater for the filled system than the pure matrix. This was attributed to the presence of rigid fibers impeding the elongation of the sample. Further evidence of the restriction caused by fibers giving by strain hardening which is not observed for the pure matrix [81]. Creasy and coworkers [85] believe that the extensional response is governed by the shearing behavior of the suspending fluid due to large local deformation rates. This is thought to be the result of fibers that cannot deform or extend with the flow field [59].

2.4.1.6 Yield Stress

The existence of a yield stress is a topic that is still up to some debate for fiber suspensions. Many researchers have reported a yield stress behavior both in shear [68, 77, 79, 86-92] and shear free flows [83, 93]. For oscillatory measurements, Roberts and Jones [94] observed a truncated sinusoidal response indicating the presence of a yield stress in continuous fiber composites while Ericsson et al. [95] stated that there was no yield behavior for long fibers in a rectilinear flow. Morrison and Harper [91] admit that their yield-like response was most likely due to wall effects rather than a true yielding behavior of the suspension. Others have attributed a yielding response to direct fiber-fiber contacts [92] which may explain a variance in yield stress with fiber concentration and aspect ratio [83, 86, 88, 93].

2.4.1.7 Fiber Flexibility

Much of the flow behavior mentioned in the previous sections is largely dependent on fiber length or aspect ratio. It has been reported by many authors that the existence of flexibility in the fibers can provide significant increases in magnitude to the rheological response [44, 52, 74, 75, 77, 81, 96, 97]. Goto and coworkers [44] reported that flexible fibers are capable of increasing the shear viscosity by a factor of two to three when compared to that of rigid fibers of the same size. A non-linear relationship between the first normal stress difference and shear stress of vinylon fibers was attributed to the fibers' flexibility because this phenomena was not observed in rigid glass fibers [77, 97]. Keshtkar and coworkers [52] attributed an increase in shear thinning to increased fiber flexibility. During the startup of shear flow they observed that the magnitudes of stress growth overshoot and steady state viscosity increased with flexibility [52, 75]. Ortman et al. [98] observed the shear stress growth overshoot to broaden for long glass fibers when compared to short fibers. The authors could not conclude whether the change in the rheological response was due to bending fibers or an increase in fiber-fiber interactions due to the increased fiber length. Under oscillatory flow, it is reported that fiber flexibility can cause the development of a fiber network at low rates [74]. It is then determined that rigid fibers are more apt to flow alignment than fibers exhibiting flexibility. Flow visualization experiments saw only a slight presence of flexibility under semi-dilute conditions [75]. However, fiber flexibility can cause the suspension to favor more fiber-fiber interactions which can give rise to increased normal stresses.

2.4.2 Rheometry

The statements in the previous section regarding the flow behavior of fiber suspension are largely observed independent of the testing methods. However, the flow geometry will significantly impact fiber orientation and rheological measurements if precautions are not taken. In this section the various methods of obtaining rheological data are discussed in further detail along with their limitations.

2.4.2.1 Shear Rheometry: Pressure Driven Flows

Capillary rheometry provides the steady shear viscosity at high shear rates that are often present in industrial processes. The largest differences in the rheological response obtained from the capillary rheometer are observed at the lowest shear rates while converging toward the response of the suspending fluid at high rates [6, 59, 63, 81, 88, 99-104]. Many authors are only able to report data in the power-law region of the suspending fluid [48, 49, 51, 57, 63, 81, 105]. Traditional corrections often associated with capillary rheometry are applied to fiber suspensions, such as: the Bagley correction [106] for entrance and exit pressure effects, Weissenberg-Rabinowitsch correction [107] for non-parabolic velocity profiles and Mooney correction [108] to account for the slip of fluid at the capillary wall. Each correction has been employed to varying degrees depending on the linearity of the measured data [61], while in other cases have been considered negligible [48, 79, 99].

There has been some mention to the presence of wall effects for capillary measurements. Chung and Cohen [109] observed that if the capillary diameter is similar to that of the fiber length then wall effects impact the viscosity similar to wall slip. These effects appear to diminish with higher matrix viscosity. It has been observed that the converging flow at the capillary causes increased pressure corrections to be applied when compared to the suspending fluid [104], which has been shown to increase with increasing fiber aspect ratio [59, 110]. The entrance angle to the capillary die does not appear to significantly influence pressure readings for short fiber suspensions when compared to long fibers [110]. The semi-angle for the contraction is defined with respect to the center line of the capillary. Pressure readings varied by 10 MPa for long fibers for entrance semi-angles of 7.5 to 90 degrees at an apparent shear rate of $5000s^{-1}$. As a comparison, a short fiber suspension saw only a variance of 1 MPa under the same testing conditions. At the contraction, circulating secondary flow was observed [111] and is attributed to the presence of normal stresses in the fiber suspensions [112]. The presence of fibers also reduces the die swell at the exit of the capillary [59, 88, 102-104]. This behavior is thought to be a function of the elasticity

of the composite as well as the die geometry and processing conditions. The quality of the extrudate has been attributed to shear rate, fiber aspect ratio, concentration and fiber flexibility, with uniform extrudates observed with short, flexible and/or well wetted fibers [6, 101, 112].

Despite the wide use of the capillary rheometer to characterize fiber suspensions, there are a number of limitations that require the data to be accepted with some caution. The high shear rates cause a significant amount of stress that will induce fiber breakage, even at relatively low rates within the capillary [5, 79, 88, 100, 101, 109, 113]. However, capillary data generally appears to coincide with steady shear data from other instruments. Other issues arise with the flow of fibers even if no breakage is reported [99]. Fibers have the ability to network which may plug the capillary entrance or create instances where localized concentration fluctuations pass through the capillary [100, 104, 114]. This reasoning aims to explain pressure fluctuations that are observed during the experiments [103, 112]. Lastly, the converging flow at the die entry causes many of the fibers to become oriented prior to entering the capillary [113, 114]. This limits the data obtained from the capillary rheometer to a steady state fiber orientation at high shear rates.

The slit die rheometer has received relatively little use in characterizing the steady shear viscosity of fiber suspensions. Good agreement has been observed between slit die data and data obtained from a capillary rheometer [48, 59]. Similar to the capillary rheometer, the slit die data has been shown to correlate with data obtained from a cone-and-plate geometry [59, 97] and parallel disks [48]. Kitano et. al. [97] observed a linear pressure profile for short fibers through the slit die indicating that the flow is fully developed. This may be indicative of fiber orientation remaining largely unchanged through the length of the slit. Rheological data obtained from the slit die may then be limited to the steady state fiber orientation and steady shear viscosity.

2.4.2.2 Shear Rheometry: Drag Flows

Rotational rheometers are commonly used because they are easily adaptable to a variety of materials and testing conditions. Commonly used fixtures for fiber suspensions are the cone-and-

plate, parallel disk and concentric cylinders, each with their own limitations. With these setups, steady shear, transient and oscillatory measurements have probed the influence of fibers on the bulk flow behavior.

Concentric cylinders have largely been used to measure rheological response of a dilute concentration of particles in low viscosity suspending fluids. Variations on this flow field can be imposed using cup-and-vane fixtures [115] or a Brabender® torque rheometer [105, 116]. Early measurements used flow visualization to observed particle rotations [9, 71, 117-119]. Researchers observed that particles aligned in the primary flow direction produce a minimum viscosity [71]. Morrison and Harper [91] saw evidence of a wall slip and yield-like behavior in particle tracking experiments of short fibers. The yield-like behavior was attributed to wall effects on fiber orientation to which they suggest using wide gaps to minimize these effects. Wall slip was investigated by covering the inner cylinder with 100 grit paper. At low rates slippage was observed at the rough cylinder and not on the smooth outer cylinder. Slippage was reported to occur on both surfaces at high rates until clusters formed at the outer surface. Particle migration then caused slip to occur at the outer surface while no slip was observed at the rough inner cylinder. Later work by Mondy et al. [120] also observed particle migration in concentrated short fiber suspensions, noting increased fiber migration with concentration. The mechanism was attributed to the variation in shear rate causing rods to migrate out of high shear regions which are balanced by gradients in concentration.

Fiber loadings above a critical concentration displayed fluctuations in viscosity which could be a result of changes in orientation and fiber-fiber interactions [121]. This work is confirmed by Anczurowski and coworkers [122] who observed changes in orientation from particle interactions through the use of a microscope attached to the concentric cylinder apparatus. They recorded that collision frequency was directly proportional to concentration. However, the final orientation state was unchanged even above the critical concentration as long as flow remains

laminar. Additional work found that orientation of dilute suspensions exhibit irreversible behavior [123]. The deviation from reversible behavior increases with increasing shear strain.

A cone-and-plate geometry is often used on polymer melts due to a linear velocity profile imposed on the test specimen and for direct measurements of the first normal stress difference. The fixture is to be operated at a designed gap thickness which is small near the center of the sample. This may affect fiber orientation and the measured stress response. Despite these limitations a number of researchers have used this geometry, mostly to characterize short fiber suspensions. Some do acknowledge the existence of gap effects but consider them negligible at low rates [89]. Carter [42] was one of the earlier researchers to measure normal force and steady shear viscosity using a cone-and-plate. Unique to their work was the use of a plate that had manometer tubes installed to measure the normal force distribution as a function of radius in oscillatory and steady shear flows. From the normal force distribution the secondary normal stress difference can be determined, which is rarely measured for polymer melts and seldom discussed for fiber suspensions. Carter regards this normal force distribution data to be only of qualitative interest because of large variations in fluid height within the monometers. This data still indicates that flow near the axis of the cone-and-plate fixtures is different than flow at larger radii. It is not clear if this is an artifact of the cone-and-plate fixture or more generally related to the flow of fiber suspensions.

Parallel disk fixtures have often been used to determine the rheological properties of fiber suspensions due to gap effects caused by using traditional cone-and-plate fixtures. Mutel and Kamal [124] found short fiber results obtained from the cone-and-plate fixtures to be irreproducible and reported results obtained with parallel disks. The parallel disk geometry creates a velocity profile that is a function of radius and gap thickness. This causes the rate of fiber orientation to reflect the different shear rates between the parallel disks. The stresses measured are now a function of an average fiber orientation which may be significantly different depending on the location within the sample. Nevertheless, many works elect to use the parallel disks because

researchers appear to be more concerned with gap effects than the velocity profile. Nearly all authors using parallel disks acknowledge the effects of gap height on the measured response and many have shown reliable responses obtained when the gap height is two to three times the fiber length [11, 124]. When gaps are too small fiber orientation is constrained which reduces the magnitude of stress growth and causes the steady state to occur at later times [11, 12]. Further caution is raised when gap heights are too large, as edge effects can also cause error in the measurement of shear and normal stresses [12]. Sepehr and coworkers [60] report on three gap heights of 1.1, 1.4 and 1.9 mm for fibers with an average length of 260 μm at 30 wt%. Stress growth curves were nearly identical for 1.1 and 1.4 mm gaps while the 1.9 mm gap matched the profile of the others but was a higher magnitude. They elected to use gap thicknesses between 1.4 and 1.5 mm for the remainder of that work. Ganani and Powell [7] were able to use relatively large plates (7.5 cm diameter) and observed variations within experimental error for gaps between 0.6 and 1.3 mm for short fibers. Keshtkar et. al. [75] used the parallel disk rheometer in combination with a microscope to observe the bending of long fibers under flow.

In using a cone-and-plate, Han and Lem [43] state that multiphase fluids may not exhibit a constant shear rate across the gap. However, most authors are concerned with the narrow gaps which occur near the cone. This narrow gap hinders particle rotations and delays the transient response [9]. Djalili-Moghaddam and coworkers [12] propose the use of a truncated cone-and-plate apparatus where the gap at the center of the fixture is approximately the fiber length to minimize gap effects. However, this geometry combines a constant shear rate near the edge of the fixture with the flow field of parallel disks near the center. These authors state that parallel disk fixtures may measure the viscosity to be too high for shear thinning fluids. Improved results were obtained using an oversized truncated fixture that had a diameter of 100 mm. An additional improvement using the cone-and-plate fixture was made by Eberle et. al. [11] to impose a homogeneous shear rate while minimizing gap effects. Their method uses a 50 mm cone-and-plate fixture and suggests removing a 25 mm plug from the center of the sample to create a donut

shaped sample. The truncated fixture creates a flow field similar to parallel disks where the shear rate is a function of radius and gap thickness. Eberle et al. hypothesized that the inhomogeneous shear rate within parallel disks would lead to increased fiber collisions, ultimately slowing the transient response. Additionally, the magnitudes of viscosity and normal stresses were reduced significantly due to the use of the donut shape sample. This method is still limited to the designed gap thickness of the cone-and-plate fixture used. Also, the suspension must be of sufficient viscosity to maintain the donut shape while testing [75]. The donut shaped sample provides an improvement over parallel disk and cone-and-plant fixtures, but stream lines within the flow remain curved which may influence fiber orientation.

A sliding plate rheometer imposes rectilinear flow on the sample thus negating many of the issues that arise from the rotational rheometers. In this instrument, fluid is sandwiched between a stationary and moveable plate. The shear rate is controlled by plate velocity and gap thickness. Stress can be calculated from measured force and the contact area of the fluid on the plates. However, reliable measurements are only obtainable if edge effects are insignificant, the contact area is known and the friction of the structure holding the plates in position is accounted for. A sandwich rheometer maintains gap thickness by shearing samples on both sides of the moveable plate preventing the gap from changing even in the presence of normal stresses [125]. However, the problems of end effects and contact area still remain. Dealy [126] proposed the use of a shear stress transducer for use on a sliding plate rheometer with the aim to overcome limitations of measuring viscoelastic properties from other rheometers. Dealy and Soong [127] incorporated a shear stress transducer to locally measure shear stress in polymer melts and noted its applicability toward transient measurements at high rates. Rheometers incorporating a shear stress transducer often follow the design of Giacomin [128] and further discussed by Giacomin and coworkers [129]. The rectilinear flow may also be limited to a set displacement, but by varying gap thickness a significant range of shear strains and shear rates are obtainable. Sliding plate rheometers are also capable of measuring the first normal stress difference [130, 131], but such measurements have

yet to be performed for fiber suspensions. It should be noted that with the shear stress transducer there is a small gap surrounding the active face which interrupts the assumption of a no slip boundary conditions. Furthermore, material ingress at this location provides some degree of unavoidable error [132].

Laun [59] used a sandwich rheometer to study the transient behavior of short fibers at varying initial orientations. Samples of 2 mm in thickness were sheared under a constant shear stress of 5×10^4 Pa. The samples with planar orientation parallel to the flow and perpendicular to the flow exhibited approximately the same strain rate under creeping shear flow and were 2.5 times more viscous than the pure matrix. Fibers oriented parallel to the velocity gradient exhibited a very low strain rate. This sample saw an increase in fluid viscosity by a factor of 18. Random orientation was found to lie between these limiting cases. However, these experiments were limited in achievable strain and only reported transient data for times less than 0.5 seconds. Servais and Måson [92] confirmed that no slip occurred in simple shear for long fiber suspensions through the use of a sandwich rheometer with protruding cylinders to roughen the surface. They were also able to show good agreement between data taken from the sandwich rheometer and a sliding plate rheometer with a shear stress transducer for both steady and oscillatory shear. Steady shear and oscillatory measurements deviated slightly at high rates.

The work of Ericsson and coworkers [95] used a sliding plate rheometer with the shear stress transducer to measure the rheology 12.7 mm long fiber suspensions with planar orientation, which is thought to minimize gap effects. Oscillatory measurements were made at 1 Hz while transient measurements ranged from 0.2 to 30 s^{-1}. They allowed samples to cool within the rheometer to verify fiber content and to evaluate changes in fiber orientation after the sample has been subjected to flow. In steady shear measurements, the viscosity had a quadratic dependency on concentration at high rates but displayed an increasing dependency on concentration as shear rates decreased. Steady shear measurements also revealed that there was no distinct difference in viscosity for aspect ratios of 1050 and 2100 at volume concentrations of 14 and 17%. Agarwal

[133] measured the shear stress growth for startup of shear flow and observed large transients for long fiber suspensions. Ortman et al. [98, 134] extended this work to investigate the effects of different general initial orientations on the transient response of long glass fibers up to a shear strain of 120 strain units. In these works, steady shear viscosity was reached at strains significantly larger than that observed for short fibers. Initial orientation also impacted the shape and magnitude of the stress growth overshoot. Measured values of orientation were extracted at different times during the flow to observe the relationship between fiber orientation and the measured stress response. This information was then used to fit fiber orientation and stress models to the experimental data for orientation and shear stress, respectively.

The use of a falling ball rheometer has been subject to limited use for short fiber suspensions. In this test a ball must pass through the center of a cylinder of fluid and the rate to which the ball falls is related to the fluid viscosity. Milliken and coworkers [135] used this method to investigate mono-disperse poly methyl methacrylate rods in a variety of suspending mediums with varying ball sizes. The rate of ball drop was recorded using a video camera. They found that viscosity was proportional to concentration below a critical value and had a cubic relationship at higher concentrations. Additionally, wall effects were observed when the ratio of column diameter to fiber length was between 1.6 and 3.2. Other researchers used an eddy current detection method to track the location of the falling ball in opaque fluids, making this method more applicable to a wider range of complex fluids [136, 137]. These tests produce viscosities higher than that from rotational rheometers when starting from random orientation. It is thought that orientation does not change significantly during these tests [136]. However, the creep flow around a ball is complex and may only provide an index of fluid properties without a reliable constitutive equation [125].

2.4.2.3 Shear Free Flows

Shear free or extensional flows are often encountered in industrial processes, but measuring extensional properties can often be a challenge. Measurements from uniaxial extension, squeeze

flow and approximation methods have all been used to characterize fiber suspensions. Weinberger and Goddard [78] devised an instrument to measure the tensile force of the extension of a fluid filament. The fiber suspension was extruded through a circular nozzle and partially taken up on a rotating cylinder. Using a concentration of 1.3 volume percent they observed an order of magnitude increase in extensional viscosity while the shear viscosity only increased 8% for short fibers. Mewis and Metzner [72] used a similar devise for fiber aspect ratios of 280 to 1260 and saw stress levels 1 to 2 orders of magnitude greater than that of shearing flow. Additionally, they report that the extensional viscosity is independent of strain rate. Recently, strain hardening has been reported in a 1 wt% suspension using a filament stretching device coupled to the exit of a capillary rheometer to achieve a draw ratio of 5 [81].

Kamal and coworkers [83] imposed uniaxial extension on short glass fibers up to 40 wt% using a commercially available rheometer. The presence of fibers caused the stress to reach a steady state faster than that of the pure suspending fluid. However, the maximum Hencky strains achievable before sample failure were significantly reduced because of the fibers. They did observe a thinning behavior with strain rate and report yield stresses at high concentrations. It has been reported in filament stretching experiments that the filament diameter decreases slower with time for the suspension than the suspending fluid [138]. Criteria for performing accurate measurements in uniaxial extension are given by Creasy et al. [84, 85]. Their experiments were designed with the constraint that the melting zone must be greater than the average fiber length by a factor of three and between 1 and 1.2 times the length of the longest fiber. They observed a stress growth overshoot dependent on rate for 60 v% graphite fibers with an average length of 5 mm.

Squeezing flow can also give information on extensional properties; moreover it is directly related to compression molding. In these experiments the gap between two lubricated parallel plates is decreased creating biaxial extension of the sample. If the rate of closure is exponential then the strain rate imposed on a fluid element is constant. Servais and coworkers [93] report for

short fibers a low yield stress and the pressure to compress the sample was independent of fiber length but sensitive to gap thickness. For long fibers a higher yield stress is reported and compression pressure was proportional to the square of fiber length and independent of gap thickness. In the case where the initial fiber orientation is anisotropic, extension of the sample will primarily be transverse to the highest degree of fiber orientation [139]. Dumont et al. [140] used flow visualization to characterize fiber flexibility in the compression of concentrated planar fiber bundles. However, they determined the planar bending of the fiber bundles to be weak, which is attributed to high in-plane bending moments. Guiraud and coworkers [141] acknowledge that a compression rheometer allows for information to be gathered on the rheology, composite compressibility and composite friction phenomena without the need to assume a friction law or stress relationship for the composite.

Under flow contractions, a fluid element is subjected to extensional flow. Kizior and Seyer [82] measured the thrust of a fluid jet exiting a sharp edged orifice. They obtained data for dilute suspensions (0.1 v% , a_r = 340). More common approximations of the extensional viscosity can be obtained from using the Cogswell [142] or Binding [143] analyses of flow contractions often used with pressure data obtained from a capillary or slit die rheometer. Mobuchon and coworkers [48] used a hyperbolic entrance to a slit die and report a maximum Trouton ratio of 40 for 30 wt% short glass fibers at low deformation rates while a value of 4 was determined for high rates. The Cogswell method predicted a higher extensional viscosity compared to the Binding method, but the authors believe the Binding method to be more meaningful because it takes into account shear and extensional components to flow. Thomasset et al. [79] also observed a varying Trouton ratio from 23 to 6 with deformation rate for long fiber (40 wt%) suspensions using the contraction on a capillary rheometer.

2.4.2.4 Fundamental Orientation Behavior

Additional investigations have been performed to study the fundamental orientation behavior of fibers subjected to different conditions. These works often deal with rigid fibers in a well-defined flow field at dilute concentrations. Rheological material functions are often not measured and instead the focus is given to the direct measurement of fiber orientation. Flow visualization experiments show that in the dilute concentration regime cylindrical bodies with for-aft symmetry experience periodic rotations under flow [144-146]. This behavior has been well documented by others and agrees with theory discussed in §2.5.1. Stover and coworkers [118] observed the periodic rotations to be hindered in the semi-dilute concentration regime. At these concentrations the interactions between fibers appeared to be hydrodynamic and not the result of direct mechanical contacts.

The interactions of flowing fibers with solid boundaries are of interest due to the relevance to all flows. Russel and coworkers [147] observed the sedimentation of fibers near and away from a vertical wall. Away from the wall, no rotation was observed which indicates that there were no effects due to inertia or odd flow behavior around the ends of the cylinder. Rotation near the wall occurred depending on orientation. Fibers mostly parallel to the wall would have the leading end rotate away from the wall while fibers perpendicular the wall would be subject to rotation that allowed the trailing end to become the leading end. Although the end of the fiber would closely approach the wall, no direct contact was observed. Moses et al. [148] subjected a single fiber to simple shear flow and when the centroid of the fiber was within the fiber length distance from the wall a higher rate of rotation was observed. This rotation rate increased logarithmically with decreasing separation distance. Once the fiber aligned with the flow direction the wall provided a stabilizing effect preventing the fiber from continued rotation. Numerical simulations coincide with these results [149]. Additional works observed fiber rotations under parabolic flow caused by flow down an incline [150, 151]. For most of the observed fibers, the velocity profile of the suspension did not differ from that of a pure fluid. Fibers close to the solid boundary did not show

a high degree of alignment in the flow direction. Instead, orientation in the neutral direction was observed, as if fibers preferred to roll down the inclined plane. This neutral orientation decreased with increasing distance from the solid surface.

2.5 Modeling Fiber Orientation

It is desirable to simulate the fiber microstructure within a composite to estimate final mechanical properties. This section presents the approaches taken to model fiber orientation kinetics of rigid and semi-flexible fibers. Sections are separated to coincide with orientation theories for the dilute (§2.5.1), semi-dilute (§2.5.2) and concentrated (§2.5.3) concentration regimes. It has become commonplace to represent orientation in terms of tensors. In this approach higher order tensors are typically approximated from lower order tensors. Such an approximation is considered a closure approximation and is reviewed in §2.5.4.

2.5.1 Dilute Ellipsoidal Suspensions

The pioneering work of Jeffery [152] provides the basis for describing the motion of naturally buoyant ellipsoidal particles in viscous fluids. Jeffery's derivation yielded the governing equations to quantify the rotation of an ellipsoid, shown in spherical coordinates as a function of time:

$$\frac{\partial \phi}{\partial t} = \frac{\dot{\gamma}}{a_r^2 + 1}\left(a_r^2 \cos^2 \phi + \sin^2 \phi\right) \tag{2.17}$$

$$\frac{\partial \theta}{\partial t} = \xi \frac{\dot{\gamma}}{4} \sin 2\theta \sin 2\phi. \tag{2.18}$$

The ξ parameter defines the shape of the ellipsoid as:

$$\xi = \frac{a_r^2 - 1}{a_r^2 + 1}. \tag{2.19}$$

The solution to the motion governing equations produces a result that is periodic preventing the particle from ever reaching a steady state value. The periodic motion has been commonly referred to as a Jeffery orbit, described by the following period of rotation:

$$T = \frac{2\pi}{\dot{\gamma}}\left(a_r + \frac{1}{a_r}\right). \tag{2.20}$$

In the assumption of an infinite aspect ratio particle, $\xi = 1$ and the period of rotation is infinite. Under this assumption, the Jeffrey's model will predict alignment of particles with the principle flow direction.

Non-ellipsoidal particles can also be described by the equations provided that the particle is represented by an ellipsoid of an effective aspect ratio [146]. Theoretical [8, 144, 153] and experimental [71, 146] efforts have been devoted to understanding the rotational behavior as a function of particle shape and relating this to an effective aspect ratio. Rigid cylinders have been found to exhibit the rotational behavior of an ellipsoid with an aspect ratio of about 70% the aspect ratio (L/d) of the cylinder [8, 146, 153].

The governing equations for the rotation of a single particle can be written in vector form using Eqs. (2.9) - (2.11). The rotation of a unit vector, $\mathbf{p}$, subject to any flow field is given as [154]:

$$\dot{\mathbf{p}} = \frac{\partial \mathbf{p}}{\partial t} = \mathbf{W} \cdot \mathbf{p} + \xi[\mathbf{D} \cdot \mathbf{p} - \mathbf{p}(\mathbf{p} \cdot \mathbf{D} \cdot \mathbf{p})] \tag{2.21}$$

where $\dot{\mathbf{p}}$ denotes the derivative of the unit vector, $\mathbf{p}$, with respect to time, the vorticity tensor $\mathbf{W} = \frac{1}{2}(\nabla\mathbf{v}^t - \nabla\mathbf{v})$ and the rate of strain tensor $\mathbf{D} = \frac{1}{2}(\nabla\mathbf{v}^t + \nabla\mathbf{v})$.

A population of fibers can be represented through the use of an orientation distribution function, $\psi(\mathbf{p}, t)$. The orientation distribution function represents the probability that a fiber will have orientation between (θ, ϕ) and $(\theta + d\theta, \phi + d\phi)$. This function must encompass certain

physical conditions. The orientation of an ellipsoid is indistinguishable between a vector $\mathbf{p}$ and $-\mathbf{p}$; therefore, the orientation distribution function must follow this symmetry condition. Additionally the normalization condition must be satisfied such that the function summed over all orientation states must equal unity.

The Smoluchowski equation, also referred to as a modified Fokker-Planck equation, has been shown to represent the change in the fiber orientation distribution function with time [155]. The centroid of the fiber is considered to move with the bulk fluid velocity, lending fiber orientation to be regarded as a convected quantity. The following continuity equation prescribes the rate of change of the orientation distribution function:

$$\frac{D\psi}{Dt} = -\frac{\partial}{\partial \mathbf{p}} \cdot (\dot{\mathbf{p}}\psi) \tag{2.22}$$

where, $\frac{D}{Dt}$ denotes the material derivative $\left(\frac{D}{Dt} = \frac{\partial}{\partial t} + \mathbf{v} \cdot \nabla\right)$. The substitution of Eq. (2.21**)** into Eq. (2.22) provides a set of equations that are typically used to describe the orientation of fibers in dilute suspensions. To predict the microstructure seen in complex industrial flows extensive computational effort is required [156]. Multiple approaches have been used to alleviate computations centered on the orientation distribution function. Orientation tensors provide a means of compactly representing the average orientation of particles. Advani and Tucker [156] developed structure tensors that have become commonplace in fiber orientation models. These tensors arise from multiple dyadic products of $\mathbf{p}$ and integrating the product of these moments with the orientation distribution function over all orientation space. Odd moments of orientation are zero because the orientation distribution function is even when assuming that fibers can be represented as rigid rods. The second and fourth moments of orientation are shown as Eq. (2.23) and Eq. (2.24), respectively. Most works typically use the second and fourth moments of orientation, but higher moments can be derived similarly.

$$\mathbf{A} = \int \mathbf{pp}\psi(\mathbf{p}, t)d\mathbf{p} \tag{2.23}$$

$$\mathbf{A_4} = \int \mathbf{pppp}\psi(\mathbf{p}, t)d\mathbf{p} \tag{2.24}$$

The second moment of orientation provides a compact means of describing the orientation state of particles within a flow. The values in the trace components of **A** correspond to the extent of orientation in each of the principle directions. For perfect alignment in the x_1 direction, the $\mathbf{A}_{11}$ component of orientation equals 1 while all other values are zero. In the case of three-dimensional random orientation, the only values which are non-zero are the trace components at values of 1/3. A property of this tensor is that the trace always equals 1. The fourth moment of orientation arises in the orientation models due to the assumption that the particle is rigid and non-extensible.

An additional approach was used by Lipscomb et al. [111] to remove the need to solve the Fokker-Planck equation [Eq.(2.22)] in order to find a representation for the fourth moment of orientation. This is based on the assumption that fiber suspensions are non-Brownian and only subject to orientation from fluid hydrodynamics. The derivation stems from the works of Evans [157] and Bretherton [144] where only the initial orientation distribution function needs to be known:

$$\mathbf{A} = \int \frac{(\mathbf{E}\cdot\mathbf{p})(\mathbf{E}\cdot\mathbf{p})}{(\mathbf{E}^t\cdot\mathbf{E}:\mathbf{pp})}\psi(\mathbf{p}, 0)d\mathbf{p} \tag{2.25}$$

$$\mathbf{A_4} = \int \frac{(\mathbf{E}\cdot\mathbf{p})(\mathbf{E}\cdot\mathbf{p})(\mathbf{E}\cdot\mathbf{p})(\mathbf{E}\cdot\mathbf{p})}{(\mathbf{E}^t\cdot\mathbf{E}:\mathbf{pp})^2}\psi(\mathbf{p}, 0)d\mathbf{p} \tag{2.26}$$

where a calculation for the deformation gradient, **E**, replaces the need to calculate the orientation distribution function,$\psi(\mathbf{p}, t)$:

$$\frac{D\mathbf{E}}{Dt} = (\mathbf{W} + \xi\mathbf{D}) \cdot \mathbf{E} \tag{2.27}$$

For isotropic initial orientation, **E** is equivalent to the identity tensor, **I**, and for infinite aspect ratio particles ($\xi = 1$), **E** is equivalent to the strain tensor. The solution for the orientation distribution function for initially isotropic orientation ($\psi = 1/4\pi$) is provided by Dinh [158]:

$$\psi(\mathbf{p}, t) = \frac{1}{4\pi}[(\mathbf{E}^{-1})^{\boldsymbol{t}} \cdot \mathbf{E}^{-1} : \mathbf{pp}]^{-3/2} \tag{2.28}$$

where, $(\mathbf{E}^{-1})^{\boldsymbol{t}} \cdot \mathbf{E}^{-1}$ is the Cauchy strain tensor. This approach is valid under the assumption that particles can be represented by an infinite aspect ratio. Numerical techniques must be used when these sets of equations do not provide an accurate description of fiber orientation [159]. Another approach is to represent the orientation distribution function as an expansion of spherical harmonics [156].

The continuity equation for the fiber orientation distribution function can be written in terms of the second and fourth order structural tensors by multiplying Eq. (2.22) by the second moment dyadic product of **p**. Through integration by parts and simplifying terms, the Jeffery's equation for ellipsoidal particles can be represented as a function of structural tensors [156]:

$$\frac{D\mathbf{A}}{\mathrm{Dt}} = (\mathbf{W} \cdot \mathbf{A} - \mathbf{A} \cdot \mathbf{W}) + \xi[\mathbf{D} \cdot \mathbf{A} + \mathbf{A} \cdot \mathbf{D} - 2\mathbf{D} : \mathbf{A}_4]. \tag{2.29}$$

In this form, the orientation distribution function does not need to be calculated and is nested in the **A** and $\mathbf{A}_4$ tensors defined as Eqs. (2.23) and (2.24), respectively. The evolution of higher order tensors can be developed using the same method. Ericssen and coworkers [139] note that the use of a fourth order evolution equation allows for direct coupling with models for stress without the need to use multiple closure approximations.

2.5.2 Semi-dilute Fiber Suspensions

The hydrodynamic interactions between fibers in semi-dilute suspensions impact the ability of fibers to freely rotate. Okagawa and coworkers [160] observed that the periodic rotations of a fiber will dampen with time. Iso et al. [161] measured fiber orientation for semi-dilute suspensions and observed fibers deviating from Jeffery orbits. They assumed that hydrodynamic fiber-fiber interactions would lead to small perturbations in the rotation of a fiber. A rotary diffusivity tensor that is dependent on the orientation states of a group of fibers is used to account for the additional interactions assuming that the viscoelasticity of the matrix is weak. The continuity equation for the orientation distribution function becomes:

$$\frac{D\psi}{Dt} = -\frac{\partial}{\partial \mathbf{p}} \cdot \left[(\dot{\mathbf{p}}\psi) - \mathbf{D_r}(\psi, \mathbf{p}) \cdot \frac{\partial \psi}{\partial \mathbf{p}} \right] \tag{2.30}$$

where, $\mathbf{D_r}$ is the rotary diffusion tensor. This tensor can be determined based on molecular theory for Brownian suspensions [162] or from experimental data [163]. Rahnama et al. [163] report the tensor containing values of order 10^{-4} for a suspension with $nL^3 = 20$ and $a_r = 17$, which was the highest concentration in their investigation. Less concentrated suspensions were observed to deviate less from Jeffery orbits and are modeled with smaller values in the rotary diffusion tensor. The small deviations from periodic rotations will eventually cause alignment in the primary direction of flow. Due to the need to calculate the orientation distribution function and the rotary diffusion term, simulations using Eq. (2.30) were limited to simple flows.

Folgar and Tucker [164] observed fibers with less alignment in the primary flow direction than what is predicted by the Jeffery's model using the infinite aspect ratio assumption. Their conclusion was that orientation is still primarily dictated by the hydrodynamics in Jeffery's equation but fiber interactions cause sudden reorientation of fibers under flow creating a randomizing effect to fiber orientation. They approached interactions to be independent of flow conditions and any anisotropy caused by the flow. The model was originally developed for use in

concentrated suspensions, but has been used to a lesser extent in semi-dilute suspensions [165, 166]. The impact of fiber interactions on orientation is governed by a phenomenological interaction coefficient, C_I and scales linearly with the magnitude of the shear rate, $\dot{\gamma} = \sqrt{2\mathbf{D} : \mathbf{D}}$. Isotropic rotary diffusion is added to Eq.(2.21), providing the governing equation for non-dilute fiber suspensions [156]:

$$\dot{\mathbf{p}} = \mathbf{W} \cdot \mathbf{p} + \xi[\mathbf{D} \cdot \mathbf{p} - \mathbf{p}(\mathbf{p} \cdot \mathbf{D} \cdot \mathbf{p})] - C_I \dot{\gamma} \frac{1}{\psi} \frac{\partial \psi(\mathbf{p})}{\partial \mathbf{p}}. \tag{2.31}$$

Similar to the derivation of Eq. (2.29), the Folgar-Tucker model is shown here using structural tensors:

$$\frac{D\mathbf{A}}{Dt} = (\mathbf{W} \cdot \mathbf{A} - \mathbf{A} \cdot \mathbf{W}) + \xi[\mathbf{D} \cdot \mathbf{A} + \mathbf{A} \cdot \mathbf{D} - 2\mathbf{D} : \mathbf{A}_4] + 2C_I \dot{\gamma}(\mathbf{I} - 3\mathbf{A}). \tag{2.32}$$

The interaction parameter is thought to be an intrinsic property of the suspension. The introduction of isotropic rotary diffusion is strictly phenomenological and not formulated on a detailed understanding of fiber interactions. As a result, the value of C_I must be determined from experimental data [164, 167]. Yamane and coworkers [165] performed numerical simulations on semi-dilute suspensions using values of C_I of order $10^{-7} - 10^{-4}$. These small values of C_I are able to reflect damped oscillations in fiber orientation. Further simulation efforts revealed the following empirical relationship for the interaction coefficient in terms of concentration and aspect ratio [166]:

$$C_I = 0.011(nL^3)^{1.10} a_r^{-1.47}. \tag{2.33}$$

2.5.3 Concentrated Fiber Suspensions

As discussed in §2.2.1, rod-like particles are subject to increasing amount of particle-particle interactions in the concentrated regime. The Folgar-Tucker model introduced in the

previous section has been widely used to describe the orientation of concentrated fiber suspensions. Increased fiber interactions are represented by larger values for C_I than what is reported for semi-dilute suspensions. Bay [168] measured the parameter to be within the range of 0.0001 to 0.016 from injection molded samples of short glass fiber composites. Values in this range are sufficient to prevent fibers from becoming fully aligned with the flow which nullifies the rotational orbits predicted with Jeffery's model. Bay was able to produce an empirical expression based on concentration in terms of volume fraction, ϕ_v and the fiber aspect ratio, a_r:

$$C_I = 0.0184 \exp(-0.7148\phi_v a_r). \tag{2.34}$$

It is notable that C_I decreases with increasing concentration and aspect ratio meaning that fiber orientation becomes more highly aligned with flow. Numerical simulations performed by Phan-Thien et al. [169] considered C_I as a tensor when solving Eq. (2.32). The trace components are averaged to produce the following expression for the isotropic rotary diffusion constant:

$$C_I = 0.03[1 - \exp(-0.224\phi_v a_r)] \tag{2.35}$$

where, the interaction coefficient increases with concentration and aspect ratio. Additionally, the function is constrained such that at an infinitely low concentration, the fiber will not deviate from Jeffery orbits. The interaction coefficients determined by Folgar and Tucker [164] are similar to that predicted by the empiricism developed through numerical simulations. Ranganathan and Advani [170] suggest that the interaction coefficient be related to interfiber spacing:

$$C_I = \frac{K}{a_c/L} \tag{2.36}$$

where, K is a proportionality constant, a_c is the interfiber spacing and L is the fiber length. This formulation allows the interaction coefficient to change with orientation, but rotary diffusion still remains isotropic.

The addition of the phenomenological interaction parameter allows for a good representation of the steady state fiber orientation, but this model over predicts the rate that fibers orient in flow when compared to experimental data [60, 171, 172]. To better reflect experimental observations a slip parameter was proposed by Sepehr et al. [60] which has a similar effect to the strain reduction factor added by Huynh [171]. The strain reduction factor (SRF) model will be discussed in the following form:

$$\frac{D\mathbf{A}}{Dt} = \alpha[(\mathbf{W}\cdot\mathbf{A} - \mathbf{A}\cdot\mathbf{W}) + \xi[\mathbf{D}\cdot\mathbf{A} + \mathbf{A}\cdot\mathbf{D} - 2\mathbf{D}:\mathbf{A}_4] + 2C_I\dot{\gamma}(\mathbf{I} - 3\mathbf{A})]. \tag{2.37}$$

The additional parameter, α, scales the hydrodynamic and isotropic rotary diffusion terms and is constrained between zero and unity. The slip parameter, α, is an empirical modification to the Folgar-Tucker model and must be determined experimentally. The primary shortcoming of this model is that it violates objectivity. The significance is that computations can produce unphysical results if the coordinate frame were to rotate, translate or change to a different coordinate system.

An objective model must retain the general stability of the SRF model in order for it to be useful in complex flow simulations. The violation of objectivity in the SRF model stems from the slip parameter scaling the off-diagonal terms in the vorticity tensor, **W**. The approach of Wang and coworkers [173] was to scale the rate of change of the eigenvalues in the orientation tensor. The rotation rate of the eigenvectors remains unchanged, making the model invariant under rigid-body rotation. In formulating this model **A** is regarded in the following form:

$$\mathbf{A} = \sum_{i=1}^{3} \lambda_i \mathbf{e}_i \mathbf{e}_i \tag{2.38}$$

where, λ_i are the eigenvalues and $\mathbf{e}_i$ are the corresponding eigenvectors. The sum of the three eigenvalues equals unity and each eigenvalue is constrained from 0 to 1 to retain the existing

definition of **A**. By scaling the growth of the eigenvalues, the reduced strain closure (RSC) model becomes the following:

$$\frac{D\mathbf{A}}{Dt} = \mathbf{W}\cdot\mathbf{A} - \mathbf{A}\cdot\mathbf{W} + \xi\{\mathbf{D}\cdot\mathbf{A} + \mathbf{A}\cdot\mathbf{D} - 2[\mathbf{A}_4 + (1-\kappa)(\mathbf{L}_4 - \mathbf{M}_4 : \mathbf{A}_4)] : \mathbf{D}\} + 2\kappa C_I\dot{\gamma}(\mathbf{I} - 3\mathbf{A}). \tag{2.39}$$

Additional fourth order tensors arise in the derivation and are defined as:

$$\mathbf{L_4} = \sum_{i=1}^{3} \lambda_i \mathbf{e}_i\mathbf{e}_i\mathbf{e}_i\mathbf{e}_i \tag{2.40}$$

$$\mathbf{M_4} = \sum_{i=1}^{3} \mathbf{e}_i\mathbf{e}_i\mathbf{e}_i\mathbf{e}_i. \tag{2.41}$$

Slowed orientation kinetics are governed through the choice of κ, constrained between 0 and 1. When $\kappa = 1$, the reduced strain closure model reduces to the Folgar-Tucker model in Eq. (2.32).

For the most part, orientation models have been based on isotropic rotary diffusion. Other numerical simulation methods predict the diffusion of particles to be anisotropic [169, 174, 175]. Further analysis into the term accounting for the effective diffusion caused by fiber interactions has yielded additional models in recent years. Anisotropy in the composite would cause fiber-fiber interactions to be dependent on orientation. The premise is that an anisotropic diffusion model would better reflect fiber interactions under flow and would improve orientation predictions. Rather than using a single parameter, a tensor is used to represent the spatial rotary diffusion in the three principle directions. Koch [176] proposed anisotropic diffusion as a function of the fourth and sixth moments of orientation. These moments can be well approximated [177], but the use of Koch's model does not yield significantly different results and requires more computational efforts than the traditional isotropic model [178]. Limitations to these works have been discussed by Phelps and Tucker [178] and a new anisotropic rotary diffusion model is

proposed. A generalized formulation of the anisotropic diffusion tensor is presented based on the work of Hand [179] and truncated to the $\mathbf{C}_A$ tensor shown below:

$$\mathbf{C}_A = b_1\mathbf{I} + b_2\mathbf{A} + b_3\mathbf{A}^2 + \frac{b_4}{\dot{\gamma}}\mathbf{D} + \frac{b_5}{\dot{\gamma}^2}\mathbf{D}^2. \tag{2.42}$$

The anisotropic tensor of Phelps and Tucker requires five coefficients (b_i) that appear to be specific to the suspension under investigation. An objective method must be used to correctly determine these parameters or else oscillations will appear in orientation predictions. The b_i parameters are solved under simple shear flow which is assumed to occur near the mold walls of injection molded composites [178]. The simple shear approximation is applied to the orientation equation instead of the anisotropic tensor. Phelps and Tucker couple this tensor with the RSC model producing the anisotropic rotary diffusion reduced strain closure model (ARD-RSC):

$$\begin{aligned}\frac{D\mathbf{A}}{Dt} = {} & \mathbf{W}\cdot\mathbf{A} - \mathbf{A}\cdot\mathbf{W} + \xi[\mathbf{D}\cdot\mathbf{A} + \mathbf{A}\cdot\mathbf{D} - 2[\mathbf{A}_4 + (1-\kappa)(\mathbf{L}_4 - \mathbf{M}_4 : \mathbf{A}_4)] : \mathbf{D}] \\ & + \dot{\gamma}[2[\mathbf{C}_A - (1-\kappa)\mathbf{M}_4 : \mathbf{C}_A] - 2\kappa(tr\mathbf{C}_A)\mathbf{A} - 5(\mathbf{C}_A\cdot\mathbf{A} + \mathbf{A}\cdot\mathbf{C}_A) \\ & + 10[\mathbf{A}_4 + (1-\kappa)(\mathbf{L}_4 - \mathbf{M}_4 : \mathbf{A}_4)] : \mathbf{C}_A]\end{aligned} \tag{2.43}$$

where, $tr\mathbf{C}_A$ represents the trace of tensor $\mathbf{C}_A$. The ARD-RSC model takes into account slowed orientation kinetics, but when $\kappa = 1$ the model reduces to fiber evolution predicted by the Folgar-Tucker model, now with anisotropic rotary diffusion. Solving the b_i parameters in simple shear flow does not provide a closed set of equations. Two values of b_i are chosen while the remaining three are solved based on the chosen values. The difficulty in using this model effectively revolves around determining these parameters. However, choosing the proper values in the anisotropic diffusion tensor have shown to improve orientation predictions in short and long fiber injection molded composites [178].

In an effort to reduce the issues in choosing the b_i parameters in the ARD-RSC model, Tseng et al. [180] took a different approach to phenomenological anisotropic rotary diffusion to

produce the improved anisotropic rotary diffusion retarded principal rate (iARD-RPR) model. This model contains up to four parameters and has shown reasonable agreement with experimental data in an end-gated plaque [181]. However, their approach to anisotropic diffusion causes the model to be non-objective.

Férec et al. [182] proposed a model that includes the effects of fiber-fiber interactions on orientation. The authors use the assumption that contacts between fibers are lubricated and occur at distances where the nearest points between fibers are less than the fiber diameter. The model shown here is for high aspect ratio particles:

$$\begin{aligned}\frac{D\mathbf{A}}{Dt} = \mathbf{W}\cdot\mathbf{A} - \mathbf{A}\cdot\mathbf{W} + (\mathbf{D}\cdot\mathbf{A} + \mathbf{A}\cdot\mathbf{D} - 2\mathbf{D}:\mathbf{A}_4) \\ - \phi\widetilde{M}(\mathbf{D}\cdot\mathbf{b} + \mathbf{b}\cdot\mathbf{D} - 2\mathbf{D}:\mathbf{b}_4) + 2f\phi\widetilde{M}q\dot{\gamma}(\mathbf{I} - 3\mathbf{A})\end{aligned} \tag{2.44}$$

where, $\widetilde{M} = 2k_F/3\pi Y_c$, $Y_c = 1/6$, $f = tr(\mathbf{b})$, k_F and q are chosen to be fitting parameters. The tensors $\mathbf{b}$ and $\mathbf{b}_4$ are interaction tensors that are formed by dyadic products of $\mathbf{p}$ weighted by the interaction potential between two fibers. For rigid fibers only even-ordered tensors are of interest:

$$\mathbf{b} = \int_{\mathbf{p}}\int_{\mathbf{p}'} \mathbf{pp}|\mathbf{p}\times\mathbf{p}'|\psi(\mathbf{p}')\psi(\mathbf{p})\, d\mathbf{p}'d\mathbf{p} \tag{2.45}$$

$$\mathbf{b}_4 = \int_{\mathbf{p}}\int_{\mathbf{p}'} \mathbf{pppp}|\mathbf{p}\times\mathbf{p}'|\psi(\mathbf{p}')\psi(\mathbf{p})\, d\mathbf{p}'d\mathbf{p}. \tag{2.46}$$

The interaction tensors follow the same symmetries found in the $\mathbf{A}$ and $\mathbf{A}_4$ orientation tensors. The second order interaction tensor can be represented as a function of the orientation tensors:

$$\mathbf{b} = \frac{3\pi}{8}(\mathbf{A} - \mathbf{A}_4 : \mathbf{A}) \tag{2.47}$$

Although this model still contains fitting parameters, the interaction term evolves with fiber orientation. A power-law type interaction has also been proposed, but it introduces an additional fitting parameter [183].

As discussed in §2.2.2, an increase in a fiber's aspect ratio makes the fiber more susceptible to bending under flow. The previously discussed models are derived on the basis that fibers can be represented as a rigid rod or maintain a constant effective aspect ratio. Strautins and Latz [184] developed a continuum model to take into account the semi-flexible nature of high aspect ratio fiber suspensions. A semi-flexible fiber is represented as three beads connected by two rigid rods, where the interactions with the flow only occur at the beads. Figure 2.2 superimposes the bead-rod representation onto a curved fiber.

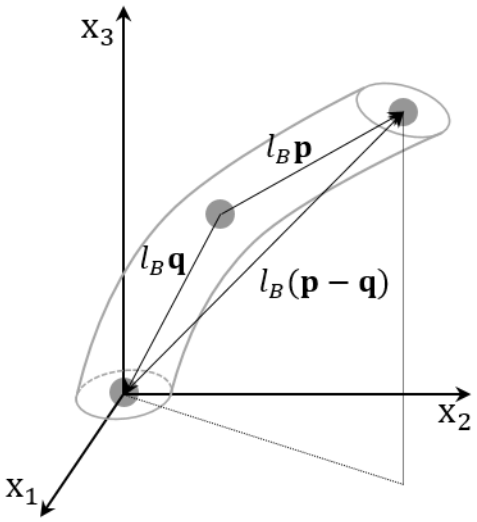

Figure 2.2: A semi-flexible fiber described by two unit vectors **p** and **q** with an average orientation vector defined as $l_B(\mathbf{p} - \mathbf{q})$.

Two indistinguishable orientation unit vectors, **p** and **q**, are constructed parallel to the rigid rods in the semi-flexible fiber system. An elastic potential governs the rigidity of the fiber and is presumed to be a function of the relative position of **p** and **q** vectors [185]:

$$U(\mathbf{p}, \mathbf{q}) = \tilde{k}(\mathbf{p} \cdot \mathbf{q} + 1)^{\tilde{m}} \tag{2.48}$$

where, the relationship could be assumed as a power-law with $\tilde{k}$ and $\tilde{m}$ taken as parameters used to fit the model to the physical fiber suspension. The potential reaches a minimum when the fiber is straight causing $\mathbf{p} = -\mathbf{q}$ such that $\mathbf{p} \cdot \mathbf{q} = -1$. Strautins and Latz [184] developed the semi-flexible orientation model for dilute concentrations and with $\tilde{m} = 1$. Additionally, the fibers are thought to only be semi-flexible where $\mathbf{p} \approx -\mathbf{q}$. The reader is referred to the work of Strautins and Latz for further details on the model development. The authors present the semi-flexible model using the following moments of orientation:

$$\mathbf{A} = \int \int \mathbf{p}\mathbf{p}\psi(\mathbf{p}, \mathbf{q}, t) d\mathbf{p} d\mathbf{q} \tag{2.49}$$

$$\mathbf{B} = \int \int \mathbf{p}\mathbf{q}\psi(\mathbf{p}, \mathbf{q}, t) d\mathbf{p} d\mathbf{q} \tag{2.50}$$

$$\mathbf{C} = \int \int \mathbf{p}\psi(\mathbf{p}, \mathbf{q}, t) d\mathbf{p} d\mathbf{q}. \tag{2.51}$$

The orientation distribution function is now a function of both orientation vectors allowing for instances where the first moment of orientation is non-zero, described by the $\mathbf{C}$ vector. The tensor $\mathbf{B}$ describes the mixed moment of orientation, where the trace of tensor $\mathbf{B}$ is a measure for the degree of fiber bending. In the case of a straight fiber, $\mathbf{B} = -\mathbf{A}$. Similarly, an infinitely flexible fiber may exhibit $\mathbf{p} = \mathbf{q}$ resulting in $\mathbf{B} = \mathbf{A}$. These two cases provide the limits on the orientation tensor $\mathbf{B}$, with the latter most likely violating the assumption that fibers are only semi-flexible. Currently the limit to where fibers can no longer be considered semi-flexible is not defined. Ortman et al. [134] described the average orientation of a fiber by the dyadic product of the end-to-end vector multiplied by the orientation function and integrated over all orientation space. The second moment of average orientation for a population of semi-flexible fibers is represented by $\mathbf{R}$ in terms of $\mathbf{A}$ and $\mathbf{B}$ tensors:

$$\mathbf{R} = \frac{\mathbf{A} - \mathbf{B}}{1 - tr\mathbf{B}}. \tag{2.52}$$

This tensor is normalized such that it has the same properties of the **A** tensor with the trace equaling unity.

The work of Ortman et al. [134] extended the semi-flexible orientation model for use in concentrated systems through the addition of isotropic rotary diffusion. Additionally the scaling parameter, α, had been added to better reflect experimental observations, but violates material objectivity. The model presented here is a product of closure approximations of the quadratic type to represent the mixed moment tensors as those described in Eqs. (2.49) - (2.51). For example in Eq. (2.54), the **AB** term is an approximation of $\langle \mathbf{ppqp} \rangle$:

$$\begin{aligned} \frac{D\mathbf{A}}{Dt} = \alpha \Big[& \mathbf{W}\cdot\mathbf{A} - \mathbf{A}\cdot\mathbf{W} + \xi(\mathbf{D}\cdot\mathbf{A} + \mathbf{A}\cdot\mathbf{D} - 2\mathbf{D}:\mathbf{A_4}) + 2C_I\dot{\gamma}(\mathbf{I} - 3\mathbf{A}) \\ & + \frac{l_B}{2}[\mathbf{Cm} + \mathbf{mC} - 2(\mathbf{m}\cdot\mathbf{C})\mathbf{A}] + 2k\big(\mathbf{B} - \mathbf{A}tr(\mathbf{B})\big)\Big] \end{aligned} \tag{2.53}$$

$$\begin{aligned} \frac{D\mathbf{B}}{Dt} = \alpha \Big[& \mathbf{W}\cdot\mathbf{B} - \mathbf{B}\cdot\mathbf{W} + \xi(\mathbf{D}\cdot\mathbf{B} + \mathbf{B}\cdot\mathbf{D} - 2(\mathbf{D}:\mathbf{A})\mathbf{B}) - 4C_I\dot{\gamma}\mathbf{B} \\ & + \frac{l_B}{2}[\mathbf{Cm} + \mathbf{mC} - 2(\mathbf{m}\cdot\mathbf{C})\mathbf{B}] + 2k\big(\mathbf{A} - \mathbf{B}tr(\mathbf{B})\big)\Big] \end{aligned} \tag{2.54}$$

$$\begin{aligned} \frac{D\mathbf{C}}{Dt} = \alpha \Big[& \nabla\mathbf{v}^t\cdot\mathbf{C} - (\mathbf{A}:\nabla\mathbf{v}^t)\mathbf{C} - 2C_I\dot{\gamma}\mathbf{C} + \frac{l_B}{2}[\mathbf{m} - \mathbf{C}(\mathbf{m}\cdot\mathbf{C})] \\ & - k\mathbf{C}\big(1 - tr(\mathbf{B})\big)\Big] \end{aligned} \tag{2.55}$$

$$\mathbf{m} = \sum_{i=1}^{3}\sum_{j=1}^{3}\sum_{k=1}^{3}\frac{\partial^2 \mathrm{v}_i}{\partial \mathrm{x}_j \partial \mathrm{x}_k}\mathrm{A}_{jk}\boldsymbol{\delta}_i \tag{2.56}$$

where, $\boldsymbol{\delta}_i$ is a basis vector. Flexibility is dependent on fiber length, $2l_B$, and caused by the flow field which is taken into account through the **m** vector. The original model derived by Strautins and Latz [184] is recovered for dilute semi-flexible suspensions by setting $\alpha = 1$ and $C_I = 0$. Bending caused by the flow occurs when there exists a second derivative in velocity along the length of a fiber. A restorative term involving k (related to the $\tilde{k}$ in Eq.(2.48) by $k = 2\tilde{k}/\zeta l_B^2$ where ζ is a drag coefficient) counteracts the bending of a fiber. This restorative potential term was approximated by Ortman et al. [134] from the bending potential of a beam under small deflection:

$$k_i = \frac{E_Y}{64\eta_m}\frac{d^3}{l_{B_i}^3}. \tag{2.57}$$

The bending potential of a fiber *i* with length $2l_{B_i}$ is a function of the Young's modulus, E_Y, matrix viscosity, η_m and the diameter of a fiber, d. This value is then averaged over the fiber length distribution to represent an average bending potential for the fiber suspension. Large values of k correspond to increased rigidity of a fiber while a value of zero would represent a fiber that is perfectly flexible.

When no flexibility is caused by the flow the model reduces to the orientation dynamics of the strain reduction factor model. It has been shown in simple shear that the choice of k can affect the orientation predictions [186]. Recent works were able to show that the semi-flexible fiber model gave improved orientation predictions in a center-gated disk and end-gated plaque when compared to the SRF model [186, 187].

A mesoscopic approach to orientation kinetics has brought together aspects of microscopic orientation from hydrodynamics and macroscopic observations through the use of the GENERIC framework [188]. The reader is directed to the following references for further information

regarding the framework's derivation [189, 190]. The argument is that not all aspects of fiber orientation can be addressed at the microscopic level. This model guarantees the compatibility of the orientation governing equations with thermodynamics. Randomizing effects on orientation are represented through a dissipation potential term that allows the free energy of the system to change with time:

$$\frac{D\mathrm{A}_{ij}}{Dt} = \mathrm{A}_{kj}\mathrm{W}_{ik} + \mathrm{A}_{ik}\mathrm{W}_{jk} + \xi\left(\mathrm{A}_{ilkl}\mathrm{D}_{jk} + \mathrm{A}_{jlkl}\mathrm{D}_{ik} - \mathrm{A}_{ilkj}\mathrm{D}_{lk} - \mathrm{A}_{ilki}\mathrm{D}_{lk}\right) - \frac{\partial \Xi}{\partial \Phi_{\mathrm{A}_{ij}}} \qquad (2.58)$$

where, Ξ is the dissipation potential and $\Phi_{\mathrm{A}_{ij}}$ is the derivative of the free energy with respect to the orientation tensor. The authors of this model use index notation to provide an additional generalization. The model will reduce to the Jeffrey's model providing a closure approximation is used that allows $\mathrm{A}_{ilkl} = \mathrm{A}_{ik}$ and the last term in the equation is omitted. The last term represents all the irreversible behavior that causes the free energy to reach a minimum. The dissipation potential has taken multiple forms in the literature [75, 188], but in either case there exist phenomenological parameters that cannot be assessed or measured directly. Coupling this orientation equation with a stress tensor also based on the GENERIC framework has shown qualitative agreement in orientation predictions for rheological data, but has not been employed in complex processing flows.

2.5.4 Closure Approximations

The use of a closure approximation is required to solve many of the orientation evolution equations that use structural orientation tensors. Solving orientation equations using structural tensors provides more computational efficiency often required for complex industrial flows. An approximation for higher order tensors as a function of lower order tensors is used to create a closed set of equations so that additional calculations are not required to solve for the orientation distribution function. The primary focus of this section is to represent the fourth order orientation

tensor as a function of the second order orientation tensor, but similar approaches can be used for approximating higher order tensors.

There are some cases where closure approximations are not required to produce a closed set of equations. If fiber-fiber interactions are neglected, which is typically not the case for industrial fiber suspensions, Eqs. (2.25) and (2.26) can be used to represent the structural orientation tensors [111]. A more industrially relevant case is the use of the fast exact closure which creates a set of coupled ordinary differential equations from the original orientation model [191]. The fast exact closure provides an exact solution to Jeffery's equation [Eq. (2.29)] and is extendable to isotropic and anisotropic rotary diffusion models. This approach provides equal to improved accuracy and computational efficiency when compared to existing closure approximations.

The linear closure approximation arises from the restrictions that the fourth order tensor must remain symmetric with regard to a pair of indices and the tensor must remain normalized [179]. These constraints allow the approximation to exactly represent the fourth order tensor for isotropic fiber orientation. Advani and Tucker [192] have demonstrated this approximation to show non-physical instabilities depending on the extent of fiber orientation. The quadratic closure approximation is formed from the dyadic product of two second order orientation tensors [193] and provides realistic predictions in all flows while remaining computationally simplistic. In an effort to bridge benefits of the quadratic and linear approximations, Advani and Tucker [192] proposed a hybrid closure. A scalar parameter based on the determinate of the second order orientation tensor weighs the contributions of the linear and quadratic closures. Hinch and Leal [194] provide additional approximations for the term including the fourth order orientation tensor often seen in orientation and stress equations, but no explicit fourth order approximation was presented. Their approximation has been shown to produce unrealistic behavior in certain flows [192].

Cintra and Tucker [195] developed a family of orthotropic closures with the constraint that the principal axis of the fourth order tensor must match the principal axis of the second order tensor. Parameters in the orthotropic closures are extracted from numerical solutions of the probability distribution function. This family of closures has improved orientation predictions but can produce oscillations depending on the value of the interaction coefficient used in the orientation model. Improvements to the orthotropic fitted closures have been proposed to mitigate oscillations in order to improve orientation predictions [196, 197].

The natural closure approximation was developed based on the general form of a fourth order tensor in terms of the second order tensor [198, 199]. Parameters weighting each of the symmetric parts of the tensor are based on the invariants of the second moment of orientation and values determined by exact solutions of the probability distribution function. This method causes the natural closure to be subject to singularities depending on the orientation state. Similarly, an invariant based optimal fitting (IBOF) closure begins with the same general form of the fourth order tensor. Chung and Kwon [200] proposed that parameters weighing each symmetric term can be represented as functions of the invariants of the orientation tensor. Parameters in the model are extracted by fitting to the probability distribution function, similar to the procedure of Cintra and Tucker [195]. The IBOF closure approximation can be considered a hybrid of the natural and orthotropic closure approximations which provides similar accuracy compared to the orthotropic closures while improving computational efficiency [200].

Closure approximations discussed here have been limited to those used to represent the fourth moment of orientation. However, in the orientation and stress model proposed by Férec et al. [182] additional closures are required to represent the fourth order interaction tensor as a function of the second order interaction tensor. For these terms, quadratic, linear and orthotropic [201] closures have been considered. These closures differ from the orientation closures in that they must properly account for the cross product that arises in the interaction tensors.

2.6 Extra Stress in Fiber Suspensions

Fiber orientation and fluid flow result in a set of highly coupled equations. The extra stress caused by fibers generally consists of contributions from the suspending medium, interaction between fibers and the suspending fluid, fiber-fiber interactions and the fibers themselves. The degree to which each mechanism contributes to the stress is largely dependent on the concentration and aspect ratio of the particles. A variety of theories have been proposed to address the impact of each contribution. Currently there does not appear to be a widely accepted theory for concentrated long fiber suspensions.

2.6.1 Stress Tensor Models

2.6.1.1 Newtonian Suspending Fluid

Early attempts to characterize the viscous behavior of particle suspensions extend the work of Einstein [202] who derived the increase to the intrinsic viscosity of spherical particles at dilute concentrations. Higher order terms were added to Einstein's equation to account for particles containing an aspect ratio [121]. Carter [42] provided a relationship for the first normal stress difference as a function of aspect ratio and concentration on the assumption that fiber collisions cause non-zero normal stresses in Newtonian fluids. However, these types of relationships cannot account for the contribution to stress caused by particle motion. Hinch and Leal [203] provide a generalized stress tensor accounting for fiber orientation:

$$\boldsymbol{\sigma} = -P\mathbf{I} + 2\eta_m\mathbf{D} + 2\eta_m\phi_v[a\mathbf{A}_4\colon\mathbf{D} + b(\mathbf{D}\cdot\mathbf{A} + \mathbf{A}\cdot\mathbf{D}) + c\mathbf{D} + f\mathbf{A}D_r] \tag{2.59}$$

where, coefficients *a*, *b*, *c*, and *f*, are material constants, P is the isotropic pressure, η_m is the suspending fluid viscosity, ϕ_v is the fiber volume fraction, and D_r is the rotary diffusivity due to Brownian motion. There are many approaches in finding the material constants in Eq. (2.59). Early approaches from Hand [154] and Giesekus [204] use an exact solution from Jeffery's [152] calculation of the flow around an ellipsoidal particle. Hinch and Leal [162] provide the limiting

material constants for oblate to prolate ellipsoidal particles. In §2.1 fiber suspensions are regarded as non-Brownian, thus removing the Brownian motion term from the stress equation. The a term scales the contribution to stress caused by fibers resisting elongation parallel to the particle's major axis. The *b* term describes the anisotropy of particle orientation in relationship to the flow field. The *c* term quantifies a contribution to stress that is independent of fiber orientation. Hinch and Leal [162] provide the following constants for dilute large aspect ratio ellipsoids:

$$a = \frac{a_r^2}{2[\ln(2a_r) - 1.5]} \tag{2.60}$$

$$b = \frac{6\ln(2a_r) - 11}{a_r^2} \tag{2.61}$$

$$c = 2 \tag{2.62}$$

For long slender particles, the ratio *b/a* decreases significantly with increasing aspect ratio for dilute suspensions [205]. Most works pertaining to fiber suspensions consider the contribution of the *b* term to be negligible.

Batchelor [206] extended the slender-body theory to the development of a stress relationship for ellipsoidal particles. In this derivation, the motion and local velocity field around each particle must be known and the continuum stress stems from averaging the stress over the surface of many particles. Further derivation of Batchelor's dilute theory has been extended to particles with arbitrary cross sections by Lubansky et al. [207]. Batchelor [208] used extensional flow to determine material parameters in the semi-dilute regime. Evans [157] and Dinh and Armstrong [209] were able to extend the slender-body theory to provide additional expressions for the material constants. Dinh and Armstrong [209] adapted theory for liquid crystalline materials to fiber suspensions to give the following expression:

$$a = \frac{a_r^2}{3\ln(2h_f/d)} \tag{2.63}$$

where $2h_f/d$ is dependent on the orientation state of the fibers:

$$\frac{2h_f}{d} = \sqrt{\frac{\pi}{\phi_v}} \qquad \text{for aligned orientation} \tag{2.64}$$

$$\frac{2h_f}{d} = \frac{\pi}{2\phi_v a_r} \qquad \text{for random orientation} \tag{2.65}$$

where, h_f is the average distance between particles. A combination of the aligned and random expressions is presented by Chung and Kwon [210] such that each contribution is weighed by a scalar dependent on the second order orientation tensor. Bibbo et al. [211] made an addition to account for the confinement of fiber rotation by solid boundaries. This improved model agreement with rheological data taken from a parallel plate rheometer. When the ratio between gap height to fiber length was greater than 1.2, wall effects were no longer important.

Shaqfeh and Fredrickson [212] improved on Dinh and Armstrong's [209] stress contribution from the fibers using a multiple scattering expansion to better quantify hydrodynamic effects from adjacent fibers. This approach is applicable to semi-dilute suspensions taking the following form:

$$a = \frac{2a_r^2}{3[\ln(1/\phi_v) + \ln\ln(1/\phi_v) + C']}. \tag{2.66}$$

The value of C' is dependent on particle shape and orientation. For cylindrical particles, C' takes a value of -0.6634 for random three-dimensional orientation and 0.1585 for aligned fibers [213]. The use of slender-body theory allows for hydrodynamic effects of adjacent particles to be addressed as an average medium. The relationships based on slender-body theory negate fiber

thickness which defines constants b and c as zero. Mackaplow and Shaqfeh [213] applied the principles of slender-body theory to numerical simulations in the semi-dilute regime. Their numerical methods were in agreement with the predictions of Eq. (2.66) and the experimental data of Bibbo [214]. Slender-body theory will capture fiber-fiber interactions in semi-dilute suspensions up to a concentration of $nL^3 \approx a_r/5$. For aligned suspensions the limiting concentration would increase. In either case, slender-body theory will eventually under predict the fiber contribution to stress above the limiting concentration [213].

Recent works have added additional contributions from fiber-fiber interactions to the slender-body stress tensor. These models are based on the probability that two fibers will interact which is dependent on the relative orientation of interacting fibers. The basis for fiber-fiber interactions can be found in the works of Ranganathan and Advani [170], Sandstrom [215],Toll [216, 217] and Toll and Mason [218]. Djalili-Moghaddam and Toll [219] developed the following expression for contribution to stress from fiber-fiber interactions assuming a Newtonian lubricating flow between interacting fibers:

$$\boldsymbol{\sigma}_{ff} = \frac{4\eta_m k_{ff} a_r^2 \phi_v^2}{3\pi^2} \langle\langle \mathbf{pppp} | \mathbf{p} \times \mathbf{p}' | \rangle\rangle : \mathbf{D} \tag{2.67}$$

where k_{ff} is an empirical parameter accounting for geometrical unknowns in the lubrication flow. The term based on orientation must be determined from a population of fibers where $\mathbf{p}$ and $\mathbf{p}'$ designate separate orientation vectors. The authors added this stress term to the expression of Shaqfeh and Fredrickson to achieve qualitative agreement of transient short fiber data. Good agreement was observed between model and experiment as aspect ratio and concentration were varied. Férec et al. [182] produced a similar expression derived from the interaction distance limited to the fiber diameter. The most significant difference is the use of a structural tensor [Eq.(2.46)] to represent the fiber-fiber interaction term. A structural tensor will improve computation time but requires a closure approximation. This model was able to capture the steady

state and transient rheology of short fiber suspensions using two fitting parameters. These two models may provide a theoretical basis for accounting for stress in more concentrated suspensions, but the models have been relatively untested outside of the original works.

Batchelor [220] accounted for fiber thickness for dilute suspensions yielding an expansion for a cylindrical particle:

$$a = \frac{4a_r^2}{6\ln(2a_r)} f(\varepsilon) \tag{2.68}$$

where, $f(\varepsilon)$ is a correction factor accounting for finite fiber thickness[221]:

$$f(\varepsilon) = \frac{1 + 0.64\varepsilon}{1 - 1.5\varepsilon} + 1.659\varepsilon^2 \tag{2.69}$$

with $\varepsilon = [\ln(2a_r)]^{-1}$. The correction for fiber thickness is significant even for aspect ratios of long fibers. With fiber thickness taken into account, the fibers will still contribute to the stress if perfect flow aligned orientation is achieved. However, this theory only applies to the dilute concentration regime. Bibbo et al. [211] addresses the thickness of fibers in the semi-dilute concentration regime with aligned fibers following the interparticle spacing given in Eq.(2.64). This method yields the following expression for steady state viscosity:

$$\frac{\eta}{\eta_m} = \frac{1}{1 - (4\phi_v/\pi)^{1/2}}. \tag{2.70}$$

The authors attempt to quantify shear thinning of the fiber suspension using the same expression. However, this method will shift thinning behavior to lower rates provided that the suspending medium is a shear thinning fluid. The use of this relationship toward material constants used in Eq. (2.59) was not addressed by the authors nor had the model been evaluated in cases where fibers are not fully aligned.

Lipscomb et al. [111] employed the use of the transverse isotropic model developed by Ericksen [222] to investigate dilute suspensions flowing through a contraction. In the case of large aspect ratios the material constants were determined as:

$$a = \frac{a_r^2}{2\ln(a_r)} \tag{2.71}$$

$$c = 2. \tag{2.72}$$

By allowing $c = 2$, the model recovers the infinite dilute case derived by Jeffery for ellipsoidal particles. Simulations performed by Lipscomb et al. using these constants show a substantial change in streamlines through the contraction compared to the suspending fluid.

Following the Lipscomb et al. stress tensor, some authors have used the material constant, a, as a fitting parameter [11, 60, 61, 79, 159]. Ausias et al. [61] made the additional simplifying assumption for simple shear that orientation and stress were a function of shear strain. Ortman et al. [134] proposed additional modifications to this stress tensor to account for shear thinning and to enhance the transient response for concentrated long glass fibers. The material constants a and c became empirical functions to better represent the transient response and shear thinning, respectively. The a function became a product of a scalar and the three invariants of the second order orientation tensor, **A**. The value of c was determined from a power-law relationship to quantify shear thinning with two empirical parameters. Reasonable fits to some experimental data were obtained, but the model's parameters varied with concentration. Additionally, this modification did not ensure that the dilute case (i.e. $a \to 0$ and $c = 2$ as $\phi_v \to 0$) was recovered.

2.6.1.2 Non-Newtonian Suspending Fluids

It may be a fair assumption that most fiber suspensions of industrial interest will not involve a Newtonian matrix. Mueller and coworkers [68] used a Herschel-Bulkley model to represent rheological data containing a yield stress for oblate to prolate ellipsoids. Parameters for the model

were represented by empirical expressions based on the concentration, aspect ratio and maximum packing fraction of the fibers. This approach provided good fits to steady shear data but is not based on the orientation of the particles. The use of the Herschel-Bulkley model was applied to the squeeze flow of short and long fiber suspensions by Servais et al. [93]. For long fibers the authors modified the model to account for localized squeeze flow between interacting fibers. The model provided good agreement with experimental data using model parameters obtained from independent measurements. Thomasset et al. [79] accounted for yield stress in long fiber suspension by adding a term to the Lipscomb stress tensor. The shear thinning of the matrix was represented as a Carreau fluid and coefficient to the fiber contribution [a in Eq. (2.59)] was used as a fitting parameter. Using this model, the authors were able to capture the shear thinning behavior at low rates. Extensional viscosity was modeled using a separate characteristic time and calculated for planar isotopic and random orientations. Apparent extensional viscosity data was between these two limiting cases.

Ghosh et al. [223] developed a stress relationship by defining a conformation tensor to represent fiber orientation and relating it to equilibrium thermodynamics. This is capable of capturing contributions from fiber orientation, Brownian motion, fiber flexibility, and fiber interactions. These contributions are weighted by a series of parameters that are fit to rheological data. A similar model from Becraft and Metzner [101] can be recovered through proper choice of model parameters. The conformation tensor model was able to predict normal stress data provided that an effective concentration was used.

To account for fibers suspended in a viscoelastic fluid, many works have replaced the Newtonian stress term in the Eq. (2.59) by the stress form of a model accounting for viscoelasticity. The following viscoelastic models have been used to represent the polymer matrix: K-BZK [224], FENE-P [51, 225-227], FENE-CR [227], Giesekus [80, 84, 227] Leonov [228] and Jeffery [84]. Beaulne and Mitsoulis [224] used the K-BZK model coupled with the Dinh-Armstrong stress equation to obtain a reasonable representation of the steady shear rheology for short fibers, but

found that the model over predicts the concentration dependence in long fiber suspensions. In modeling fiber orientation, most studies also tend to use the Folgar-Tucker model [Eq. (2.37)] for simplicity.

Azaiez [227] extended the work of Ait-Kadi et al. [226] to modify the Giesekus, FENE-P, and FENE-CR stress models to include fiber orientation using the argument that the orientation of the fibers induce an anisotropic hydrodynamic force on the polymer chains. The influence of the polymer-fiber coupling on the shear viscosity was minimal, but the first normal stress difference displayed a larger overshoot and steady state with increased polymer-fiber coupling. The FENE-CR model was able to capture the shear thinning behavior at low deformation rates, which was not evident in the use of the other two models. However, Ait-Kadi et al. [226] observed shear thinning in their predictions using the FENE-P model with a quadratic closure approximation in the fiber orientation equation. The Giesekus model, shown in Eq. (2.73), provides an example of the polymer-fiber coupling. Additional polymer-fiber coupling is accounted for in the FENE-P and FENE-CR models:

$$\lambda \boldsymbol{\sigma}_{p(1)} + s\boldsymbol{\sigma}_p - \frac{\alpha_p \lambda}{\eta_0}\left(\boldsymbol{\sigma}_p \cdot \boldsymbol{\sigma}_p\right) + \frac{3(1-s)}{2}\left(\mathbf{A} \cdot \boldsymbol{\sigma}_p + \boldsymbol{\sigma}_p \cdot \mathbf{A}\right) = -2\eta_0 \mathbf{D} \tag{2.73}$$

where, $\boldsymbol{\sigma}_{p(1)}$ denotes the upper-convected derivative of the polymer stress $\boldsymbol{\sigma}_p$, λ describes the nature of the bead-spring representation of a polymer chain, s is the polymer fiber coupling factor ranging between 0 and 1, and η_0 is the zero shear viscosity of the polymer matrix. The degree of polymer-fiber coupling is determined by the choice of s. When s equals unity, the unmodified Giesekus model for the polymer chain is recovered.

Just as fiber orientation may affect polymer motion, Park and Kwon [228] propose an phenomenological expression for the effect of the viscoelastic matrix on fiber orientation. The interaction coefficient in the Folgar-Tucker model has been modified as:

$$C_I = \frac{C_I^*}{\frac{h_f}{L}[tr(\mathbf{A} \cdot \mathbf{c_e})]^n} \tag{2.74}$$

where, C_I^* and n are empirical parameters that must be determined experimentally, h_f is the interfiber distance described for example in Eqs. (2.63) and (2.64), $\mathbf{c_e}$ is the Finger strain tensor, L is the fiber length. The n parameter describes the level of polymer-fiber coupling and is recommended to be below 0.5. This parameter has its greatest impact on stress at high deformation rates. Modeling the suspending fluid as a multi-modal Leonov viscoelastic model, the authors fit model parameters to the steady shear viscosity of the suspensions. Predictions of the first normal stress difference overestimated the experimental data by less than an order of magnitude.

2.6.1.3 Fiber Flexibility

As discussed in §2.4.1.7, the rheology of a suspension appears to be sensitive to fibers that exhibit flexibility under flow. Forgacs and Mason [117] derived an expression to determine the critical stress required to bend a fiber under shear flow:

$$(\dot{\gamma}\eta_m)_{crit.} \cong \frac{E_b(\ln 2a_r - 1.75)}{2a_r^4} \tag{2.75}$$

where, E_b is the bending modulus of the fiber. Experimentally determined values of bending modulus calculated through Eq. (2.75) were found to be 2 to 4 times the value of the Young's modulus, E_Y, of the fiber. This expression is dependent on the fiber aspect ratio and not the fiber's physical dimensions. It is notable that the critical stress is inversely proportional to a_r^4 which is also present in Switzer and Klingenburg's effective stiffness parameter discussed in §2.2.2.

A thermodynamically derived theory for fiber suspensions is based on the GENERIC framework [189, 229]. The model takes into account fiber-fiber, fiber-polymer and fiber semi-flexibility. These contributions are weighed through the use of phenomenological parameters rooted in thermodynamics, but cannot be directly measured. Ramazani et al. [64] and Rajabian et

al. [188] used a conformation tensor to represent the polymeric suspending fluid, making the model applicable to non-Newtonian fluids. Keshtkar et al. [75] regarded the suspending fluid as Newtonian and fit the model parameters to transient data at a single shear rate. These works observed good agreement between model predictions and steady state rheological properties. The model over predicts the stress growth overshoot's dependency on shear rate for rigid and semi-flexible fibers.

Ortman et al. [134] derived the stress contribution of a fiber bending due to flow based on Strautins and Latz's [184] representation of a semi-flexible fiber:

$$\boldsymbol{\sigma}_{Bend} = \eta_m k \frac{3\phi_v a_r}{2} (\mathbf{B} - \mathbf{A}\ tr\mathbf{B}). \tag{2.76}$$

A limitation of this stress model is that it must be coupled with the semi-flexible orientation model given in Eqs. (2.53) - (2.57) to determine the **A** and **B** tensors. The additional stress is also dependent on the bending potential, k, which Ortman et al. estimated using Eq.(2.57). The bending stress term becomes zero when no flexibility is observed (i.e. $\mathbf{B} = -\mathbf{A}$).

2.6.2 Additional Modelling Methods

Although most methods to simulate fiber orientation stem from the work of Jeffery, other approaches have been developed as well. Le Corre and coworkers [230, 231] consider fibers as a periodic network where fibers are linked by viscous point interactions taking the form of a power-law. The power-law interactions on the local scale cause the global suspension to exhibit power-law behavior with the same power-law index. The fiber network approach is applicable to concentrated suspensions and suspensions of fiber bundles. Simulations saw some agreement with the compression molding data of Dumont et al. [232].

Numerical simulations based on the physics of a single fiber provide fundamental information on the flow of fiber suspensions. Typically the equations of motion are solved for

each particle subjected to specified forces and torques. Using multiple segments to represent a fiber, flexible fibers can be addressed using numerical simulations. Results can be dependent on the number of segments used to represent a fiber [233]. Optimization of fiber segments and computation time has been addressed by Wang and coworkers [234]. In most works, the rigid fiber case provides a first test of the model, verifying the work of Jeffery. Hinch [235] was one of the earliest works to address fiber flexibility. Simulations using slender-body theory do not exhibit periodic rotations, but if slight flexibility is included then periodic rotations will be observed. The slender-body approach was then extended to fibers consisting of finite segments. S-shaped fibers were observed to straighten in shear flow and did not achieve full alignment. These results are somewhat contrary to the experiments of Forgacs and Mason [117] who continued to observe periodic rotations with bent fibers. Yamamoto and Matsuoka [236] represented flexible fibers as bonded spheres with the capabilities of controlling stretching, bending and twisting between spheres. Their work prescribed bending to be in good agreement with Eq. (2.75) above aspect ratios of 15.

Thomasset and coworkers [237] modeled long fiber suspensions in 2-dimensional flows with fiber interactions represented as a stick-slip type behavior. When interaction occurred near the ends of the fibers then the fibers would align parallel to one another. However, when interactions were near the fiber center, small flocculations would form and would exhibit a star shaped conformation. Skjetne et al. [238] modeled flexible fibers as spheres with ball and socket joints. Near solid boundaries they report similar behavior as Thomasset et al. [237] in that fibers will migrate due to the interaction and bending at the boundary. Depending on initial orientation, flow field and degree of bending, a flexible fiber will experience a drift in orientation rotation. Further investigation was performed by Wang et al. [175] who determined that planar drift was periodic. In fibers that had 3-dimensional orientation, drift and rotation caused particle migration. Schmid and coworkers [239] observed irregular equilibrium fiber shapes caused by fiber interactions. Interfiber friction was determined to cause flocculations to form which increase with

increasing concentration. Viscosity increases with concentration up to a point then a jump in the trend is observed due to the formation of flocculations [18]. The formation and large increase in viscosity can be attributed to anisotropic bending and non-affine motion [233]. In these works fiber flocculation can result from the friction between fibers alone.

Joung et al. [240] observed that by increasing the flexibility of fibers in the simulations the magnitudes of the rheological response also increased. Simulation results on a single fiber match that of Hinch [235]. In semi-concentrated suspensions, viscosity was observed to reach a maximum when fibers had 5 to 10 degrees of curvature [241]. The magnitude of viscosity was less for higher degrees of curvature. Tang and Advani [242] extend the work of Joung et al. [240] and Hinch [235] to include direct simulation of two interacting bent fibers. The fibers were observed to fold against each other before aligning with the flow. Viscosity reached a maximum value when the central segment of a fiber was 39 degrees to the direction of flow. Yamanoi and coworkers [243] simulated the transient rheological response and observed the typical stress growth profile at low shear rates. At a shear rate of 10 s^{-1}, secondary overshoots were observed indicating additional fiber motion after steady state was reached. Similar behavior was seen in the first normal stress difference. This work negated fiber-fiber interactions to which no flocculations were formed. Shear thinning was attributed to a smaller hydrodynamic radius created by a bent fiber, which would then reduce the viscosity. Kittipoomwong and Jabbarzadeh [244] used a network of spheres to represent a fiber and included the Rotne-Prager velocity disturbance. Stress growth simulations showed an undershoot after the initial overshoot before reaching a steady state. Steady state first normal stress difference matched that of Carter [42]. This work saw no apparent change in the first normal stress due to fiber curvature.

Numerical simulations can provide interesting information on semi-flexible fibers while avoiding many of the experimental pitfalls. Much of the work has validated the periodic motion described by Jeffery and then added flexibility. Many of the works also observed good quantitative agreement with experiments. These simulations can yield similar rheological behavior despite

differences in numerical techniques. For example, Switzer and Klingenburg [233] observed shear thinning to occur at lower rates due to flocculations while Yamanoi et al. [243] observed similar shear thinning in the absence of flocculations and attributed thinning to fiber flexibility. The complexity of numerical simulations has largely limited this method to simple flows. Since the direct simulation of fibers is based on first principles, results can provide information to how experiments can be tailored to address specific aspects of flexible fiber suspensions.

2.6.3 Impact of Stress Tensor on Flow

As mentioned at the beginning of the section, fiber orientation and the equations of momentum are highly coupled. However, assumptions can be made to simplify these equations depending on the fiber contribution to stress ($N_p = a\phi_v/(1 + c\phi_v)$ and the out-of-plane fiber orientation (δ). Tucker [205] discusses four flow regimes that arise based on the dimensionless group $N_p\delta^2$. More simplistically, fiber orientation can be coupled or decoupled from the equations of momentum. When $N_p\delta^2 \ll 1$ the flow of the suspension can be modeled by the suspending fluid alone with orientation being post calculated. This approach has been successfully applied to injection molding simulations [178, 245, 246]. Lipscomb et al. [111] noted that the streamlines changed significantly for dilute concentrations of long fibers in a 4:1 asymmetric contraction when flow and orientation were coupled. Tucker describes additional flow regimes coupling flow and orientation which result in significantly different velocity profiles. However, molding simulations comparing coupled versus decoupled have not shown a significant discrepancy in orientation predictions [247, 248]. Perhaps an additional argument for the decoupling assumption is the absence of a stress relationship that can accurately represent concentrated fiber suspensions.

2.7 References

[1] Advani SG, Sozer EM. Process Modeling in Composites Manufacturing. New York: Marcel Dekker, Inc.; 2003.

[2] Plueddemann EP. Silane Coupling Agents: Plenum Press, New York; 1991.

[3] Kalia S, Kaith BS, Kaur I. Pretreatments of natural fibers and their application as reinforcing material in polymer composites-A review. Polym Eng Sci. 2009;49:1253-72.
[4] Han CD, Van Den Weghe T, Shete P, Haw JR. Effects of coupling agents on the rheological properties, processability, and mechanical properties of filled polypropylene. Polym Eng Sci. 1981;21:196-204.
[5] Kalaprasad G, Mathew G, Pavithran C, Thomas S. Melt rheological behavior of intimately mixed short sisal-glass hybrid fiber-reinforced low-density polyethylene composites. I. Untreated fibers. J Appl Polym Sci. 2003;89:432-42.
[6] Kalaprasad G, Thomas S. Melt rheological behavior of intimately mixed short sisal-glass hybrid fiber-reinforced low-density polyethylene composites. II. Chemical modification. J Appl Polym Sci. 2003;89:443-50.
[7] Ganani E, Powell RL. Rheological properties of rodlike particles in a Newtonian and a non-Newtonian fluid. J Rheol. 1986;30:995-1013.
[8] Burgers JM. Second Report on Viscosity and Plasticity. Academy of Sciences, Amsterdam 1938. 133-84.
[9] Ivanov Y, van de Ven GM, Mason SG. Damped oscillations in the viscosity of suspensions of rigid rods. I. Monomodal suspensions. J Rheol. 1982;26:213-30.
[10] Chaouche M, Koch DL. Rheology of non-Brownian rigid fiber suspensions with adhesive contacts. J Rheol. 2001;45:369-82.
[11] Eberle APR, Baird DG, Wapperom P, Vélez-García GM. Obtaining reliable transient rheological data on concentrated short fiber suspensions using a rotational rheometer. J Rheol. 2009;53:1049-68.
[12] Djalili-Moghaddam M, Ebrahimzadeh R, Toll S. Study of geometry effects in torsional rheometry of fibre suspensions. Rheol Acta. 2004;44:29-37.
[13] Doi M, Edwards SF. The Theory of Polymer Dynamics: Oxford University Press, New York; 1986.
[14] Flory PJ. Phase equilibria in solutions of rod-like particles. Proc R Soc London, Ser A. 1956;A234:79-89.
[15] Huq AMA, Azaiez J. Effects of length distribution on the steady shear viscosity of semiconcentrated polymer-fiber suspensions. Polym Eng Sci. 2005;45:1357-68.
[16] Kunc V, Frame BJ, Nguyen BN, Tucker CL, Vélez-García GM. Fiber length distribution measurement for long glass and carbon fiber reinforced injection molded thermoplastics. Society of Plastics Engineers Automotive Composites Conference & Exhibition. Troy, Michigan. 2007.
[17] Crosby JM. Long-Fiber Molding Materials. Thermoplastic Composite Materials 1991;7:139-65.
[18] Switzer LH, Klingenberg DJ. Rheology of sheared flexible fiber suspensions via fiber-level simulations. J Rheol. 2003;47:759-78.
[19] Switzer LH. Simulating Systems of Flexible Fibers. PhD Thesis: University of Wisconsin; 2002.
[20] Clarke AR, Archenhold G, Davidson NC. A novel technique for determining the 3D spatial distribution of glass fibres in polymer composites. Compos Sci Technol. 1995;55:75-91.
[21] Kawamura M. Unambiguous determination of 3D fiber orientation distribution in thermoplastic composites using SAM image of elliptical mark and interference fringe. J Compos Mater. 2005;39:287-99.
[22] Avérous L, Quantin JC, Crespy A. Evolution of the three-dimensional orientation distribution of glass fibers in injected isotactic polypropylene. Polym Eng Sci. 1997;37:329-37.
[23] Young SA. High resolution x-ray tomography of fiber reinforced polymeric composites. Master's Thesis: University of Tennessee-Knoxville; 2009.
[24] Teßmann M, Mohr S, Gayetskyy S, Haßler U, Hanke R, Greiner G. Automatic Determination of Fiber-Length Distribution in Composite Material Using 3D CT Data. EURASIP J Adv Sig Pr. 2010;2010:545030.
[25] Darlington MW, Mcginley PL. Fibre orientation distribution in short fibre reinforced plastics. Journal of Materials Science. 1975;10:906-10.

[26] Konicek TS. A method to determine the three-dimensional fiber orientation in fiber reinforced polymers. Master's Thesis: University of Illinois at Urbana-Champaign; 1987.
[27] Vélez-García GM, Wapperom P, Kunc V, Baird DG, Zink-Sharp A. Sample preparation and image acquisition using optical-reflective microscopy in the measurement of fiber orientation in thermoplastic composites. J Microsc. 2012;248:23-33.
[28] Clarke AR, Davidson NC, Arhenhold G. Mesostructural characterization of aligned fibre composites. In: Papathanasious TD, Guell DC, editors. Flow-induced alignment in composite materials. Cambridge: Woodhead Publishing Limited; 1997. 230-92.
[29] Mlekusch B, Lehner EA, Geymayer W. Fibre orientation in short-fibre-reinforced thermoplastics I. Contrast enhancement for image analysis. Compos Sci Technol. 1999;59:543-5.
[30] Hine PJ, Duckett RA. Fiber orientation structures and mechanical properties of injection molded short glass fiber reinforced ribbed plates. Polym Compos. 2004;25:237-54.
[31] Bay RS, Tucker CL. Stereological measurement and error estimates for three-dimensional fiber orientation. Polym Eng Sci. 1992;32:240-53.
[32] Vélez-García GM, Wapperom P, Baird DG, Aning AO, Kunc V. Unambiguous orientation in short fiber composites over small sampling area in a center-gated disk. Composites Part A. 2012;43:104-13.
[33] Hofmann JT, Vélez-García GM, Baird DG, Whittington AR. Application and evaluation of the method of ellipses for measuring the orientation of long, semi-flexible fibers. Polym Compos. 2013;34:390-8.
[34] Hofmann JT. Extension of the Method of Ellipses to Determining the Orientation of Long, Semi-Flexible Fibers in Model 2- and 3-Dimensional Geometries. PhD Thesis: Virginia Polytechnic Institute and State University; 2013.
[35] Ganani E, Powell RL. Suspensions of rodlike particles: literature review and data correlations. J Compos Mater. 1985;19:194-215.
[36] Maschmeyer RO, Hill CT. The rheology of concentrated suspensions of fibers. Adv Chem Ser. 1974;134:95-105.
[37] Metzner AB. Rheology of suspensions in polymeric liquids. J Rheol. 1985;29:739-75.
[38] Powell RL. Rheology of suspension of rodlike particles. J Stat Phys. 1991;62:1073-94.
[39] Zirnsak MA, Hur DU, Boger DV. Normal stresses in fibre suspensions. J Non-Newton Fluid Mech. 1994;54:153-93.
[40] Eberle APR, Baird D, Wapperom P. Rheology of non-Newtonian fluids containing glass fibers: a review of experimental literature. Ind Eng Chem Fundam. 2008;47:3470-88.
[41] Petrie CJS. The rheology of fibre suspensions. J Non-Newton Fluid Mech. 1999;87:369-402.
[42] Carter LF. A Study of the Rheology of Suspensions of Rod-Shaped Particles in a Navier-Stokes Liquid. PhD Thesis: University of Michigan; 1967.
[43] Han CD, Lem K-W. Rheology of unsaturated polyester resins. I. Effects of filler and low-profile additive on the rheological behavior of unsaturated polyester resin. J Appl Polym Sci. 1983;28:743-62.
[44] Goto S, Nagazono H, Kato H. The flow behavior of fiber suspensions in Newtonian fluids and polymer solutions. I. Mechanical properties. Rheol Acta. 1986;25:119-29.
[45] Mary B, Dubois C, Carreau PJ, Brousseau P. Rheological properties of suspensions of polyethylene-coated aluminum nanoparticles. Rheol Acta. 2006;45:561-73.
[46] Djalili-Moghaddam M, Toll S. Fibre suspension rheology: effect of concentration, aspect ratio and fibre size. Rheol Acta. 2006;45:315-20.
[47] Cox WP, Merz EH. Correlation of dynamic and steady flow viscosities. J Polym Sci. 1958;28:619-22.
[48] Mobuchon C, Carreau PJ, Heuzey M-C, Sepehr M, Ausias G. Shear and extensional properties of short glass fiber reinforced polypropylene. Polym Compos. 2005;26:247-64.
[49] Marcaníková L, Hausnerová B, Kitano T. Rheological behavior of composites based on carbon fibers recycled from aircraft waste. American Institute of Physics International Conference. 2009.

[50] Kitano T, Kataoka T, Nagatsuka Y. Dynamic flow properties of vinylon fibre and glass fiber reinforced polyethylene melts. Rheol Acta. 1984;23:408-16.
[51] Guo R, Azaiez J, Bellehumeur C. Rheology of fiber filled polymer melts: role of fiber-fiber interactions and polymer-fiber coupling. Polym Eng Sci. 2005;45:385-99.
[52] Keshtkar M, Heuzey MC, Carreau PJ. Rheological behavior of fiber-filled model suspensions: effect of fiber flexibility. J Rheol. 2009;53:631-50.
[53] Greene JP, Wilkes JO. Steady-state and dynamic properties of concentrated fiber-filled thermoplastics. Polym Eng Sci. 1995;35:1670-81.
[54] Hashmi SAR, Kitano T, Vashishtha SR, Chand N. Organic/inorganic hybrid fibre reinforced thermoplastic composites and their rheological properties. Indian J Eng Mater Sci. 2002;9:289-94.
[55] Starý Z, Krückel J, Weck C, Schubert DW. Rheology and conductivity of carbon fibre composites with defined fibre lengths. Compos Sci Technol. 2013;85:58-64.
[56] Férec J, Heuzey MC, Ausias G, Carreau PJ. Rheological behavior of fiber-filled polymers under large amplitude oscillatory shear flow. J Non-Newton Fluid Mech. 2008;151:89-100.
[57] Carneiro OS, Maia JM. Rheological behavior of (short) carbon fiber/thermoplastic composites. Part II: the influence of matrix type. Polym Compos. 2000;21:970-7.
[58] Petrich MP, Caouche M, Koch DL, Cohen C. Oscillatory shear alignment of a non-Brownian fiber in a weakly elastic fluid. J Non-Newton Fluid Mech. 2000;91:1-14.
[59] Laun HM. Orientation effects and rheology of short glass fiber-reinforced thermoplastics. Colloid Polym Sci. 1984;262:257-69.
[60] Sepehr M, Ausias G, Carreau PJ. Rheological properties of short fiber filled polypropylene in transient shear flow. J Non-Newton Fluid Mech. 2004;123:19-32.
[61] Ausias G, Agassant JF, Vincent M, Lafleur PG, Lavoie PA, Carreau PJ. Rheology of short glass fiber reinforced polypropylene. J Rheol. 1992;36:525-42.
[62] Barbosa SE, Ercoli DR, Bibbo MA, Kenny JM. Rheology of short-fiber composites: a systematic approach. Compos Struct. 1994;27:83-91.
[63] Carneiro OS, Maia JM. Rheological behavior of (short) carbon fiber/thermoplastic composites. Part I: the influence of fiber type, processing conditions and level of incorporation. Polym Compos. 2000;21:960-9.
[64] Ramazani S. A. A, Ait-Kadi A, Grmela M. Rheology of fiber suspensions in viscoelastic media: experiments and model predictions. J Rheol. 2001;45:945-62.
[65] Sepehr M, Carreau PJ, Moan M, Ausias G. Rheological properties of short fiber model suspensions. J Rheol. 2004;48:1023-48.
[66] Rajabian M, Dubois C, Grmela M, Carreau PJ. Effects of polymer–fiber interactions on rheology and flow behavior of suspensions of semi-flexible fibers in polymeric liquids. Rheol Acta. 2008;47:701-17.
[67] Marín-Santibáñez BM, Pérez-González J, Vargas L. Shear rheometry and visualization of glass fiber suspensions. Rheol Acta. 2009;49:177-89.
[68] Mueller S, Llewellin EW, Mader HM. The rheology of suspensions of solid particles. Proc R Soc London, Ser A. 2010;466:1201-28.
[69] Hausnerova B, Zdrazilova N, Kitano T, Saha P. Rheological properties of carbon fibre filled low-density polyethylene under the parallel steady and oscillatory shear flows. Polimery. 2006;51:33-41.
[70] Chan Y, White JL, Oyanagi Y. Influence of glass fibers on the extrusion and injection molding characteristics of polyethylene and polystyrene melts. Polym Eng Sci. 1978;18:268-72.
[71] Nawab MA, Mason SG. The viscosity of dilute suspensions of thread-like particles. J Phys Chem. 1958;62:1248-53.
[72] Mewis J, Metzner AB. The rheological properties of suspensoins of fibres in Newtonian fluids subject to extensionsal deformations. J Fluid Mech. 1974;62:593-600.
[73] Bird RB, Armstrong RC, Hassager O. Dynamics of Polymeric Liquids. Volume 1: Fluid Mechanics. 2nd ed: Wiley Interscience, New York, 1987; 1987.

[74] Keshtkar M, Heuzey MC, Carreau PJ. Rheology of LDPE-based semiflexible fiber suspensions. Polym Compos. 2009;31:1474-86.
[75] Keshtkar M, Heuzey MC, Carreau PJ, Rajabian M, Dubois C. Rheological properties and microstructural evolution of semi-flexible fiber suspensions under shear flow. J Rheol. 2010;54:197-222.
[76] Czarnecki L, White JL. Shear flow rheological properties, fiber damage, and mastication characteristics of aramid-, glass-, and cellulose-fiber-reinforced polystyrene melts. J Appl Polym Sci. 1980;25:1217-44.
[77] Kitano T, Kataoka T. The rheology of suspension of vinylon fibers in polymer liquids. I. Suspensions in silicone oil. Rheol Acta. 1987;20:390-402.
[78] Weinberger CB, Goddard JD. Extensional flow behavior of polymer solutions and particle suspensoins in a spinning motion. Int J Multiphase Flow. 1974;1:465-86.
[79] Thomasset J, Carreau PJ, Sanschagrin B, Ausias G. Rheological properties of long glass fiber filled polypropylene. J Non-Newton Fluid Mech. 2005;125:25-34.
[80] Kagarise C, Miyazono K, Mahboob M, Koelling KW, Bechtel SE. A constitutive model for characterization of shear and extensional rheology and flow induced orientation of carbon nanofiber/polystyrene melt composites. J Rheol. 2011;55:781-807.
[81] Yokohara T, Nobukawa S, Yamaguchi M. Rheological properties of polymer composites with flexible fine fibers. J Rheol. 2011;55:1205-18.
[82] Kizior TE, Seyer FA. Axial stress in elongational flow of fiber suspension. Trans Soc Rheol. 1974;18:271-85.
[83] Kamal MR, Mutel AT, Utracki LA. Elongational behavior of short glass fiber reinforced polypropylene melts. Polym Compos. 1984;5:289-98.
[84] Creasy TS, Advani SG, Okine RK. Non-linear response of a long, discontinuous fiber/melt system in elongational flows. Rheol Acta. 1996;35:347-55.
[85] Creasy TS, Advani SG, Okine RK. Transient rheological behavior of a long discontinuous fiber-melt system. J Rheol. 1996;40:497-519.
[86] Kitano T, Kataoka T. The rheology of suspensions of vinylon fibers in polymer liquids. II. Suspensions in polymer solutions. Rheol Acta. 1987;20:403-15.
[87] Wu G, Asai W, Sumita M, Hattori T, Higuchi R, Washiyama J. Estimation of flocculation structure in filled polymer composites by dynamics rheological measurements. Colloid Polym Sci. 2000;278:220-8.
[88] Hausnerova B, Honkova N, Lengalova A, Kitano T, Saha P. Rheology and fiber degradation during shear flow of carbon-fiber-reinforced polypropylenes. Polym Sci Ser A. 2006;48:951-60.
[89] Hausnerova B, Honkova N, Lengalova A, Kitano T, Saha P. Rheological behavior of fibre-filled polymer melts at low shear rate. Part II. Experimental investigation. Polimery. 2008;53:649-57.
[90] Kim JK, Song JH. Rheological properties and fiber orientations of short fiber-reinforced plastics. J Rheol. 1997;41:1061-85.
[91] Morrison SR, Harper JC. Wall effecct in couette flow of non-Newtonian suspensions. Ind Eng Chem Fundam. 1965;4:176-81.
[92] Servais C, Månson J-AE. The relationship between steady-state and oscillatory shear viscosity in planar randomly oriented concentrated fiber suspensions. J Rheol. 1999;43:1019-31.
[93] Servais C, Luciani A, Månson J-AE. Squeeze flow of concentrated long fibre suspensions: experiments and model. J Non-Newton Fluid Mech. 2002;104:165-84.
[94] Roberts RW, Jones RS. Rheological characterization of continuous fibre composites in oscillatory shear flow. Comp Manuf. 1995;6:161-7.
[95] Ericsson KA, Toll S, Månson J-AE. Sliding plate rheometry of planar oriented concentrated fiber suspension. Rheol Acta. 1997;36:397-405.
[96] Ortman KC. Assessing an Orientation Model and Stress Tensor for Semi-Flexible Glass Fibers in Polypropylene Using a Sliding Plate Rheometer: for the Use of Simulating Processes. Virginia Polytechnic Institute and State University; 2011.

[97] Kitano T, Kataoka T, Nagatsuka Y. Shear flow rheological properties of vinylon- and glass-fiber reinforced polyethylene melts. Rheol Acta. 1984:20-30.
[98] Ortman KC, Agarwal N, Eberle APR, Baird DG, Wapperom P, Jeffrey Giacomin A. Transient shear flow behavior of concentrated long glass fiber suspensions in a sliding plate rheometer. J Non-Newton Fluid Mech. 2011;166:884-95.
[99] Maschmeyer RO, Hill CT. Rheology of concentrated suspensions of fibers in tube flow. III. Suspensions with the same fiber length distribution. Trans Soc Rheol. 1977;21:195-206.
[100] Maschmeyer RO, Hill CT. Rheology of concentrated suspensions of fibers in tube flow. II. An exploratory study. Trans Soc Rheol. 1977;21:183-94.
[101] Becraft ML, Metzner AB. The rheology, fiber orientation, and processing behavior of fiber-filled fluids. J Rheol. 1992;36:143-74.
[102] Nair KCM, Kumar RP, Thomas S, Schit SC, Ramamurthy K. Rheological behavior of short sisal fiber-reinforced polystyrene composites. Composites Part A. 2000;31:1231-40.
[103] Crowson RJ, Folkes MJ, Bright PF. Rheology of short glass fiber-reinforced thermoplastics and its application to injection molding I. Fiber motion and viscosity measurement. Polym Eng Sci. 1980;20:925-33.
[104] Crowson RJ, Folkes MJ. Rheology of short glass fiber-reinforced thermoplastics and its application to injection molding. II. The effect of material parameters. Polym Eng Sci. 1980;20:934-40.
[105] Zhang D-W, Li Y-J, Feng Y-H, Qu J-P, He H-Z, Xu B-P. Effect of initial fiber length on the rheological properties of sisal fiber/polylactic acid composites. Polym Compos. 2011;32:1218-24.
[106] Bagley EB. End corrections in the capillary flow of polyethylene. J Appl Phys. 1957;28:624-7.
[107] Wiessenberg K, as cited by Rabinowitsch B. Über die Viskosität und Elastizität von Solen. Z Phys Chem. 1929;A145:1-26.
[108] Mooney M. Explicit formulas for slip and fluidity. J Rheol. 1931;2:210-22.
[109] Chung B, Cohen C. Glass fiber-filled thermoplastics. I. wall and processing effects on rheological properties. Polym Eng Sci. 1985;25:1001-7.
[110] McClelland AN, Gibson AG. Rheology and fibre orientation in the injection moulding of long fibre reinforced nylon 66 composites. Comp Manuf. 1990;1:15-25.
[111] Lipscomb GG, Denn MM, Hur DU, Boger DV. The flow of fiber suspensions in complex geometries. J Non-Newton Fluid Mech. 1988;26:297-325.
[112] Goto S, Nagazono H, Kato H. The flow behavior of fiber suspensions in Newtonian fluids and polymer solutions. II. Capillary flow. Rheol Acta. 1986;25:246-56.
[113] Vaxman A, Narkis M, Siegmann A, Kenig S. Short-fiber-reinforced thermoplastics. Part III: effect of fiber length on rheological properties and fiber orientation. Polym Compos. 1989;10:454-62.
[114] Akay G. Rheology of reinforced thermoplastics and Its application to injection-molding: IV. Transient injection capillary flow and injection-molding. Polym Eng Sci. 1982;22:1027-42.
[115] Ouari N, Kaci A, Tahakourt A, Chaouche M. Rheological behaviour of fibre suspension in non-Newtonian fluids. Appl Rheol. 2011;21:54801.
[116] Feng Y-H, Li Y-J, Xu B-P, Zhang D-W, Qu J-P, He H-Z. Effect of fiber morphology on rheological properties of plant fiber reinforced poly(butylene succinate) composites. Composites Part B. 2013;44:193-9.
[117] Forgacs OL, Mason SG. Particle motions in sheared suspensions IX. Spin and deformation of threadlike particles. J Colloid Interface Sci. 1959:457-72.
[118] Stover CA, Koch DL, Cohen C. Observations of fibre orientation in simple shear flow of semi-dilute suspensions. J Fluid Mech. 1992;238:277-96.
[119] Iso Y, Cohen C, Koch DL. Orientation in simple shear flow of semi-dilute fiber suspensions 2. Highly elastic fluids. J Non-Newton Fluid Mech. 1996;62:135-53.
[120] Mondy LA, Brenner H, Altobelli SA, Abbott JR, Graham AL. Shear-induced particle migration in suspensions of rods. J Rheol. 1994;38:444-52.
[121] Blakeney WR. The viscosity of suspension of straight, rigid rods. J Colloid Interface Sci. 1966;22:324-30.

[122] Anczurowski E, Cox RG, Mason SG. The kinetics of flowing dispersions IV: Transient orientation of Cylinders. J Colloid Interface Sci. 1967;23:547-62.
[123] Okagawa A, Mason SG. Suspensions: fluids with fading memories. Science. 1973;181:159-61.
[124] Mutel AT, Kamal MR. The effect of glass fibers on the rheological behavior of polypropylene melts between rotating parallel plates. Polym Compos. 1984;5:29-35.
[125] Macosko CW. Rheology - Principles, Measurements and Applications: John Wiley & Sons; 1994.
[126] Dealy JM. A shear stress transducer for molten polymers. Rheol Acta. 1982;21:475-7.
[127] Dealy JM, Soong SS. A parallel plate melt rheometer incorporating a shear stress transducer. J Rheol. 1984;28:355-65.
[128] Giacomin AJ. A sliding plate melt rheometer incorporating a shear stress transducer. PhD Thesis: McGill University; 1987.
[129] Giacomin AJ, Samurkas T, Dealy JM. A novel sliding plate rheometer for molten plastics. Polym Eng Sci. 1989;29:499-504.
[130] Oakley JG, Giacomin AJ. A sliding plate normal thrust rheometer for molten plastics. Polym Eng Sci. 1994;34:580-4.
[131] Xu J, Costeux S, Dealy JM, Decker MN. Use of a sliding plate rheometer to measure the first normal stress difference at high shear rates. Rheol Acta. 2007;46:815-24.
[132] Kolitawong C, Giacomin AJ, Johnson LM. Local shear stress transduction. Rev Sci Instrum. 2010;81:021301.
[133] Agarwal N. Transient Shear Flow Rheology of Concentrated Long Glass Fiber Suspensions in a Sliding Plate Rheometer. Master's Thesis: Virginia Polytechnic Institute and State University; 2009.
[134] Ortman K, Baird D, Wapperom P, Whittington A. Using startup of steady shear flow in a sliding plate rheometer to determine material parameters for the purpose of predicting long fiber orientation. J Rheol. 2012;56:955-81.
[135] Milliken WJ, Gottleib M, Graham AL, Mondy LA, Powell RL. The viscosity-volume fraction relation for suspensions of rod-like particles by falling-ball rheometry. J Fluid Mech. 1989;202:217-32.
[136] Powell RL, Mondy LA, Stoker GG, Milliken WJ, Graham AL. Development of a falling ball rheometer with applications to opaque systems: measurements of the rheology of suspensions of rods. J Rheol. 1989;33:1173-88.
[137] Mondy LA, Morrison TG, Graham AL, Powell RL. Measurements of the viscosities of suspensions of oriented rods using a falling ball rheometry. Int J Multiphase Flow. 1990;16:651-62.
[138] Naccache MF, Corrêa JP, Soares IF, Abdu A. Rheological characterization of polymers fiber composite. Polym Compos. 2013;34:1269-78.
[139] Ericsson KA, Toll S, Mason SG. The two-way interaction between anisotropic flow and fiber orientation in squeeze flow. J Rheol. 1997;41:491.
[140] Dumont P, Vassal J-P, Orgéas L, Michaud V, Favier D, Månson J-AE. Processing, characterisation and rheology of transparent concentrated fibre-bundle suspensions. Rheol Acta. 2007;46:639-51.
[141] Guiraud O, Dumont PJJ, Orgéas L, Favier D. Rheometry of compression moulded fibre-reinforced polymer composites: Rheology, compressibility, and friction forces with mould surfaces. Composites Part A. 2012;43:2107-19.
[142] Cogswell FN. Converging flow of polymer melts in extrusion dies. Polym Eng Sci. 1972;12:64-73.
[143] Binding DM. An approximate analysis for the contraction and converging flows. J Non-Newton Fluid Mech. 1988;27:173-89.
[144] Bretherton FP. The motion of rigid particles in a shear flow at low Reynolds number. J Fluid Mech. 1962;14:625-57.
[145] Anczurowski E, Mason SG. The kinetics of flowing dispersions III. Equilibrium orientations of rods and disks (experimental). J Colloid Interface Sci. 1967;23:533-46.

[146] Trevelyan BJ, Mason SG. Particle motions in sheared suspensions. I. Rotations. J Colloid Interface Sci. 1951;6:354-67.
[147] Russel WB, Hinch EJ, Leal LG, Tieffenbruck G. Rods falling near a vertical wall. J Fluid Mech. 1977;83:273-87.
[148] Moses KB, Advani SG, Reinhardt A. Investigation of fiber motion near solid boundaries in simple shear flow. Rheol Acta. 2001;40:296-306.
[149] Ku X, Lin J. Effect of two bounding walls on the rotational motion of a fiber in the simple shear flow. Fibers and Polymers. 2009;10:302-9.
[150] Carlsson A, Lundell F, Söderberg D. The wall effect on the orientation of fibres in a shear flow. Annual Transactions of the Nordic Rheology Society. 2006;14.
[151] Holm R, Söderberg D. Shear influence on fibre orientation. Rheol Acta. 2007;46:721-9.
[152] Jeffery GB. The motion of ellipsoidal particles immersed in a viscous fluid. Proc R Soc London, Ser A. 1922;102:161-79.
[153] Cox RG. The motion of long slender bodies in a viscous fluid. Part 2. Shear flow. J Fluid Mech. 1971;45:625-57.
[154] Hand GL. A theory of dilute suspensions. Arch Rational Mech. 1961;7:81-6.
[155] Hinch EJ, Leal LG. The effect of weak Brownian rotations on particles in shear flow. J Fluid Mech. 1971;46:685-703.
[156] Advani SG, Tucker CL. The use of tensors to describe and predict fiber orientations in short fiber composites. J Rheol. 1987;31:751-84.
[157] Evans JCE. The Flow of a Suspension of Force-Free Rigid Rods in a Newtonian Fluid. PhD Thesis: University of Cambridge; 1975.
[158] Dinh SM. On the Rheology of Concentrated Fiber Suspensions. PhD Thesis: Massachusetts Institute of Technology; 1981.
[159] Férec J, Heniche M, Heuzey MC, Ausias G, Carreau PJ. Numerical solution of the Fokker–Planck equation for fiber suspensions: application to the Folgar–Tucker–Lipscomb model. J Non-Newton Fluid Mech. 2008;155:20-9.
[160] Okagawa A, Cox RG, Mason SG. The kintetics of flowing dispersions VI. Transient orientation and rheological phenomena of rods and disks in shear flow. J Colloid Interface Sci. 1973;45:303-29.
[161] Iso Y, Koch DL, Cohen C. Orientation in simple shear flow of semi-dilute fiber suspensions 1. Weakly elastic fluids. J Non-Newton Fluid Mech. 1996;62:115-34.
[162] Hinch EJ, Leal LG. The effect of Brownian motion on the rheological properties of non-spherical particles. J Fluid Mech. 1972;52:683-712.
[163] Rahnama M, Koch DL, Shaqfeh ESG. The effect of hydrodynamic interactions on the orientation distribution in a fiber suspension subject to simple shear flow. Phys Fluids. 1995;7:487.
[164] Folgar F, Tucker CL. Orientation behavior of fibers in concentrated suspensions. J Reinf Plast Compos. 1984;3:98-119.
[165] Yamane Y, Kaneda Y, Doi M. Numerical simulation of semi-dilute suspensions of rodlike particles in shear flow. J Non-Newton Fluid Mech. 1994;54:405-21.
[166] Yamane Y, Kaneda Y, Doi M. The effect of interaction of rodlike particles in semi-dilute suspensions under shear flow. J Phys Soc Jpn. 1995;64:3265-74.
[167] Bay RS, Tucker CL. Fiber orientation in simple injection moldings. Part II: experimental results. Polym Compos. 1992;13:332-41.
[168] Bay RS. Fiber Orientation in Injection Molded Composites: A Comparison of Theory and Experiment. PhD Thesis: University of Illinois Urbana-Champaign; 1991.
[169] Phan-Thien N, Fan XJ, Tanner RI, Zheng R. Folgar-Tucker constant for fiber suspension in a Newtonian fluid. J Non-Newton Fluid Mech. 2002;103:251-60.
[170] Ranganathan S, Advani SG. Fiber-fiber interactions in homogeneous flows of nondilute suspensions. J Rheol. 1991;35:1499-522.

[171] Huynh HM. Improved Fiber Orientation Predictions for Injection-Molded Composites. Master's Thesis: University of Illinois Urbana-Champaign; 2001.
[172] Eberle APR. The Dynamic Behavior of a Concentrated Composite Fluid Containing Non-Brownian Glass Fibers in Rheometrical Flows. PhD Thesis: Virginia Polytechnic Institute and State University; 2008.
[173] Wang J, O'Gara JF, Tucker CL. An objective model for slow orientation kinetics in concentrated fiber suspensions: theory and rheological evidence. J Rheol. 2008;52:1179-200.
[174] Fan XJ, Phan-Thien N, Zheng R. A direct simulation of fibre suspensions. J Non-Newton Fluid Mech. 1998;74:113-35.
[175] Wang J, Tozzi EJ, Graham MD, Klingenberg DJ. Flipping, scooping, and spinning: drift of rigid curved nonchiral fibers in simple shear flow. Phys Fluids. 2012;24:123304.
[176] Koch DL. A model for orientational diffusion in fiber suspensions. Phys Fluids. 1995;7:2086.
[177] Jack DA, Smith DE. An invariant based fitted closure of the sixth-order orientation tensor for modeling short-fiber suspensions. J Rheol. 2005;49:1091.
[178] Phelps JH, Tucker CL. An anisotropic rotary diffusion model for fiber orientation in short- and long-fiber thermoplastics. J Non-Newton Fluid Mech. 2009;156:165-76.
[179] Hand GL. A theory of anisotropic fluids. J Fluid Mech. 1962;13:33-46.
[180] Tseng H-C, Chang R-Y, Hsu C-H. Phenomenological improvements to predictive models of fiber orientation in concentrated suspensions. J Rheol. 2013;57:1597-631.
[181] Foss PH, Tseng H-C, Snawerdt J, Chang Y-J, Yang W-H, Hsu C-H. Prediction of fiber orientation distribution in injection molded parts using Moldex3D simulation. Polym Compos. 2014;35:671-80.
[182] Férec J, Ausias G, Heuzey MC, Carreau PJ. Modeling fiber interactions in semiconcentrated fiber suspensions. J Rheol. 2009;53:49-72.
[183] Natale G, Heuzey MC, Carreau PJ, Ausias G, Férec J. Rheological modeling of carbon nanotube suspensions with rod-rod interactions. AlChE J. 2013:1-12.
[184] Strautins U, Latz A. Flow-driven orientation dynamics of semiflexible fiber systems. Rheol Acta. 2007;46:1057-64.
[185] Strautins U. Flow-driven orientation dynamics in two classes for fibre suspensions. ScD Thesis: Technischen Universität Kaiserslautern; 2008.
[186] Meyer KJ. Improved Prediction of Glass Fiber Orientation in Basic Injection Molding Geometries. PhD Thesis: Virginia Polytechnic Institute and State University; 2013.
[187] Mazahir S. Improvement in Orientation Predictions of High-Aspect Ratio Particles in Injection Mold Filling Simulations. PhD Thesis: Virginia Polytechnic Institute and State University; 2013.
[188] Rajabian M, Dubois C, Grmela M. Suspensions of semiflexible fibers in polymeric fluids: rheology and thermodynamics. Rheol Acta. 2005;44:521-35.
[189] Grmela M, Öttinger HC. Dynamics and thermodynamics of complex fluids. I. Development of a general formalism. Physical Review E. 1997;56.
[190] Grmela M, Aït-Kadi A, Lafleur PG. Suspensions of fibers in viscoelastic fluids: Rheology. The Journal of Chemical Physics. 1998;109:6973.
[191] Montgomery-Smith S, Jack D, Smith DE. The fast exact closure for Jeffery's equation with diffusion. J Non-Newton Fluid Mech. 2011;166:343-53.
[192] Advani SG, Tucker CL. Closure approximations for three-dimensional structure tensors. J Rheol. 1990;34:367-86.
[193] Doi M. Molecular dynamics and rheological properties of concentrated solutions of rodlike polymers in isotropic and liquid crystalline phases. J Polym Sci, Part B: Polym Phys. 1981;19:229-43.
[194] Hinch EJ, Leal LG. Constitutive equations in suspension mechanics. Part 2. Approximate forms of a suspension of rigid particles affected by Brownian rotations. J Fluid Mech. 1976;76:187-208.
[195] Cintra JS, Tucker CL. Orthotropic closure approximations for flow-induced fiber orientation. J Rheol. 1995;36:1095-122.

[196] VerWeyst BE, Tucker CL, Foss PH, O'Gara JF. Fiber orientation in 3-D injection molded features: prediction and experiment. Int Polym Proc. 1999;14.
[197] Chung DH, Kwon TH. Improved model of orthotropic closure approximation for flow induced fiber orientation. Polym Compos. 2000;22:636-49.
[198] Verleye V, Dupret F. Numerical prediction of fiber orientation in complex injection molded parts. ASME Winter Annual Meeting. 1994.
[199] Dupret F, Verleye V. Modelling the flow of fiber suspensions in narrow gaps. In: Siginer DA, De Kee D, Chhabra RP, editors. Advances in the Flow and Rheology of Non-Newtonian Fluids. Amsterdam: Elsevier; 1999. 1347-98.
[200] Chung DH, Kwon TH. Invariant-based optimal fitting closure approximation for the numerical prediction of flow-induced fiber orientation. J Rheol. 2002;46:169-94.
[201] Férec J, Abisset-Chavanne E, Ausias G, Chinesta F. On the use of interaction tensors to describe and predict rod interactions in rod suspensions. Rheol Acta. 2014;53:445-56.
[202] Einstein A. Eine neue bestimmung der moleküldimensionen. Ann Phys (Leipzig). 1906;19:289-306.
[203] Hinch EJ, Leal LG. Time-dependent shear flows of a suspension of particles with weak Brownian rotations. J Fluid Mech. 1973;57:753-67.
[204] Giesekus H. Elasto-viskose Flüssigkeiten, für die in stationären Schichtströmungen sämtliche Normalspannungskomponenten verschieden groß sind. Rheol Acta. 1962;2:50-62.
[205] Tucker CL. Flow regimes for fiber suspensions in narrow gaps. J Non-Newton Fluid Mech. 1991;39:239-68.
[206] Batchelor GK. The stress system in a suspension of force-free particles. J Fluid Mech. 1970;41:545-70.
[207] Lubansky AS, Boger DV, Cooper-White JJ. Batchelor's theory extended to elongated cylindrical or ellipsoidal particles. J Non-Newton Fluid Mech. 2005;130:57-61.
[208] Batchelor GK. The stress generated in a non-dilute suspension of elongated particles by pure straining motion. J Fluid Mech. 1971;46:813-29.
[209] Dinh SM, Armstrong RC. A rheological equation of state for semiconcentrated fiber suspensions. J Rheol. 1984;28:207-27.
[210] Chung DH, Kwon TH. Fiber orientation in the processing of polymer composites. Korea-Aust Rheol J. 2002;14:175-88.
[211] Bibbo MA, Dinh SM, Armstrong RC. Shear flow properties of semiconcentrated fiber suspensions. J Rheol. 1985;29:905.
[212] Shaqfeh ESG, Fredrickson GH. The hydrodynamic stress in a suspension of rods. Phys Fluids A. 1990;2:7-24.
[213] Mackaplow MB, Shaqfeh ESG. A numerical study of the rheological properties of suspension of rigid, non-brownian fibres. J Fluid Mech. 1996;329:155-86.
[214] Bibbo MA. Rheology of Semiconcentrated Fiber Suspensions. PhD Thesis: Massachusetts Institute of Technology; 1987.
[215] Sandstrom CR. Interactions and orientation in concentrated suspensions of rigid rods: Theory and experiment. PhD Thesis: University of Illinois at Urbana-Champaign; 1993.
[216] Toll S. Note: On the tube model for fiber suspensions. J Rheol. 1993;37:123.
[217] Toll S. Packing mechanics of fiber reinforcements. Polym Eng Sci. 1998;38:1337-50.
[218] Toll S, Månson J-AE. Dynamics of a planar concentrated fiber suspension with non-hydrodynamic interaction. J Rheol. 1994;38:985-97.
[219] Djalili-Moghaddam M, Toll S. A model for short-range interactions in fibre suspensions. J Non-Newton Fluid Mech. 2005;132:73-83.
[220] Batchelor GK. Slender-body theory for particles of arbitrary cross section in stokes flow. J Fluid Mech. 1970;44:419-40.
[221] Ranganathan S, Advani SG. A simultaneous solution for flow and fiber orientation in axisymmetri diverging radial flow. J Non-Newton Fluid Mech. 1993;47:107-36.

[222] Ericksen JL. Transversely isotropic fluids. Kolloid Z. 1960;173:117-22.
[223] Ghosh T, Grmela M, Carreau PJ. Rheology of short fiber filled thermoplastics. Polym Compos. 1995;16.
[224] Beaulne M, Mitsoulis E. Rheological characterization of fiber-filled polymer composites via constitutive modeling. J Reinf Plast Compos. 2003;22:1625-40.
[225] Ramazani A, Alt-Kadi A, Grmela M. Rheological modelling of short fiber thermoplastic composites. J Non-Newton Fluid Mech. 1997;73:241-60.
[226] Ait-Kadi A, Grmela M. Modelling the rheological behaviour of fibre suspensions in viscoelastic media. 1994.
[227] Azaiez J. Constitutive equations for fiber suspensions in viscoelastic media. J Non-Newton Fluid Mech. 1996;66:35-54.
[228] Park JM, Kwon TH. Irreversible thermodynamics bases constitutive theory for fiber suspended polymeric liquids. J Rheol. 2011;55:517-43.
[229] Öttinger HC, Grmela M. Dynamics and thermodynamics of complex fluids. II. Illustrations of a general formalism. Physical Review E. 1997;56:6633-55.
[230] Le Corre S, Caillerie D, Orgéas L, Favier D. Behavior of a net of fibers linked by viscous interactions: theory and mechanical properties. J Mech Phys Solids. 2004;52:395-421.
[231] Le Corre S, Dumont PJJ, Orgéas L, Favier D. Rheology of highly concentrated planar fiber suspensions. J Rheol. 2005;49:1029.
[232] Dumont PJJ, Orgéas L, Le Corre S, Favier D. Anisotropic viscous behavior of sheet molding compounds (SMC) during compression molding. Int J Plast. 2003;19:625-46.
[233] Switzer LH, Klingenberg DJ. Flocculation in simulations of sheared fiber suspensions. Int J Multiphase Flow. 2004;30:67-87.
[234] Wang G, Yu W, Zhou C. Optimization of the rod chain model to simulate the motions of a long flexible fiber in simple shear flows. Eur J Mech B-Fluid. 2006;25:337-47.
[235] Hinch EJ. The distortion of a flexible inextensible thread in a shearing flow. J Fluid Mech. 1976;72:317-33.
[236] Yamamoto S, Matsuoka T. Dynamic simulation of flow-induced fiber fracture. Polym Eng Sci. 1995;35:1022-30.
[237] Thomasset J, Grmela M, Carreau PJ. Microstructure and rheology of polymer melts reinforced by long glass fibers: direct simulations. J Non-Newton Fluid Mech. 1997;73:195-203.
[238] Skjetne P, Ross RF, Klingenberg DJ. Simulation of single fiber dynamics. J Chem Phys. 1997;107:2108-21.
[239] Schmid CF, Switzer LH, Klingenberg DJ. Simulations of fiber flocculation: effects of fiber properties and interfiber friction. J Rheol. 2000;44:781.
[240] Joung CG, Phan-Thien N, Fan XJ. Direct simulation of flexible fibers. J Non-Newton Fluid Mech. 2001;99:1-36.
[241] Joung CG, Phan-Thien N, Fan XJ. Viscosity of curved fibers in suspension. J Non-Newton Fluid Mech. 2002;102:1-17.
[242] Tang W, Advani SG. Dynamic simulation of long flexible fibers in shear flow. CMES-Comp Model Eng. 2005;8:165-76.
[243] Yamanoi M, Maia J, Kwak T-s. Analysis of rheological properties of fibre suspensions in a Newtonian fluid by direct fibre simulation. Part 2: flexible fibre suspensions. J Non-Newton Fluid Mech. 2010;165:1064-71.
[244] Kittipoomwong P, Jabbarzadeh A. Effect of fibre curvature on the rheology of particulate suspensions. J Non-Newton Fluid Mech. 2011;166:1347-55.
[245] Bay RS, Tucker CL. Fiber orientation in simple injection moldings. Part I: theory and numerical methods. Polym Compos. 1992;13:317-31.
[246] Wang J, Silva CA, Viana JC, van Hattum FWJ, Cunha AM, Tucker CL. Prediction of fiber orientation in a rotating compressing and expanding mold. Polym Eng Sci. 2008;48:1405-13.

[247] VerWeyst BE, Tucker CL. Fiber suspensions in complex geometries: flow/orientation coupling. Can J Chem Eng. 2002;80:1093-106.
[248] Mazahir SM, Vélez-García GM, Wapperom P, Baird D. Evolution of fibre orientation in radial direction in a center-gated disk: experiments and simulation. Composites Part A. 2013;51:108-17.

Chapter 3 Influence of Fiber Concentration on the Startup of Shear Flow Behavior of Long Fiber Suspensions

Chapter 3 Influence of Fiber Concentration on the Startup of Shear Flow Behavior of Long Fiber Suspensions

Mark J. Cieslinski[1], Peter Wapperom[2], Donald G. Baird[1*]

1. Department of Chemical Engineering, Virginia Tech, VA 24061
2. Department of Mathematics, Virginia Tech, VA 24061

*Author to whom correspondence should be addressed, email: dbaird@vt.edu

3.1 Abstract

In order to use rheological measurements as a tool to investigate fiber orientation in simple flows, the relationship between stress and fiber orientation must be understood. In this work, a sliding plate rheometer was used to measure the shear stress growth during the startup of simple shear flow of a polymer melt containing long glass fibers. The concentrations of the suspensions were varied from 10 to 40 wt% and tested over three shear rates spanning an order of magnitude. Significant shear thinning was observed in the suspension as concentration increased. Additionally, the magnitude of stress and breadth of the stress growth overshoot increased with concentration. A larger distinction between the different concentrations is observed in the shear stress growth than the measured evolution of fiber orientation. Measured values of fiber orientation were used with a semi-dilute stress equation to show that the fiber motion in these experiments was not responsible for the stress overshoot and that additional stress contributions must be considered.

3.2 Introduction

The enhancement of tensile, flexural and impact properties for a discontinuous fiber reinforced composite is largely dictated by the concentration, orientation and length of the fibers

within the part. Tensile, flexural and impact strengths have been measured to reach a maximum near 40 wt% glass fiber content in polypropylene for injection molded composites [1]. Additionally, the moduli of these parts were found to increase linearly with concentration. Flexural, creep and impact properties have been shown to increase with fiber length, while tensile properties will plateau for glass fibers above 1 mm in length [2-5]. Fibers less than the 1 mm threshold have been considered short while fibers with lengths greater than 1 mm are considered long. Furthermore, the degree of this mechanical enhancement can vary within a molded part depending on the underlying fiber microstructure [6, 7].

Concentration regimes for fiber composites stem from theories of rod-like molecules provided by Doi and Edwards [8]. In terms of volume fraction, ϕ_v , and fiber aspect ratio (a_r= fiber length/diameter), fiber suspensions can be divided into dilute ($\phi_v < a_r^{-2}$), semi-dilute ($a_r^{-2} < \phi_v < a_r^{-1}$), and concentrated ($\phi_v \geq a_r^{-1}$) regimes. Generally, composites of commercial interest have $\phi_v > 0.1$ [9]. In the concentrated regime, the motion of an individual fiber is restricted by surrounding fibers through hydrodynamic and fiber-fiber interactions. As ϕ_v or a_r increases, the motion of an individual fiber will become more constrained. Additionally, Bay and Tucker [10] noted that glass fibers with aspect ratios above 100 can exhibit curvature, which may also impact fiber motion.

Fiber orientation equations for concentrated fiber suspensions often rely on phenomenological adaptations to Jeffery's equation describing the motion of an ellipsoidal particle [11]. Folgar and Tucker [12] introduced isotropic rotary diffusion to Jeffery's model to account for the randomizing effect on orientation due to fiber interactions. The rotary diffusion constant in the Folgar-Tucker model has been empirically represented as a function of the product of aspect ratio and concentration by Bay [13] and Phan-Thien et al. [14]. Ranganathan and Advani [15] represented the diffusion constant as a function of the interparticle spacing. Including the interparticle spacing allows the diffusion constant to depend on the state of fiber orientation.

Phelps and Tucker [16] accounted for orientation dependent particle diffusion through the use of a diffusivity tensor in the anisotropic rotary diffusion (ARD) orientation model. These approaches in modelling fiber orientation require that material parameters be determined experimentally.

A stress equation provides the coupling between fiber orientation and the equations of momentum and energy. A general form of the stress tensor was provided by Hinch and Leal [17] for ellipsoidal particles. For high aspect ratio fibers, Lipscomb et al. [18] provide the parameters in the stress equation for dilute suspensions. Stress in semi-dilute suspensions is accounted for in theories from Dinh and Armstrong [19] and Shaqfeh and Fredrickson [20]. The material constants in the general stress equation have been empirically adjusted to fit experimental data for concentrated suspensions, due to lack of available theory [21-23].

To understand the orientation kinetics of fiber suspensions, rheological experiments have been performed during the startup of flow. Fibers subjected to flow will orient with the primary flow direction creating a stress growth overshoot that will reduce to a steady value. As concentration increases the magnitude of the stress growth overshoot and steady state has been shown to also increase [24, 25]. The addition of fibers will also cause shear thinning to occur at low rates when no shear thinning is observed in the matrix. Ortman et al. [26] observed a higher degree of shear thinning to occur in addition to a broadened shear stress overshoot as fiber aspect ratio increased.

Previous investigations of the rheology of fiber suspensions have shown a monotonic increase in stress with concentration. Laun [24] and Bibbo [25] measured the shear stress during the startup of flow for short fiber suspensions and observed that the maximum stress occurred at the same shear strain for concentrations ranging from the semi-dilute to concentrated regimes. Eberle et al. [27] observed the shear stress to decay from an initial value to a steady state for concentrations less than 10 wt% short glass fiber in a Newtonian matrix. Above 10 wt%, a stress growth overshoot was observed and the strain where the maximum stress occurred increased with

increasing concentration. This shift in strain for the location of maximum stress was also observed by Ortman et al. [22, 26] for long glass fiber suspensions at 10 and 30 wt%. However, these works were unable to conclude how the changes in the transient response reflected changes in fiber orientation.

Measurements of stress from a rheometer provide an indirect assessment of the underlying fiber microstructure. As a result, some works have experimentally measured fiber orientation in addition to stress. Petrich et al. [28] and Keshtkar et al. [29] used flow visualization experiments to observe the orientation of the fibers during flow. Eberle et al. [30] and Ortman et al. [22] used thermoplastic matrices that were allowed to cool within the rheometer to preserve the fiber orientation. The sample was removed from the rheometer and orientation was measured from a polished cross section of the sample using an optical microscope. This method requires multiple samples to be used to assess fiber orientation as a function of time and the assumption must be made that there is little variability between each sample. Both of these approaches have shown that the kinetics of fiber orientation will decrease with increasing fiber length.

The purpose of this work is to further understand the relationship of stress and the evolution of fiber orientation during the startup of simple shear flow for long fiber suspensions. The methods of Ortman et al. [22] were used as a guide to investigate the effects of concentration on the orientation and stress response of high aspect ratio glass fiber suspensions. We aim to show that the shape of the stress response and fiber orientation will change with concentration which is different than what has been observed for short fiber suspensions. The contribution to stress that is dependent on fiber orientation was investigated using a model valid for semi-dilute suspensions. The fourth order term in the stress equation was calculated from experimental measurements of fiber orientation which allows for the assessment of the stress model without inducing additional error caused by approximating the fourth order term.

3.3 Theory

The orientation of a single rigid fiber can be denoted by a unit vector, **p**, parallel to the axis of the fiber. The average orientation for a population of fibers can be compactly represented through the use of even-ordered structural tensors [31]. The second and fourth order orientation tensors are defined as the product of the orientation distribution function, $\psi(\mathbf{p})$, with the dyadic product of the orientation vector integrated over all orientation space:

$$\mathbf{A} = \int \mathbf{pp}\psi(\mathbf{p})d\mathbf{p} \qquad \mathbf{A}_4 = \int \mathbf{pppp}\psi(\mathbf{p})d\mathbf{p}. \tag{3.1}$$

In order to assess orientation through measured values of stress within a rheometer, a stress theory encompassing orientation is used. Shaqfeh and Fredrickson [20] applied a multiple scattering expansion to the slender-body theory to quantify the hydrodynamic effects from adjacent fibers on the bulk stress, **σ**:

$$\boldsymbol{\sigma} = -P\mathbf{I} + 2\mathbf{D}\eta_m + \frac{4\eta_m\phi_v a_r^2}{3[\ln(1/\phi_v) + \ln\ln(1/\phi_v) + C']}\,\mathbf{D} : \mathbf{A}_4 \tag{3.2}$$

where, P is the isotropic pressure, **I** is the identity tensor, $\mathbf{D} = \frac{1}{2}(\nabla\mathbf{v}^t + \nabla\mathbf{v})$ is the rate-of-deformation tensor, η_m is the matrix viscosity. The parameter C' is dependent on the particle shape and orientation. For cylindrical particles, C' has a value of -0.6634 for random three-dimensional orientation and 0.1585 for completely aligned fibers. This stress equation takes into account stress contributions from the isotropic pressure, matrix and the tension imposed on an inextensible rod. In simple shear flow the maximum tension occurs when a fiber has an in-plane orientation angle 45° with respect to the flow and thickness directions. The theory of Shaqfeh and Fredrickson has shown good agreement with numerical simulations of Mackaplow and Shaqfeh [32] and the experimental data of Bibbo [25].

The use of a semi-dilute stress equation with the data from concentrated fiber suspensions presented in this work is intended to provide a comparison between orientation and stress without introducing any empirical parameters. The slender-body theory should reflect the fiber interactions in semi-dilute suspensions up to a concentration of $\phi_v \approx \pi/20a_r$. It is expected that the stress equation will under predict data above this concentration [32].

3.4 Experimental

3.4.1 Material Preparation

The suspensions under investigation were 10, 20, 30 and 40 wt% glass fibers in a low viscosity polypropylene matrix. The material was received from SABIC as 13 mm long pellets created through a pultrusion process in 30 and 50 wt% formulations (Verton MV006S-GYLTNAT). The pellets contain a bundle of fibers that must be dispersed in order to obtain repeatable rheological data. Each formulation was processed in a 25 mm, 20L/D Killion extruder (KLB-100) equipped with a gradually tapering screw. The temperature profile along the length of the screw was set to 220, 230 and 245 °C with a die temperature set to 150 °C. The circular die measured 1.5 mm in diameter. Concentrations less than 30 wt% were diluted with neat polypropylene, while 30 and 50 wt% pellets were used to create the 40 wt% suspension. Suspensions at 50 wt% were found to exceed the stress limitations of the transducer in the rheometer and were not studied as a result. Extruded strands were pelletized to a length of 15 mm which were used to compression mold samples with approximately planar random orientation. The mold dimensions were 250 by 50 mm and sample thickness was between 1.6 to 1.7 mm. Samples were compression molded for 5 minutes in a preheated mold at 180 °C. This procedure was found to minimize voids which could greatly impact the measurements of stress.

Measurements of fiber length were obtained from the 15 mm pellets used to create the samples for rheological testing. Pellets were placed in an oven at 500 °C for 2 hours to remove the polypropylene matrix. Loose glass fibers were then dispersed on a glass slide and imaged on

a desktop scanner at 1200 dpi resolution. At least 1500 fibers per sample were measured using ImageJ software. The fiber length distribution followed the typical log-normal distribution commonly observed for fiber suspensions. Three samples were used to produce the averages in Table 1. The average fiber diameter was measured to be 13.3 μm using an optical microscope at 20x magnification. The number average (L_n) and weight average (L_w) fiber lengths were calculated according to Eqs. (3.3) and (3.4), respectively:

$$L_n = \frac{\sum_i n_i L_i}{\sum_i n_i} \tag{3.3}$$

$$L_w = \frac{\sum_i n_i L_i^2}{\sum_i n_i L_i} \tag{3.4}$$

where, n_i is the number of fibers within the distribution with length L_i. The sampling method for fiber length measurements from Kunc et al. [33] was used to confirm that no reduction in fiber length occurred as a result of compression molding or rheological testing. The average lengths are above the 1 mm threshold and can be considered as long fiber suspensions. However, the number average fiber lengths are close to 1 mm which is due to a significant number of short fibers in the length distribution.

3.4.2 Rheological Measurements

Rheological tests on the fiber suspensions were performed using a sliding plate rheometer made in-house based on the design of Giacomin [34] and further discussed by Giacomin and coworkers [35]. Details on the development and implementation of this particular sliding plate rheometer can be found elsewhere [36]. The rheometer was enclosed in a forced convection oven manufactured by Russells Technical Products (model RB-2-340). The sliding plate was controlled through the use of an Instron-4204 universal testing instrument. A shear stress transducer was flush mounted to the stationary plate. The shear stress transducer contains a lever arm suspended by a diaphragm which determines the instrument's range and sensitivity. Two diaphragms were

used to cover the range of stresses measured in this work. The deflection of the lever arm was measured using a capacitance probe (Capacitec, Model HPT-75I-V-T-2-B). Signals from the probe were amplified using a Capacitec 4100-SL-BNC amplifier and interfaced with a computer using a National Instruments data acquisition devise (USB-6008). Voltage readings were recorded using National Instruments Labview SignalExpress software (version 2.5.1). Shear stress was determined based on the measured voltage and calibration of the diaphragm in the shear stress transducer.

The rheometer was heated to a temperature of 200 °C for 2 hours prior to sample loading. A sample was placed between the two heated plates and the plates were tightened enough to touch both surfaces of the sample. After heating for 5 minutes the plates were tightened to the final thickness of 1.5 mm. Testing the suspensions at greater gap thicknesses confirms that the 1.5 mm gap thickness did not greatly influence the stress response. In addition, Ortman et al. [26] used the same gap thickness for similar fiber suspensions and concluded that gap effects were minimized due to the mostly planar fiber orientation. The sample remains in the rheometer 15 minutes prior to testing. Shear rates of 0.4, 1.0 or 4.0 s^{-1} were imposed on the sample for 120 strain units. Physical limitations in the design of this sliding plate rheometer and the Instron testing machine determines the maximum achievable strain at 120 strain units and a maximum shear rate of 5.6 s^{-1} at a gap thickness of 1.5 mm. We chose to limit data collection to a shear rate of 4.0 s^{-1} in order to be within the limits of the instrument. Five replicates were averaged to produce the reported stress growth profiles. A similar heating cycle and duration was imposed on the polypropylene matrix and tested using a cone-and-plate rheometer (Rheometrics RMS-800). The suspensions were observed at a constant frequency in small amplitude oscillatory shear for a duration of 30 minutes with and without nitrogen protection. There was no observable difference in the storage or loss moduli due to testing under air or nitrogen. As a result, it can be concluded that the flow behavior of the matrix does not change during the time frame that tests were performed using the sliding plate. Upon completion of the tests in the sliding plate rheometer, a fan was used to cool

the rheometer to room temperature over the duration of 1 hour. The sample remained within the rheometer during this time period to preserve fiber orientation for later investigation.

The rheology of the polypropylene matrix was determined from a combination of oscillatory and steady shear tests performed on a cone-and-plate rheometer (Rheometrics RMS-800) and a capillary rheometer (Göttfert Rheograph 2001) at 200 °C. A 50 mm cone-and-plate fixture was used. Oscillatory data was reported due the matrix following the Cox-Merz relationship. Transient tests on the matrix were also performed on the cone-and-plate rheometer due to stresses below the measurable limit of the sliding plate rheometer. The capillary rheometer used a 0.5 mm diameter die at lengths of 10 and 15 mm. Bagley and Wiessenberg-Rabinowitsch corrections were applied to the data [37].

3.4.3 Fiber Orientation Measurements

Measurements of fiber orientation were made to further investigate its relationship to the measured stress response. Samples were prepared and tested according to the same procedure but sheared to different strain units. Separate samples were used for each strain. Therefore, it was assumed that the initial orientation for each sample were the same. Orientation measurements were taken along the x_1x_2-midplane, such that x_1 denotes the flow direction with a change in velocity in the x_2-direction. Details of the development of the sample preparation procedure can be found in the works of Vélez-García et al. [38] and Hofmann et al. [39]. Samples were polished using modified metallographic techniques and oxygen plasma etched to enhance the contrast of the glass fiber and polypropylene matrix. Images were obtained at 20x magnification on an optical microscope with a motorized stage and image-stitching software (Nikon Eclipse LV100, NIS-Elements Basic Research Software, version 3.10). Hofmann et al. [39] suggested that the image analysis width be modified to 5.5 mm for fiber suspensions with a number average length of 3.9 mm. This analysis width was found to be acceptable for all concentrations investigated here. The two-dimensional projections of the fibers on the imaging plane are displayed as ellipses. An

example of the digital micrograph can be seen in Figure 3.1 where the dark background is the polypropylene matrix and the lighter colored elliptical objects are the fibers. Based on the ratio of the minor, m, to major, M, axes of the ellipse and the in-plane angle, ϕ, a unit vector , **p**, can be reconstructed each fiber [10, 40]. The components of the vector **p** are described in Cartesian coordinates:

$$\mathrm{p}_1 = \sin\theta \, cos\phi \tag{3.5}$$

$$\mathrm{p}_2 = \sin\theta \cos\phi \tag{3.6}$$

$$\mathrm{p}_3 = \cos\theta \tag{3.7}$$

$$\theta = \arccos\left(\frac{m}{M}\right) \tag{3.8}$$

Moments of orientation were construction from the dyadic product of **p** for a population of fibers and a weighting function to correct for imaging bias imparted from the use of an inspection plane:

$$\mathbf{A} = \frac{\sum_k \ (\mathbf{pp})_k L_k F_k}{\sum_k \ L_k F_k} \tag{3.9}$$

where $(\mathbf{pp})_k$ is the second moment of orientation for the k-th fiber, L_k is the length of the fiber and F_k is the weighting function. The fourth moment of orientation was constructed similarly. The weighting function developed by Bay and Tucker [10] was used in this work to include partial ellipses in the orientation measurements:

$$F_k = \begin{cases} \dfrac{1}{L_k \cos\theta_k} & \theta_k \leq \ \theta_c \\ \\ \dfrac{1}{d_k} & \theta_k > \theta_c \end{cases} \tag{3.10}$$

where the cut-off angle, $\theta_c = \arccos(d_k/L_k)$, d_k is the fiber diameter and the out-of-plane angle, θ_k, calculated from Eq. (3.8). This method for measuring fiber orientation cannot determine the

length of each fiber. As a result, the length of each fiber is approximated by the number average fiber length ($L_k \approx L_n$). This method is applicable for suspensions that do not exhibit significant curvature.

Additional images of fiber orientation were obtained in the x_2x_3-plane to observe the extent to which fibers were bending. Very few fibers were found to exhibit any bending in the x_1x_2- or x_2x_3-inspection planes. Obtaining fiber orientation from elliptical cross sections cannot assess if fibers bend during flow and straighten upon the cessation of flow. Keshtkar et al. [29] denoted the orientation of bent fibers with an end-to-end vector, but did not quantify the extent of fiber bending. Bending of fibers may significantly influence flow behavior and orientation kinetics. A two-rod system from Strautins and Latz [41] and Ortman et al. [22] would allow for the degree of fiber bending to be quantified and the average orientation of a fiber could be prescribed by an end-to-end vector. In the limit that a fiber has no curvature, the orientation of the end-to-end vector is equivalent to the orientation of the rods. Hofmann [7] was able to show good agreement between fiber orientation measurements obtained from elliptical cross sections and measurements of the fibers' end-to-end vectors. For the stress and fiber orientation presented in this work, the designation of a rigid fiber will be used due to the large amount of short fibers that exist in the suspensions. However, we recognize that the two-rod system may provide a more complete description of fiber orientation dynamics. This approach may be necessary to describe longer fibers in the suspension (e.g. fiber lengths above 5 mm). Although there are relatively few fibers with these large fiber lengths in the suspensions studied in this work, the impact these fibers have on the bulk stress and the orientation behavior of the system is of continued interest.

3.5 Results and Discussion

3.5.1 Stress Results

Rheological data and orientation evolution have been obtained for concentrations of 10, 20, 30 and 40 wt% glass fibers at shear rates of 0.4, 1.0 and 4.0 s^{-1}. Error bars in Figure 3.2

represent the standard deviation amongst the five samples averaged to produce the reported stress profiles. We attribute this error to the localized measurements of stress and localized variations in fiber orientation within the sample. The pellets used to compression mold the samples have some preferential alignment. Additional error may arise from the unspecified A_{12} orientation component due to the method used to prepare the samples. The extent to which a fiber must rotate to align with the flow direction is dependent on whether A_{12} is positive or negative.

The influence of glass fiber concentration on the shear stress growth is shown in Figure 3.2(a) for a shear rate of 0.4 s^{-1}. An overshoot is observed for all concentrations tested, but is not observed in the unfilled polypropylene. Within the strain limitations of the sliding plate rheometer, all samples appear to have reached a steady shear viscosity which infers a steady state fiber orientation. The presence of fibers greatly increases the fluid viscosity such that an order of magnitude increase is observed at 30 wt% compared to the neat matrix. The stress growth overshoot appears to occur at later strains when concentration is increased. This shift in the maximum stress may indicate that fiber orientation evolves slower for a more concentrated system. Laun [24] did not observe any change in strain for the maximum stress as concentration was increased for glass fibers with an aspect ratio of 22. The aspect ratios presented in this work are greater than Laun's by at least a factor of 4. Additionally, Laun observed the magnitude of the stress overshoot and steady state to increase with concentration up to 35 wt%. The suspensions tested in this work exhibit an increase in the magnitude of the overshoot and steady state values for concentrations of 10 to 30 wt%. At 40 wt%, the magnitude of the stress overshoot is smaller than what might be expected based on the trends observed at 10 to 30 wt%. In comparing the stress overshoot to the steady state value, the relative overshoot at 40 wt% is less than the relative overshoots at 20 and 30 wt%. This may indicate that the orientation dynamics are different for the 40 wt% suspension when compared to the other concentrations. Figure 3.2(b) contains the transient response of the four glass fiber concentrations at a shear rate of 1.0 s^{-1}. The transient response follows a similar trend compared to the 0.4 s^{-1} data in that the increase concentration causes a

significant increase to the viscosity. The broadening of the overshoot is not as pronounced at 1.0 s^{-1} shear rate in comparison to the 0.4 s^{-1} data. Similar trends are also observed in the data obtained at 4.0 s^{-1}, shown in Figure 3.2(c). The viscosity over the range of 0.4 to 4.0 s^{-1} is significantly dependent on shear rate. At 4.0 s^{-1}, the difference in the viscosity 40 wt% data compared to the other concentrations is relatively small when compared to the differences at a shear rate of 0.4 s^{-1}. The overshoot relative to the steady state for 40 wt% data at 0.4 and 1.0 s^{-1} appears to be less than the relative overshoot for the other concentrations. The overshoot at 0.4 s^{-1} for the 40 wt% concentration appears to be unique when compared to all other transient responses.

Figure 3.3 shows transient viscosity data for the polypropylene matrix and 10 and 40 wt% glass fiber suspensions at the three tested shear rates. The polypropylene exhibits no measurable overshoot or significant shear thinning within the range of shear rates achieved in the sliding plate rheometer. For the 10 wt% glass fiber suspension, shear thinning is observed along with a stress growth overshoot. Figure 3.3(b) contains the stress growth response for the 40 wt% glass fiber suspension at the three shear rates. The transients take longer to reach a maximum and steady state than the lower concentrations. The 0.4 s^{-1} data does exhibit a different profile than the higher shear rate data but the steady state values do appear to show a power-law dependency with shear rate.

To further view the shear thinning effects, the steady shear viscosity for all the suspensions is plotted with the matrix viscosity in Figure 3.4 as a function of shear rate. The polypropylene does not show significant thinning behavior until rates are at least an order of magnitude above what was tested in the sliding plate rheometer. As the fiber concentration increases, the intensity of shear thinning also increases. This was observed to a lesser degree in short fiber suspensions at similar concentrations by Mobuchon et al. [42]. Shear thinning in suspensions is believed to be related to the amount of microstructure that must be rearranged to necessitate flow. Larson [43] provides an possible explanation to this shear thinning behavior, in that shear rates are high enough to disturb the interparticle spacings from equilibrium.

It can be inferred that the steady shear viscosity of these fiber suspensions will not show a significant plateau before thinning of the matrix is encountered at higher rates. It is interesting to note that that the shear thinning behavior at a concentration of 40 wt% approaches that of the polypropylene matrix at high shear rates. The data is insufficient to make any conclusions on the behavior of the suspensions at high shear rates. However, Thomasset et al. [21] observed the same degree of shear thinning to occur for fiber suspensions as the polypropylene matrix for similar fiber aspect ratios presented in this work.

3.5.2 Orientation Evolution

The suspending fluid appears to be Newtonian in the region that has been investigated for the fiber suspensions, making the motion and interactions of the glass fibers responsible for the non-Newtonian response. The second moment of orientation tensor, **A**, is constructed based on the measured orientation of for population fibers. The evolution of the trace components of the orientation tensor are shown in Figure 3.5. Differences in fiber orientation for the 10 and 40 wt% fiber suspensions appear to be evident in fiber orientation data. The orientation profiles for 20 and 30 wt% are indistinguishable, and their values may be considered an average of the 10 and 40 wt% data. Initial orientation was measured to vary by less than 5% between all concentrations, with fibers slightly more oriented in the flow direction than the neutral direction. The A_{22} component of orientation is small indicating mostly planar orientation. The largest value of A_{22} occurs at zero strain and reduces in magnitude under flow. Little difference is observed in the A_{22} component of orientation with concentration.

The A_{11} and A_{33} components exhibit a mirrored profile, because A_{22} is small due to mostly planar fiber orientation. The 10 wt% long fiber systems orient in the flow direction and reach a steady state at a slower rate than the short fiber suspensions investigated by Eberle et al. [27]. The 40 wt% suspension comparatively shows a delayed response in fiber orientation at low strains. This delay in fiber evolution can provide an explanation for the stress growth maximums occurring

at larger strains at the higher concentrations. After 20 strain units the orientation of the 40 wt% suspension appears to change at a faster rate ultimately achieving a higher degree of flow aligned fiber orientation than the other concentrations. It is not clear from the stress growth measurements that there is a difference in steady state fiber orientation.

Figure 3.6 provides measured fiber orientation as a function of strain for the 30 wt% suspensions and is representative of the effect of shear rate on orientation at all other concentrations. Orientation appears to be independent of shear rate and only a function of applied shear strain which had been acknowledged theoretically [44]. The dependency of viscosity on shear rate cannot be attributed to changes in orientation. However, the stress required to change orientation does show a rate dependency. Ortman et al.[22] noted a slight dependency of orientation as a function of shear rate for 30 wt% glass fibers, but the authors stated that orientation was primarily strain dependent. Larger variations in orientation data at different shear rates was reported in their data relative to what is observed in this work.

The intended variable of interest was concentration, but we do acknowledge that fiber lengths also differed for each concentration. This appears to be an unavoidable consequence of using an extruder to disperse fibers in the matrix. Increasing the concentration caused more fiber length attrition to occur. It is expected that the decrease in fiber length will decrease the magnitude of the stress response. The rate of fiber orientation should also increase with a decrease in fiber length. The experimental fiber orientation data still exhibits a slower orientation evolution with increasing concentration. This trend may be slightly more pronounced if the fiber lengths were equivalent for each concentration. The work of Bay [13] and Phan-Thien et al. [14] showed for short fibers that changes in the extent of fiber alignment decreased with increasing fiber lengths. Based on these findings, it is expected that the steady state fiber orientation would not change by a significant amount if the fiber lengths were equivalent.

3.5.3 Stress Predictions

The stress model presented in Eq. (3.2) was used to predict stress based on the measured orientation of a population of fibers. Typically a closure approximation is used in the fiber orientation or stress equations as a computationally efficient way of representing a higher order tensor as a function of lower order tensors. However, the use of a closure approximation induces error that can significantly impact the stress predictions [45]. As a result, the evaluation of the stress equation becomes dependent on the closure approximation. For example, the use of the invariant based optimal fitting (IBOF) closure to approximate the fourth order term in the stress equation from the experimentally obtained second order tensor yielded an over prediction in stress by a factor of 2 to 3 [46]. To overcome issues with the closure approximation, the component of interest in the fourth order term for the shear stress, A_{1212}, was calculated based on the measured fiber orientation. The orientation dependent parameter in the model, C', was set to the value for three-dimensionally random orientation. It is understood that this term is orientation dependent and increases in value from isotropic to aligned orientation states. This trend would cause the coefficient to the fourth order term to decrease in magnitude with increasing fiber alignment. However, our interest is on the ability of the fourth order term in the stress equation, which is present in other stress theories, to reflect the transients observed in the experimental stress data.

Figure 3.7 shows the predicted stress at a shear rate of 1.0 s^{-1} based on the values in Table 3.1, the zero shear viscosity for the matrix and measured values of fiber orientation. The stress model under predicts the experimental data as expected, with the greatest deviation occurring at the highest concentration. Additionally, this provides some reinforcement in the measurement of fiber length because any significant errors in length measurements are magnified due to stress scaling with a_r^2. Stress predictions at a strain of 2 are a result of experimental orientation data obtained at zero strain. At zero strain the sample is not subjected to flow which would result in zero stress. In addition, transients at low strains may be a result of the instrument and not the

fibers' contribution to stress. The stress predictions are not intended to infer a stress overshoot at lower strains than the experimental data, but rather that there is no stress overshoot prediction using the measured fiber orientation. The prediction of no stress overshoot is directly related to no overshoot observed in fiber orientation. As a result the stress model is only capable of representing a decrease in stress from the initial orientation toward a steady state value at higher strains at all concentrations and shear rates. Similar results would be obtained from the stress theories of Lipscomb et al. [18] and Dinh and Armstrong [19].

The absence of a stress growth overshoot and under prediction of the steady state value indicates that there are additional contributions that must be included to the stress theory. In addition, the use of an empirical coefficient to scale the fiber contribution to stress would not aid in predicting the transient response. The difference between semi-dilute theory and the concentrated data presented in this work could be accounted for by including stress contributions due to fiber-fiber interactions or other interactions between fibers that may result in larger network structures or flocculations.

3.6 Conclusions

Measurements of shear stress have been performed during the startup of shear flow in a sliding plate rheometer at concentrations from 10 to 40 wt% long glass fibers in polypropylene. Experimental measurements of fiber orientation were obtained to investigate the relationship between shear stress and fiber orientation. The increase in fiber length over short fiber suspensions caused the stress response and fiber orientation to evolve at a slower rate. Shear thinning was observed in the fiber suspensions which cannot be attributed to differences in orientation, because fiber orientation appears to be solely a function of strain. As fiber concentration increased, the stress growth overshoot broadened which indicates slower orientation kinetics. However, changes in measured fiber orientation are small over the range of investigated concentrations.

Stress predictions were performed using measured fiber orientation data in order to avoid any approximations in calculating the orientation dependent term in the stress equation. The stress theory of Shaqfeh and Fredrickson was used as an example to show that a shear stress growth overshoot will not be predicted if there is no overshoot in fiber orientation. Empirically scaling the orientation dependent term in the stress equation could better reflect the steady state, but would not provide a good representation of the transient response. Additional contributions to stress should be considered in order to reflect the stress response for fiber suspensions.

3.7 Acknowledgments

The financial support for this work from the American Chemistry Council and National Science Foundation CMMI-0853537 is gratefully acknowledged. The authors would also like to thank the Material Science and Engineering department and the Sustainable Energy laboratory at Virginia Tech for use of laboratory equipment.

3.8 References

[1] Thomason JL. The influence of fibre length and concentration on the properties of glass fibre reinforced polypropylene. 6. The properties of injection moulded long fibre PP at high fibre content. Composites Part A. 2005;36:995-1003.

[2] Thomason JL. The influence of fibre length and concentration on the properties of glass fibre reinforced polypropylene: 5. Injection moulded long and short fibre PP. Composites Part A. 2002;33:1641-52.

[3] Chin W-K, Liu H-T, Lee Y-D. Effects of fiber length and orientation distribution on the elastic modulus of short fiber reinforced thermoplastics. Polym Compos. 1988;9:27-35.

[4] Silverman EM. Effect of glass fiber length on the creep and impact resistance of reinforced thermoplastics. Polym Compos. 1987;8:8-15.

[5] Truckenmüller F, Fritz HG. Injection molding of long fiber-reinforced thermoplastics: a comparison of extruded and pultruded materials with direct addition of roving strands. Polym Eng Sci. 1991;31:1316-29.

[6] Gupta M, Wang KK. Fiber orientation and mechanical properties of short-fiber-reinforced injection molded composites: simulated and experimental results. Polym Compos. 1993;14:367-82.

[7] Hofmann JT. Extension of the Method of Ellipses to Determining the Orientation of Long, Semi-Flexible Fibers in Model 2- and 3-Dimensional Geometries. PhD Thesis: Virginia Polytechnic Institute and State University; 2013.

[8] Doi M, Edwards SF. The Theory of Polymer Dynamics: Oxford University Press, New York; 1986.

[9] Advani SG, Sozer EM. Process Modeling in Composites Manufacturing. New York: Marcel Dekker, Inc.; 2003.

[10] Bay RS, Tucker CL. Stereological measurement and error estimates for three-dimensional fiber orientation. Polym Eng Sci. 1992;32:240-53.
[11] Jeffery GB. The motion of ellipsoidal particles immersed in a viscous fluid. Proc R Soc London, Ser A. 1922;102:161-79.
[12] Folgar F, Tucker CL. Orientation behavior of fibers in concentrated suspensions. J Reinf Plast Compos. 1984;3:98-119.
[13] Bay RS. Fiber Orientation in Injection Molded Composites: A Comparison of Theory and Experiment. PhD Thesis: University of Illinois Urbana-Champaign; 1991.
[14] Phan-Thien N, Fan XJ, Tanner RI, Zheng R. Folgar-Tucker constant for fiber suspension in a Newtonian fluid. J Non-Newton Fluid Mech. 2002;103:251-60.
[15] Ranganathan S, Advani SG. Fiber-fiber interactions in homogeneous flows of nondilute suspensions. J Rheol. 1991;35:1499-522.
[16] Phelps JH, Tucker CL. An anisotropic rotary diffusion model for fiber orientation in short- and long-fiber thermoplastics. J Non-Newton Fluid Mech. 2009;156:165-76.
[17] Hinch EJ, Leal LG. Time-dependent shear flows of a suspension of particles with weak Brownian rotations. J Fluid Mech. 1973;57:753-67.
[18] Lipscomb GG, Denn MM, Hur DU, Boger DV. The flow of fiber suspensions in complex geometries. J Non-Newton Fluid Mech. 1988;26:297-325.
[19] Dinh SM, Armstrong RC. A rheological equation of state for semiconcentrated fiber suspensions. J Rheol. 1984;28:207-27.
[20] Shaqfeh ESG, Fredrickson GH. The hydrodynamic stress in a suspension of rods. Phys Fluids A. 1990;2:7-24.
[21] Thomasset J, Carreau PJ, Sanschagrin B, Ausias G. Rheological properties of long glass fiber filled polypropylene. J Non-Newton Fluid Mech. 2005;125:25-34.
[22] Ortman K, Baird D, Wapperom P, Whittington A. Using startup of steady shear flow in a sliding plate rheometer to determine material parameters for the purpose of predicting long fiber orientation. J Rheol. 2012;56:955-81.
[23] Eberle APR, Baird DG, Wapperom P, Vélez-García GM. Obtaining reliable transient rheological data on concentrated short fiber suspensions using a rotational rheometer. J Rheol. 2009;53:1049-68.
[24] Laun HM. Orientation effects and rheology of short glass fiber-reinforced thermoplastics. Colloid Polym Sci. 1984;262:257-69.
[25] Bibbo MA. Rheology of Semiconcentrated Fiber Suspensions. PhD Thesis: Massachusetts Institute of Technology; 1987.
[26] Ortman KC, Agarwal N, Eberle APR, Baird DG, Wapperom P, Jeffrey Giacomin A. Transient shear flow behavior of concentrated long glass fiber suspensions in a sliding plate rheometer. J Non-Newton Fluid Mech. 2011;166:884-95.
[27] Eberle APR, Vélez-García GM, Baird DG, Wapperom P. Fiber orientation kinetics of a concentrated short glass fiber suspension in startup of simple shear flow. J Non-Newton Fluid Mech. 2010;165:110-9.
[28] Petrich MP, Koch DL, Cohen C. An exerimental determination of the stress-microstructure relationship in semi-concentrated fiber suspensions. J Non-Newton Fluid Mech. 2000;95:101-33.
[29] Keshtkar M, Heuzey MC, Carreau PJ, Rajabian M, Dubois C. Rheological properties and microstructural evolution of semi-flexible fiber suspensions under shear flow. J Rheol. 2010;54:197-222.
[30] Eberle APR, Baird DG, Wapperom P, Vélez-García GM. Using transient shear rheology to determine material parameters in fiber suspension theory. J Rheol. 2009;53:685-705.
[31] Advani SG, Tucker CL. The use of tensors to describe and predict fiber orientations in short fiber composites. J Rheol. 1987;31:751-84.
[32] Mackaplow MB, Shaqfeh ESG. A numerical study of the rheological properties of suspension of rigid, non-brownian fibres. J Fluid Mech. 1996;329:155-86.

[33] Kunc V, Frame BJ, Nguyen BN, Tucker CL, Vélez-García GM. Fiber length distribution measurement for long glass and carbon fiber reinforced injection molded thermoplastics. Society of Plastics Engineers Automotive Composites Conference & Exhibition. Troy, Michigan. 2007.
[34] Giacomin AJ. A sliding plate melt rheometer incorporating a shear stress transducer. PhD Thesis: McGill University; 1987.
[35] Giacomin AJ, Samurkas T, Dealy JM. A novel sliding plate rheometer for molten plastics. Polym Eng Sci. 1989;29:499-504.
[36] Agarwal N. Transient Shear Flow Rheology of Concentrated Long Glass Fiber Suspensions in a Sliding Plate Rheometer. Master's Thesis: Virginia Polytechnic Institute and State University; 2009.
[37] Bird RB, Armstrong RC, Hassager O. Dynamics of Polymeric Liquids. Volume 1: Fluid Mechanics. 2nd ed: Wiley Interscience, New York, 1987; 1987.
[38] Vélez-García GM, Wapperom P, Kunc V, Baird DG, Zink-Sharp A. Sample preparation and image acquisition using optical-reflective microscopy in the measurement of fiber orientation in thermoplastic composites. J Microsc. 2012;248:23-33.
[39] Hofmann JT, Vélez-García GM, Baird DG, Whittington AR. Application and evaluation of the method of ellipses for measuring the orientation of long, semi-flexible fibers. Polym Compos. 2013;34:390-8.
[40] Hine PJ, Davidson NC, Duckett RA, Clarke AR, Ward IM. Hydrostatically extruded glass-fiber reinforced polyoxymethylene. I: the development of fiber and matrix orientation. Polym Compos. 1996;17:720-9.
[41] Strautins U, Latz A. Flow-driven orientation dynamics of semiflexible fiber systems. Rheol Acta. 2007;46:1057-64.
[42] Mobuchon C, Carreau PJ, Heuzey M-C, Sepehr M, Ausias G. Shear and extensional properties of short glass fiber reinforced polypropylene. Polym Compos. 2005;26:247-64.
[43] Larson RG. The Structure and Rheology of Complex Fluids: Oxford University Press Inc.; 1999.
[44] Ausias G, Agassant JF, Vincent M, Lafleur PG, Lavoie PA, Carreau PJ. Rheology of short glass fiber reinforced polypropylene. J Rheol. 1992;36:525-42.
[45] Sepehr M, Ausias G, Carreau PJ. Rheological properties of short fiber filled polypropylene in transient shear flow. J Non-Newton Fluid Mech. 2004;123:19-32.
[46] Chung DH, Kwon TH. Invariant-based optimal fitting closure approximation for the numerical prediction of flow-induced fiber orientation. J Rheol. 2002;46:169-94.

3.9 Figures and Tables

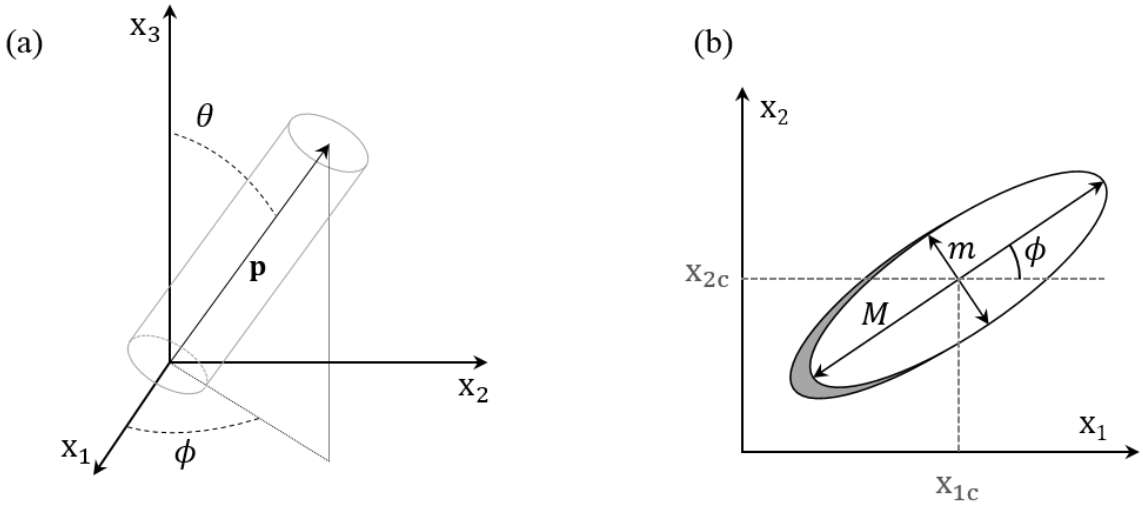

Figure 3.1: (a) Micrograph obtained from an optical microscope at 20x magnification of a 30 wt% glass fiber suspension and (b) important geometrical information measured using the method of ellipses: ellipse center (x_{1c}, x_{2c}), major axis (***M***), minor axis (***m***) and in-plane angle (***ϕ***).

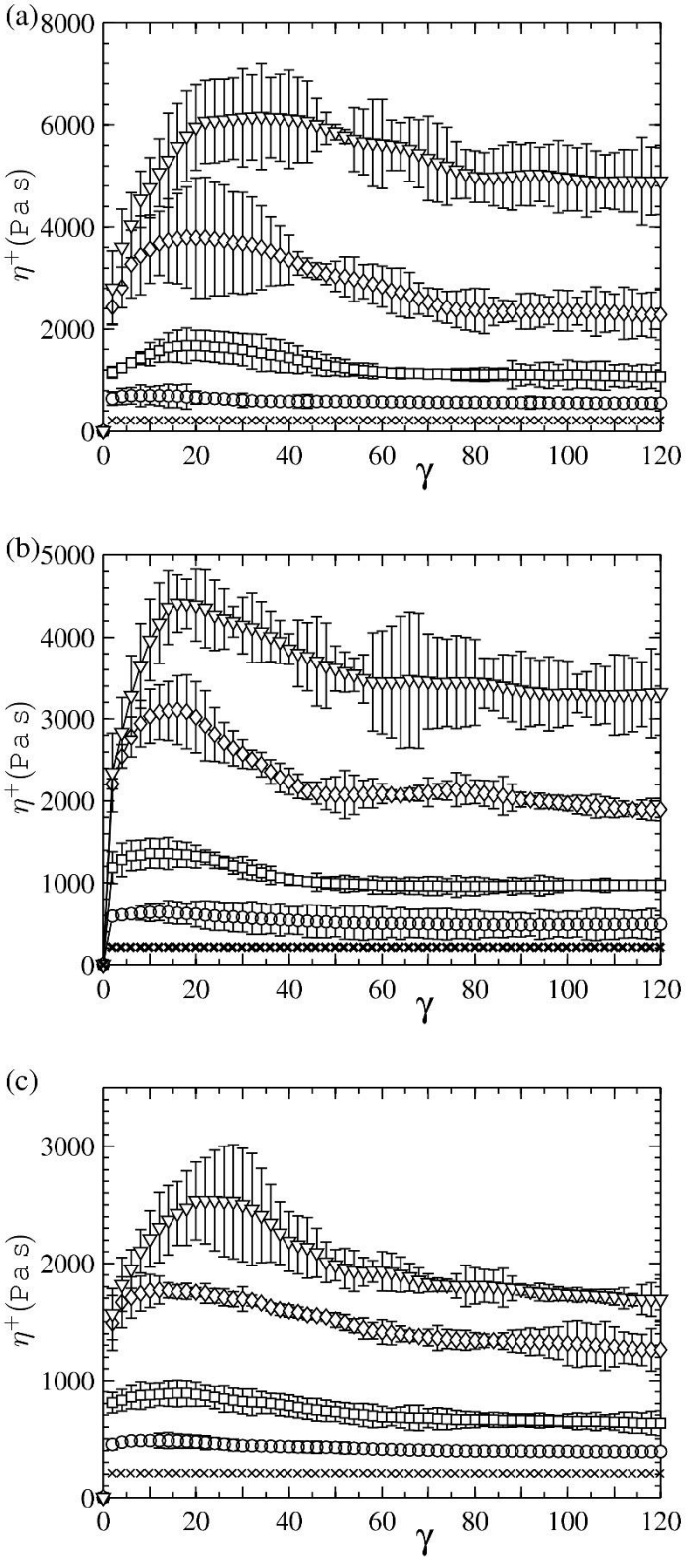
(a)
8000
6000
4000
2000
0
η^+(Pa s)
0
20
40
60
80
100
120
γ
(b)
5000
4000
3000
2000
1000
0
η^+(Pa s)
0
20
40
60
80
100
120
γ
(c)
3000
2000
1000
0
η^+(Pa s)
0
20
40
60
80
100
120
γ

Figure 3.2: Viscosity as a function of shear strain for the polypropylene matrix (×) and glass fiber at 10 wt% (○), 20 wt% (□), 30 wt% (◊) and 40 wt% (∇) at shear rates of (a) 0.4, (b) 1.0 and (c) 4.0 s^{-1}.

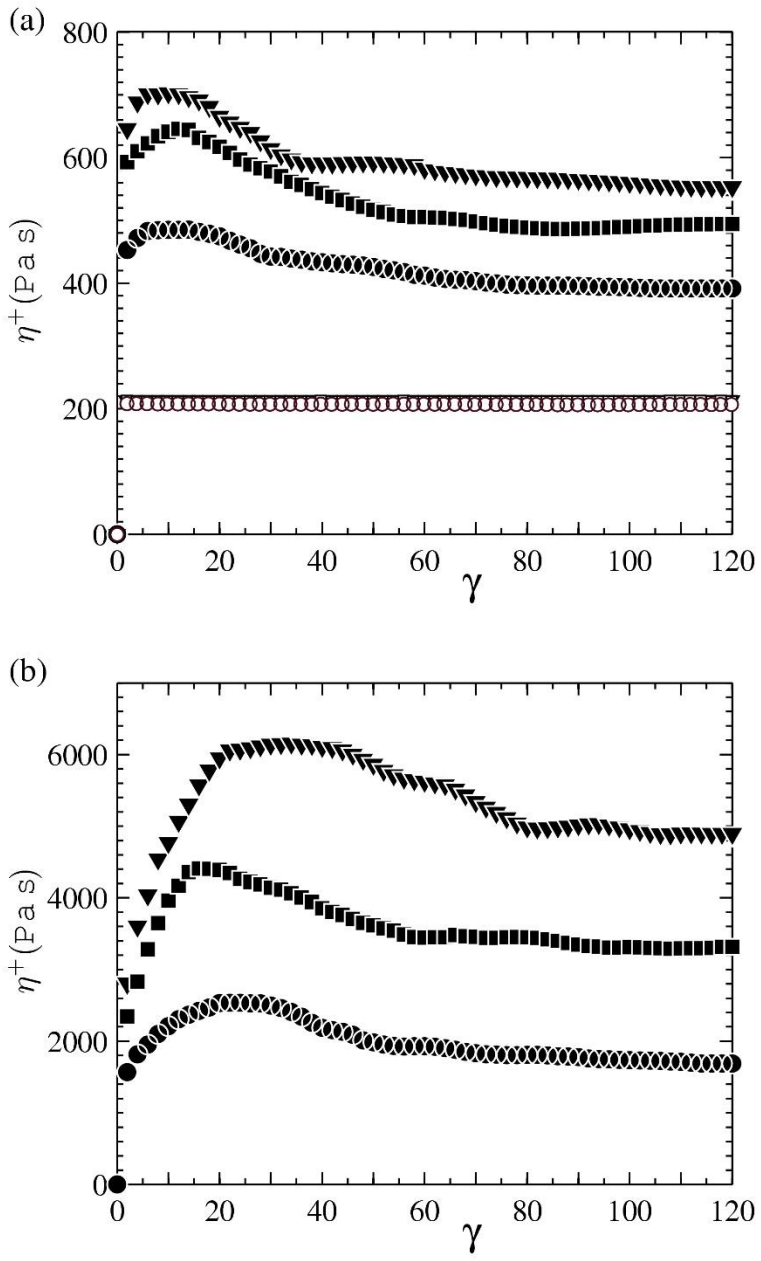

Figure 3.3: Viscosity as a function of shear strain for unfilled polypropylene matrix [(a), open symbols] and 10 [(a) filled symbols] and 40 wt% [(b) filled symbols] glass fiber, for shear rates of 0.4 (∇), 1.0 (□) and 4.0 (○) s^{-1}.

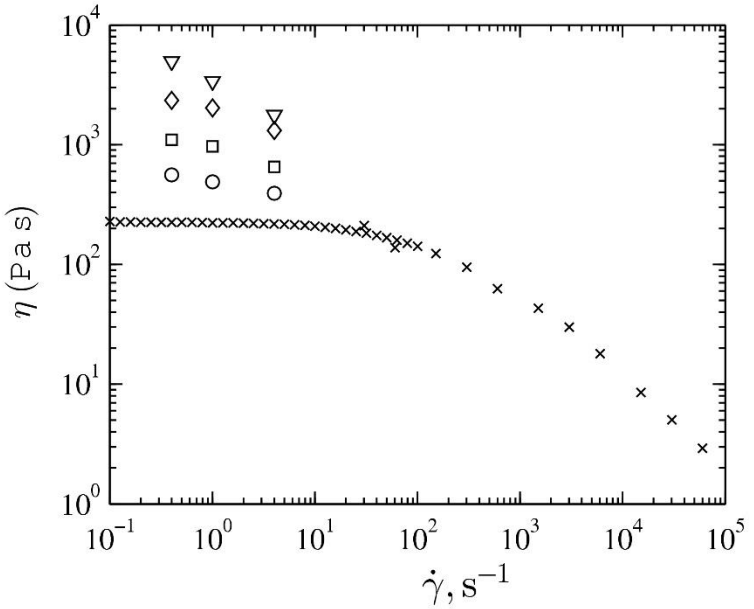

Figure 3.4: Steady shear viscosity for the polypropylene matrix (×) and glass fiber at 10 wt% (○), 20 wt % (□), 30 wt % (◊) and 40 wt% (∇).

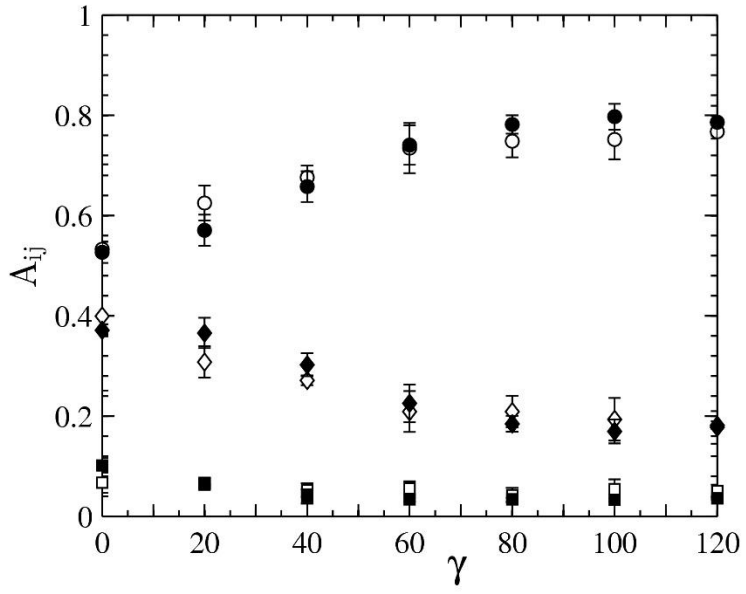

Figure 3.5: Orientation components A_{11}(○), A_{22}(□), and A_{33}(◊) as a function of shear strain at 1.0 s^{-1} for 10 (open symbols) and 40 wt% (filled symbols) glass fiber.

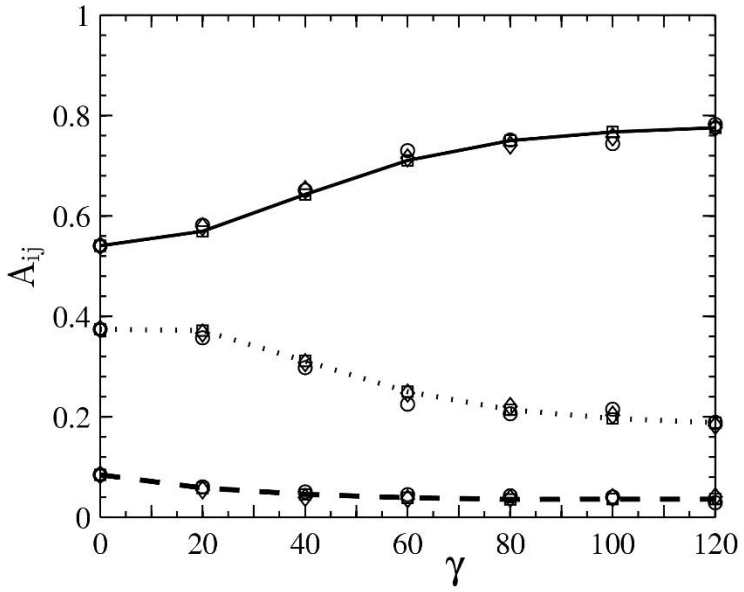

Figure 3.6: Orientation evolution for 30 wt% glass fiber at shear rates of 0.4 (○), 1.0 (□) and 4.0 (▽) s^{-1}. Trends in A_{11}, A_{22} and A_{33} are designated by solid, dashed and dotted lines, respectively.

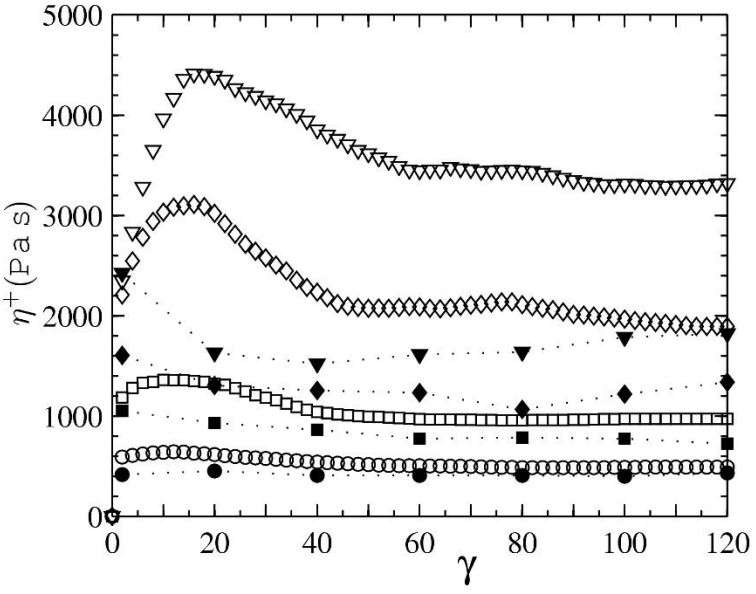

Figure 3.7: Stress predictions (closed symbols) at a shear rate of 1.0 s^{-1} as a function of concentration for 10 wt% (○), 20 wt% (□), 30 wt% (◊) and 40 wt% (▽) glass fiber. Open symbols represent the experimental data.

Table 3.1: Fiber Suspension Concentrations and Lengths

Glass Fiber Content		Number Average Fiber	Aspect Ratio	Weight Average Fiber
wt%	v%	Length (L_n), mm	(L_n/d)	Length (L_w), mm
10	3.8	1.40 ± 0.074	105	3.59 ± 0.61
20	8.2	1.28 ± 0.078	97	2.95 ± 0.37
30	13.3	1.25 ± 0.065	94	2.28 ± 0.24
40	19.2	1.06 ± 0.080	79	1.96 ± 0.35

Chapter 4 A Comparison between the Transient Shear Flow Behavior of Glass and Carbon Fiber Suspensions

Chapter 4 A Comparison between the Transient Shear Flow Behavior of Glass and Carbon Fiber Suspensions

4.1 Abstract

The transient shear stress and fiber orientation evolution were measured for glass and carbon fiber suspensions in a polypropylene matrix at equivalent volume fractions and fiber aspect ratios (length/diameter) of about 100 based on the number average fiber length. Shear stress was measured during the startup of simple shear flow in a sliding plate rheometer at three shear rates spanning an order of magnitude. The transient shear stress response and measured fiber orientation for both systems exhibited a similar dependency on concentration and shear rate. Above a certain concentration, the shear deformation of the carbon fiber suspension was inhomogeneous and resulted in unreliable measurements of stress and fiber orientation. Increased fiber interactions or differences in fiber sizing offer two potential explanations to account for the different behaviors of glass and carbon fiber suspensions at high concentrations.

4.2 Introduction

Carbon based fillers have been widely explored in an effort to improve mechanical, thermal and electrical properties when compared to neat polymers [1, 2]. These materials exist in a variety of forms with different shapes and length scales, such as carbon black [1], graphene platelets [3, 4], carbon nanotubes [5, 6], vapor grown carbon fibers [7] and carbon fibers derived from precursor fibers [8]. The implementation of these materials has been dependent on the application, which may dictate the importance of cost versus the desired performance [2].

Carbon fibers derived from precursor fibers have received recent interest to directly replace glass fibers in molded composites due to the improved strength and modulus to weight ratio properties. Some general properties of glass and carbon fiber are provided in Table 4.1 [2, 9-11]. Carbon fibers are also considered a transversely isotropic material, in that properties parallel to the

length of the fiber are different than in the transverse direction [11-13]. The transverse modulus, for example, has been reported to be about an order of magnitude less than the modulus in the longitudinal direction [12].

A limited amount of research has been devoted to characterizing the rheology of discontinuous carbon fiber suspensions. Many of the studies used extrusion to disperse the fibers in the suspending matrix which resulted the number average fiber length to be in the range of 100 to 200 μm [14-18]. Hausnerova et al. [19, 20] reported the increase in the bulk viscosity of carbon fiber suspensions with length distributions that contained fibers up to 0.5 mm. These studies do not appear to report any unique behavior for carbon fiber that was not found in the well-studied glass fiber suspensions.

Transient rheological measurements of fiber filled systems are performed to investigate the evolution of fiber orientation. During the startup of simple shear flow, glass fibers have been shown to align in the flow direction while producing an overshoot in the shear stress and the first normal stress difference [21, 22]. The overshoot peak has been observed to broaden and the shear stress increase in magnitude with increases in fiber length and concentration [23].

Fiber orientation measurements have also been obtained during flow in a rheometer to verify the evolution of fiber orientation. Petrich et al [24] and Keshtkar et al. [25] used flow visualization to track the fiber orientation evolution while the suspension was under flow. Eberle et al. [21], Ortman et al. [26] and Cieslinski et al. [23] allowed the thermoplastic composite to cool in the rheometer to preserve the fiber orientation of glass fibers which was later measured from a polished cross section of the sample. With both measurement methods, the time required for the average fiber orientation to change from the initial state to a steady state increased with increases in fiber length and aspect ratio. Keshtkar et al. [25] measured the orientation of different types of fiber suspensions corresponding to different fiber flexibilities and observed that the increase in flexibility caused fibers to orient in the flow direction at a slower rate.

Many theories for fiber suspensions are dependent on the fiber aspect ratio (a_r = length/diameter) and volume fraction (ϕ_v) and do not consider the fiber type or specific fiber dimensions. Concentration regimes derived from rod-like molecules are divided into dilute ($\phi_v < a_r^{-2}$), semi-dilute ($a_r^{-2} < \phi_v < a_r^{-1}$) and concentrated ($\phi_v \geq a_r^{-1}$) regimes [27]. Toll [28] derived the number of contacts per fiber to scale with the product $\phi_v a_r$ for slender fibers. Theories for the extra stress in fiber suspensions can scale by as much as $\phi_v a_r^2$ [29-32]. The flexibility of a fiber in simple shear flow was represented as a non-dimensional effective stiffness parameter by Switzer and Klingenberg [33]:

$$S^{eff} = \frac{E_Y \pi}{\eta_m \dot{\gamma} a_r^4} \tag{4.1}$$

where, E_Y is the Young's modulus of the fiber, η_m is the matrix viscosity and $\dot{\gamma}$ is the shear rate. This term describes the ratio of a fiber's bending moment with the viscous torque transferred from the fluid to the fiber [34].

The purpose of the work is to compare the transient shear stress response of carbon fiber suspensions to previously reported glass fiber data at an average fiber aspect ratio of about 100. The samples were prepared at equivalent volume fractions and similar aspect ratios to examine if theories employed for glass fiber suspensions are extendable to carbon fiber suspensions. Fiber orientation as a function of shear strain is also obtained to investigate the evolution of orientation during shear flow. Lastly, this work showcases some unexpected sample deformation of carbon fiber suspensions at higher concentrations. Two potential explanations for the inhomogeneous deformation are discussed.

4.3 Experimental

4.3.1 Material Preparation

The glass fiber reinforced polypropylene material was received as 13 mm long pellets containing 30 wt% glass fibers (MV006S-GYLTNAT provided by Sabic). The polypropylene matrix displayed no significant transient rheological behavior and had a zero shear viscosity of 223 Pa s at a temperature of 200 °C [23]. The carbon fiber reinforced polypropylene was provided by Ticona as 13 mm long pellets containing 40 wt% carbon fiber (PP-CF40-03 AF3004 Natural). Equivalent fiber volume fractions were created by diluting the composite pellets with neat polypropylene in a Killion 25 mm 20L/D single screw extruder (KLB-100). The temperature zones in the extruder were set to 220, 230 and 245 °C with the 1.5 mm diameter die set to 150 °C. Composite materials were extruded at 20 rpm and pelletized to 15 mm. The pellets containing dispersed fibers were compression molded at 180 °C to produce samples with dimensions of 250 x 50 x 1.6 mm for testing in a sliding plate rheometer. Compression molded disks were also produced in a shape to match the 0.1 radian cone angle of a 50 mm cone-and-plate fixture for a rotational rheometer. A 25 mm hole was cut in to the disk-shaped sample after compression molding to alleviate the restriction of fiber motion at small gap thicknesses near the cone apex. The extrusion and compression molding procedure was used by Cieslinski et al. [23] to generate samples used to report the transient rheology from a sliding plate rheometer of 10 and 20 wt% glass fiber suspensions. To equate the glass and carbon fiber suspensions on a volumetric basis, carbon fibers were diluted to 9.2 and 15.3 wt%, which corresponds to 3.8 and 8.2 v%, respectively.

Fiber length measurements were obtained from the 15 mm pellets used to form the compression molded samples. The pellets were placed in a preheated oven at 450 °C for a duration of 30 minutes to remove the matrix. These conditions were found to minimize the degradation of the carbon fibers during the matrix burn-off [35, 36]. Carbon fibers were dispersed on a piece of white paper and imaged on a desktop scanner at 3000 dpi resolution. At least 1500 fibers were

measured using NIH ImageJ software to produce the fiber length distributions. The number average diameters of the glass and carbon fiber were found to be 13.3 and 6.68 μm, respectively, using an optical microscope. A summary of the glass and carbon fiber lengths is provided in Table 4.2.

4.3.2 Stress Measurements

A cone-and-plate rheometer with donut-shaped samples and a sliding plate rheometer were used to investigate the transient shear rheology of the carbon fiber suspensions. The donut shaped sample was employed by Eberle et al. [37] for short glass fibers (L_n = 0.3 mm). The transient responses of short glass fibers reported by Eberle et al. [37] were replicated using a sliding plate rheometer by Agarwal [38]. A major constraint with the cone-and-plate fixture is the designed gap thickness of the fixture. This limits the length (not the aspect ratio) of fibers that can be measured. Because many of the carbon fibers are below 1 mm in length the use of the cone-and-plate rheometer was explored to measure the transient shear response of the carbon fiber suspensions. The use of a sliding plate rheometer to measure the transient response of glass fiber suspensions with an average fiber length above 1 mm was investigated by Agarwal [38] due to gap and edge effects associated with a cone-and-plate fixture. The sliding plate rheometer was used to measure the transient response from the startup of simple shear flow for both the glass and carbon fiber suspensions.

A 50 mm cone-and-plate fixture with a cone angle of 0.1 radians was used in a Rheometrics RMS-800. The rheometer was heated to 200 °C for 2 hours to minimize any thermal expansion of the cone-and-plate fixtures during the test. A donut-shaped sample was then loaded and tested at a shear rate of 1.0 s^{-1} for 60 strain units. The dimensions of the sample required about 100-200 μm squeezing to set the cone-and-plate fixtures to the designed spacing. This results in little sample deformation prior to the startup of flow. The sample was allowed to cool within the

rheometer after shearing to the desired strain to preserve the fiber orientation for later measurement.

The sliding plate rheometer with a shear stress transducer based on the work of Giacomin et al. [39, 40] was used. The design and validation of this particular sliding plate rheometer can be found in the thesis of Agarwal [38]. A forced convection oven (Russells Technical Products model RB-2-340) was used to control the temperature of the rheometer. An instron-4204 universal testing machine controlled the displacement of the sliding plate. A shear stress transducer measures shear stress locally on the sample by the small deflection of a lever arm contacting the fluid. The lever arm is held in place by a diaphragm and the dimensions of the diaphragm determine the stress range and sensitivity. A capacitance probe measured the displacement of the lever arm (Capacitec, Model HPT-75I-V-T-2-B with 4100-SL-BNC amplifier). A National Instruments data acquisition module (USB-6008) allows the voltage data from the capacitance probe to be recorded by a computer using National Instruments SignalExpress software (version 2.5.1).

The experimental procedure for the sliding plate rheometer was similar to the cone-and-plate rheometer. Thermal expansion was mitigated by heating the rheometer to 200 °C for 2 hours prior to sample loading. The sample was placed in the rheometer and the plates were closed enough to touch both surfaces of the sample. After 5 minutes in the rheometer, the plates were closed to a final thickness of 1.5 mm. This gap thickness was used to report the transient viscosity for 10 and 20 wt% fiber suspensions at a number average fiber length of at least 1.28 mm [23]. After an additional 10 minutes in the rheometer, the sample was subjected to 120 strain units of deformation at shear rates of 0.4, 1.0 and 4.0 s^{-1}. After testing, the sample was cooled to room temperature using forced convection to preserve the fiber orientation for further analysis.

4.3.3 Fiber Orientation Measurements

Fiber orientation measurements were obtained by viewing fibers that intersected the x_1x_2-midplane, with x_1 denoting the direction of flow and a change in velocity in the x_2-direction. The samples removed from the rheometer were cut, mounted and polished following the procedure described by Vélez-García et al. [41]. Oxygen plasma was used to etch the polished surface in order to enhance the contrast between the glass fibers and polypropylene matrix. This step was not necessary for the carbon fiber composites. Orientation measurements were obtained at 20x on an optical microscope (Nikon Eclipse LV100, NIS Basic Research Software, version 3.10) for glass fibers. At 20x magnification for the carbon fiber samples, the average orientation obtained in the x_1x_2-midplane from samples tested in the sliding plate rheometer differed by as much as 15 % when compared to measurements obtained in the x_2x_3-plane. Increasing the magnification to 50x, decreased the variation in the average orientation between the perpendicular planes to within about 4 %, which is similar to what has been reported for glass fiber suspensions at 20x magnification [42]. The image analysis width was suggested by Hofmann et al. [43] to be extended to 5.5 mm in a 1-dimensional flow to account for highly elongated glass fibers. This was used for the glass fiber suspensions and an image analysis width of 2.75 mm was used for the carbon fibers because the average carbon fiber length is about half the length of the glass fibers. The fibers crossing the inspection plane were displayed as elliptical objects. A unit vector of orientation can be associated with each elliptical object by measuring the major and minor axes of the ellipse and the in-plane angle. A second moment of orientation tensor, **A**, was calculated from a population of fibers and a weighting function proposed by Bay and Tucker [44] to correct for imaging bias. The in-plane orientation was not measured unambiguously, as a result the A_{13} and A_{23} components of orientation cannot be accurately reported. Four imaging locations in the x_1x_2-midplane for samples obtained from the sliding plate rheometer consider the average orientation through the entire sample thickness to produce the reported fiber orientation averages. Separate samples must be used for each strain because the method of ellipses is a destructive process.

4.4 Results and Discussion

4.4.1 Fiber Aspect Ratio Distributions

Figure 4.1 provides the fiber aspect ratio distributions (L_i/d) of the glass and carbon fiber suspensions at concentrations of 3.8 and 8.2 v%. The histograms show the fraction of the total fibers measured as a function of fiber aspect ratio to compare the two fiber types with different fiber diameters. The fiber aspect ratios were sorted by increments of 10 from 0 to 1000. A majority of the fibers are below an aspect ratio of 200, but there is a small population of the longer fibers. At 3.8 v%, the most frequent glass fiber aspect ratio was 34 while the carbon fiber suspension was at 60. The glass fiber suspension has many fibers with a very short aspect ratio, but the distribution is broad, extending to fibers with aspect ratios above 800. A more narrow distribution is observed with the carbon fibers which are measured to have a maximum length of about 7 mm. None of the measured carbon fibers maintained the initial fiber length of 13 mm after processing in the extruder. At a concentration of 8.2 v%, there is much more similarity between the aspect ratio distributions of the glass and carbon fiber suspensions. The most frequent fiber aspect ratio for both fiber types is approximately 70. The longer fiber aspect ratios also favor the glass fiber suspensions, but the quantity of fibers for both systems above an aspect ratio of 500 is decreased compared to 3.8 v%.

4.4.2 Cone-and-Plate Rheometry Results

The measured torque and normal force for a 3.8 v% carbon fiber sample at a shear rate of 1.0 s^{-1} is provided in Figure 4.2. From the torque and normal force, the viscosity and first normal stress difference can be calculated, respectively [37]. A maximum is observed in the measured torque response at a shorter time scale than what is typically observed for short glass fiber suspensions [45]. The normal force generally increases with a local maximum at about 27 s. Upon the cessation of flow, the torque and normal forced did not return to zero. Upon visual inspection of the sample after testing in the rheometer it is clear that the sample deformation is not as expected.

An example of a sample obtained after shearing in the cone-and-plate rheometer is shown in Figure 4.3. Upon the startup of flow, severe necking occurs in the sample and the 25 mm hole in the center of the sample begins to close. While necking occurs halfway between the two plates, fibers closer to the plates appear to be pushed out of the gap. The extent of this behavior is different at each circumferential location in the donut-shaped sample. Similar behavior was observed for the glass fiber suspension, but the average fiber length of the glass is about twice the carbon fiber average length. Stress measurements from a donut-shaped sample are reliable provided that the sample maintains its shape under shear deformation. With the dimensions of the carbon fiber samples changing significantly during flow, a derivation of the shear flow material functions from the measured torque and normal force cannot be completed.

4.4.3 Sliding Plate Rheometry Results

Flow within the sliding plate rheometer proved to be much more repeatable than the donut-shaped samples in the cone-and-plate rheometer. Figure 4.4 shows a comparison of glass and carbon fibers at concentrations of 3.8 and 8.2 v% at shear rates of 0.4, 1.0 and 4.0 s^{-1}. The rheological behavior of the carbon fiber suspensions parallels the transient response of the glass fiber suspensions at equal volume concentrations. The largest deviation between the suspensions of the two fiber types is observed at a shear rate of 0.4 s^{-1}. It appears that the carbon fiber stress overshoot is more pronounced than with the glass fibers. It is unclear why this occurs only at one shear rate, but for both concentrations. Both suspensions appear to have similar shear-thinning behavior. With the standard deviation of the data being within ±10 % of the measured value, the steady state value for the glass and carbon fiber suspensions at equal shear rates are within the experimental error. The measured stress responses appear to confirm that the stress theories should be dependent on the fiber aspect ratio and fiber volume fraction. In addition, the similarity of these results also supports the use of a 1.5 mm gap thickness to provide unbiased shear stress

measurements, as the ratio of rheometer gap to fiber length for carbon fibers is twice the ratio for glass fibers.

The steady shear viscosity as a function of shear rate provides another perspective into the viscosity enhancement from high aspect ratio fibers (Figure 4.5). The neat polypropylene data was measured under small amplitude oscillatory flow using a cone-and-plate rheometer and a capillary rheometer was used to measure the viscosity at the high shear rates [23]. The polypropylene matrix does not exhibit shear thinning behavior until a shear rate of about 50 s^{-1}. The addition of fibers causes shear thinning to occur at lower shear rates than the neat matrix. As is evident in Figure 4.4, the shear thinning behavior of the carbon fiber suspensions parallels that of the glass fiber suspensions. Figure 4.5 also includes viscosity versus shear rate data for glass fiber suspensions at higher concentrations. Increased shear thinning behavior occurs at the higher concentrations. It is expected that carbon fiber suspensions should behave similarly to glass fibers at higher concentrations based on the agreement between the two systems at 3.8 and 8.2 v%, but repeatable stress and orientation results could not be obtained using the sliding plate rheometer at carbon fiber concentrations above 8.2 v% (15.3 wt%).

At carbon fiber concentrations greater than 8.2 v%, the sample deformation is not uniform in the sliding plate rheometer. Carbon fiber suspensions at 20 wt% (11 v%) were tested using a 1.5 mm gap thickness for shear rates of 0.4, 1.0 and 4.0 s^{-1} and temperatures up to 230 °C, but these conditions did not improve the irregular sample deformation. A 20 wt% (11 v%) carbon fiber suspension is shown in Figure 4.6 at a gap thickness of 3 mm. It appears that some regions in the sample do not deform significantly which results in what might be considered melt fracture between these regions. At some locations, fluid also detaches from the plates. Dhori et al. [46] reported that a viscoelastic polymer melt can detach from the plates of a sliding plate rheometer at large deformation above a critical shear rate. The unexpected deformation observed with the carbon fiber suspensions at high concentrations does not appear to be rate dependent nor is the

sample failure relegated to a specific location in the sample. The sample featured in Figure 4.6, shows a hole that penetrates the entire thickness of the sample near the shear stress transducer. With holes forming in the sample and the sample detaching from the plates of the rheometer, the shear stress measurements are not repeatable. This behavior was not observed with glass fiber suspensions for concentrations up to 40 wt% (19.1 v%) [23].

The evolution of fiber orientation was investigated for the carbon and glass fiber samples that appeared to deform uniformly in the sliding plate rheometer. Measured values of fiber orientation averaged over the entire inspection region are shown in Figure 4.7 for concentrations of 3.8 and 8.2 v% at a shear rate of 1.0 s^{-1}. There is no observable difference in the fiber orientation averages at the shear rates of 0.4 and 4.0 s^{-1}. The evolution of fiber orientation does not appear to be different outside of experimental error between the glass and carbon fiber suspensions. Additionally, differences in orientation as a function of concentration are also within the experimental error. The A_{11} component of fiber orientation increases gradually from a value near 0.54 up to a value near 0.78 for both concentrations. The value for A_{22} is small and does not show any significant changes with shear strain, indicating that the fibers, on average, remain mostly in the x_1x_3-plane throughout the test. With a mostly planar fiber orientation, the evolution of A_{33} has a mirrored profile in comparison to A_{11}.

4.5 Accounting for Differences in the Suspensions

There appears to be a distinct difference in the sample deformation for suspensions containing high concentrations of carbon fibers in comparison to glass fibers. From inspection of the polished cross sections used to measure the fiber orientation, it does not appear that the fiber dispersion was different for the glass and carbon fiber suspensions. The fiber aspect ratios and concentrations are similar between the glass and carbon fiber suspensions, but characteristics such as the surface treatment of the fibers and the physical fiber dimensions are different. Surface treatments for fibers in composites often consist of a lubricant, antistatic, binder and coupling agent

[47]. Commercial suppliers of these composite materials typically have a proprietary sizing formulation. Glass fibers are typically coated with a silane based sizing agent. Improved coupling of carbon fibers to a polymer matrix has been achieved with titanate or zirconate based fiber treatments [48]. The similarity in the transient stress responses of the glass and carbon fiber suspensions at 3.8 and 8.2 v% does not provide much support for chemical differences influencing the rheology of these systems. The physical dimensions of the fibers may contribute to a mechanical network based on the density of fiber-fiber interactions. Based on the geometry of a cylinder, the number of fibers per unit volume, n, is [27]:

$$n = \frac{4\phi a_r^2}{\pi L^3} \tag{4.2}$$

where L is the fiber length. The number of carbon fibers in a suspension is greater than glass fibers by approximately a factor of eight at equal volume fractions and aspect ratios. The increased number of fibers then would increase the number of fiber interactions per unit volume. Toll [28] derived the number of contacts per fiber, N_c, as:

$$N_c = \frac{8}{\pi} a_r \phi_v f + 4\phi_v (g + 1) \tag{4.3}$$

where, f and g are dependent on the fiber orientation. In the case of high aspect ratio fibers, the above equation can be approximated as:

$$N_c = \frac{8}{\pi} a_r \phi_v f. \tag{4.4}$$

The interactions that a single fiber experiences would be equal between glass and carbon fiber suspensions if the aspect ratio, concentration and orientation are equal. Yet, by considering that the number of fibers per unit volume is greater for carbon fiber than glass fiber by about a factor of eight, the number of fiber-fiber interactions per unit volume would also be greater by a factor

of eight. It is thought that the carbon fiber composite may be a much more entangled network than the glass fiber composite. This may be the case, but the transient shear stress measurements at 3.8 and 8.2 v% suggest that the rheology is based on aspect ratio and volume fraction. Perhaps there may be a critical threshold that is met above these concentrations that causes the carbon fiber suspension to behave differently than the glass suspension. At this point, a definitive mechanism to explain the differences in glass and carbon fiber at higher concentrations is unclear and requires further investigation.

4.6 Conclusions

A comparison of the transient viscosity and fiber orientation was reported for glass and carbon fiber suspensions in a polypropylene matrix at concentrations of 3.8 and 8.2 v% in a sliding plate rheometer. Differences between glass and carbon fiber at these concentrations appear minor and largely attributed to the experimental error, indicating that the rheology is primarily dependent on the fiber aspect ratio and volume concentration. At concentrations of carbon fiber above 8.2 v% the sample deformation was not uniform in the rheometer which does not appear to be the case for equivalent glass fiber suspensions. Two proposed explanations of this behavior are the potential chemical differences in the fiber sizing and an increased density of fiber interactions due to the smaller carbon fiber diameter in comparison to glass. Further investigation is necessary to clarify the cause of the irregular sample deformation for carbon fiber suspensions at high concentrations.

It appears that much of the transient behavior of the glass and carbon fiber suspensions is indistinguishable up to 8.2 v% for suspensions with a number average fiber aspect ratio of about 100. Much of the knowledge derived using glass fiber suspensions can be extended to carbon fibers at an equivalent volume fraction and number average fiber aspect ratio. The simple shear flow imposed by a sliding plate rheometer could not capture the transient rheology at higher carbon

fiber concentrations. Other rheological methods must be investigated in order to provide transient stress and orientation information at higher carbon fiber loadings.

4.7 Acknowledgements

The financial support for this work from the American Chemistry Council and National Science Foundation CMMI-0853537 is gratefully acknowledged. The authors would also like to thank the Material Science and Engineering department and the Sustainable Energy laboratory at Virginia Tech for use of laboratory equipment.

4.8 References

[1] Donnet JB, Bansal RC, Wang MJ. Carbon Black. 2nd ed. New York: Marcel Dekker; 1993.
[2] Fitzer E, Manocha LM. Carbon Reinforcements and Carbon/Carbon Composites: Springer; 1998.
[3] Kim H, Abdala AA, Macosko CW. Graphene/polymer nanocomposites. Macromolecules. 2010;43:6515-30.
[4] Potts JR, Dreyer DR, Bielawski CW, Ruoff RS. Graphene-based polymer nanocomposites. Polymer. 2011;52:5-25.
[5] Coleman JN, Khan U, Blau WJ, Gun'ko YK. Small but strong: A review of the mechanical properties of carbon nanotube–polymer composites. Carbon. 2006;44:1624-52.
[6] Han Z, Fina A. Thermal conductivity of carbon nanotubes and their polymer nanocomposites: A review. Prog Polym Sci. 2011;36:914-44.
[7] Tibbetts G, Lake M, Strong K, Rice B. A review of the fabrication and properties of vapor-grown carbon nanofiber/polymer composites. Compos Sci Technol. 2007;67:1709-18.
[8] Chand S. Review carbon fibers for composites. Journal of Materials Science. 2000;35:1303-13.
[9] Hyer MW. Stress Analysis of Fiber-Reinforced Composite Materials. Updated Edition ed: DEStech Publications, Inc.; 2009.
[10] Fu S-Y, Lauke B, Mäder E, Yue C-Y, Hu X. Tensile properties of short-glass-fiber- and short-carbon-fiber-reinforced polypropylenes. Composites Part A. 2000;31:1117-25.
[11] Krucinska I, Stypka T. Direct measurement of the axial Poisson's ratio of single carbon fibres Compos Sci Technol. 1991;41:1-12.
[12] Kriz RD, Stinchcomb WW. Elastic moduli of transversely isotropic graphite fibers and their composites. Experimental Mechanics. 1979;19:41-9.
[13] Dean GD, Turner P. The elastic properties of carbon fibres and their composites. Composites. 1973;4:174-80.
[14] Schmitt Y, Paulick C, Bour Y, Royer FX. Short carbon fibers composites with high filler contents rheology and mechanical properties. MD (American Society of Mechanical Engineers). 1999;88:17-24.
[15] King JA, Keith JM, Smith RC, Morrison FA. Electrical conductivity and rheology of carbon fiber/liquid crystal polymer composites. Polym Compos. 2007;28:168-74.

[16] Kim YH, Yoon SH, Jang SH, Lee YK, Sung Y-T, Lee HS, et al. Effects of fiber characteristics on the rheological and mechanical properties of polycarbonate/carbon fiber composites. Compos Interfaces. 2009;16:477-91.
[17] Starý Z, Krückel J, Weck C, Schubert DW. Rheology and conductivity of carbon fibre composites with defined fibre lengths. Compos Sci Technol. 2013;85:58-64.
[18] Marcaníková L, Hausnerová B, Kitano T. Rheological behavior of composites based on carbon fibers recycled from aircraft waste. American Institute of Physics International Conference. 2009.
[19] Hausnerova B, Zdrazilova N, Kitano T, Saha P. Rheological properties of carbon fibre filled low-density polyethylene under the parallel steady and oscillatory shear flows. Polimery. 2006;51:33-41.
[20] Hausnerova B, Honkova N, Lengalova A, Kitano T, Saha P. Rheology and fiber degradation during shear flow of carbon-fiber-reinforced polypropylenes. Polym Sci Ser A. 2006;48:951-60.
[21] Eberle APR, Baird DG, Wapperom P, Vélez-García GM. Using transient shear rheology to determine material parameters in fiber suspension theory. J Rheol. 2009;53:685-705.
[22] Sepehr M, Ausias G, Carreau PJ. Rheological properties of short fiber filled polypropylene in transient shear flow. J Non-Newton Fluid Mech. 2004;123:19-32.
[23] Cieslinski MJ, Wapperom P, Baird DG. Influence of fiber concentration on the startup of shear flow behavior of long fiber suspensions. J Non-Newton Fluid Mech. 2015;222:165-70.
[24] Petrich MP, Koch DL, Cohen C. An exerimental determination of the stress-microstructure relationship in semi-concentrated fiber suspensions. J Non-Newton Fluid Mech. 2000;95:101-33.
[25] Keshtkar M, Heuzey MC, Carreau PJ, Rajabian M, Dubois C. Rheological properties and microstructural evolution of semi-flexible fiber suspensions under shear flow. J Rheol. 2010;54:197-222.
[26] Ortman K, Baird D, Wapperom P, Whittington A. Using startup of steady shear flow in a sliding plate rheometer to determine material parameters for the purpose of predicting long fiber orientation. J Rheol. 2012;56:955-81.
[27] Doi M, Edwards SF. The Theory of Polymer Dynamics: Oxford University Press, New York; 1986.
[28] Toll S. Packing mechanics of fiber reinforcements. Polym Eng Sci. 1998;38:1337-50.
[29] Hinch EJ, Leal LG. The effect of Brownian motion on the rheological properties of non-spherical particles. J Fluid Mech. 1972;52:683-712.
[30] Dinh SM, Armstrong RC. A rheological equation of state for semiconcentrated fiber suspensions. J Rheol. 1984;28:207-27.
[31] Lipscomb GG, Denn MM, Hur DU, Boger DV. The flow of fiber suspensions in complex geometries. J Non-Newton Fluid Mech. 1988;26:297-325.
[32] Shaqfeh ESG, Fredrickson GH. The hydrodynamic stress in a suspension of rods. Phys Fluids A. 1990;2:7-24.
[33] Switzer LH, Klingenberg DJ. Rheology of sheared flexible fiber suspensions via fiber-level simulations. J Rheol. 2003;47:759-78.
[34] Switzer LH. Simulating Systems of Flexible Fibers. PhD Thesis: University of Wisconsin; 2002.
[35] Vélez-García GM, Kunc V. Personal Communication. 2014
[36] Kunc V, Frame BJ, Nguyen BN, Tucker CL, Vélez-García GM. Fiber length distribution measurement for long glass and carbon fiber reinforced injection molded thermoplastics. Society of Plastics Engineers Automotive Composites Conference & Exhibition. Troy, Michigan. 2007.
[37] Eberle APR, Baird DG, Wapperom P, Vélez-García GM. Obtaining reliable transient rheological data on concentrated short fiber suspensions using a rotational rheometer. J Rheol. 2009;53:1049-68.
[38] Agarwal N. Transient Shear Flow Rheology of Concentrated Long Glass Fiber Suspensions in a Sliding Plate Rheometer. Master's Thesis: Virginia Polytechnic Institute and State University; 2009.
[39] Giacomin AJ. A sliding plate melt rheometer incorporating a shear stress transducer. PhD Thesis: McGill University; 1987.

[40] Giacomin AJ, Samurkas T, Dealy JM. A novel sliding plate rheometer for molten plastics. Polym Eng Sci. 1989;29:499-504.
[41] Vélez-García GM, Wapperom P, Kunc V, Baird DG, Zink-Sharp A. Sample preparation and image acquisition using optical-reflective microscopy in the measurement of fiber orientation in thermoplastic composites. J Microsc. 2012;248:23-33.
[42] Vélez-García GM, Wapperom P, Baird DG, Aning AO, Kunc V. Unambiguous orientation in short fiber composites over small sampling area in a center-gated disk. Composites Part A. 2012;43:104-13.
[43] Hofmann JT, Vélez-García GM, Baird DG, Whittington AR. Application and evaluation of the method of ellipses for measuring the orientation of long, semi-flexible fibers. Polym Compos. 2013;34:390-8.
[44] Bay RS, Tucker CL. Stereological measurement and error estimates for three-dimensional fiber orientation. Polym Eng Sci. 1992;32:240-53.
[45] Eberle APR, Vélez-García GM, Baird DG, Wapperom P. Fiber orientation kinetics of a concentrated short glass fiber suspension in startup of simple shear flow. J Non-Newton Fluid Mech. 2010;165:110-9.
[46] Dhori PK, Giacomin AJ, Slattery JC. Common line motion II: sliding plate rheometry. J Non-Newton Fluid Mech. 1997;71:215-29.
[47] Plueddemann EP. Silane Coupling Agents: Plenum Press, New York; 1991.
[48] Morgan P. Carbon Fibers and their Composites: CRC Press, Taylor & Francis Group, LLC; 2005.

4.9 Figures and Tables

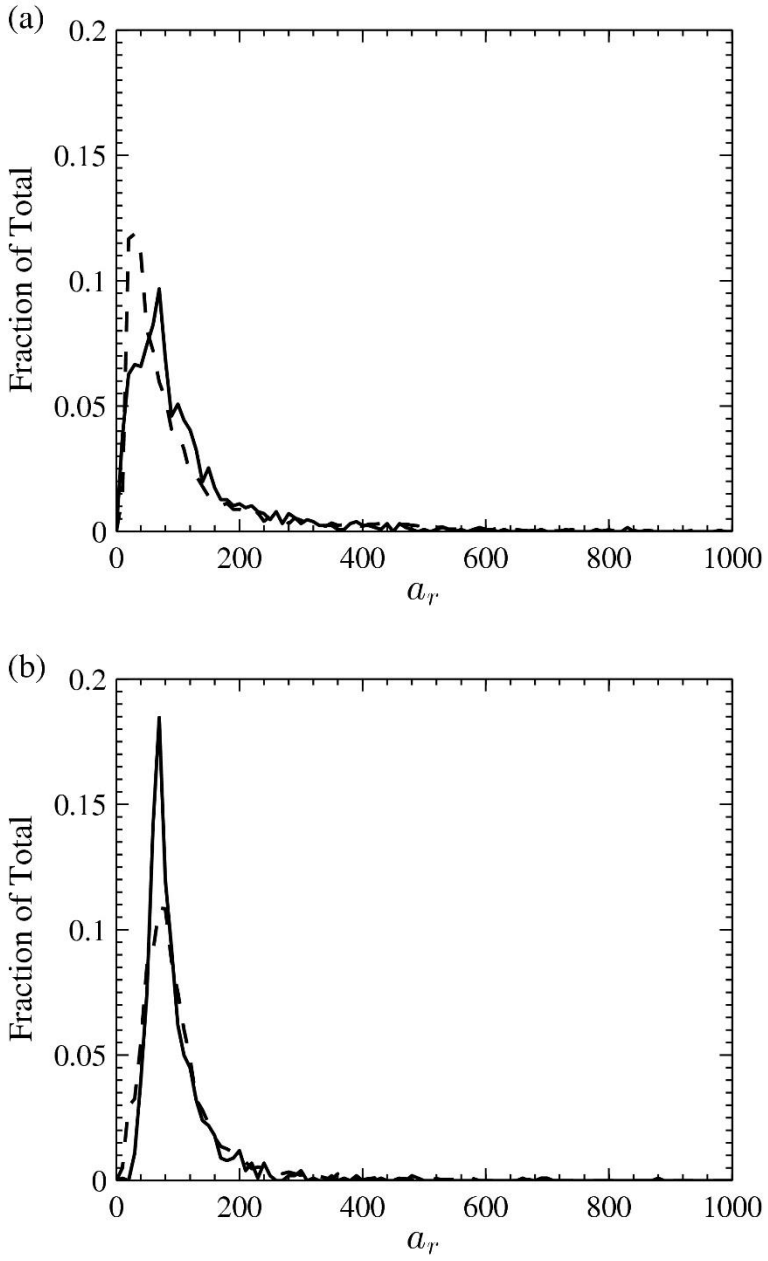

Figure 4.1: Fiber length distributions for glass (dashed line) and carbon (solid line) fiber at concentrations of (a) 3.8 and (b) 8.2 v%.

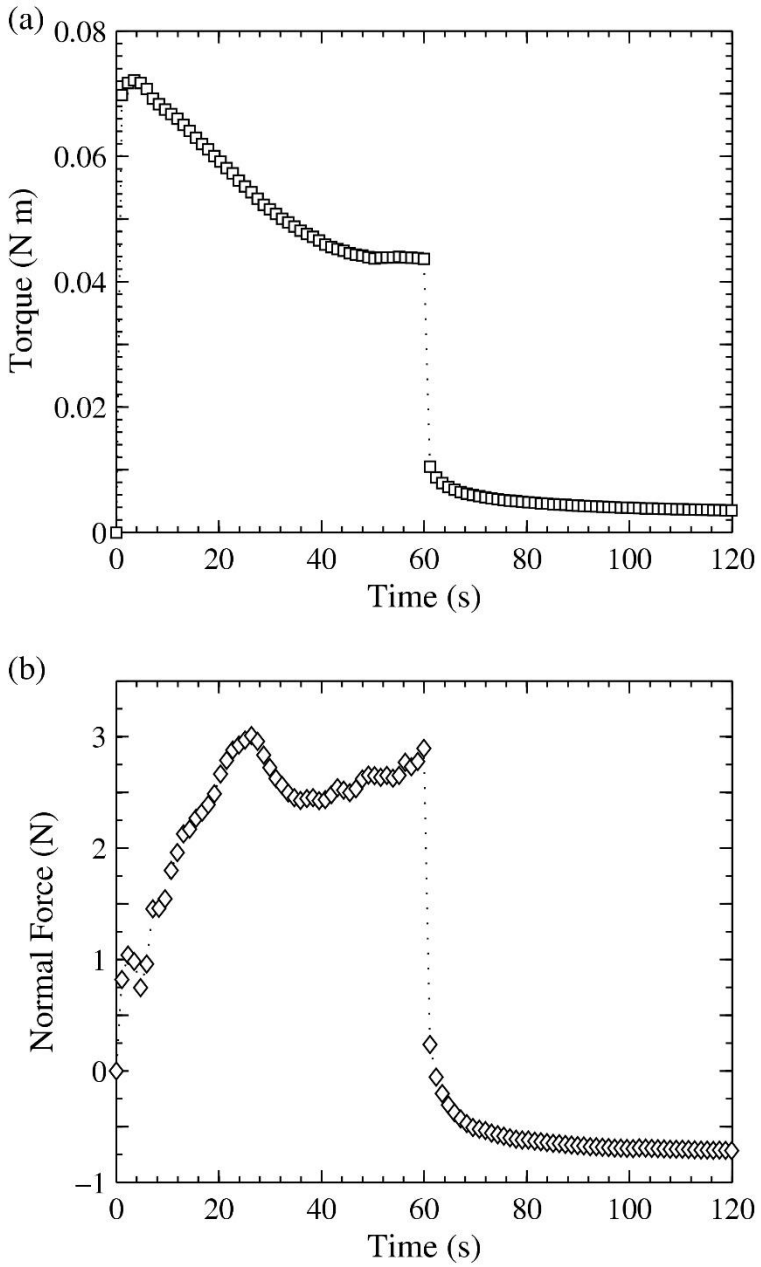

Figure 4.2: An example of the measured (a) torque and (b) normal force for the 3.8 v% carbon fiber suspension at a shear rate of 1.0 s^{-1}.

Figure 4.3: A 50 mm donut-shaped sample at 20 wt% carbon fiber – polypropylene prior to sample loading in a cone-and-plate rheometer (left), sample removed from rheometer at 60 strain units (middle) and the same sample shown in the rheometer prior to removal (right).

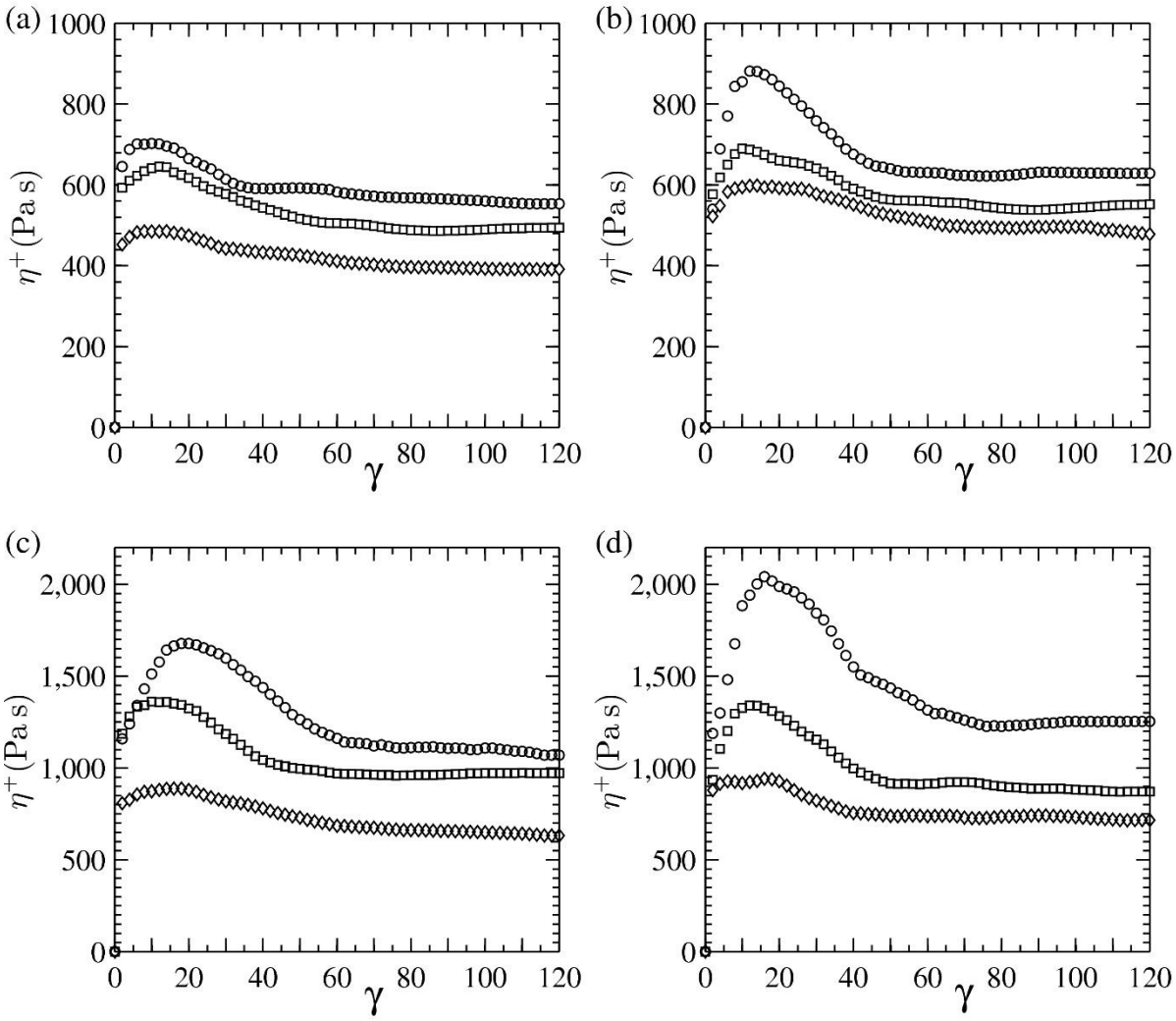

Figure 4.4: Measured transient viscosity of (a,c) glass and (b,d) carbon fiber at concentrations of (a,b) 3.8 and (c,d) 8.2 v% at shear rates of 0.4 (o), 1.0 (□) and 4.0 (◊) s^{-1}.

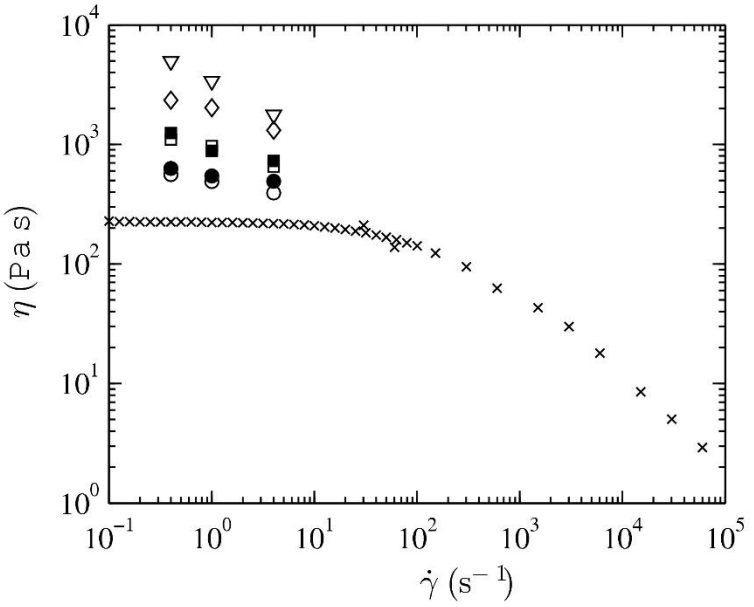

Figure 4.5: Steady shear viscosity of neat polypropylene (×) obtained from a cone-and-plate rheometer below 100 s^{-1} and a capillary rheometer above 100 s^{-1} and glass (open symbols) and carbon (filled symbols) fiber suspensions at volume concentrations of 3.8 (○), 8.2 (□),13.2 (◊) and 19.1 (▽) % from the sliding plate rheometer.

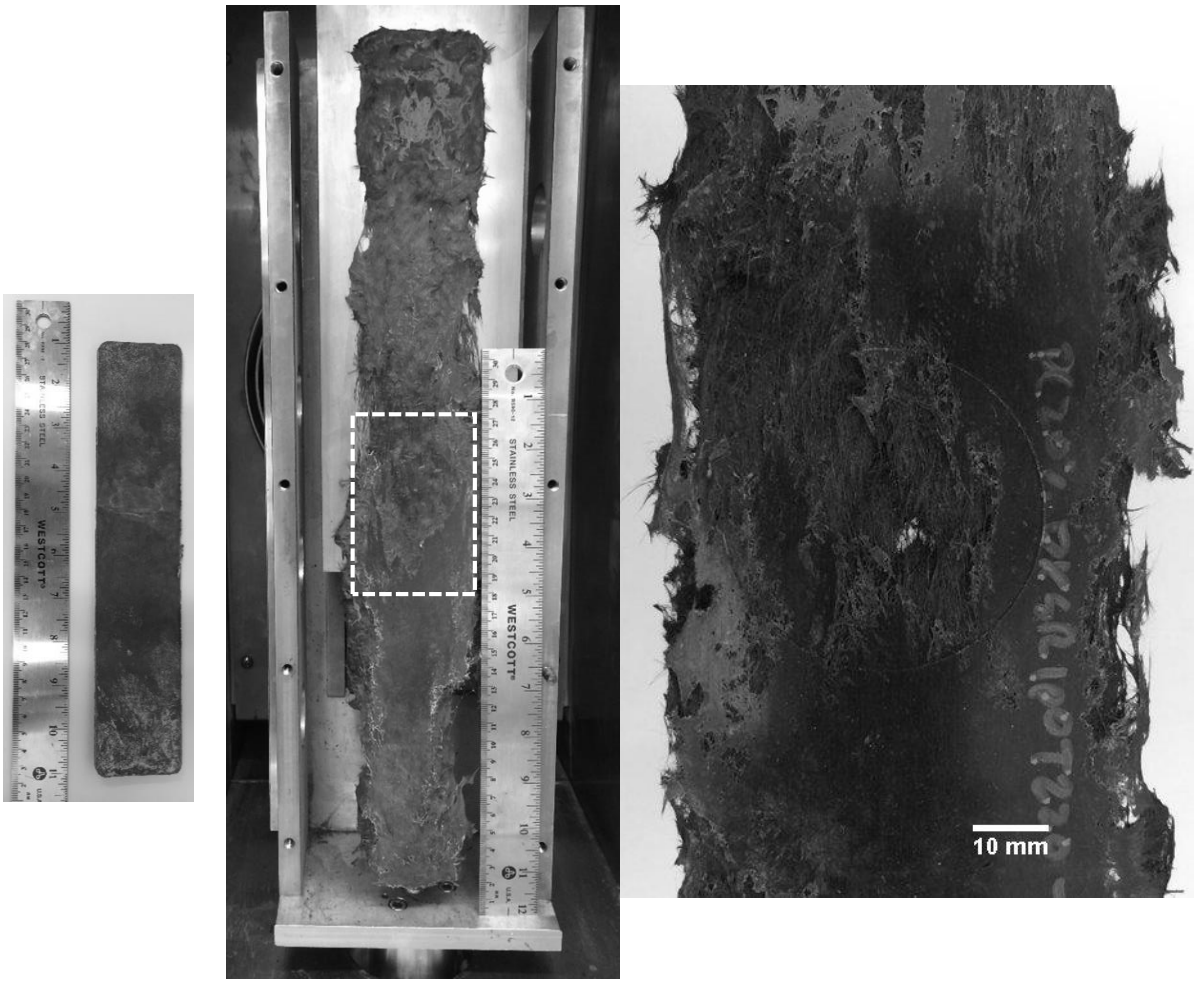

Figure 4.6: Sliding plate rheometer at a gap thickness of 3 mm using a 20 wt% carbon fiber – polypropylene sample prior to testing (left), sample after 60 strain units (middle) and close up of shear stress transducer contact area (right).

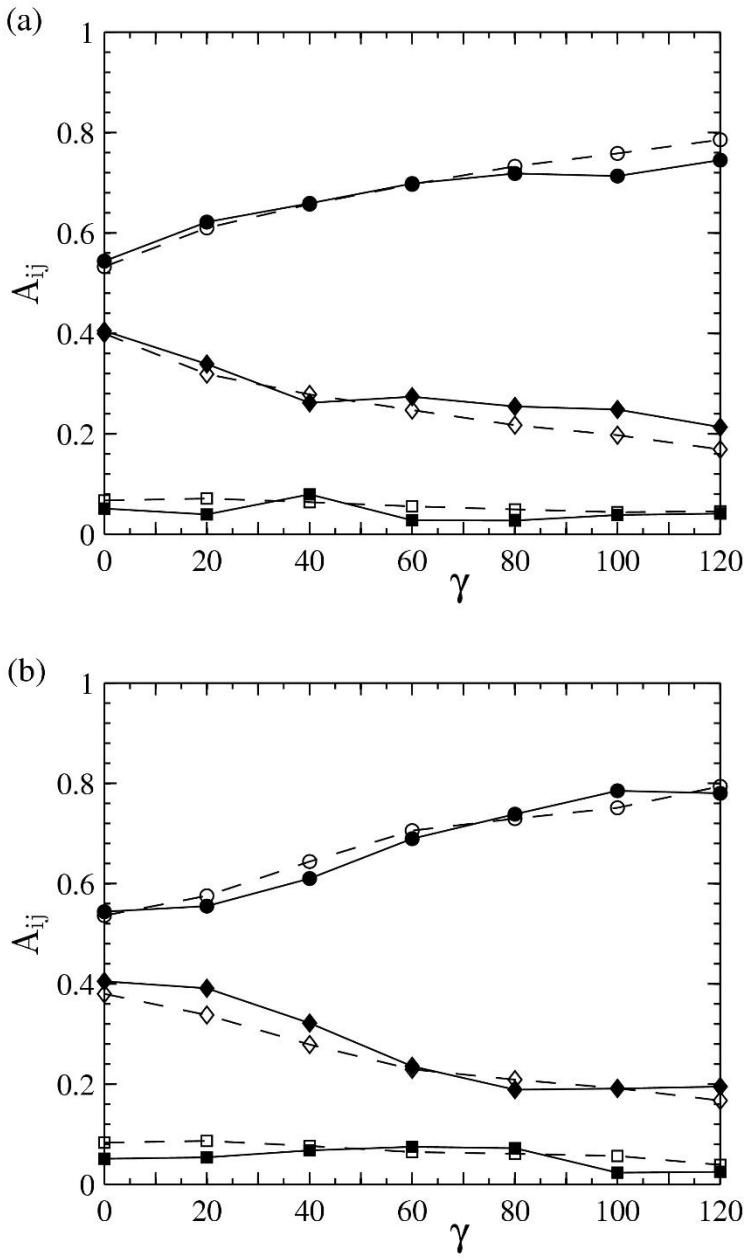

Figure 4.7: Measured fiber orientation evolution for (a) 3.8 and (b) 8.2 v% glass (open symbols) and carbon (filled symbols) fiber suspensions at a shear rate of 1.0 s^{-1}. A_{11}, A_{22} and A_{33} are denoted by ●,■ and ♦, respectively.

Table 4.1: Mechanical properties of glass and carbon fiber

	Glass Fiber	Carbon Fiber
Density (g/cm^3)	2.55	1.7 – 1.8
Tensile Modulus (GPa)	70 – 80	225 – 275
Tensile Strength (GPa)	3 – 3.5	2.4 – 3
Elongation at Break (%)	0.5-2	1.8 – 3.2

Table 4.2: Lengths and diameters of the glass and carbon fiber suspensions

	3.8 v%		8.2 v%	
	Glass	Carbon	Glass	Carbon
wt %	10	9.2	20	15.3
L_n (mm)	1.4	0.74	1.28	0.68
L_w (mm)	3.59	1.39	2.28	0.96
d (μm)	13.3	6.68	13.3	6.68
a_r (L_n/d)	105	110	97	101

Chapter 5 Obtaining Repeatable Initial Fiber Orientation for the Transient Rheology of Fiber Suspensions in Simple Shear Flow

Chapter 5 Obtaining Repeatable Initial Fiber Orientation for the Transient Rheology of Fiber Suspensions in Simple Shear Flow

Mark J. Cieslinski[1], Peter Wapperom[2], Donald G. Baird[1*]

1. Department of Chemical Engineering, Virginia Tech, VA 24061
2. Department of Mathematics, Virginia Tech, VA 24061

*Author to whom correspondence should be addressed, email: dbaird@vt.edu

5.1 Abstract

Many researchers reporting the transient rheology of fiber suspensions have not experimentally verified the initial fiber orientation. An assumption for the initial orientation is then required to simulate the fiber orientation evolution and stress response. Measurements of fiber orientation obtained prior to testing in a rheometer can confirm the homogeneity of fiber orientation throughout a sample and repeatability between multiple samples. In this work, the transient rheology of glass fiber suspensions above 0.5 mm in length was measured in a sliding plate rheometer with the initial fiber orientation generated through compression molding, flow reversal and injection molding. Measurements of shear stress and fiber orientation were obtained to evaluate each sample preparation method and to gain insight into the stress-microstructure relationship. Preshearing and applying flow reversal was used in an effort to control the initial fiber orientation for transient shear stress measurements, but fiber orientation did not change significantly, and the stress response was variable with little stress overshoot. Samples created through injection molding provided a repeatable transient stress response with measurable changes in fiber orientation. Components of the fourth order orientation tensor were also reported to compare with current theories for stress. An overshoot profile in fiber orientation was not observed during the startup of flow, and little change in orientation occurred during the flow reversal tests.

Based on experimental values of fiber orientation, a stress theory dependent on the fourth order orientation tensor was not able to reflect an overshoot in shear stress and could, at best, capture the steady state.

5.2 Introduction

Discontinuous fiber composites created through compression or injection molding develop a complex flow-induced fiber microstructure. The orientation of the fibers in the molded part allow for the mechanical properties to be greatly enhanced when compared to the suspending matrix. Simulations to predict the fiber orientation during the molding process require knowledge of fiber orientation evolution and the rheological properties of the suspension. It is then of interest to test these materials under well-defined flow conditions in a rheometer in order to better understand the relationship between stress and fiber orientation. Reliable stress and fiber orientation evolution data can then be used to further assess stress and orientation models.

The transient shear flow rheology of fiber suspensions typically has an overshoot in the shear stress and the first normal stress difference that reduces to a steady state, even when no significant transients were observed for the suspending matrix [1, 2]. Ausias et al. [3] reported the shear stress reproducibility to be ± 10% and acknowledged that one of the major issues associated with transient shear flow measurements was preparing a sample with a homogeneous and repeatable initial fiber orientation between different samples. Similarly, Sepehr et al. [2] attributed variations in the stress response to the uncertainty of the fiber orientation prior to the startup of flow.

Various approaches have been used to control the initial fiber orientation for transient rheological measurements. Fibers have been often mixed by hand in low viscosity matrices in an effort to prepare samples with random fiber orientation [4-6]. Petrich et al. [7] noted that this technique may not provide a 3D random fiber orientation everywhere within a the sample at higher fiber concentrations. In other works, compression molded disks were used in rotational rheometers

to provide an initial orientation that was mostly planar random [8-10]. Ortman et al. [10] obtained samples with different general orientation states by compression molding extruded strands of dispersed fibers. However, this sample preparation procedure may not be able to provide repeatable off-diagonal components of the fiber orientation tensor in different samples. The fiber orientation evolution would not be consistent between multiple samples because each sample would have a different initial fiber orientation. Other researchers prepared thick samples and squeezed them in the parallel disk rheometer to the desired gap thickness prior to testing [11, 12]. The authors did not confirm experimentally that this produced a fiber orientation that was random in the plane parallel to the disks. The small amount of strain that the sample experienced during squeezing may not have been enough to completely override the previous orientation state. Barbosa et al. [13] used an electric field to align semi-dilute nylon fibers, but this method may be limited to the fiber type, concentration and low viscosity matrices. The approach of Laun [1] was to use injection molded plaques of 30 wt% glass fiber in nylon 6 as the initial fiber orientation for measurements in a sliding plate rheometer. This provided a repeatable complex initial fiber orientation, but this rheometer was limited in achievable strain and fiber orientation was only assessed qualitatively.

Reversing the flow direction after reaching a steady state is another approach for producing a repeatable initial fiber orientation for transient shear flow experiments. In this way, the flow history is responsible for setting the fiber orientation for the subsequent flow reversal experiment. Flow reversal tests exhibit a shear stress overshoot that typically has a smaller magnitude and occurs at later times than the stress overshoot from the startup of flow [14, 15]. The delayed response was attributed to the evolution of fiber orientation from an aligned state caused by the startup of flow to an aligned orientation determined by the flow reversal.

A primary focus in obtaining the transient stress response is to gain insight into the fiber microstructure evolution, but few works have made direct measurements of fiber orientation in conjunction with stress measurements. The techniques used to measure fiber orientation during

flow [7, 16] and from a sample removed from the rheometer after testing [14, 17, 18] impose additional limitations. Petrich et al. [7] measured the rheology in a concentric cylinder rheometer and then obtained orientation data in a separate instrument from a set of test fibers placed in the flow between counter-rotating cylinders. The counter-rotating cylinders allowed for the fiber to change orientation during flow while remaining stationary to the observer. The authors did not include fibers that were near the cylinders in the orientation measurements, but these fibers still contributed to the measured stress response. Keshtkar et al. [16] performed flow visualization experiments in a parallel disk rheometer but the authors were only able to view fibers that were within 60 μm of the plates. Fiber orientation evolution may have been influenced by interactions with the solid boundary which might not be representative of fibers near the center of the sample. Additionally, their experimental setup only allowed for the projection of fiber orientation parallel to the plates to be measured. The out-of-plane fiber orientation component could not be measured as a result. The flow visualization measurements of Petrich et al. [7] and Keshtkar et al. [16] were performed on semi-dilute fiber suspensions in low viscosity matrices which may not be extendible to highly concentrated suspensions in polymer melts used for commercial composites. Methods used for characterizing fiber orientation in molded fiber composites can be used to measure orientation in a sample if the sample does not change shape once it is removed from the rheometer. Eberle et al. [14], Ortman et al. [17] and Cieslinski et al. [18] obtained fiber orientation from a polished cross section of a sample after it was tested in the rheometer. This method is a destructive process and requires multiple samples to have the same initial fiber orientation in order to investigate the development of fiber orientation during flow.

The purpose of this work is to provide reliable transient shear stress and fiber orientation evolution data in a well-defined shear flow to aid in the development of a stress tensor and fiber orientation model for use in orientation simulations of molded thermoplastic composites. We aim to demonstrate that a compression molding sample preparation procedure is unable to provide samples with repeatable initial fiber orientation for transient shear flow experiments. Samples

subjected to flow reversal and samples made from injection molded parts are methods proposed to provide improved repeatability in the initial fiber orientation. The shear stress growth and fiber orientation as a function of shear strain are presented under the startup and reversal of flow. The sample preparation methods are evaluated based on the repeatability of the stress response and the extent to which fiber orientation changes with strain. Finally, measured components of the fourth order fiber orientation tensor are presented to provide an assessment of a stress equation that is in the form of the model developed by Dinh and Armstrong [19].

5.3 Experimental

5.3.1 Stress Measurements

Shear stress measurements were obtained in a sliding plate rheometer based on the design of Giacomin et al. [20]. This rheometer was chosen over a rotational rheometer to overcome significant edge effects observed due to the fiber lengths and the volume fraction of fibers used in this work. Further details of the design of this particular rheometer were reported by Agarwal [21]. The rheometer was contained in a convection oven (Russells Technical Producets model RB2-340) and plate displacement controlled by an Instron-4204 universal testing instrument. A shear stress transducer was flush mounted to the stationary plate. The lever arm contacting the fluid was held in place by a diaphragm, which determines the instruments range and sensitivity. The active face of the lever arm contacts the fluid over a 10 mm diameter area. Stress measurements were determined from calibration of the diaphragm and the measured deflection of the lever arm by a capacitance probe (Capacitec model HPT-75l-V-T-2-B). A Capacitec 4100-SL-BNC amplifier and a National Instruments data acquisition module (USB-6008) were used to record the measured stress using National Instruments Labview SignalExpress software (version 2.5.1).

The amount of strain that can be imposed on a sample was dependent on the displacement of the moveable plate, gap thickness and sample dimensions. This sliding plate rheometer was

limited to a maximum plate displacement of 180 mm. A gap thickness of 1.5 mm was found to yield unbiased results within the repeatability of the stress measurements. This gap thickness also produced repeatable shear stress measurements for fiber lengths longer (L_n = 1.25 mm, L_w = 2.3 mm) [18] than what is reported here. Keshtkar et al. [22] reported that gap effects were negligible in a parallel disk rheometer for 1 mm long fibers with a gap to fiber length ratio of 2.5:2 with the stipulation that the fiber orientation is mostly planar. The projection of fiber orientation through the thickness of the sample is relatively small compared to the gap height.

The sliding plate rheometer was heated to 200 °C for 2 hours prior to sample loading. Upon sample loading the gap between the two plates was closed enough to fully contact the sample. The plates were tightened to the final gap thickness of 1.5 mm after 5 minutes. After an additional 10 minutes of heating, the sample was tested at a shear rate of 1.0 s^{-1} during the startup of flow. Forced convection was used to cool the sample to room temperature to preserve fiber orientation for further analysis. Five replicates were used to produce the reported stress results.

Additional measurements were obtained from flow reversal experiments after a sample was deformed to the desired strain during the startup of flow. The samples were allowed to rest for 60 seconds prior to flow reversal at a shear rate of 1.0 s^{-1} back toward 0 strain units. Stresses relax upon the cessation of flow within about 1 second. The 60 second rest time was used to be certain no residual stresses remained prior to the flow reversal experiments. After the flow reversal tests, fiber orientation was preserved in the sample for later measurement by allowing the samples to cool in the rheometer.

5.3.2 Sample Preparation

The fiber suspension used in this work was a 30 wt% glass fiber in a polypropylene matrix (Verton MV006S-GYLTNAT), provided by SABIC. The fiber diameter was measured to be 13.3 μm using an optical microscope. The polypropylene matrix had a zero-shear viscosity at 200 °C of 223 Pa s and does not show significant shear thinning behavior until a shear rate of 50 s^{-1} [18].

No significant transient responses were observed for the neat matrix under the startup or cessation of flow. The matrix is considered as a generalized Newtonian fluid under the test conditions presented in this work. The use of a polymer melt as the matrix avoids any concerns of fiber sedimentation due to gravity [23]. The composite materials were received as 13 mm long pellets created through a pultrusion process where a bundle of fibers are the same length as the pellet. The average fiber length was reduced to about 1 mm when from the processes used to disperse the fibers in the polypropylene matrix. Two separate processes were used to prepare samples that were tested in the sliding plate rheometer. The first method combined extrusion to disperse the fibers with compression molding to form the proper sample dimensions. The second approach was to use injection molded plaques to create a sample for the rheometer.

The first sample preparation procedure used an extruder to disperse the fibers in the polypropylene matrix prior to compression molding. The die diameter of the extruder and pelletization length of the extruded material were varied to produce two different fiber length samples which have number average fiber lengths (L_n) of 0.54 ± 0.01 and 0.90 ± 0.05 mm and weight average lengths (L_w) of 0.7 ± 0.02 and 1.5 ± 0.17 mm, respectively. The fiber diameter was measured to be 13.3 ± 0.03 μm. These samples will be referenced in this work with regard to their number average lengths. It is noted that these fiber length distributions contain fibers that are longer than what is often reported for these types of transient measurements. For the 0.54 mm fibers, a 25 mm 20 L/d extruder equipped with a gradually tapering screw and fitted with a 1.0 mm die was used to disperse the fibers in the polypropylene matrix. Three temperature zones in the extruder were set to 220, 230 245 °C and the die temperature was set to 150 °C. The composite was extruded at 20 rpm and pelletized into 8 mm long pellets and then compression molded at 180 °C to produce a sample 250 x 50 x 1.7 mm in size for use in the sliding plate rheometer. The 0.9 mm long fibers were prepared using a 1.5 mm diameter die and pelletized to 15 mm long pellets.

The second sample preparation procedure involved injection molding end-gated plaques from the as-received pellets. The injection molding process produced samples with a number (L_n)

and weight (L_w) average fiber lengths of 0.7 and 0.89 mm, respectively. The temperature profile in the injection molder (Arburg Allrounder, Model 221-55-250) was set to 190, 210, 210 and 210 °C with a mold temperature set to 80 °C. The end-gated plaque geometry has a gate that spans the entire width of the plaque region. The gate has a length of 6.33 mm and a thickness of 6.25 mm. The plaque measures 79.5 mm in length and 76 mm in width. Injection molded plaques varied in thickness from 1.58 to 1.64 mm. The gate and sprue were removed so that the plaque region could be used as a sample in the sliding plate rheometer.

Fiber length measurements in the molded parts follow the method described by Kunc et al. [24]. A section of the sample was subjected to matrix burn-off at 500 °C for 2 hours and a subset of fibers was selected by injecting a cylindrical plug of epoxy (Epon 828 resin with 55 phr Versamid 125) through the sample thickness using a syringe. Loose fibers were removed from the cured epoxy cylinder with compressed air and the subset of fibers contained in the epoxy cylinder was subjected to a secondary burn-off to remove the epoxy. Fibers were imaged using a desktop scanner at 3000 dpi resolution and counted using NIH ImageJ software. The fiber length measurements were adjusted with a weighting function to account for sampling bias that is a consequence of the sample collection procedure [24]. Fiber orientation was dependent on location in the end-gated plaque. Likewise, fiber length may also differ depending on location. Fiber length measurements were obtained at six locations in the end-gated plaque corresponding to 15, 50 and 85 % plaque length and 0 and 75 % width. The number average fiber length through the thickness of the part at the six locations was L_n = 0.70 ± 0.03 mm and the weight average was L_w = 0.89 ± 0.04 mm. The variation in length does not appear to be dependent on the different sampling locations. Some unavoidable error is incurred in creating a uniform epoxy cylinder through the sample thickness and estimating the cylinder diameter to account for sampling bias.

5.3.3 Measurements of Fiber Orientation

Orientation measurements were made by viewing fibers intersecting the x_1x_2-midplane of the sample, such that in simple shear flow the x_1-direction is the flow direction with the velocity varying in the x_2-direction. Samples were tested and allowed to cool within the rheometer to preserve the fiber orientation. Fiber orientation is represented compactly with ever-order tensors [25]. The method of ellipses was used to measure fiber orientation following the procedure developed by Vélez-García et al. [26], which is an extension the techniques of Bay and Tucker [27] and Clarke et al. [28] to measure the off-diagonal components of the second order orientation tensor unambiguously. Samples from the rheometer were cut, mounted and polished using metallographic techniques described by Vélez-García et al. [29]. The polished samples were then subjected to oxygen plasma etching to enhance the contrast between the glass fibers and polypropylene matrix. Images were obtained at 20x magnification (0.24 μm/pixel resolution) using an optical microscope (Nikon Eclipse LV100, NIS-Elements Basic Research Software, version 3.21) equipped with a motorized stage and image stitching software. It had been suggested by Hofmann et al. [30] that the image analysis width be extended in a 1-dimensional flow to account for highly aligned fibers in the flow field. An analysis region of 1.5 x 2 mm was used to capture the fiber orientation from all samples measured in this work. Fibers intersecting the imaged cross section are displayed as elliptical or rectangular objects. Based on the major and minor axes of an ellipse and the in-plane angle, a unit vector describing the orientation of each fiber can be constructed. The unambiguous fiber orientation was measured from any object that was greater than half an ellipse. Fibers parallel to the inspection plane were displayed as rectangular objects, to which their orientation was measured using the in-plane angle. This approach is valid under the assumption that fibers can be represented as rigid objects with a circular cross section. There was no evidence of fibers bending in any of the images used to measure fiber orientation for all fiber lengths and flow conditions. Approximately 500 objects were measured in the 1.5 x 2 mm image. The second and fourth order orientation tensors, $\mathbf{A}$ and $\mathbf{A}_4$, can be

reconstructed from a population of fibers and a weighting function provided by Bay and Tucker [27] to account for imaging bias imposed from the use of an inspection plane.

Fiber orientation measurements for the samples created through injection molding were obtained in the x_1x_2-midplane where the middle of the shear stress transducer contacts the sample. Select measurements taken at the outer rim of the transducer contact area did not deviate by greater than the measurement error. The measurement and averaging techniques of Vélez-García et al. [26] were used to calculate the fiber orientation through the sample thickness. Error estimates follow the work of Bay and Tucker [27] assuming a measurement error of 5 pixels in fitting ellipses to fibers in the digital micrograph. The 95% confidence interval of the measurement error is reported in the orientation figures and is greater than the sampling error due to the large number of objects measured in the 1.5 x 2 mm sampling area. The sample is divided into 15 bins through the thickness, but the profile of fiber orientation is largely unchanged if, for example, 11 or 19 bins are used. Partial ellipses and rectangles had some influence on the orientation averages using 15 bins. When partial objects were not included, A_{11} was under predicted by about 0.04, and negating rectangular objects had about the same effect. Although, not all bins contained rectangular objects. This influence might be more significant if more bins were used or fewer fibers per bin were measured. For the average orientation over the entire 1.5 x 2 mm sampling area (1 bin through the thickness), the value of A_{11} was under represented by about 0.07 when partial ellipses and rectangles were not included.

5.4 Results and Discussion

5.4.1 Compression Molded Samples: Startup of Flow

The measured stress response from the compression molded samples subjected to a shear rate of 1.0 s^{-1} for 120 strain units is provided in Figure 5.1. Both the 0.54 and 0.9 mm fiber lengths have a stress growth overshoot that reduces to a steady state value within the strain limitations of the sliding plate rheometer. As the fiber length increases, it appears that the magnitude and breadth

of the overshoot also increases. Sample variability also seems to increase with the increase in fiber length.

The stress profiles in Figure 5.1 should be regarded as an indirect measurement of the underlying fiber microstructure. To test the homogeneity in fiber orientation throughout the sample, fiber orientation was measured at four sampling locations along the x_1x_2-midplane. Each measurement was separated by at least 13 mm, such that each average could be considered independent of the other sampling locations. An orientation tensor was measured for each of the four locations. The fiber orientation components, A_{11}, A_{12} and A_{22}, are of most interest for simple shear flow in the x_1x_2-plane

The A_{11} and A_{22} components of orientation are shown in Figure 5.2 for fiber lengths of 0.54 and 0.9 mm. The small value of A_{22} indicates that the orientation of these fibers is mostly in the x_1x_3-plane. Any trends in A_{22} are difficult to observe because the fibers, on average, maintain a mostly planar orientation throughout the test. The general trend of A_{11} begins at a value of approximately 0.5 and evolves to a steady state aligned orientation. The values of A_{11} from the four sampling locations at zero strain units were close in value near 0.5. This appears to be the case for both fiber lengths, and it may be a reasonable assumption that most of the sample contains values of A_{11} near 0.5. However, at small strains for the 0.9 mm material, there was a large variation between the four sampling locations. This dissimilarity may be a result of creating samples by compression molding which did not allow for the off-diagonal components of orientation, i.e. A_{12}, to be controlled.

The measured values of the A_{12} component of orientation corresponding to the data in Figure 5.2 is provided in Figure 5.3. The A_{12} orientation at zero strain could have either a positive or negative value depending on the sampling location. After the sample is subjected to small strains, the general trend of A_{12} is to become positive. There is large variability in the values of A_{12} obtained at the separate sampling locations that decreases slightly at larger strains. It appears

that the local orientation can retain a negative value for A_{12} until at least 80 strain units. With the variability in orientation throughout the sample, a length dependency cannot be concluded for the A_{12} component of orientation using samples prepared by compression molding.

A schematic is provided in Figure 5.4 showing the influence of a positive or negative value for A_{12} on the orientation evolution of a fiber. When the initial value of A_{12} is positive, the fiber will continue to align in the flow direction, while a negative initial value will result in a fiber that must flip to become oriented in the flow direction. It should be recognized that the extent of fiber orientation in the x_2-direction is small and the fiber also has orientation in the x_3-direction. In reference to Figure 5.2(b), the negative value of A_{12} in the initial orientation can explain the small values of A_{11} at 10 strain units. A slight decrease in A_{11} was also observed in some of the average orientation data reported by Ortman et al. [17] for longer fibers than what is reported here. It appears that this issue may be more easily observed in longer fibers due to a slower rate of fiber orientation. Reporting an average of the four imaging locations may produce a poor representation of the fiber orientation evolution. It would be expected that a fiber with a negative A_{12} initial orientation would take longer to align with the flow direction than an equivalent fiber with a positive A_{12} initial orientation.

Stress measurements obtained during the startup of flow had repeatability of about ±10 %, but the fiber orientation measurements have much more variability. This is likely due to the localized measurements of orientation in comparison to stress. The shear stress transducer in this sliding plate rheometer measures stress locally over a 10 mm diameter contact area. In contrast, fiber orientation measurements were obtained from a 1.5 x 2 mm cross section in the x_1x_2-midplane. This sampling region produces a digital micrograph about 300 MB in size. Increasing the imaging region by several factors results in large file sizes and a significant increase in the time required to measure the fiber orientation. At this time, it is impractical to measure the orientation over the entire region that is in contact with the shear stress transducer using the method of ellipses.

The issue of the unspecified A_{12} component of orientation still remains despite the details of the fiber orientation measurement methods.

5.4.2 Compression Molded Samples: Flow Reversal

The premise of the flow reversal test is to remove the effects of the initial orientation created through compression molding and use the steady state orientation generated from the startup of flow as the initial orientation for flow in the opposite direction. This would allow flow reversal tests to be independent of the procedure used to create a sample before loading it into the rheometer. The population of fibers will have a positive A_{12} from the startup of flow and when flow is reversed (negative shear rate), fibers should follow the path similar to that of the negative A_{12} in Figure 5.4. It is expected that fibers will eventually flip in the x_1x_2-plane and produce a stress overshoot.

The flow reversal stress responses are shown in Figure 5.5 for fiber lengths of 0.54 and 0.9 mm. The data from the startup of flow is also shown for comparison. Stresses measured during flow reversal present a significant amount of error for both fiber lengths. For the shorter fiber system, a gradual stress increase is observed between 120 to 100 strain units. The stress overshoot has a smaller magnitude than what is observed during the startup of flow, which supports the previous observations of Sepehr et al. [2]. The steady state stress measured during flow reversal is similar to the steady state from the startup of flow.

For the longer fibers, stress increases during flow reversal from the steady state reached during the startup of flow to a much greater magnitude than the startup stress overshoot. A very broad overshoot is observed and stresses drop between 20 to 0 strain units, but do not recover a steady state value within the strain limitations of the rheometer. Additionally, the large variability in shear stress centered around 40 strain units makes it difficult to assess the true shape of the stress response.

The influence of the gap between the sliding plates was investigated up to a 3 mm sample thickness to check if this caused poor repeatability in the stress measurements of the 0.9 mm fibers. The displacement was limited in the sliding plate rheometer such that only 60 strain units could be applied on the 3 mm thick sample. A large variability still occurs under flow reversal at larger gap thicknesses to the point that it is difficult to determine if there is a gap influence under flow reversal for this fiber length.

The effect of material entering the gap between the active face of the shear stress transducer and the stationary plate was another concern for causing the poor repeatability in the flow reversal stress response of the 0.9 mm material. Measurements of orientation obtained at the edge of the active face did not support the theory of material entering the gap when the rheometer was in operation. Additionally, samples were subjected to forward and reversal flows for three repetitions. The stress responses proved to not be reliable with each succession, but the amount of material entering the gap also did not noticeably change when compared to the startup of flow or flow reversal experiments. It appears that the material caught between the active face of the transducer and stationary plate was a result of the slight squeezing flow imposed during sample loading.

Fiber orientation measurements from four sampling locations in the x_1x_2-midplane for the samples subjected to flow reversal are shown in Figure 5.6. The data for the 0.54 mm fibers shows little variation between four sampling locations and averages a nearly constant fiber orientation over 120 strain units. The 0.9 mm fibers have a slight decrease in orientation in the x_1-direction from the value at 120 strain units. The minimal change in orientation did not reflect the pronounced stress transient. At 40 strain units the orientation is more variable throughout the sample, which corresponds to the larger variability in the stress measurements. For both fiber lengths, A_{22} also remains a constant small value, which indicates that the fibers remain mostly in the x_1x_3-plane.

Upon sample removal from the sliding plate rheometer, the 0.9 mm fiber system appears to deform in the neutral (x_3) direction during the flow reversal test. The material furthest from the x_1x_2-midplane contains a large number of voids. The distance between the voids and the x_1x_2-midplane decreases with increasing reversal strain. Additionally, the edges of the sample in the x_1x_2-plane become more irregular with increasing strain. A completed flow reversal test will typically have voids that are about 10 mm away from the x_1x_2-midplane. The voids may not directly affect the area in contact by the shear stress transducer but it is unclear how this impacts the fiber microstructure. It appears that air may be brought into the sample by the complex flow behavior of edge effects at the fluid-air interface at the sample edges in the x_1x_2-plane. Due to the complexity of this system, it is difficult to define this unexpected deformation as a secondary flow. However, secondary flows have been reported in simple shear flow within a sliding plate rheometer for viscoelastic fluids and were attributed to a normal stress difference in the x_1- and x_3-directions [31-34]. In the case of the fiber suspensions, the polypropylene matrix alone was likely not the cause of this unforeseen flow. Normal stress are present in fiber filled systems, although they cannot be measured with this particular sliding plate rheometer. The fiber orientation in Figure 5.6 shows that the value of A_{11} and A_{33} differ by about a factor of four. Coupling this with current stress theories (such as Lipscomb et al. [35] or Shaqfeh and Fredrickson [36]) which scale the fiber contribution to stress with the square of the fiber aspect ratio $\left(a_r^2\right)$, the normal stress differences may be significant enough to cause this unexpected flow. Yet, it cannot be discounted that this behavior may be the result of fiber-fiber interactions which increase with fiber length [37]. Occasional edge anomalies were observed in the 0.54 mm samples, but these appear isolated to the edge of the sample and the general rectangular shape of the sample was retained.

5.4.3 Injection Molded Samples: Startup of Flow

Injection molded end-gated plaques were used to create samples for the sliding plate rheometer with a repeatable initial orientation that will show greater changes in fiber orientation

when compared to the fiber orientation from flow reversal. Thomasset et al. [12] used injection molded parts in a parallel disk rheometer, but their approach was to squeeze the sample to half its original thickness in order to create a random in-plane orientation. A film-gated plaque was used by Laun [1] in a sliding plate rheometer, but the rheometer design was limited to 8 strain units which could not capture the typical stress overshoot and steady state response associated with fiber suspensions.

The injection molding process provides a repeatable flow history that will yield fiber orientation that is consistent among different samples. In addition, the voids within the sample are reduced due to the higher molding pressures. The molding process produces a complex fiber orientation that varies throughout the plaque. Based on the dimensions of our mold, three plaques must be used in order to create a sample that is similar in length to the compression molded samples. The sprue and gate region are removed from the sample prior to loading the plaques in the rheometer. Slight squeezing of the sample from about 1.6 to 1.5 mm limits voids from forming at the weld lines between the different plaques. This slight squeezing does not appear to noticeably influence the fiber orientation. The fiber orientation and the sample loading procedure can be simplified in the future using larger plaques or samples created through sheet extrusion.

The layout of the three plaques tested in the sliding plate rheometer is shown in Figure 5.7, where the arrow and radial front indicate the primary flow direction of fluid filling the end-gated plaque during the molding process. Two locations in the plaque were used to provide different initial fiber orientations for testing in the sliding plate rheometer. These locations correspond to 0 and 50 % plaque width at 50 % plaque length. The plaques were also cut lengthwise for the 50 % plaque width location and reassembled in the rheometer so that an equal amount of material was on either side of the shear stress transducer. Measuring stress at greater plaque widths resulted in poor repeatability. The 0 and 50 % plaque width locations will be referred to with regards to the fiber orientation through the sample thickness as non-uniform and uniform initial orientations, respectively.

The trace components of orientation for the non-uniform and uniform initial orientations obtained at zero strain for the samples prepared through injection molding are shown in Figure 5.8. Orientation is represented as a function of normalized gap thickness in the sliding plate rheometer, where 0 indicates the stationary plate encompassing the shear stress transducer and 1 corresponds to the movable plate. The non-uniform fiber orientation has the common shell-core-shell profile associated with injection molded composites. A slight asymmetric profile through the thickness is a result of the flow entering the plaque region from the gate during injection molding. The orientation is largely in the x_1x_3-plane, but the degree of orientation in the x_1-direction varies through the thickness. A high degree of orientation in the x_1-direction is present near the walls while the primary fiber orientation in the core is in the x_3-direction. The uniform initial fiber orientation is much more consistent through the thickness with a less defined core region. The uniform initial orientation also has a higher degree of fiber alignment in the x_1-direction than the non-uniform case.

The stress response measured for the non-uniform initial orientation during the startup of flow exhibits a broadened profile with improved sample repeatability [Figure 5.9(a)]. The broadening of the stress response may be a result of the more complex initial fiber orientation. A steady state is observed from 70 to 100 strain units and is in good agreement amongst all 5 tested samples. Above 100 strain units the stress drops significantly which is a result of either voids or the smaller sample length.

The stress obtained under the startup of flow using the uniform initial orientation is shown in Figure 5.9(b). A more defined stress overshoot is observed which reduces to a steady state value at lower strains than the non-uniform initial orientation data. The steady state stresses are in good agreement between both initial orientations created through injection molding. Sample variability is greater with the uniform initial orientation than the non-uniform case until about 80 strain units where voids seem to significantly influence the stress response. Upon sample removal, it is clear that voids trail from the shear stress transducer in the direction of flow, as shown by Figure 5.10.

To our knowledge, the formation of voids at the shear stress transducer has not been reported. These voids can penetrate up to about one third the sample thickness. Because of the sample variability created through compression molding, it is unclear if void formation also occurred in these samples. Ortman et al. [10] also reported a drop in stresses at high strains for glass fiber suspensions. We postulate that these voids form as a result of the gap at the active face of the shear stress transducer where the no slip boundary condition is interrupted. The inextensible fiber will cause some flow of the matrix around the fiber [1] which would lead to deviations from simple shear flow at the air-fluid boundary. This irregular flow may then allow for air to be entrapped by the polymer matrix. Further investigation is required to confirm this proposed mechanism of void formation.

The average orientation obtained at the shear stress transducer through the sample thickness for the samples prepared by injection molding is shown as a function of shear strain in Figure 5.11. For the non-uniform initial orientation, fibers gradually align in the flow direction over 100 strain units. The gradual change in fiber orientation for the non-uniform initial orientation corresponds well with the stress response that exhibits a broad overshoot before reaching a steady value near 70 strain units. This shows that shear stress might be somewhat insensitive to small changes in fiber orientation. The uniform initial fiber orientation has high value for A_{11} at zero strain that decreases in value at 20 strain units before increasing to a steady state value at 40 strain units. A slight increase in fiber orientation in the thickness direction for the uniform initial orientation is difficult to conclude at 20 strain units, but an increase in A_{22} could help explain the more pronounced stress overshoot. The constant orientation starting at 40 strain units corresponds well to the stress measurements that exhibit a steady state beginning at 50 strain units.

The detailed fiber orientation through the sample thickness is lost in Figure 5.11. Select A_{11} fiber orientation distributions through the sample thickness are shown in Figure 5.12 for shear strains of 20, 60 and 100. The non-uniform initial orientation shows that the shell-core-shell profile is largely unchanged at 20 strain units when compared to the initial orientation in Figure

5.8(a). At 60 strain units this profile diminishes with the most significant change in orientation occurring in the core. Upon shearing to 100 strain units, fiber orientation is mostly constant through the thickness, perhaps indicating a steady state fiber orientation. The uniform initial fiber orientation is less defined by shell and core regions. At 20 strain units, there is some core region, but a majority of through-thickness values are less than the initial orientation in Figure 5.8(b). A flat orientation profile is observed at 60 strain units which is largely unchanged at 100 strain units. The variability in the values of A_{11} through the thickness at 100 strain units is thought to be a product of the voids forming at the shear stress transducer. The presence of voids reduces the number of fibers that were measured at a location through the sample thickness.

5.4.4 Injection Molded Samples: Flow Reversal

The samples prepared by injection molding used in the previous section were subjected to flow reversal tests to examine if the flow reversal results were unique to the compression molding sample preparation procedure. The development of voids at high strains and high degrees of fiber alignment limited the startup strain that could be subjected to each sample. A net deformation of 100 strain units was used with the non-uniform initial orientation while the earlier development of voids for the uniform initial orientation limited the total deformation to 80 strain units.

A comparison between the flow reversal stress responses for the compression molded samples and injection molded samples is summarized in Figure 5.13, where the stress is plotted as a function of strain in the reversal tests. The injection molded samples both yield a similar stress response with a small overshoot that then decreases gradually. A steady state value for stress is not well-defined, which is likely a result of the variability in the stress response between multiple samples. The standard deviation of these samples is about ±10 % up to about 60 reversal strain units where the variability increases to about 15 %. These results are similar to the 0.54 mm fiber data and reaffirm the results presented earlier for the flow reversal tests.

5.4.5 Off-Diagonal Fiber Orientation Components

As mentioned previously, the initial value of the A_{12} component of fiber orientation is most significant in determining the fiber orientation evolution. Additionally, theories for stress consider the fourth moment of orientation:

$$\boldsymbol{\sigma} = -P\mathbf{I} + 2\eta_m\mathbf{D} + 2\eta_m\phi_v(\mu_1\mathbf{D} + \mu_2\mathbf{D} : \mathbf{A}_4) \tag{5.1}$$

where P is the isotropic pressure, η_m is the matrix viscosity, $\mathbf{D} = \frac{1}{2}(\nabla\mathbf{v}^t + \nabla\mathbf{v})$ is the rate of deformation tensor, ϕ_v is the fiber volume fraction, and μ_1 and μ_2 are material constants that are typically a function of fiber aspect ratio (a_r = length/diameter) and volume fraction [19, 35, 36]. For concentrated fiber suspensions ($\phi_v \geq a_r^{-1}$), the material constants have been fit to experimental data [2, 38]. The A_{1212} component contributes to shear stress while A_{1211}, A_{1222} and A_{1233} are responsible for normal stresses in simple shear flow. The magnitudes of A_{1222} and A_{1233} are measured to be below 0.005, which predicts the second normal stress difference to be small. The A_{1211} component parallels A_{12} and would be the most significant contribution to the first normal stress difference because A_{1222} is relatively small in comparison. Petrich et al. [7] also observed A_{1211} to be the most significant component of orientation compared to A_{1222} and A_{1233} in shear flow.

The A_{12}, A_{1211} and A_{1212} components of fiber orientation are presented in Figure 5.14 for the compression molded samples subjected to flow reversal. The A_{12} component of orientation changes from a positive to negative value as expected. However, for both fiber lengths, a higher magnitude of A_{12} is achieved after 120 strain units of startup flow than for 120 strain units of flow reversal. A_{1211} parallels this trend. This may indicate that not all the fibers changed orientation during the flow reversal. The transition of A_{12} and A_{1211} from positive to negative is less smooth for the 0.90 mm fibers than the 0.54 mm fibers, which is to be expected based on stress response and the issues of secondary flow. The value of A_{1212} is mostly constant over the entire range of

strain. The 0.54 mm sample did not provide a significant stress overshoot in flow reversal and the A_{1212} orientation reflects this stress response. Similarly, the 0.9 mm fibers also do not show a significant change in A_{1212} orientation under flow reversal, which does not correspond to the measured stress response.

Changes in A_{12}, A_{1211} and A_{1212} as a function of strain during the startup of flow for samples prepared through injection molding are provided in Figure 5.15. For the non-uniform initial orientation, the values of A_{12} and A_{1211} begin at a negative value and quickly increases to a positive value, settling at a steady value near 0.02. The uniform initial orientation samples also reach a value near 0.02 at large strains, but the transition to the steady value takes at least 40 strain units. The values of A_{12} and A_{1211} at 40 strain units are consistent between both measured samples. It appears that the transition to an aligned orientation is more complex for the uniform initial orientation which may correspond to the more pronounced shear stress response. However, the value of A_{1212} gradually increases as a function of strain and does not exhibit an overshoot. The non-uniform initial orientation also does not show a pronounced overshoot in A_{1212}.

In both Figures 5.14 and 5.15, the A_{1212} component of orientation does not have an overshoot profile. As a result, stress predictions from experimental A_{1212} values will also not have the overshoot profile. The best stress predictions based on the experimental fiber orientation would be obtained if the values of μ_1 and μ_2 are fit to steady state in shear stress. For the semi-dilute theories of Dinh and Armstrong [19] and Shaqfeh and Fredrickson [36], the value of μ_1 is zero while the expressions for μ_2 will under predict the stress in fiber suspensions with $a_r\phi_v > 20/\pi$ [39]. Following the same general form of the stress equation, the value of μ_1 is set to zero, while μ_2 is fit to the steady state in shear stress. For fiber lengths 0.54, 0.7 and 0.9 mm, the value of μ_2 is found to be 840, 1150 and 995, respectively. The value of μ_2 for the longest fiber length is lower than expected relative to the other fiber lengths, which is likely a result of the poor stress

repeatability. Additionally, changes in A_{1212} can cause μ_2 to change significantly because any change in A_{1212} is relatively large compared to its magnitude.

5.5 Conclusions

Samples generated by compression molding did not exhibit repeatable orientation evolution data during the startup of simple shear flow in a sliding plate rheometer. The compression molding preparation method was unable to produce samples with controlled and repeatable initial values of the A_{12} component of orientation even though the trace components of the orientation tensor were in good agreement between different sampling locations in the sliding plate rheometer. A correlation between the transient stress response and measured fiber orientation evolution could not be concluded due the variability of the initial fiber orientation. The influence of the initial orientation was removed at high strains which was evident in a steady state for the shear stress and the trace components of the orientation tensor.

Performing flow reversal tests on the compression molded samples after they reached a steady state in the startup of flow was proposed as a way to define the initial fiber orientation for the transient shear stress and fiber orientation measurements. Repeatability in the shear stress responses did not improve during flow reversal compared to the stresses for the compression molded samples subjected to the startup of flow. The shear stress overshoot during flow reversal was typically small compared to the overshoot measured in the startup of flow. In addition, only small changes in fiber orientation were observed. The relationship between stress and fiber orientation is difficult to conclude under flow reversal due to small changes in the shear stress and orientation as a function of shear strain.

Samples created from injection molded end-gated plaques provided improved repeatability in shear stress and orientation measurements during the startup of flow when compared to compression molded samples subjected to the startup of flow or flow reversal. Good agreement was also observed in the steady state for shear stress and fiber orientation for samples with different

initial orientations. Similar stress responses were obtained under flow reversal for the samples prepared through injection molding and the compression molded samples with an average fiber length of 0.54 mm.

The fourth order components of the orientation tensor that contribute to shear and normal stresses were also measured. It was observed that the values of A_{1211} parallel A_{12}, while A_{1212} did not show a distinct overshoot that was reflective of the measured shear stress response. A stress theory dependent on the fourth order orientation tensor alone was only able to capture the steady state in shear stress. Additional contributions to the stress equation must be determined and developed in order to capture the shear stress overshoot. Although this rheometer was not capable of measuring normal stresses, the A_{1211} component of orientation changed with shear strain which suggests that normal stresses may be a better measurement of the fiber microstructure than shear stresses.

Lastly, some unexpected flow behavior occurred in the experiments which will require further investigation. Under flow reversal, the samples with a number average fiber length of 0.9 mm would deform in the neutral (x_3) direction. Fiber-fiber interactions or normal stress differences are two potential explanations for this unforeseen behavior. In the injection molded parts with a fiber length L_n = 0.7 mm, voids were observed to originate at the shear stress transducer where the no slip boundary condition is interrupted. The undesired flow behavior appears to be specific to the aforementioned experimental conditions and should not detract from the primary conclusions of this paper.

5.6 Acknowledgements

The authors wish to thank the American Chemistry Council for financially supporting this work. Additional acknowledgement is given to the Material Science and Engineering Department at Virginia Tech for use of their polishing facilities and Prof. Michael Ellis for access to the

microscope used for orientation measurements. We also thank Kevin Herrington and Rebecca Minnick for help in polishing samples.

5.7 References

[1] Laun HM. Orientation effects and rheology of short glass fiber-reinforced thermoplastics. Colloid Polym Sci. 1984;262:257-69.

[2] Sepehr M, Ausias G, Carreau PJ. Rheological properties of short fiber filled polypropylene in transient shear flow. J Non-Newton Fluid Mech. 2004;123:19-32.

[3] Ausias G, Agassant JF, Vincent M, Lafleur PG, Lavoie PA, Carreau PJ. Rheology of short glass fiber reinforced polypropylene. J Rheol. 1992;36:525-42.

[4] Sepehr M, Carreau PJ, Grmela M, Ausias G, Lafleur PG. Comparison of rheological properties of fiber suspensions with model predictions. J Polym Eng. 2004;24:579-610.

[5] Marín-Santibáñez BM, Pérez-González J, Vargas L. Shear rheometry and visualization of glass fiber suspensions. Rheol Acta. 2009;49:177-89.

[6] Bibbo MA. Rheology of Semiconcentrated Fiber Suspensions. PhD Thesis: Massachusetts Institute of Technology; 1987.

[7] Petrich MP, Koch DL, Cohen C. An exerimental determination of the stress-microstructure relationship in semi-concentrated fiber suspensions. J Non-Newton Fluid Mech. 2000;95:101-33.

[8] Mobuchon C, Carreau PJ, Heuzey M-C, Sepehr M, Ausias G. Shear and extensional properties of short glass fiber reinforced polypropylene. Polym Compos. 2005;26:247-64.

[9] Eberle APR, Baird DG, Wapperom P, Vélez-García GM. Obtaining reliable transient rheological data on concentrated short fiber suspensions using a rotational rheometer. J Rheol. 2009;53:1049-68.

[10] Ortman KC, Agarwal N, Eberle APR, Baird DG, Wapperom P, Jeffrey Giacomin A. Transient shear flow behavior of concentrated long glass fiber suspensions in a sliding plate rheometer. J Non-Newton Fluid Mech. 2011;166:884-95.

[11] Djalili-Moghaddam M, Toll S. A model for short-range interactions in fibre suspensions. J Non-Newton Fluid Mech. 2005;132:73-83.

[12] Thomasset J, Carreau PJ, Sanschagrin B, Ausias G. Rheological properties of long glass fiber filled polypropylene. J Non-Newton Fluid Mech. 2005;125:25-34.

[13] Barbosa SE, Ercoli DR, Bibbo MA, Kenny JM. Rheology of short-fiber composites: a systematic approach. Compos Struct. 1994;27:83-91.

[14] Eberle APR, Baird DG, Wapperom P, Vélez-García GM. Using transient shear rheology to determine material parameters in fiber suspension theory. J Rheol. 2009;53:685-705.

[15] Sepehr M, Carreau PJ, Moan M, Ausias G. Rheological properties of short fiber model suspensions. J Rheol. 2004;48:1023-48.

[16] Keshtkar M, Heuzey MC, Carreau PJ, Rajabian M, Dubois C. Rheological properties and microstructural evolution of semi-flexible fiber suspensions under shear flow. J Rheol. 2010;54:197-222.

[17] Ortman K, Baird D, Wapperom P, Whittington A. Using startup of steady shear flow in a sliding plate rheometer to determine material parameters for the purpose of predicting long fiber orientation. J Rheol. 2012;56:955-81.

[18] Cieslinski MJ, Wapperom P, Baird DG. Influence of fiber concentration on the startup of shear flow behavior of long fiber suspensions. J Non-Newton Fluid Mech. 2015;222:165-70.

[19] Dinh SM, Armstrong RC. A rheological equation of state for semiconcentrated fiber suspensions. J Rheol. 1984;28:207-27.
[20] Giacomin AJ, Samurkas T, Dealy JM. A novel sliding plate rheometer for molten plastics. Polym Eng Sci. 1989;29:499-504.
[21] Agarwal N. Transient Shear Flow Rheology of Concentrated Long Glass Fiber Suspensions in a Sliding Plate Rheometer. Master's Thesis: Virginia Polytechnic Institute and State University; 2009.
[22] Keshtkar M, Heuzey MC, Carreau PJ. Rheological behavior of fiber-filled model suspensions: effect of fiber flexibility. J Rheol. 2009;53:631-50.
[23] Chaouche M, Koch DL. Rheology of non-Brownian rigid fiber suspensions with adhesive contacts. J Rheol. 2001;45:369-82.
[24] Kunc V, Frame BJ, Nguyen BN, Tucker CL, Vélez-García GM. Fiber length distribution measurement for long glass and carbon fiber reinforced injection molded thermoplastics. Society of Plastics Engineers Automotive Composites Conference & Exhibition. Troy, Michigan. 2007.
[25] Advani SG, Tucker CL. The use of tensors to describe and predict fiber orientations in short fiber composites. J Rheol. 1987;31:751-84.
[26] Vélez-García GM, Wapperom P, Baird DG, Aning AO, Kunc V. Unambiguous orientation in short fiber composites over small sampling area in a center-gated disk. Composites Part A. 2012;43:104-13.
[27] Bay RS, Tucker CL. Stereological measurement and error estimates for three-dimensional fiber orientation. Polym Eng Sci. 1992;32:240-53.
[28] Clarke AR, Davidson NC, Arhenhold G. Mesostructural characterization of aligned fibre composites. In: Papathanasious TD, Guell DC, editors. Flow-induced alignment in composite materials. Cambridge: Woodhead Publishing Limited; 1997. 230-92.
[29] Vélez-García GM, Wapperom P, Kunc V, Baird DG, Zink-Sharp A. Sample preparation and image acquisition using optical-reflective microscopy in the measurement of fiber orientation in thermoplastic composites. J Microsc. 2012;248:23-33.
[30] Hofmann JT, Vélez-García GM, Baird DG, Whittington AR. Application and evaluation of the method of ellipses for measuring the orientation of long, semi-flexible fibers. Polym Compos. 2013;34:390-8.
[31] Koran F. Anomalous wall slip behavior of linear low density polyethylenes. Master's Thesis: McGill University; 1994.
[32] Mhetar VR, Archer LA. Secondary flow of entangled polymer fluids in plane Couette shear. J Rheol. 1996;40:549-71.
[33] Dhori PK, Giacomin AJ, Slattery JC. Common line motion II: sliding plate rheometry. J Non-Newton Fluid Mech. 1997;71:215-29.
[34] Reimers MJ, Dealy JM. Sliding plate rheometer studies of concentrated polystyrene solutions: Large amplitude oscillatory shear of a very high molecular weight polymer in diethyl phthalate. J Rheol. 1996;40:167-86.
[35] Lipscomb GG, Denn MM, Hur DU, Boger DV. The flow of fiber suspensions in complex geometries. J Non-Newton Fluid Mech. 1988;26:297-325.
[36] Shaqfeh ESG, Fredrickson GH. The hydrodynamic stress in a suspension of rods. Phys Fluids A. 1990;2:7-24.
[37] Toll S. Packing mechanics of fiber reinforcements. Polym Eng Sci. 1998;38:1337-50.
[38] Mazahir SM, Vélez-García GM, Wapperom P, Baird D. Fiber orientation in the frontal region of a center-gated disk: Experiments and simulation. J Non-Newton Fluid Mech. 2015;216:31-44.
[39] Mackaplow MB, Shaqfeh ESG. A numerical study of the rheological properties of suspension of rigid, non-brownian fibres. J Fluid Mech. 1996;329:155-86.

5.8 Figures

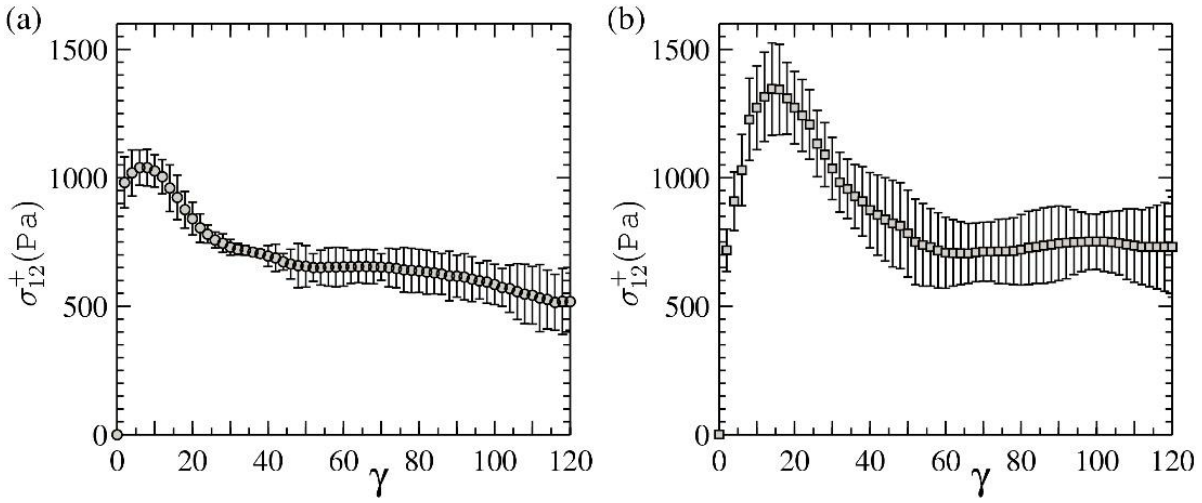

Figure 5.1: Transient shear stress response during the startup of flow for compression molded samples at fiber lengths (a) L_n = 0.54 and (b) 0.9 mm. Error bars denote the standard deviation of five samples.

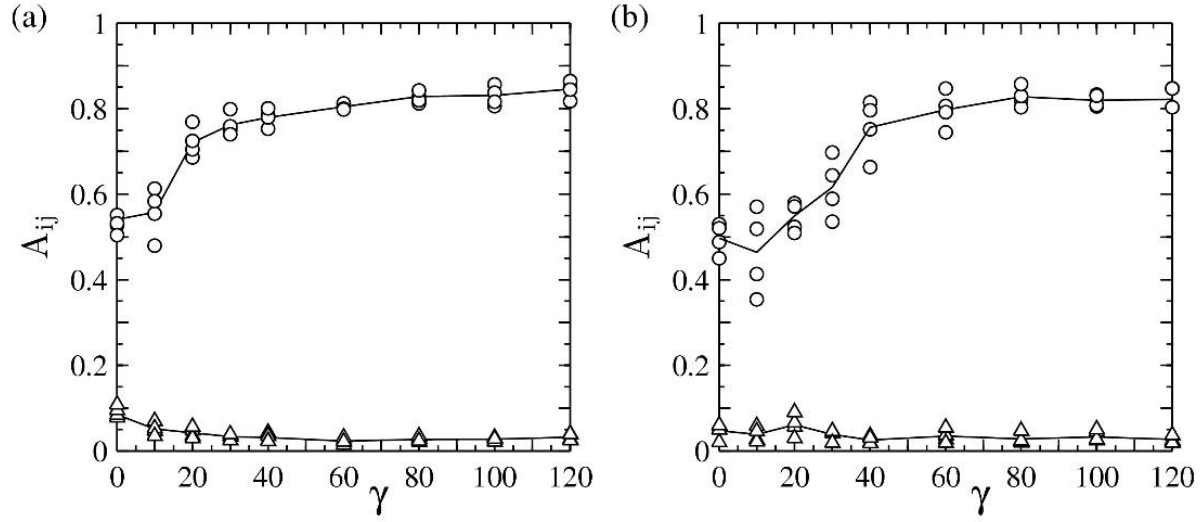

Figure 5.2: Fiber orientation from four sampling locations in the compression molded samples as a function of shear strain for fiber lengths (a) L_n = 0.5 and (b) 0.9 mm. A_{11} and A_{22} are designated by ○ and Δ, respectively. The line represents the average of all measured fibers.

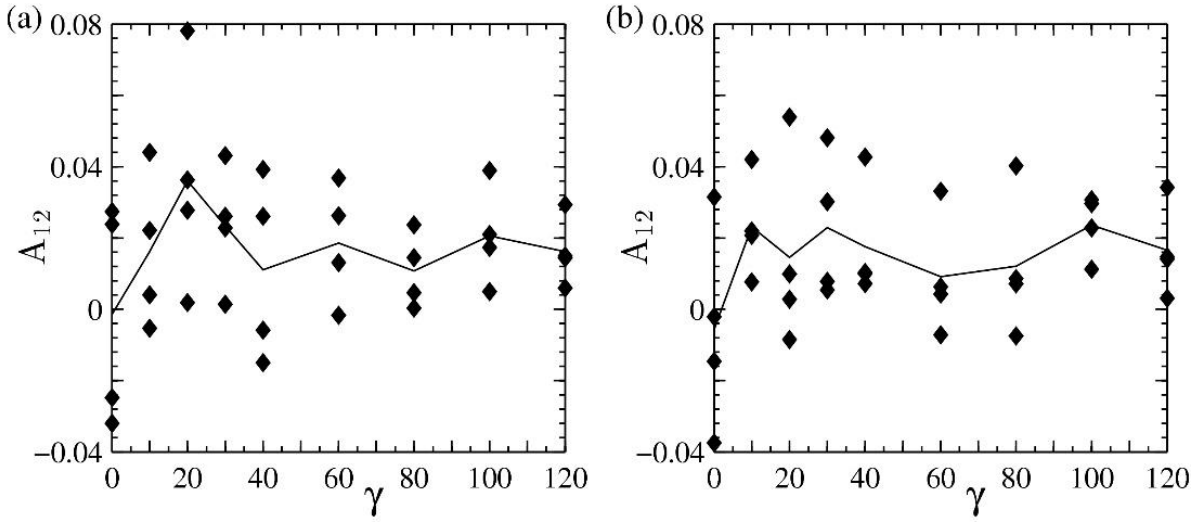

Figure 5.3: Experimental values of A_{12} fiber orientation from four sampling locations in the compression molded samples for fiber lengths (a) L_n = 0.54 and (b) 0.9 mm. The line represents the average of all measured fibers.

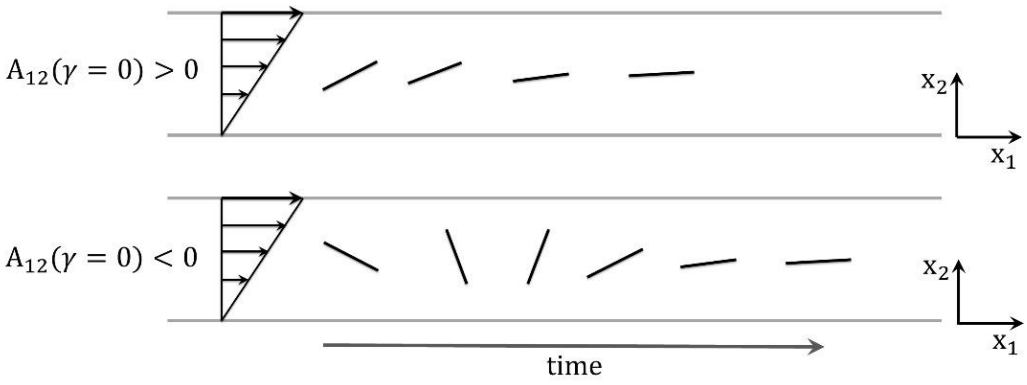

Figure 5.4: Influence of a positive or negative A_{12} initial orientation at zero strain on the orientation evolution of a sample fiber in simple shear flow.

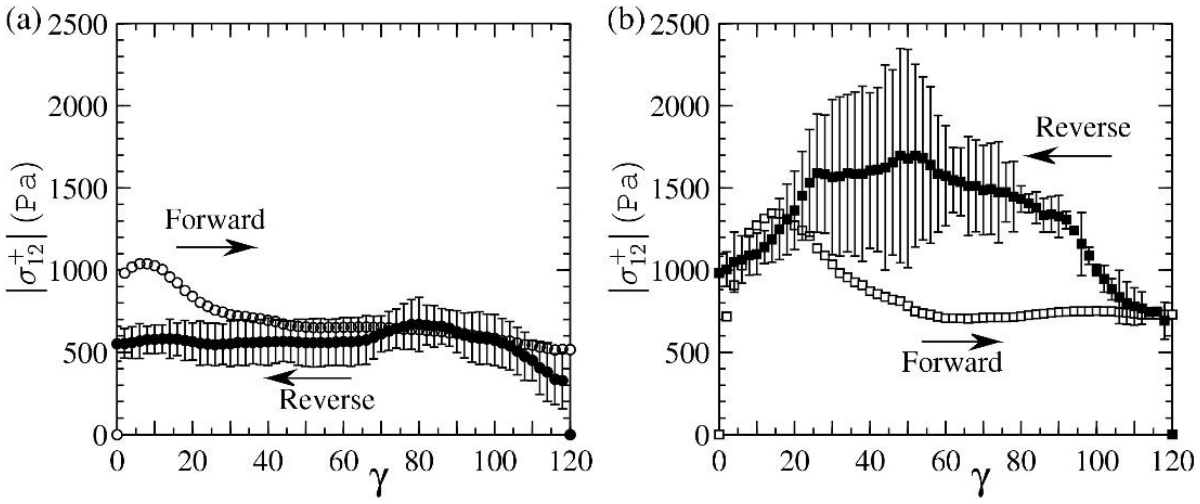

Figure 5.5: Transient shear stress response of compression molded samples during the startup of flow (open symbols) and flow reversal (closed symbols) as a function of shear strain for fiber lengths (a) L_n = 0.54 and (b) 0.9 mm. Flow reversal begins at 120 strain units. Error bars denote the standard deviation of five samples.

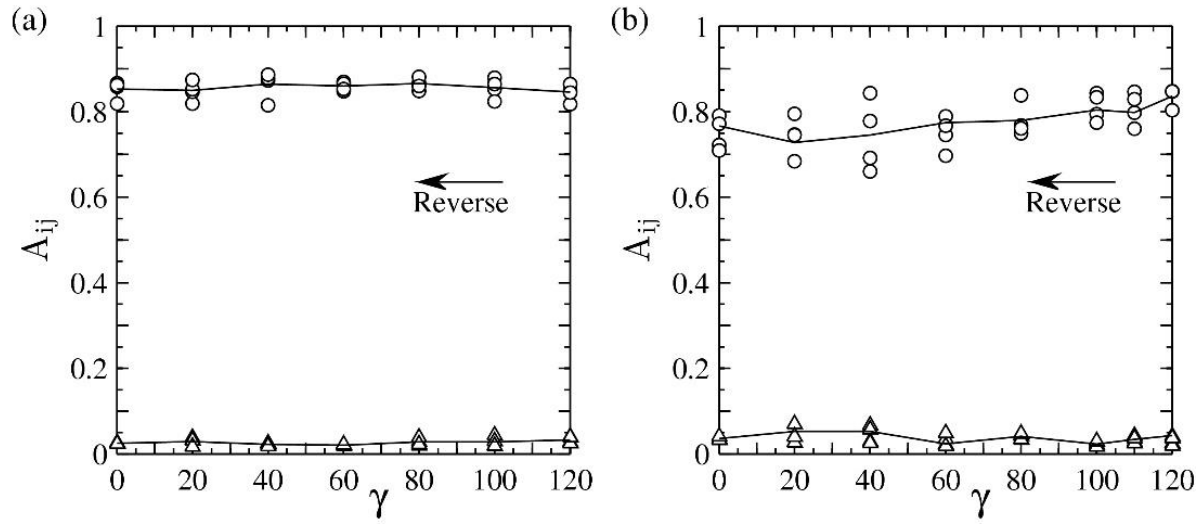

Figure 5.6: Fiber orientation from four sampling locations in the compression molded samples as a function of shear strain under flow reversal for fiber lengths (a) L_n = 0.54 and (b) 0.9 mm. A_{11} and A_{22} are designated by ○ and Δ, respectively. The line represents the average of all measured fibers. Flow reversal begins at 120 strain units.

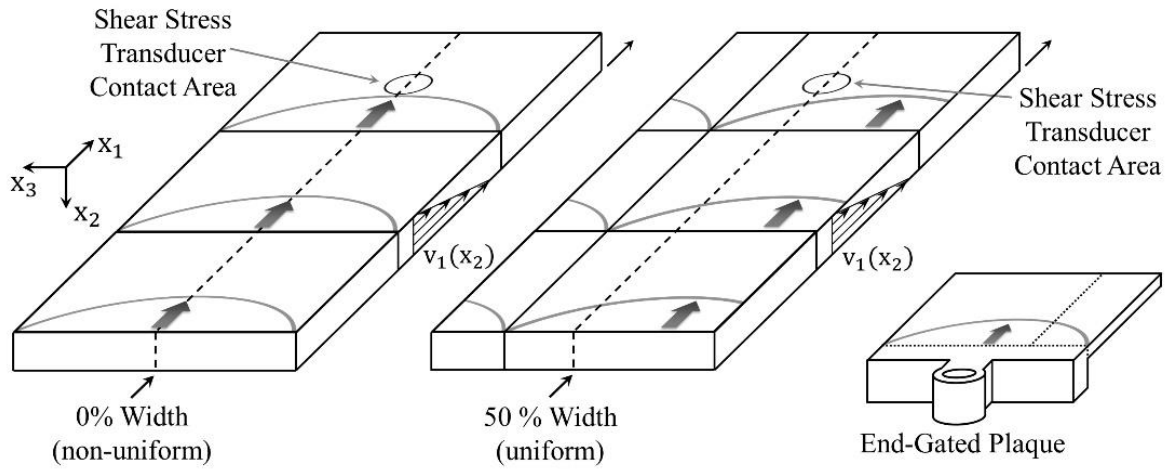

Figure 5.7: End-gated plaque configuration for shear stress measurements in the sliding plate rheometer obtained at 0 and 50 % plaque width corresponding to a non-uniform and uniform initial fiber orientation, respectively.

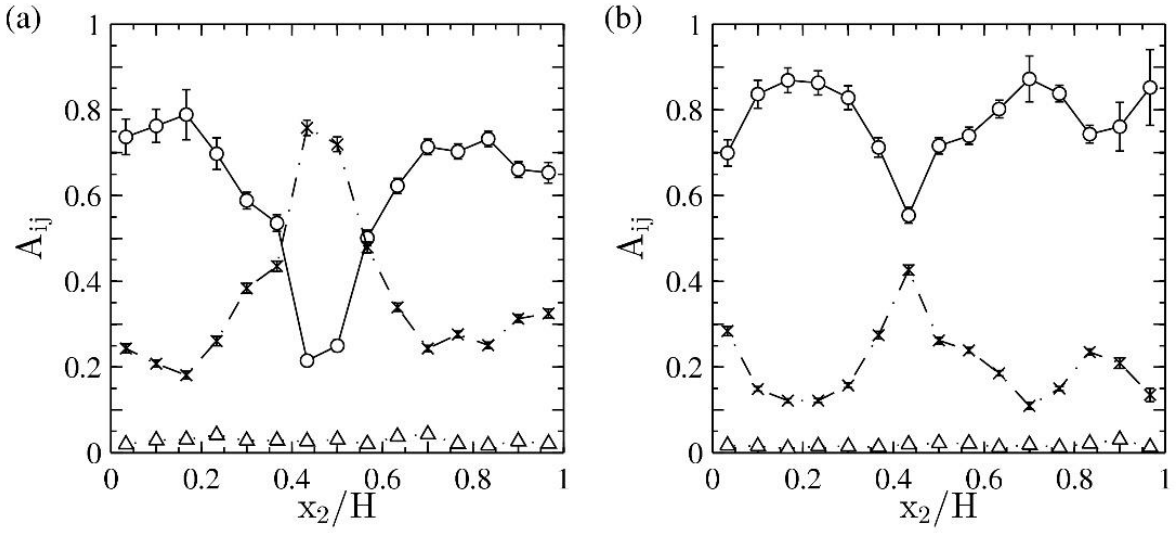

Figure 5.8: Initial fiber orientation with measurement error for injection molded samples with a fiber length L_n = 0.7 mm corresponding to (a) non-uniform and (b) uniform initial fiber orientation for simple shear flow tests. A_{11}, A_{22} and A_{33} are designated by (○), (Δ) and (x), respectively.

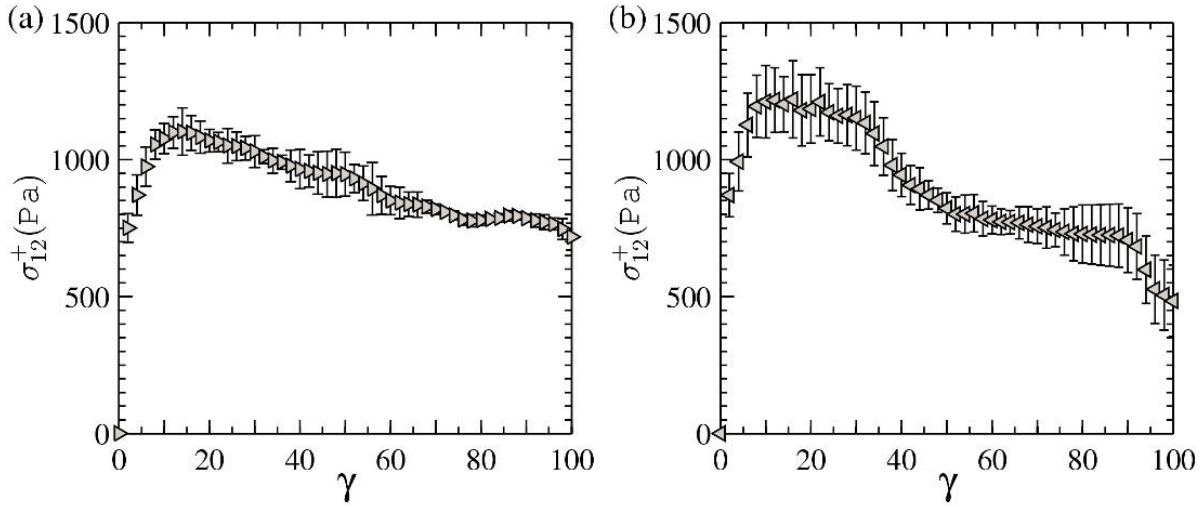

Figure 5.9: Transient shear stress response at a shear rate of 1.0 s^{-1} obtained from the (a) non-uniform and (b) uniform initial fiber orientation samples with a fiber length L_n = 0.7 mm. Error bars denote the standard deviation of five samples.

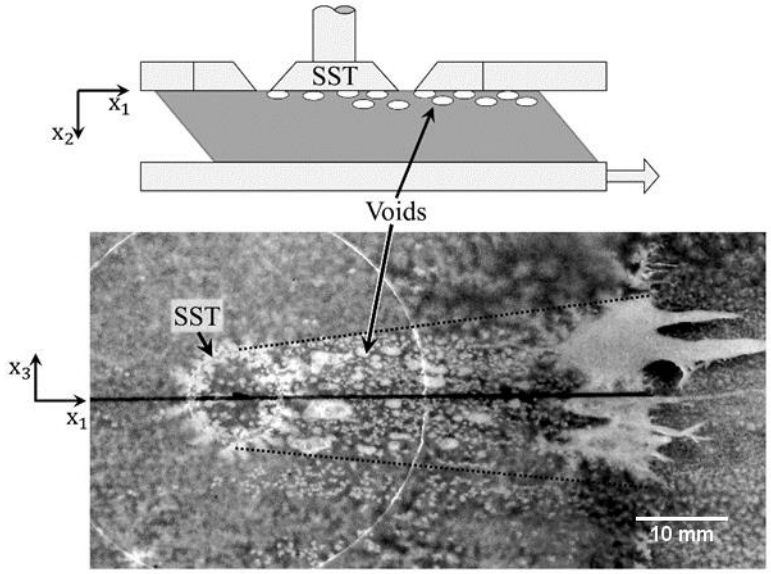

Figure 5.10: An example of voids trailing from the shear stress transducer (SST) in the direction of flow. The example shown is from an injection molded sample with the non-uniform initial orientation subjected to 100 strain units of flow.

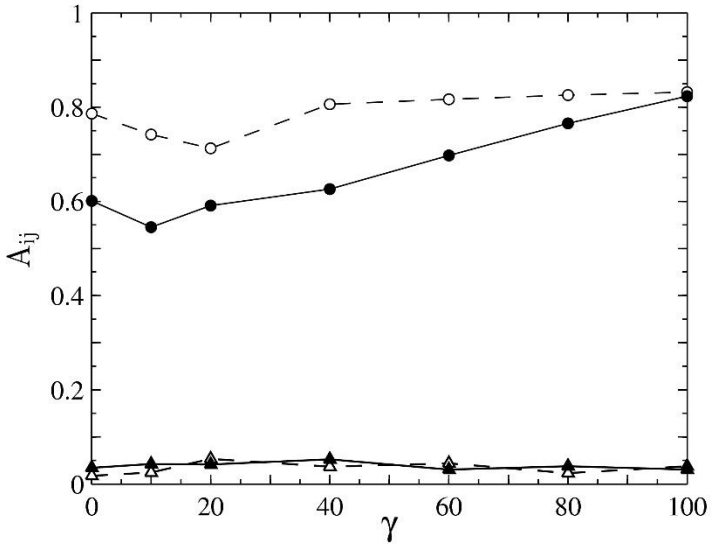

Figure 5.11: Fiber orientation averaged through the thickness of two samples prepared through injection molding as a function of strain for non-uniform (filled symbols) and uniform (open symbols) initial orientation. A_{11} and A_{22} are denoted by (○) and (Δ), respectively.

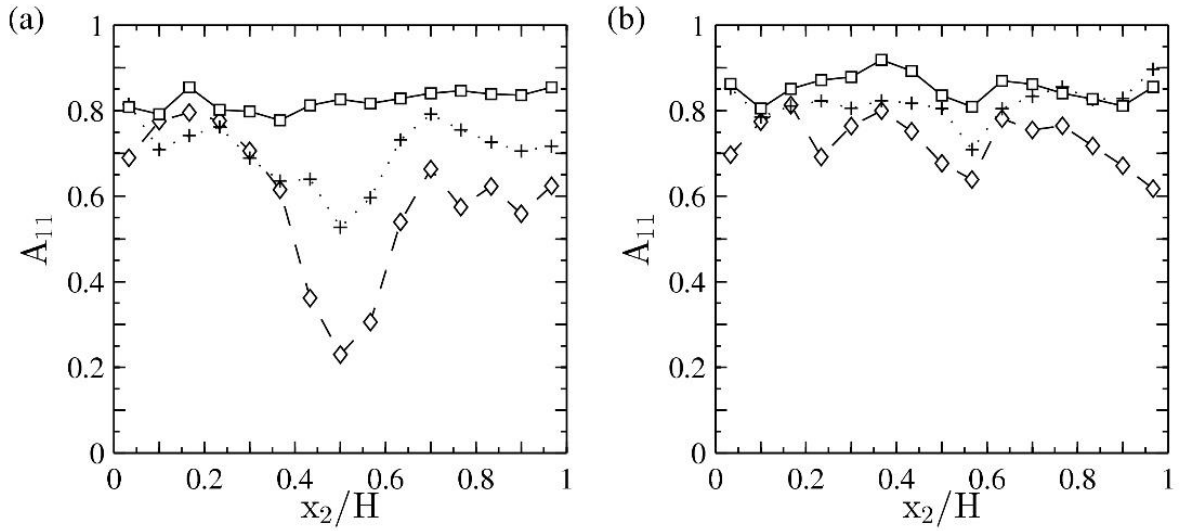

Figure 5.12: Fiber orientation obtained through thickness of two injection molded samples for (a) non-uniform and (b) uniform initial orientations at strain units of 20 (◊), 60 (+) and 100 (□).

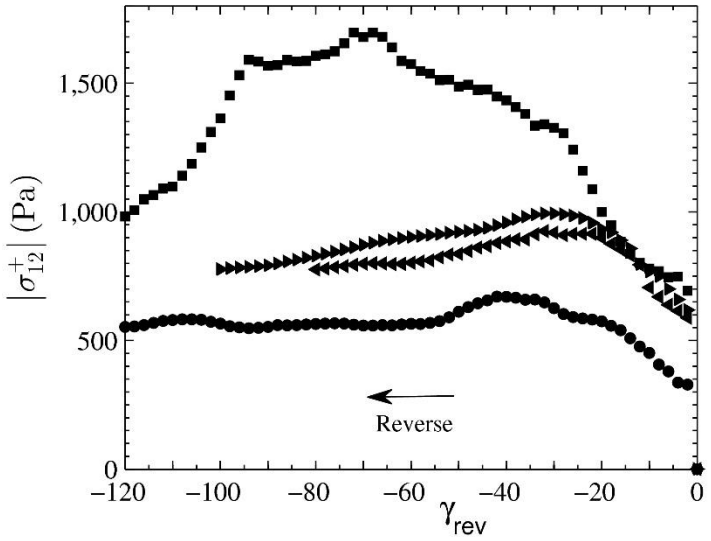

Figure 5.13: Flow reversal stress from the compression molded samples at fiber lengths, L_n = 0.54 (●) and 0.9 mm (■) and samples prepared through injection molding with non-uniform (►) and uniform (◄) initial orientations at a length of 0.7 mm. Zero strain corresponds to the start of flow reversal.

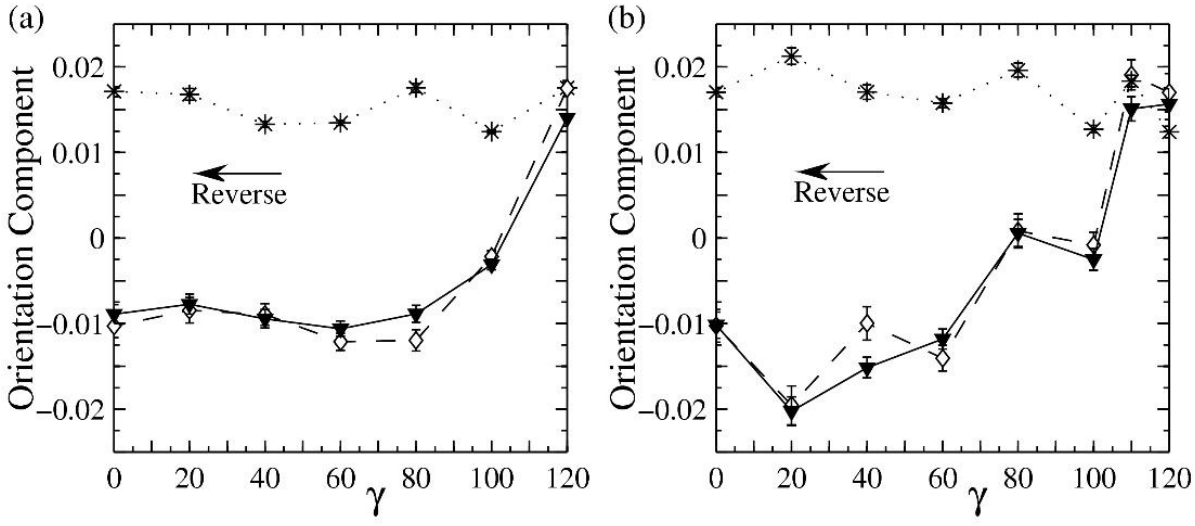

Figure 5.14: Fiber orientation components A_{12} (◊), A_{1211} (▼) and A_{1212} (*) averaged through the sample thickness for compression molded samples subjected to flow reversal with fiber lengths (a) L_n = 0.54 and (b) 0.9 mm.

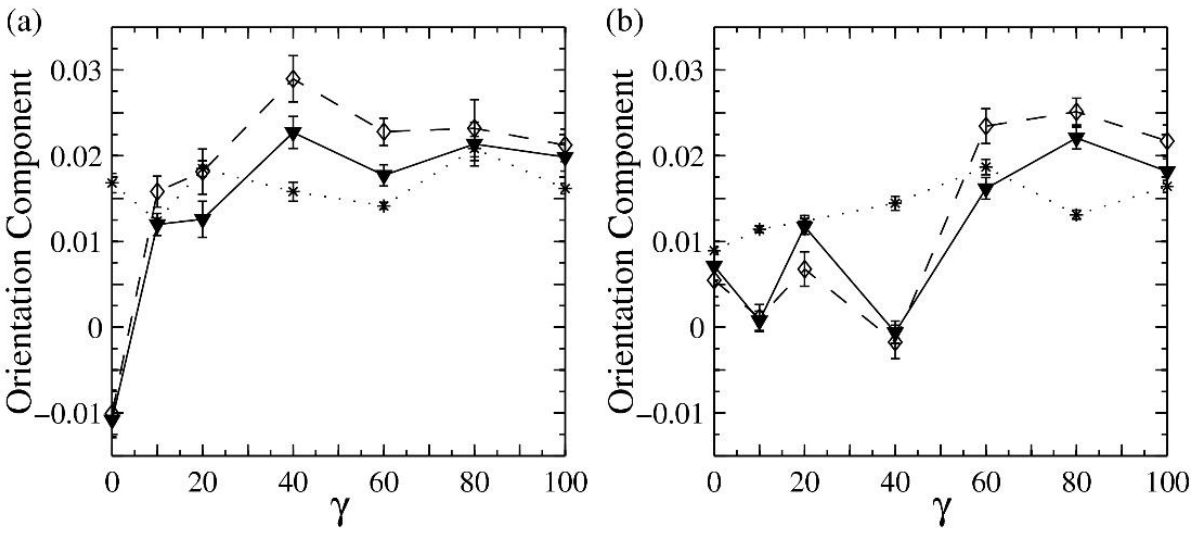

Figure 5.15: Fiber orientation components A_{12} (◊), A_{1211} (▼) and A_{1212} (∗) averaged through the sample thickness from two samples during the startup of flow for injection molded samples with (a) non-uniform and (b) uniform initial orientations.

Chapter 6 The Role of the Initial Fiber Orientation in Obtaining Material Parameters from Experimental Data in Simple Shear Flow

Chapter 6 The Role of the Initial Fiber Orientation in Obtaining Material Parameters from Experimental Data in Simple Shear Flow

Mark J. Cieslinski[1], Peter Wapperom[2], Donald G. Baird[1*]

1. Department of Chemical Engineering, Virginia Tech, VA 24061
2. Department of Mathematics, Virginia Tech, VA 24061

*Author to whom correspondence should be addressed, email: dbaird@vt.edu

6.1 Abstract

Experimental fiber evolution data from a rheometer can be used to determine material parameters in fiber orientation models independent from processing flows. The Folgar-Tucker orientation model was demonstrated in simple shear flow to predict distinctly different trends in the orientation evolution depending on the initial fiber orientation. Repeatable orientation data obtained from samples generated through injection molding was used to determine the material parameters in the strain reduction factor (SRF) and reduced strain closure (RSC) models. Material parameters provide reasonable agreement between model predictions and two sets of experimental fiber evolution data averaged through the sample thickness. Measured values of fiber orientation were used to show that variations in orientation through the sample thickness may result in small deviations from simple shear flow. The SRF and RSC orientation models were applied to fiber orientation that varied through the sample thickness. Slightly better agreement with the experimental data was observed for the SRF model than the RSC model, but both models were unable to quantitatively predict the slow orientation kinetics at low strain units while maintaining agreement with experimental data at high shear strains.

6.2 Introduction

Discontinuous fiber composites are often manufactured by adapting injection or compression molding processes [1]. During the mold filling process, a complex fiber orientation develops within the part which is dictated by the mold geometry and processing conditions. The variations in fiber orientation throughout the part largely influence the degree to which mechanical properties are improved compared to the polymer matrix [2]. Simulating the development of the fiber microstructure during the molding process can then allow for the optimization of mold designs and processing conditions in order to improve a part's mechanical performance.

The hydrodynamic theory for fiber orientation was derived by Jeffery [3] for the motion of an ellipsoidal particle. A phenomenological isotropic rotary diffusion term was added to Jeffery's theory by Folgar and Tucker [4] to account for fiber interactions in concentrated fiber suspensions. The strain reduction factor (SRF) [5] and the reduced strain closure (RSC) model [6] models are empirical modifications of the Folgar-Tucker model to better reflect the experimental observations of slower orientation kinetics. Further adaptation of the RSC model has been employed by Phelps et al. [7] to include anisotropic rotary diffusion to account for fiber interactions that are dependent on the fiber orientation state.

In order to use fiber orientation models to provide an accurate description of the fiber orientation in a molded part, empirical parameters in the models must be determined. Empirical relationships for the isotropic rotary diffusion term in the Folgar-Tucker model have been fit to numerical simulations [8, 9] or to experimental orientation data obtained from injection molded parts [10]. Wang et al. [6] proposed that the empirical parameters in the RSC fiber orientation model could be obtained from the transient rheological response in shear flow using a stress equation that is dependent on fiber orientation. Eberle et al. [11] and Ortman et al. [12] measured fiber orientation during the startup of flow along with transient stress data to provide an additional comparison between stress and orientation model predictions when fitting parameters in the

models. The stress predictions using orientation model parameters fit to experimental data did not reflect the measured stress response. Based on their sample preparation procedure, the initial fiber orientation is not well-controlled which is necessary to reliably assess orientation and stress models during the startup of flow [13].

The overlying goal is to obtain unbiased material parameters used in the fiber orientation models from a fundamental flow that can then be used to simulate complex molding processes. The purpose of the work presented here is to demonstrate the importance of the initial fiber orientation when extracting material parameters in fiber orientation models from experimental orientation evolution data. The Folgar-Tucker model is used to establish that the orientation evolution is highly dependent on the initial fiber orientation. The strain reduction factor (SRF) and reduced strain closure (RSC) models are used to reflect the slowed orientation kinetics in the experimental orientation data of fibers with a number average fiber length of 0.7 mm. These two models are also chosen because they provide different approaches to slow the orientation evolution rate while predicting the same steady state fiber orientation. The SRF and RSC orientation models are compared to experimental fiber orientation evolution data with different initial orientations. The information gathered from the well-defined shear flow can be used to determine and validate material parameters in orientation models that can then be applied to complex molding simulations.

6.3 Fiber Orientation Equations

The orientation of a single fiber can be described by a unit vector, $\mathbf{p}$, parallel to the length of the fiber. Even-order tensors can be used to compactly represent a population of fibers [14]. The second and fourth order orientation tensors are described, respectively, as:

$$\mathbf{A} = \int \mathbf{pp}\psi(\mathbf{p})\,\mathrm{d}\mathbf{p} \qquad \mathbf{A}_4 = \int \mathbf{pppp}\psi(\mathbf{p})\,\mathrm{d}\mathbf{p} \tag{6.1}$$

where ψ is the orientation distribution function.

Fiber orientation evolution equations have been developed in terms of orientation tensors to improve computational efficiency by avoiding calculations of the orientation distribution function. To apply Jeffery's theory for the orientation of ellipsoidal particles to concentrated fiber suspensions, Folgar and Tucker [4] added a phenomenological rotary diffusion term to account for fiber interactions. The Folgar-Tucker model was modified empirically by Huynh [5] to better reflect slower orientation kinetics. This model is referred to as the strain reduction factor (SRF) model:

$$\frac{D\mathbf{A}}{Dt} = \alpha[(\mathbf{W}\cdot\mathbf{A} - \mathbf{A}\cdot\mathbf{W}) + \xi(\mathbf{D}\cdot\mathbf{A} + \mathbf{A}\cdot\mathbf{D} - 2\mathbf{D}:\mathbf{A}_4) + 2C_I\dot{\gamma}(\mathbf{I} - 3\mathbf{A})] \tag{6.2}$$

where D/Dt is the material derivative, $\mathbf{W} = \frac{1}{2}(\nabla\mathbf{v}^t - \nabla\mathbf{v})$ is the vorticity tensor, $\mathbf{D} = \frac{1}{2}(\nabla\mathbf{v}^t + \nabla\mathbf{v})$ is the rate-of-deformation tensor, $\xi = (a_r^2 - 1)/(a_r^2 + 1)$ is the particle shape parameter of an ellipsoid with the aspect ratio, a_r = length/diameter, $\dot{\gamma} = \sqrt{2\mathbf{D}:\mathbf{D}}$ is the magnitude of the rate-of-deformation tensor, $\mathbf{I}$ is the unit tensor, α is the strain reduction factor ranging from 0 to 1 and C_I is the rotary diffusion coefficient. For slender fibers, ξ is often defined as one, which also helps alleviate non-physical oscillations when approximating $\mathbf{A}_4$ [6]. When $\alpha = 1$, the Folgar-Tucker model [4] is recovered. The addition of the strain reduction factor causes the model to violate material objectivity, meaning that model predictions could be dependent on the chosen coordinate system.

Wang and coworkers [6] addressed material objectivity in the reduced strain closure (RSC) model by empirically scaling the evolution of the eigenvalues of $\mathbf{A}$ while the eigenvectors remain unchanged:

$$\frac{D\mathbf{A}}{Dt} = \mathbf{W}\cdot\mathbf{A} - \mathbf{A}\cdot\mathbf{W} + \xi\{\mathbf{D}\cdot\mathbf{A} + \mathbf{A}\cdot\mathbf{D} - 2[\mathbf{A}_4 + (1-\kappa)(\mathbf{L}_4 - \mathbf{M}_4:\mathbf{A}_4)]:\mathbf{D}\} + 2\kappa C_I\dot{\gamma}(\mathbf{I} - 3\mathbf{A}). \tag{6.3}$$

The value of κ ranges from 0 to 1. The Folgar-Tucker model is recovered when $\kappa = 1$. The two additional fourth order tensors that arise in the model are:

$$\mathbf{L}_4 = \sum_{i=1}^{3} \lambda_i \mathbf{e}_i \mathbf{e}_i \mathbf{e}_i \mathbf{e}_i \qquad \mathbf{M}_4 = \sum_{i=1}^{3} \mathbf{e}_i \mathbf{e}_i \mathbf{e}_i \mathbf{e}_i \tag{6.4}$$

where λ_i are the eigenvalues and $\mathbf{e}_i$ the eigenvectors of $\mathbf{A}$.

A primary focus is given to the evolution of the second order orientation tensor, but theories for the extra stress consider the fourth order orientation tensor [15-18]. In simple shear flow, the A_{1212} component of orientation determines the shear stress whereas A_{1211} has been shown to have the largest contribution to the first normal stress difference [19, 20].

6.4 Fiber Orientation Measurements

Repeatable fiber orientation data was obtained from 30 wt% glass fiber in a polypropylene matrix subjected to simple shear flow within a sliding plate rheometer [20]. The initial fiber orientation was generated from injection molded end-gated plaques. Two locations in the plaque were used in the rheometer. These two locations are given the general designation of non-uniform and uniform initial fiber orientation, which is in reference to the orientation through the sample thickness. The molding process produced samples with a number average (L_n) and weight average (L_w) fiber length of 0.70 and 0.89 mm, respectively. The fiber lengths averaged through the sample thickness were verified to not change within experimental error from 0 to 75 % plaque width. The fiber diameter was measured to be 13.3 μm.

The method of ellipses was used to measure the fiber orientation of samples subjected to simple shear flow in the sliding plate rheometer. A cross section of a sample was polished using metallographic techniques and imaged under an optical microscope at 20x magnification [21]. A unit vector $\mathbf{p}$ for each fiber is defined by the geometry of the fiber that intersects the inspection plane. The method of Vélez-García et al. [22] was used to determine the in-plane orientation angle

unambiguously. Orientation tensors are calculated based on a population of fibers and a weighting function to account for imaging bias [23]. An additional weighing function was proposed by Vélez-García et al. [22] to more accurately sort fibers into bins through the sample thickness. The second and fourth order fiber orientation tensors are calculated from the experimental data as:

$$\mathbf{A} = \frac{\sum_k \ (\mathbf{pp})_k L_k F_k B_k}{\sum_k \ L_k F_k B_k} \tag{6.5}$$

$$\mathbf{A}_4 = \frac{\sum_k \ (\mathbf{pppp})_k L_k F_k B_k}{\sum_k \ L_k F_k B_k} \tag{6.6}$$

where L_k is the length of the k-th fiber, F_k is the weighting function accounting for imaging bias, B_k is a factor to account for fractional objects that arise when sorting the fibers into bins through the sample thickness. To understand the general orientation evolution, orientation tensors were calculated from all the fibers through the sample thickness. The injection molding sample preparation procedure produced orientation that varies through the sample thickness. This was captured by dividing the sample in to 15 bins through the thickness. A separate second and fourth order orientation tensor is associated with each bin. The method of ellipses is a destructive process that does not allow for the length of each fiber to be known. The orientation tensors were calculated assuming that the length of each fiber has the number average fiber length. Orientation data is plotted with the estimated measurement error following the analysis of Bay and Tucker [23].

6.5 Simulation Approach

Simulations of the second order orientation tensor using the Folgar-Tucker, SRF and RSC models were performed in Matlab® (version 8.3.0.532). The fiber evolution equations were solved numerically using the built-in Matlab® differential equation solver based on the explicit Runge-Kutta 4,5 method [24]. The orientation evolution equations for the second order orientation

tensor require an approximation for the fourth order tensor in terms of lower order tensors in order to avoid calculations of the orientation distribution function. The invariant-based optimal fitting closure (IBOF) was used to approximate the fourth order orientation tensor in the orientation evolution equations. This closure method has been shown to produce equivalent results when compared to eigenvalue based closure approximations while being more computationally efficient [25].

The empirical parameters in the orientation models were fit to the experimental values of fiber orientation averaged through the sample thickness of the injection molded samples with non-uniform initial fiber orientation. The value for C_I = 0.005 was fit to A_{11} = 0.83, which was reported to be the steady state orientation for these samples [20]. The parameters associated with slowing the evolution of fiber orientation (α for the SRF and κ for the RSC) were then adjusted to best fit the experimental values of A_{11} while maintaining a value of A_{11} at 100 strain units near 0.80. The slowed orientation kinetics were best captured by $\alpha = 0.25$ and $\kappa = 0.2$ for the SRF and RSC models, respectively. Further discussion of the SRF and RSC model predictions is provided in § 6.6.4.

Stochastic simulations of the Folgar-Tucker model were performed using the method of Fan et al. [26] to verify the sensitivity of the initial value of A_{12} o the orientation evolution predictions without the influence of a closure approximation. Using the value of C_I = 0.005 in the stochastic simulation yielded a steady state for A_{11} of 0.77. The initial fiber orientation for the stochastic simulations was based on a population of experimentally measured **p** vectors. The different initial values of A_{12} were determined by setting the vector components, p_1 and/or p_2, to their absolute value then the sign of the components was changed to reflect a positive or negative value for A_{12}. For an initial value of A_{12} = 0.014, the measured p_2 value was set to its absolute value for all measured fibers and p_1 was unchanged. For A_{12} = 0.078, both measured values of p_1 and p_2 were set to the absolute value for all **p** vectors. To produce a negative initial value for A_{12},

the sign was changed for the p_1 component. This approach maintains the same trace components of the second order orientation tensor but provides different initial values for A_{12}. A total of 230600 **p** vectors were used in the stochastic simulations.

6.6 Results and Discussion

The first two parts of this section demonstrate the need to have a well-defined initial fiber orientation in order to accurately extract orientation model parameters from experimental orientation data. The first part focuses on the transient behavior predicted from a 3D random, planar random and experimental initial orientation. The second part addresses the sensitivity of the initial value of A_{12} on the predicted orientation evolution in simple shear flow. Next, an analysis is performed on the influence of a complex fiber orientation on the velocity profile in plane Couette flow generated in a sliding plate rheometer. Finally, model parameters are extracted and model predictions are compared to repeatable experimental orientation evolution data.

6.6.1 Orientation Evolution from the Initial State

The fiber evolution equations are initial value problems where the transient orientation behavior relies heavily on the initial orientation. To demonstrate this importance, simulations are performed in simple shear flow using the Folgar-Tucker model with $C_I = 0.005$ at a shear rate $\dot{\gamma}$ = dv_1/dx_2 = 1.0 s^{-1} with the initial orientations of 3D random $\left(A_{ii} = \frac{1}{3}, A_{ij} = 0 \text{ for } i \neq j\right)$, random in the x_1x_3-plane $\left(A_{11} = A_{33} = \frac{1}{2};\ A_{22} = A_{ij} = 0 \text{ for } i \neq j\right)$ and the measured experimental fiber orientation averaged through the thickness of the sample designated as the non-uniform initial orientation:

$$\mathbf{A} = \begin{bmatrix} 0.601 & -0.0094 & -0.0068 \\ -0.0094 & 0.028 & -0.0023 \\ -0.0068 & -0.0023 & 0.371 \end{bmatrix}. \tag{6.7}$$

A fourth initial fiber orientation considers the experimental initial orientation with the sign of A_{12} changed to a positive value with the same magnitude. This can be easily implemented experimentally in a sliding plate rheometer by changing how the sample is loaded in the rheometer prior to testing.

The evolution of A_{11} and A_{22} predicted by the Folgar-Tucker model with the IBOF closure is shown for the different initial fiber orientations in Figure 6.1(a). Using a 3D random initial orientation causes A_{11} to increase rapidly and slightly overshoot the steady state value, while a rapid decrease is observed for A_{22}. With an initial orientation of random in the x_1x_3-plane, the value of A_{11} decreases slightly at small strains before gradually increasing to the steady state. The experimental orientation has an initial value of A_{11} closer to the steady state value than the two random cases. The measured initial orientation with a negative A_{12} predicts a slight decrease in A_{11} prior to increasing in value to the steady state. If instead the value of A_{12} is initially positive, a gradual increase in A_{11} is predicted from the initial value to the steady state. For the initial fiber orientation of planar random and the experimental orientations with a positive or negative value for A_{12}, a slight overshoot followed by a smaller undershoot is observed in A_{22}, although the differences between these three cases are small. The largest overshoot is observed for the experimental orientation with a negative A_{12} while the least pronounced overshoot-undershoot profile is predicted from the random in the x_1x_3-plane initial orientation.

The predicted evolution of A_{12} is shown in Figure 6.1(b). From a 3D random initial fiber orientation, the evolution of A_{12} has a significant overshoot before reducing to the steady state value. With the initial orientations of planar random and the experimentally measured data, a gradual increase in A_{12} is observed between the initial value and the steady state. The small differences in the evolution of A_{12} in these cases appear to coincide with the small differences in the initial value of A_{12}, while the evolution of A_{12} for the 3D random initial orientation is largely influenced by a large out-of-plane initial value (i.e. $A_{22} = 1/3$).

The A_{1212} component of orientation is presented in Figure 6.1(c) and is proportional to the shear stress. The random initial orientation causes a significant overshoot that is greater in magnitude than the steady state by about a factor of three. The experimental data with a negative initial value of A_{12} produces a slight overshoot in A_{1212}, but not to the extent of the random initial orientation. A gradual increase in A_{1212} is observed for the random in the x_1x_3-plane initial orientation and the experimental initial orientation with a positive A_{12}. Using the 3D random initial orientation, a significant stress overshoot would be predicted. The experimental initial orientation with a negative A_{12}, would only predict a slight overshoot that is similar in magnitude to the steady state value. However, using the other two initial fiber orientations, predicted stresses would only increase gradually to a steady state without a pronounced overshoot. Predictions of shear stress using the 3D random initial fiber orientation have shown reasonable agreement with experimental stress data [27], but a 3D random initial orientation is likely far from the actual initial orientation which was reported in similar experiments to be mostly parallel to the plates [28].

The predicted evolution of A_{1211} is provided in Figure 6.1(d) and would be the most significant contribution to the first normal stress difference in simple shear flow. The value of A_{1211} appears to reach a steady state at slightly larger shear strains than A_{12} or A_{1212}. Experimentally, the first normal stress difference reaches a maximum at greater strain units than the shear stress [28]. Similar to the predictions of shear stress, the first normal stress would exhibit a significant overshoot for the 3D random initial orientation and a small overshoot would be predicted for the experimental initial orientation with a negative A_{12}. The random in the x_1x_3-plane and the experimentally measured initial orientation with a positive A_{12} would gradually increase from the initial value to the steady state.

The orientation simulation using a 3D random initial orientation predicts a distinctly different fiber orientation evolution than an initial orientation that is either random in the x_1x_3-plane or the experimentally measured values. In terms of determining the orientation kinetics for the SRF or RSC models, an initial orientation of 3D random may be an incorrect assumption if not

verified experimentally. In samples where the thickness is relatively small compared to the other two dimensions, the planar random initial orientation may be a reasonable first assumption if experimental values for the initial orientation are not available. However, from this exercise, the greatest difference between each initial orientation occurred at small strains which may significantly impact conclusions on the orientation kinetics.

6.6.2 Sensitivity of Initial A_{12} on Orientation Evolution

The sensitivity of the Folgar-Tucker model is evaluated with regard to the initial value of A_{12}. The work of Ortman et al. [12] reported initial values of A_{12} to range between 0.025 to 0.065. Eberle et al. [11] reported the value of A_{12} to be as large as 0.07 from a sample prepared for a cone-and-plate rheometer. It may be difficult to evaluate experimentally the sensitivity of A_{12} to the orientation evolution of a population of concentrated fibers due to the experimental error associated with orientation components that are small in magnitude. Simulations are performed using the trace components of the experimental initial orientation presented in Eq. (6.7) with the value of A_{12} varied from -0.06 to +0.06 in increments of 0.02. If the model's sensitivity to A_{12} is better understood, then the orientation model can be fit with greater certainty to experimental fiber evolution data.

The predicted evolution of A_{11} and A_{22} is shown in Figure 6.2(a) using the Folgar-Tucker model with the IBOF closure approximation. When the initial value of A_{12} is positive, the value of A_{11} increases monotonically to the steady state, while an initially negative A_{12} causes A_{11} to first decrease before an increase to the steady state. The greatest influence of the A_{12} initial value on the evolution of A_{11} occurs below 10 strain units for the Folgar-Tucker model. The A_{22} component of orientation exhibits a dynamic orientation profile depending on the initial value of A_{12}. For a large positive initial A_{12}, the values of A_{22} increases monotonically toward the steady state value. If A_{12} is initially small or negative, an overshoot is observed followed by a small

undershoot before reaching a steady state. The value of A_{22} at about 12 strain units appears to be independent of the initial value of A_{12}.

The evolution of A_{12} begins at the specified initial value and displays an overshoot at about 10 strain units if the initial value is far from the steady state [Figure 6.2(b)]. The A_{12} prediction at about 7 strain units is nearly independent of the A_{12} initial value. For largest two positive initial values of A_{12}, there is little change in A_{12} as a function of strain.

The A_{1212} component of orientation, which is associated with the shear stress, follows a similar trend as A_{22} [Figure 6.2(c)]. When A_{12} is initially negative, an overshoot followed by an undershoot is observed, while the larger positive initial values for A_{12} cause a monotonic increase in A_{1212} to the steady state. The value of A_{1212} at 12 strain units appears to be insensitive to the initial A_{12} value. This location is of interest when comparing shear stress predictions to a measured shear stress response, because it is not sensitive to the initial orientation.

The value of the A_{1211} component of orientation is shown in Figure 6.2(d) and governs the first normal stress difference in simple shear flow. The prediction of A_{1211} is very similar to the evolution of the A_{12} component of orientation. At about 7 strain units the value of A_{1211} is similar between each initial value of A_{12}. The insensitivity of A_{1211} to the initial A_{12} value at 7 strain units is of interest in evaluating model predictions with experimental data.

The sensitivity of the initial value of A_{12} on the orientation evolution predictions was explored with stochastic simulations to be certain that the closure approximation did not influence the aforementioned observations (Figure 6.3). Some fluctuations are observed in the evolution of orientation tensor components due to the number of fibers used in the simulations. The population of fibers used to conduct the simulations had average initial values for A_{12} of -0.078, -0.014, +0.014 and +0.078. For an initial value of A_{12} = +0.078, a slightly different orientation evolution is predicted compared to Figure 6.2 because the initial value of A_{12} is greater than the steady state. The prediction that there is a location prior to the steady state that is insensitive to the initial value

of A_{12} is also confirmed with the stochastic simulations. It appears that the IBOF closure approximation has only a minor influence on the orientation evolution predictions in simple shear flow compared to orientation simulations that do not use a closure approximation.

Values of orientation that are predicted to be insensitive to the initial value for A_{12} are also predicted in the SRF and RSC models. These values are important for fitting model parameters to experimental data because any experimental error in determining A_{12} can be relatively large. However, the independent value is close to the steady state value in this example, while much of the transient behavior occurs before this point. This may change with changes in the initial fiber orientation. The experimental focus should be applied to control A_{12} in simple shear flow so that the orientation models can accurately be assessed.

6.6.3 Non-Uniform Orientation in Simple Shear Flow

The use of an injection molded part to generate the initial fiber orientation for the startup of simple shear flow test introduces fiber orientation that can vary through the sample thickness. This complex initial orientation is repeatable between different samples, which is a concern when other sample preparation methods, like compression molding, are used [20]. Additional analysis is done here to investigate the influence of the complex initial orientation on the sample deformation in a sliding plate rheometer (plane Couette flow). The concern is that fiber orientation that varies through the sample thickness may cause the shear rate to be inhomogeneous.

The velocity profile within the sliding plate rheometer is approximated by dividing the flow into layers through the thickness. It is then assumed that the local viscosity of the material in each layer through the sample's thickness is a function of the matrix viscosity and local fiber orientation. The velocity profile is calculated assuming that the shear stresses and velocities are equivalent at the layer interfaces. This analysis is based on the fluid mechanics exercise that considers layers of immiscible fluids in plane Couette flow [29, 30]. A schematic of the problem description is shown in Figure 6.4. The movable plate has a velocity, V, and H is the gap between

the parallel plates. There are a total of M layers through the thickness with the i-th layer having a viscosity, $\eta^{(i)}$, between the boundaries located at $\kappa^{(i)}H$ and $\kappa^{(i+1)}H$. Simple shear flow is assumed to occur in each layer according to:

$$\mathrm{v}_1^{(i)}(x_2) = \frac{c_1^{(i)} x_2}{\eta^{(i)}} + c_2^{(i)} \tag{6.8}$$

where c_1 and c_2 are constants. A no slip boundary condition is imposed at each of the parallel plates:

$$\mathrm{v}_1^{(1)}(H) = V \qquad \mathrm{v}_1^{(M)}(0) = 0. \tag{6.9}$$

In the case where the viscosity is constant through the gap thickness ($M = 1$), the velocity profile is:

$$\mathrm{v}_1(x_2) = \frac{V}{H} x_2. \tag{6.10}$$

Fiber orientation through the thickness can vary which could influence the local viscosity of the material. In order to determine the constants in Eq. (6.8) for each layer in the flow, the velocity and shear stresses are assumed equivalent at the layer boundaries:

$$\mathrm{v}_1^{(i)}\left(\kappa^{(i+1)}H\right) = \mathrm{v}_1^{(i+1)}\left(\kappa^{(i+1)}H\right) \tag{6.11}$$

$$\sigma_{12}^{(i)}\left(\kappa^{(i+1)}H\right) = \sigma_{12}^{(i+1)}\left(\kappa^{(i+1)}H\right) \tag{6.12}$$

where $\sigma_{12} = \eta \mathrm{dv}_1/\mathrm{dx}_2$. Applying the boundary conditions in Eqs. (6.9), (6.11) and (6.12) allows for the constants in Eq. (6.8) to be solved:

$$c_1^{(1)} = c_1^{(2)} = \cdots = c_1^{(M)} = \frac{V}{H \sum_{i=1}^{M} \frac{\kappa^{(i)} - \kappa^{(i+1)}}{\eta^{(i)}}} \tag{6.13}$$

$$c_2^{(i)} = c_2^{(i+1)} + c_1 \kappa^{(i+1)} H \left(\frac{1}{\eta^{(i+1)}} - \frac{1}{\eta^{(i)}} \right) \tag{6.14}$$

noting that $\kappa^{(1)} = 1$, $\kappa^{(M+1)} = 0$, and $c_2^{(M)} = 0$. Eq. (6.10) is recovered when $M = 1$ for the constants in Eq. (6.13) and (6.14). The viscosity for each layer is the sum of contributions from the matrix and fiber orientation [17]:

$$\eta^{(i)} = \eta_m \left(1 + N_p \mathrm{A}_{1212}^{(i)} \right) \tag{6.15}$$

where N_p is the particle number that weights the contribution of fiber orientation and $\mathrm{A}_{1212}^{(i)}$ is the component of the fourth order orientation tensor contributing to shear stress. The analysis here will consider the particle number as an adjustable parameter and the orientation component is calculated from measured orientation data.

The largest variation in fiber orientation through the sample thickness was obtained from the sample generated by injection molding designated as the non-uniform initial fiber orientation (Figure 6.5). This sampling location corresponds to 50 % plaque length and 0 % plaque width. The orientation through the thickness has the common shell-core-shell orientation profile associated with injection molded parts. The A_{1212} component of orientation is expected to contribute to the shear stress and has the highest value near the walls. A second sampling location in the plaque (50 % plaque width and 50 % plaque length) produced an initial fiber orientation where the trace components of the orientation tensor were much more constant through the thickness, which is designated here as the uniform initial orientation. Here, the value of A_{1212} is much more consistent through the sample thickness and would not influence the velocity profile significantly even though there is some variation in the trace components of the second order orientation tensor through the sample thickness.

The velocity profile predictions in Figure 6.6 show the discrepancy between the ideal case of a constant velocity gradient and an orientation dependent profile. Short fiber suspensions often have a value for N_p that is less than 50 [27, 31], which does not predict a large deviation from the constant velocity gradient using the non-uniform fiber orientation data. At the value of 500 for N_p the velocity profile is almost completely dependent on the local fiber orientation. When N_p is increased by another order of magnitude, the velocity profile is nearly equivalent to the N_p = 500 case. The 3D random theory of Shaqfeh and Fredrickson [18] predicts the value of N_p to be about 120 for 0.7 mm glass fibers at 30 wt% in polypropylene which causes the maximum deviation from the constant velocity gradient of about 8 %.

As more strain is imposed on the sample, the variation in A_{1212} decreases through the sample thickness causing the velocity profile to better reflect a constant velocity gradient. This is quantified by determining the average difference between the predicted velocity profile and simple shear flow:

$$|\text{Error}| = \left[\int_0^H \left(\mathrm{v}_1^{\text{Predicted}} - \mathrm{v}_1^{\text{Simple Shear}}\right)^2 dx_2 \Big/ \int_0^H \left(\mathrm{v}_1^{\text{Simple Shear}}\right)^2 dx_2\right]^{\frac{1}{2}}. \qquad (6.16)$$

The average deviation between the predicted velocity profile and simple shear flow is shown in Figure 6.7 for N_p = 120. The largest discrepancy occurs with the non-uniform initial orientation at zero strain units. Above 40 strain units, the calculated error appears to plateau. The error is slightly greater than expected at high strains. The value of A_{1212} closest to the walls can be about 20 % different when compared to a mostly constant A_{1212} through the sample thickness at large strains. The resulting velocity profile parallels that of simple shear flow. The different A_{1212} values near the walls may be a result of the solid boundary restricting the motion of the fibers. However, the differences between A_{1212} closest to the wall and in the sample core are small. Any experimental error in measuring the value of A_{1212} is relatively large. The fiber orientation

predictions in the next sections are completed under simple shear flow because the approximated deviations from simple shear flow are limited to small strains.

6.6.4 Determining Model Parameters

The empirical orientation model parameters were determined from measured fiber orientation averaged through the sample thickness beginning from the non-uniform initial orientation. The fiber evolution data is best captured with $\alpha = 0.25, C_I = 0.005$ for the SRF model and $\kappa = 0.20, C_I = 0.005$ for the RSC model. The comparison of the SRF and RSC orientation model predictions to the non-uniform experimental data are provided in Figure 6.8. The choice of values for α and κ does not allow the model predictions to completely reach a steady state value in 100 strain units. Decreasing these values provides better agreement between the simulation and experimental data at low strain units, but experimental values of A_{11} become under predicted at high strain units. Fitting the models to the orientation data at high strains is given priority, because there is likely less experimental variation in orientation for large sample deformation. The greatest difference in the SRF and RSC model predictions occurs below 20 strain units. The SRF model predicts a decrease in A_{11} before increasing toward a steady state value, while the RSC model does not predict this decrease to the same extent.

Model predictions using the same material parameters to reflect the non-uniform initial fiber orientation data were compared with experimental evolution data from the uniform initial fiber orientation in Figure 6.9. The average fiber orientation through the sample thickness for the uniform initial orientation sample at zero strain units is:

$$\mathbf{A} = \begin{bmatrix} 0.787 & 0.0055 & -0.012 \\ 0.0055 & 0.017 & -0.002 \\ -0.012 & -0.002 & 0.196 \end{bmatrix}. \tag{6.17}$$

From the uniform initial orientation, a slight decrease in A_{11} is predicted by the SRF and RSC models before increasing to the steady state value. The predicted transient behavior of A_{11} and

A_{33} is in good agreement between the experimental data and both model predictions. The SRF model predicts a greater decrease in A_{11} at small strains, which is slightly more reflective of the experimental data than the RSC model. The values of A_{12} and A_{22} are over predicted by both orientation models. The SRF model predicts a small overshoot in A_{12} and A_{22} before reaching the steady state while the RSC model predicts a gradual increase monotonically from the initial orientation to the steady state value.

The measured fiber evolution data from the uniform initial orientation does not change to a large extent with strain. It is difficult to extract the model parameters that slow the kinetics of fiber orientation accurately from experimental data that does not have significant changes with strain to minimize the effect of experimental error. However, because the model parameters provided a good representation of fiber evolution beginning with the non-uniform initial orientation, successful predictions of the uniform initial orientation data provides some verification of the orientation model parameters. Ortman et al. [12] was not able to provide good quantitative agreement in model predictions of experimental data between different initial orientations using the same model parameters. Their sample preparation procedure could not provide good control of the off-diagonal components of the second order orientation tensor, which may result in significant variations in the measured fiber evolution data [20].

6.6.5 Orientation Evolution through the Sample Thickness

The material parameters determined in the previous section are applied to the non-uniform initial fiber orientation that varies through the sample thickness. The sample is divided into 15 bins through the thickness. The average orientation for each bin at zero strain is taken as the initial fiber orientation for the simulations. The model predictions are compared to experimental data obtained through the sample thickness as a function of strain.

The predicted orientation evolution from the SRF and RSC models as a function of strain is shown in Figure 6.10 for different initial fiber orientations in the sample thickness. Four general

initial orientation states are investigated through the sample thickness that correspond to flow aligned with a positive A_{12}, transversely aligned, random in the x_1x_3-plane and flow aligned with a negative A_{12} at $x_2/H = 0.17$, 0.43, 0.56 and 0.83, respectively. At a value for x_2/H of 0.17, model predictions of A_{11} for both the SRF and RSC models are indistinguishable because A_{12} is initially positive, and there is little difference between the initial value of A_{11} and the steady state. Both models do not capture the decrease in A_{11} that is observed in the experimental data between 40 and 80 strain units. At $x_2/H = 0.43$, the initial value of A_{11} in the core of the sample is small because most of the fibers have preferential orientation in the x_3-direction. A gradual increase is predicted by the SRF model which reflects the general evolution of the experimental data. The RSC model predicts that fibers quickly transition from a transverse alignment toward a flow alignment below 20 strain units, while above 20 strain units the model predicts a gradual increase in A_{11} to the steady state value. For a value of $x_2/H = 0.83$, the initial value of A_{11} is slightly less than the steady state but the initial value of A_{12} is negative. The initially negative A_{12} causes the models to predict a decrease in A_{11} prior to an increase to the steady state. A faster decrease in A_{11} is predicted by the RSC model compared to the SRF model, but both models are in good agreement with experimental data.

A comparison between the orientation predictions through the sample thickness and experimental values of A_{11} are presented in Figure 6.11. The experimental orientation data at 20 strain units has a very similar shell-core-shell profile when compared to the initial fiber orientation. The simulations show orientation changing in the core at a faster rate than what is observed experimentally. The SRF model better reflects the orientation through the thickness than the RSC model. Both models under predict the data in the shell region at low values of x_2/H while an over prediction is observed at high values of x_2/H. At 60 strain units the shell-core-shell profile is less pronounced in the measured data. The SRF and RSC orientation models over predict the measured values throughout most of the sample thickness and are equivalent in the shell regions. The SRF model maintains the core region for larger strain units than the RSC model. Both orientation

models have equivalent predictions at 100 strain units and are able to reflect a constant orientation through the sample thickness. Good agreement between the models and experimental data is observed because the data averaged through the thickness was used to fit the C_I parameter. Reducing α or κ parameters to better capture the orientation at smaller strain units causes a shell-core-shell profile to be predicted at 100 strain units, which is not observed in the experimental data.

6.7 Conclusions

The orientation evolution predicted by the Folgar-Tucker model was demonstrated in a simple shear flow to produce different orientation kinetics that depend on the initial fiber orientation. The initial value of A_{12} could impact whether components of orientation evolved monotonically to a steady state or presented an overshoot and/or undershoot prior to reaching a steady state. Predictions of the fourth order components contributing to shear stress (A_{1212}) and the first normal stress difference (A_{1211}) also showed that their transient behavior was highly dependent on the initial fiber orientation. The influence of the initial fiber orientation on the orientation evolution in simple shear flow was confirmed to be independent of the IBOF closure approximation.

Repeatable initial fiber orientation was obtained from samples generated through injection molding, which produced a sample that varied in orientation through the sample thickness. The impact of a non-uniform fiber orientation on the velocity profile in a sliding plate rheometer was approximated. Deviations between simple shear flow and the calculated velocity profile were greatest at zero strain, but significantly decreased at small strains as the orientation became more consistent through the sample thickness. Based on this set of experimental data and the error associated with measuring A_{1212}, orientation that varies through the sample thickness does not appear to significantly alter the velocity profile in a sliding plate rheometer.

Parameters in the SRF and RSC orientation models were obtained from the experimental orientation evolution data averaged through the sample thickness from samples generated by injection molding. Predictions of fiber orientation evolution through the sample thickness provided different initial fiber orientations to test the model parameters. In general, the SRF model better captured the orientation evolution data, but both the SRF and RSC models over predicted the orientation kinetics at low values of shear strain while maintaining a steady state orientation. Model parameters that allow orientation models to predict reasonable agreement to fiber orientation evolution data from different initial fiber orientations in a well-defined flow should allow for a better assessment of fiber orientation models in complex flow simulations.

This study demonstrated the importance of the initial fiber orientation on the orientation predictions from rigid fiber models that have been widely studied in the literature. The approach of using the orientation evolution produced in a sliding plate rheometer to extract orientation model parameters allowed for the parameters to not be dependent on a complex processing flow. The multiple initial fiber orientations generated in samples from an injection molded part allow for evaluation of the orientation models in a well-defined flow with different initial fiber orientations. This procedure can be easily extended to different orientation models and fiber length systems. Samples generated for the simple shear flow tests can be from any basic injection molded plaque-like geometry. Furthermore, the injection molding of the basic plaque geometry could be performed on the same machine used to make the intended part with a more complex geometry which would allow for material parameters to better reflect the fibers in the intended injection molded part.

6.8 Acknowledgements

The authors wish to thank the American Chemistry Council for financially supporting this work. Additional acknowledgement is given to the Material Science and Engineering Department

at Virginia Tech for use of their polishing facilities and Prof. Michael Ellis for access to the microscope used for orientation measurements.

6.9 References

[1] Advani SG, Sozer EM. Process Modeling in Composites Manufacturing. New York: Marcel Dekker, Inc.; 2003.
[2] Gupta M, Wang KK. Fiber orientation and mechanical properties of short-fiber-reinforced injection molded composites: simulated and experimental results. Polym Compos. 1993;14:367-82.
[3] Jeffery GB. The motion of ellipsoidal particles immersed in a viscous fluid. Proc R Soc London, Ser A. 1922;102:161-79.
[4] Folgar F, Tucker CL. Orientation behavior of fibers in concentrated suspensions. J Reinf Plast Compos. 1984;3:98-119.
[5] Huynh HM. Improved Fiber Orientation Predictions for Injection-Molded Composites. Master's Thesis: University of Illinois Urbana-Champaign; 2001.
[6] Wang J, O'Gara JF, Tucker CL. An objective model for slow orientation kinetics in concentrated fiber suspensions: theory and rheological evidence. J Rheol. 2008;52:1179-200.
[7] Phelps JH, Tucker CL. An anisotropic rotary diffusion model for fiber orientation in short- and long-fiber thermoplastics. J Non-Newton Fluid Mech. 2009;156:165-76.
[8] Yamane Y, Kaneda Y, Doi M. Numerical simulation of semi-dilute suspensions of rodlike particles in shear flow. J Non-Newton Fluid Mech. 1994;54:405-21.
[9] Phan-Thien N, Fan XJ, Tanner RI, Zheng R. Folgar-Tucker constant for fiber suspension in a Newtonian fluid. J Non-Newton Fluid Mech. 2002;103:251-60.
[10] Bay RS. Fiber Orientation in Injection Molded Composites: A Comparison of Theory and Experiment. PhD Thesis: University of Illinois Urbana-Champaign; 1991.
[11] Eberle APR, Baird DG, Wapperom P, Vélez-García GM. Using transient shear rheology to determine material parameters in fiber suspension theory. J Rheol. 2009;53:685-705.
[12] Ortman K, Baird D, Wapperom P, Whittington A. Using startup of steady shear flow in a sliding plate rheometer to determine material parameters for the purpose of predicting long fiber orientation. J Rheol. 2012;56:955-81.
[13] Sepehr M, Carreau PJ, Grmela M, Ausias G, Lafleur PG. Comparison of rheological properties of fiber suspensions with model predictions. J Polym Eng. 2004;24:579-610.
[14] Advani SG, Tucker CL. The use of tensors to describe and predict fiber orientations in short fiber composites. J Rheol. 1987;31:751-84.
[15] Lipscomb GG, Denn MM, Hur DU, Boger DV. The flow of fiber suspensions in complex geometries. J Non-Newton Fluid Mech. 1988;26:297-325.
[16] Batchelor GK. The stress generated in a non-dilute suspension of elongated particles by pure straining motion. J Fluid Mech. 1971;46:813-29.
[17] Dinh SM, Armstrong RC. A rheological equation of state for semiconcentrated fiber suspensions. J Rheol. 1984;28:207-27.
[18] Shaqfeh ESG, Fredrickson GH. The hydrodynamic stress in a suspension of rods. Phys Fluids A. 1990;2:7-24.
[19] Petrich MP, Koch DL, Cohen C. An exerimental determination of the stress-microstructure relationship in semi-concentrated fiber suspensions. J Non-Newton Fluid Mech. 2000;95:101-33.

[20] Cieslinski MJ, Wapperom P, Baird DG. Obtaining repeatable initial fiber orientation for the transient rheology of fiber suspensions in simple shear flow. (submitted to the Journal of Rheology). 2015.
[21] Vélez-García GM, Wapperom P, Kunc V, Baird DG, Zink-Sharp A. Sample preparation and image acquisition using optical-reflective microscopy in the measurement of fiber orientation in thermoplastic composites. J Microsc. 2012;248:23-33.
[22] Vélez-García GM, Wapperom P, Baird DG, Aning AO, Kunc V. Unambiguous orientation in short fiber composites over small sampling area in a center-gated disk. Composites Part A. 2012;43:104-13.
[23] Bay RS, Tucker CL. Stereological measurement and error estimates for three-dimensional fiber orientation. Polym Eng Sci. 1992;32:240-53.
[24] Shampine LFR, M.W. The MATLAB ODE Suite. 24 Prime Park Way, Natick, MA 01760.
[25] Chung DH, Kwon TH. Invariant-based optimal fitting closure approximation for the numerical prediction of flow-induced fiber orientation. J Rheol. 2002;46:169-94.
[26] Fan XJ, Phan-Thien N, Zheng R. Simulation of fibre suspension flows by the Brownian configuration field method. J Non-Newton Fluid Mech. 1999;84:257-74.
[27] Sepehr M, Ausias G, Carreau PJ. Rheological properties of short fiber filled polypropylene in transient shear flow. J Non-Newton Fluid Mech. 2004;123:19-32.
[28] Eberle APR, Baird DG, Wapperom P, Vélez-García GM. Obtaining reliable transient rheological data on concentrated short fiber suspensions using a rotational rheometer. J Rheol. 2009;53:1049-68.
[29] Morrison FA. Understanding Rheology: Oxford University Press,, Inc. New York; 2001.
[30] Cengel YA, Cimbala JM. Fluid Mechanics: Fundamentals and Applications, 2nd Ed.: McGraw-Hill; 2009.
[31] Mazahir SM, Vélez-García GM, Wapperom P, Baird D. Fiber orientation in the frontal region of a center-gated disk: Experiments and simulation. J Non-Newton Fluid Mech. 2015;216:31-44.

6.10 Figures

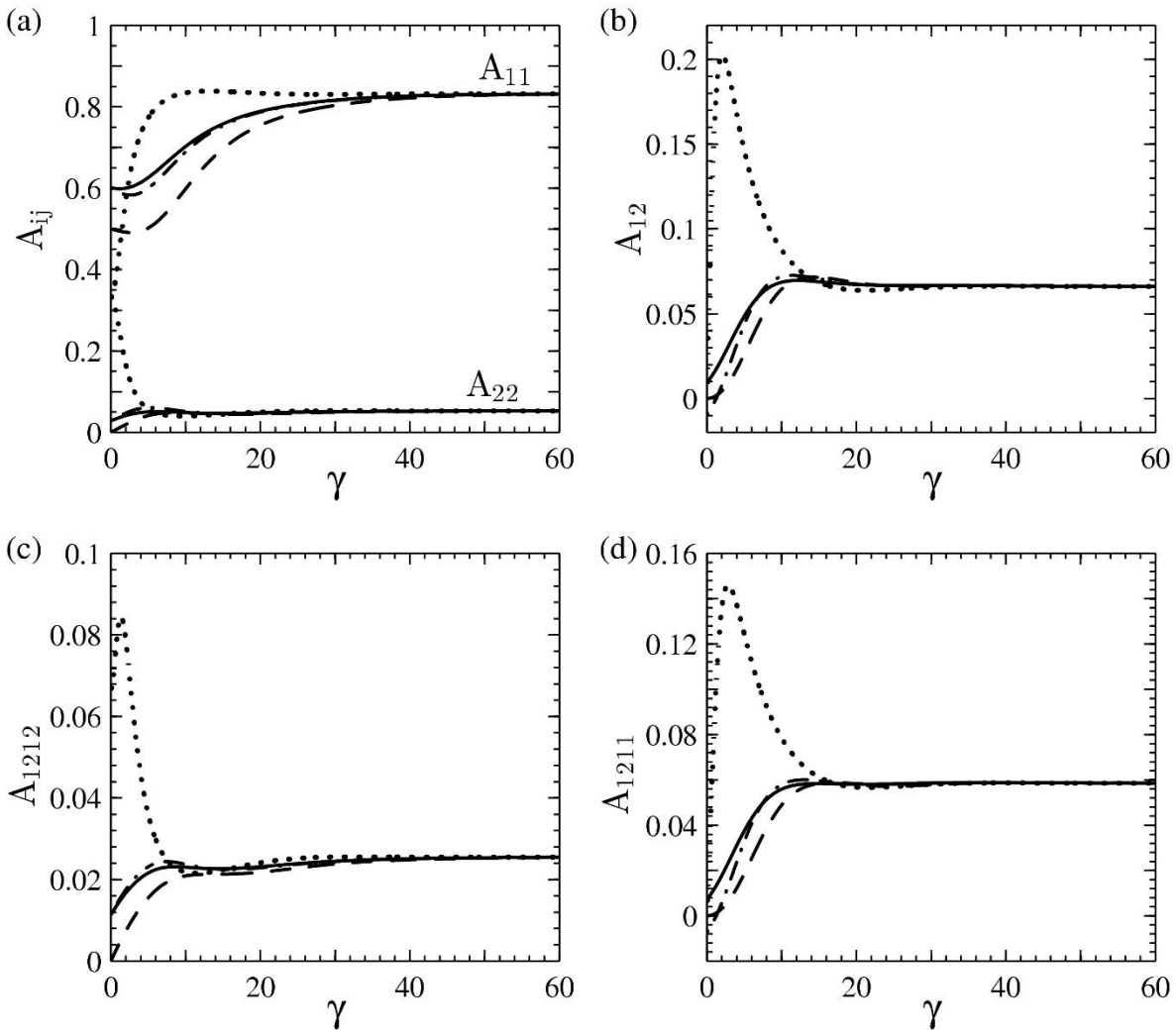

Figure 6.1: Fiber orientation predictions of (a) A_{11}, A_{22}, (b) A_{12}, (c) A_{1212} and (d) A_{1211} using the Folgar-Tucker model (C_I = 0.005) with initial fiber orientations of 3D random (dotted), random in the x_1x_3-plane (dashed) and experimental orientation from the non-uniform initial orientation sample [Eq.(6.7)] with positive A_{12} (solid) and negative A_{12} (dash-dot).

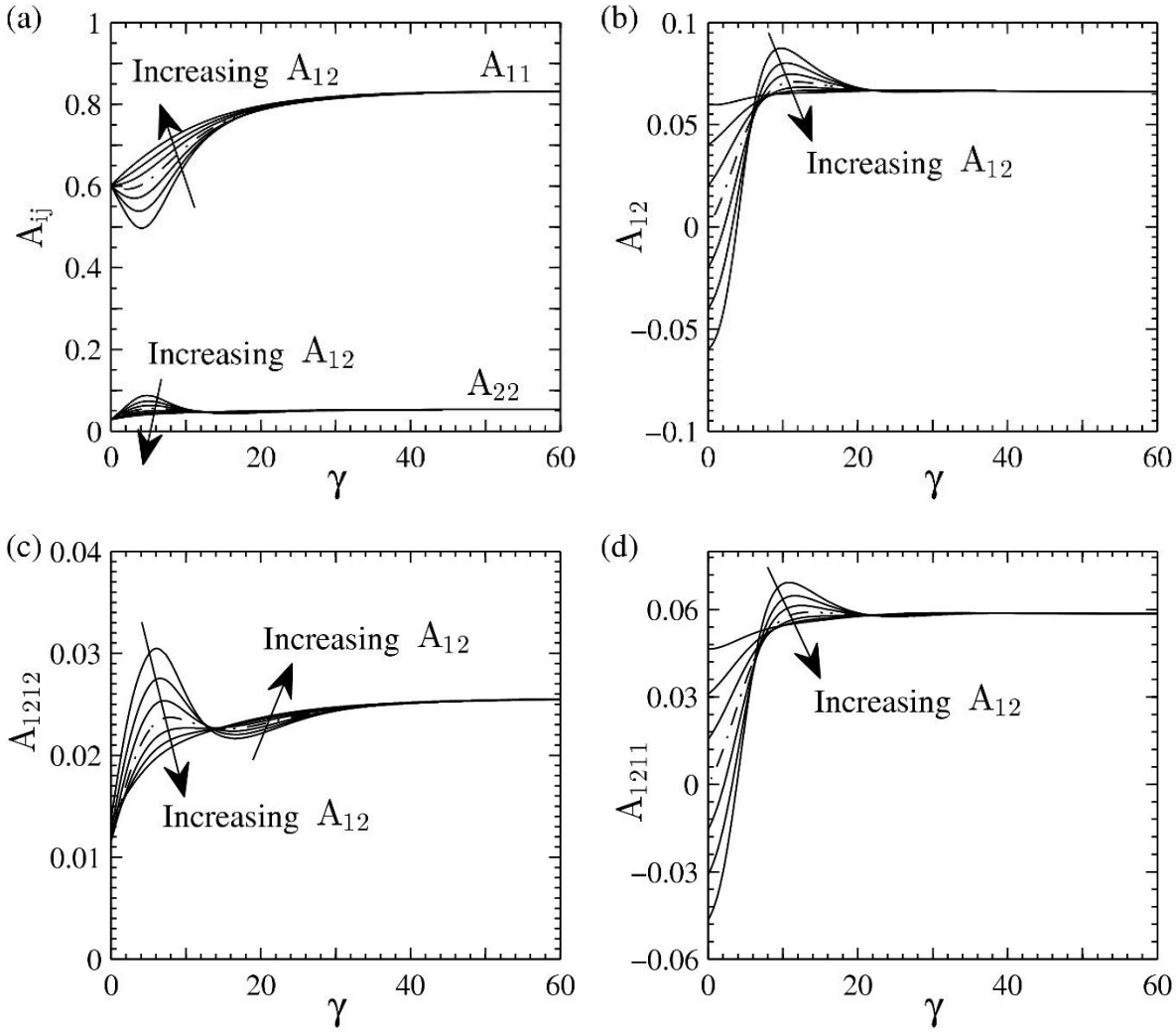

Figure 6.2: Predictions of (a) A_{11}, A_{22} (b) A_{12} (c) A_{1212}, and (d) A_{1211} using the Folgar-Tucker model (C_I = 0.005) with experimental values of A_{11}, A_{22} and A_{33} from the injection molded non-uniform initial orientation and the initial value of A_{12} varied from -0.06 to +0.06 in increments of 0.02. The initial value of A_{12} = 0 is denoted by the dash-dot line.

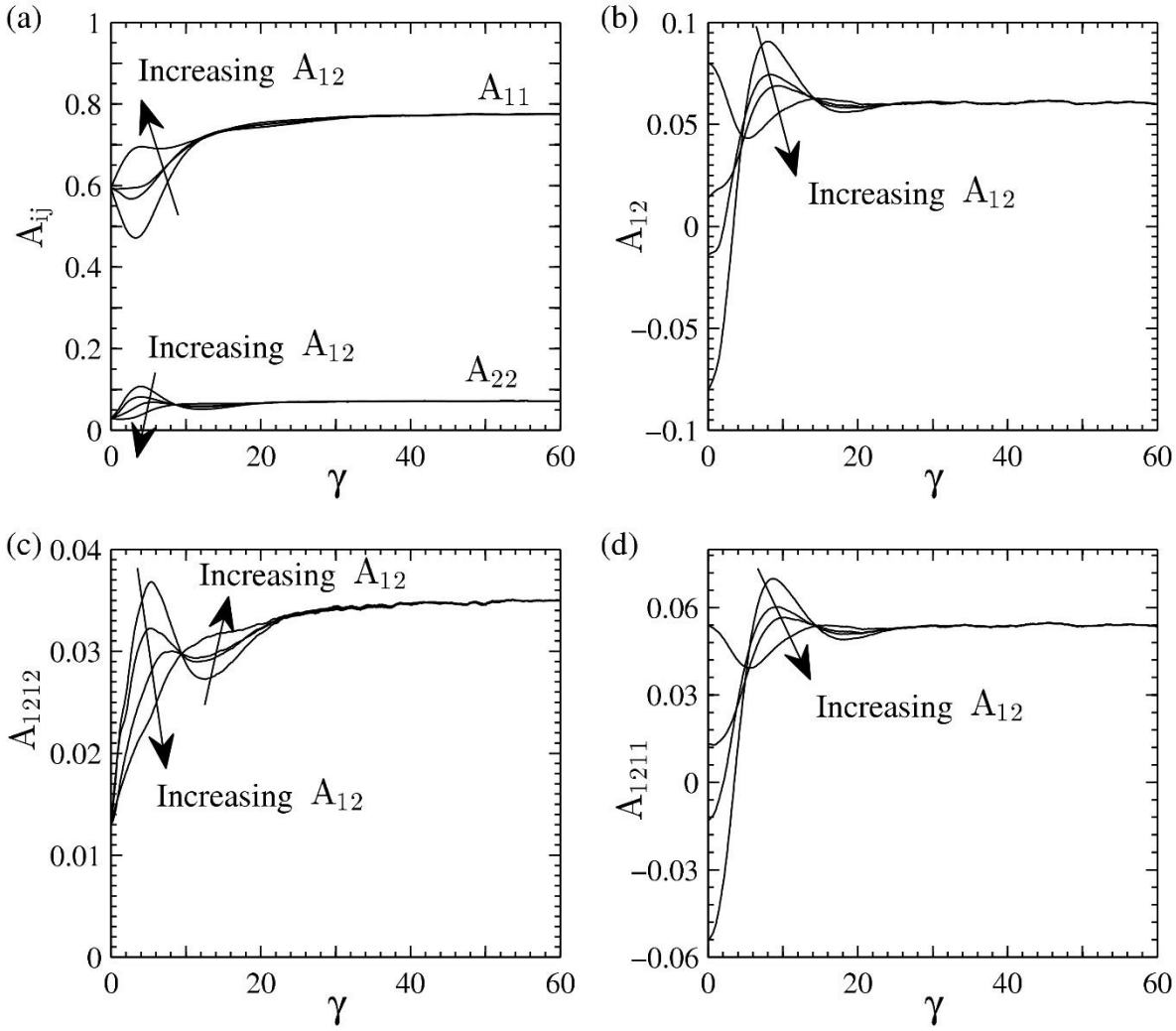

Figure 6.3: Predictions of (a) A_{11}, A_{22} (b) A_{12} (c) A_{1212}, and (d) A_{1211} from stochastic simulations using the Folgar-Tucker model (C_I = 0.005) and experimental **p** vectors with the initial values of A_{12} of -0.078, -0.014, +0.014 and +0.078.

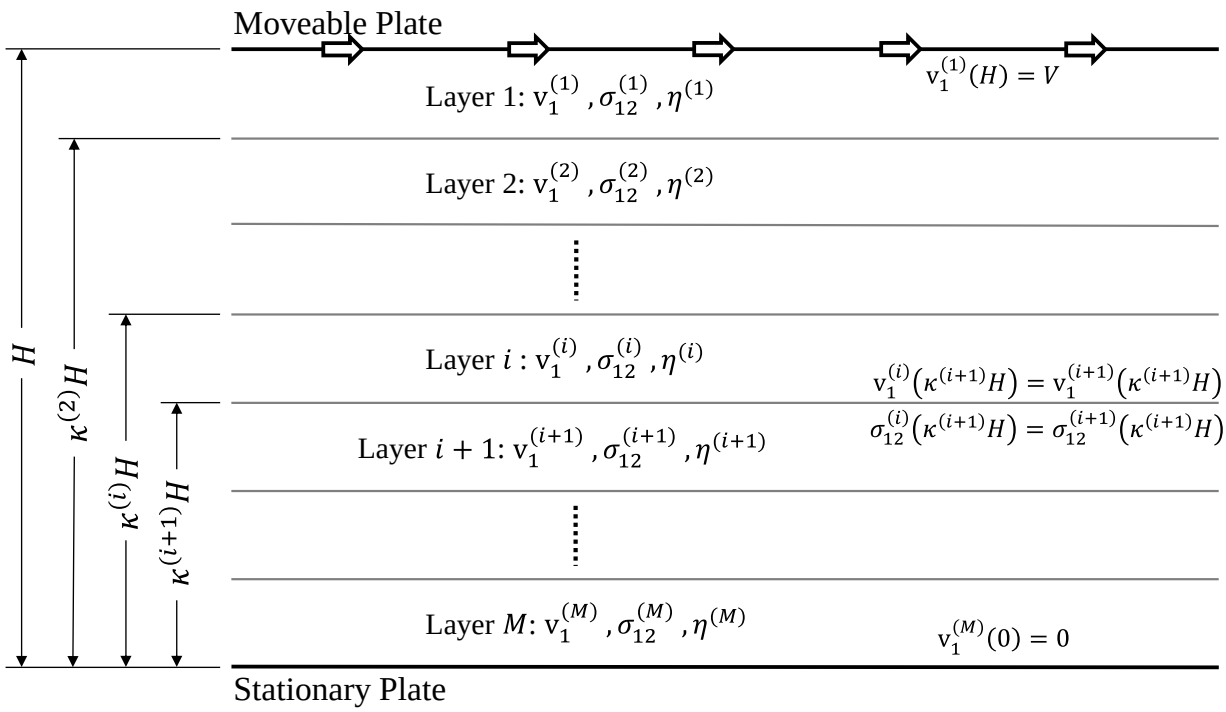

Figure 6.4: The fluid flow divided through the thickness of a sample in a sliding plate rheometer

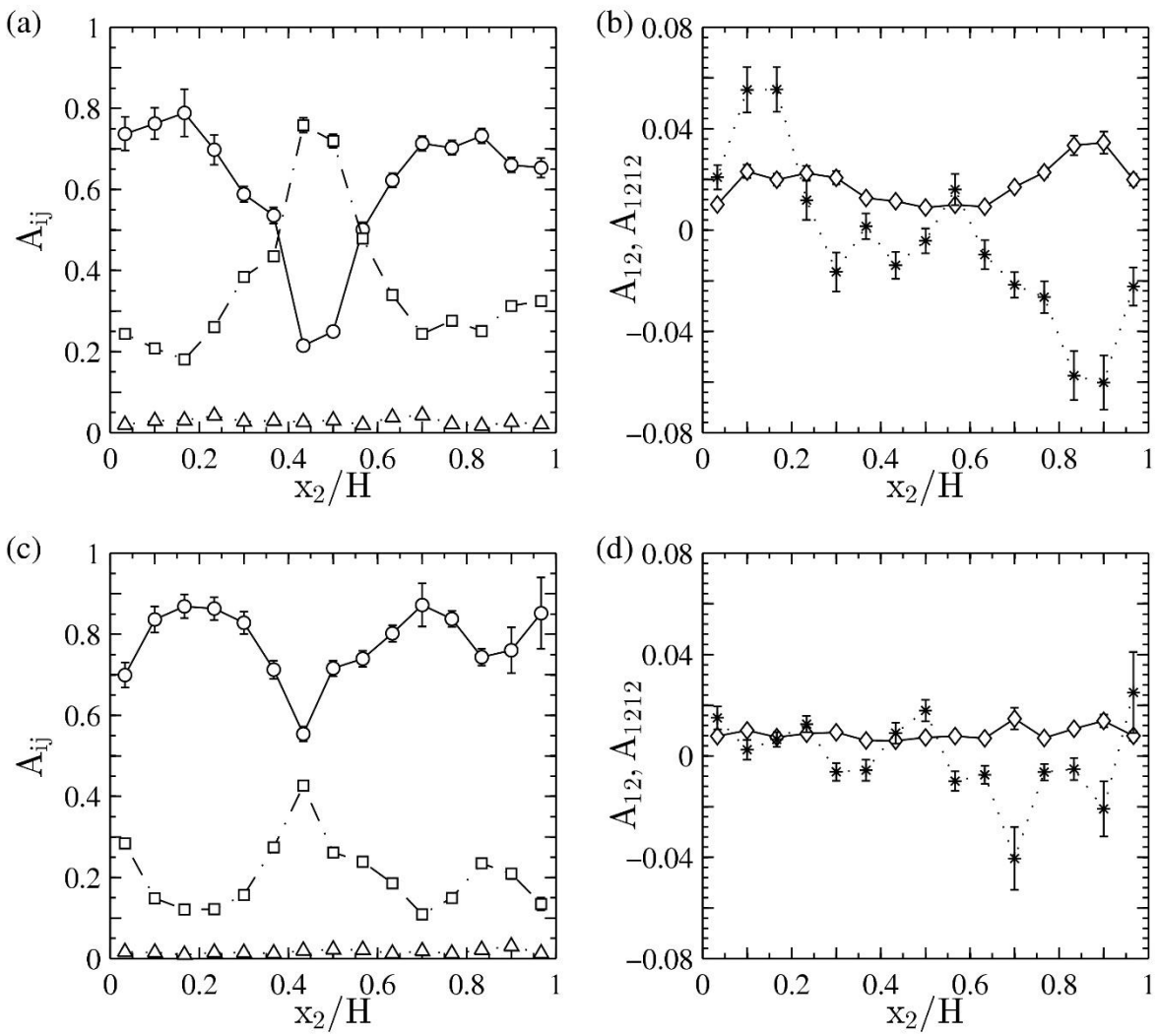

Figure 6.5: Experimental measurements of A_{11} (○), A_{22} (Δ), A_{33} (□), A_{12} (∗) and A_{1212} (◊) for the samples with (a,b) non-uniform and (c,d) uniform initial orientations generated through injection molding.

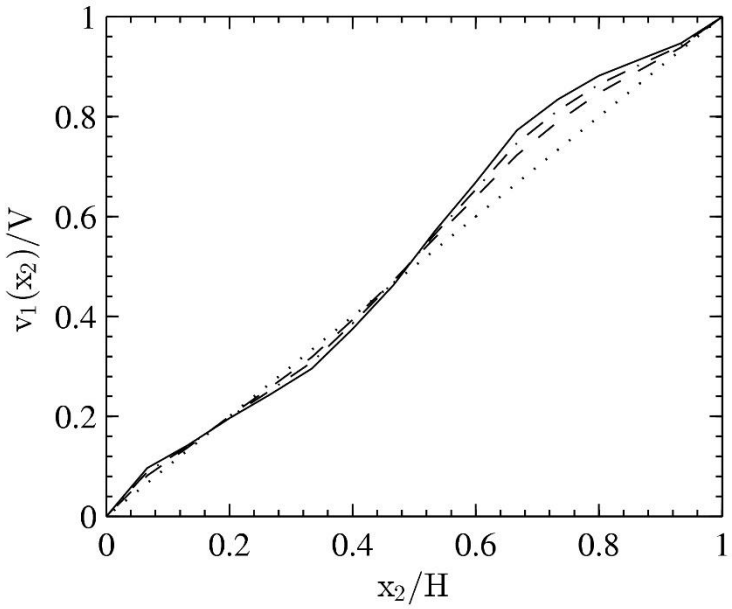

Figure 6.6: Normalized velocity profile divided into 15 layers through the sample thickness based on the non-uniform initial fiber orientation generated by injection molding for N_p = 0 (dotted line), 50 (dashed line), 120 (dash-dot line) and 500 (solid line).

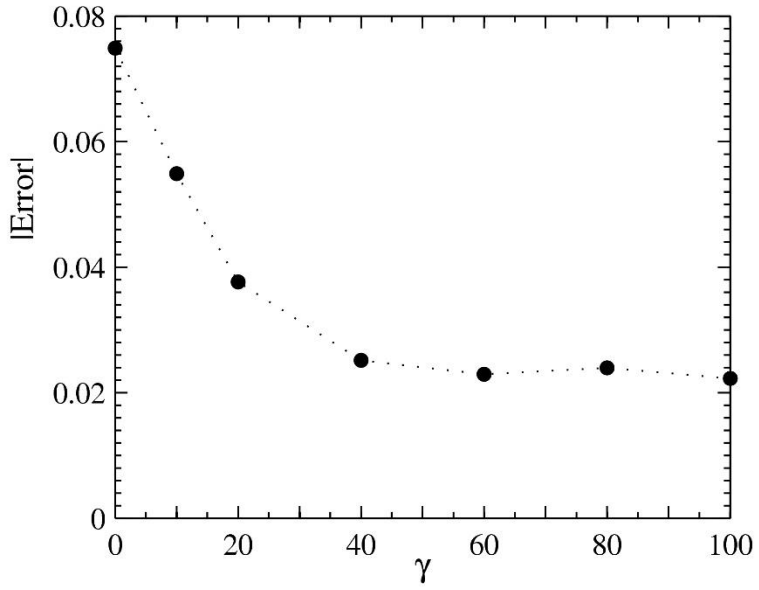

Figure 6.7: Average error between the velocity profiles calculated based on measured values of A_{1212} and simple shear flow within a sliding plate rheometer for N_p = 120.

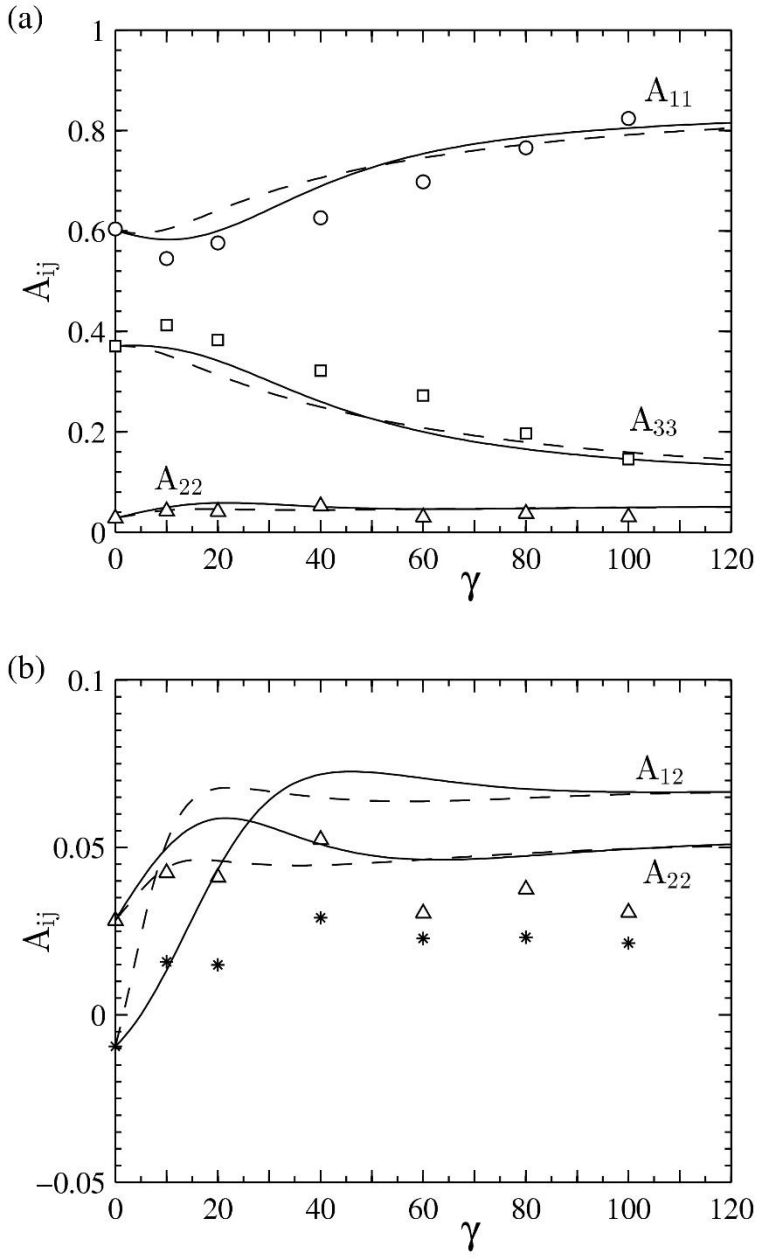

Figure 6.8: Comparison of fiber orientation simulations fit to measured values of orientation using the SRF (solid line) and RSC (dashed line) model with experimental values of A_{11} (○), A_{12} (∗), A_{22} (Δ) and A_{33} (□).

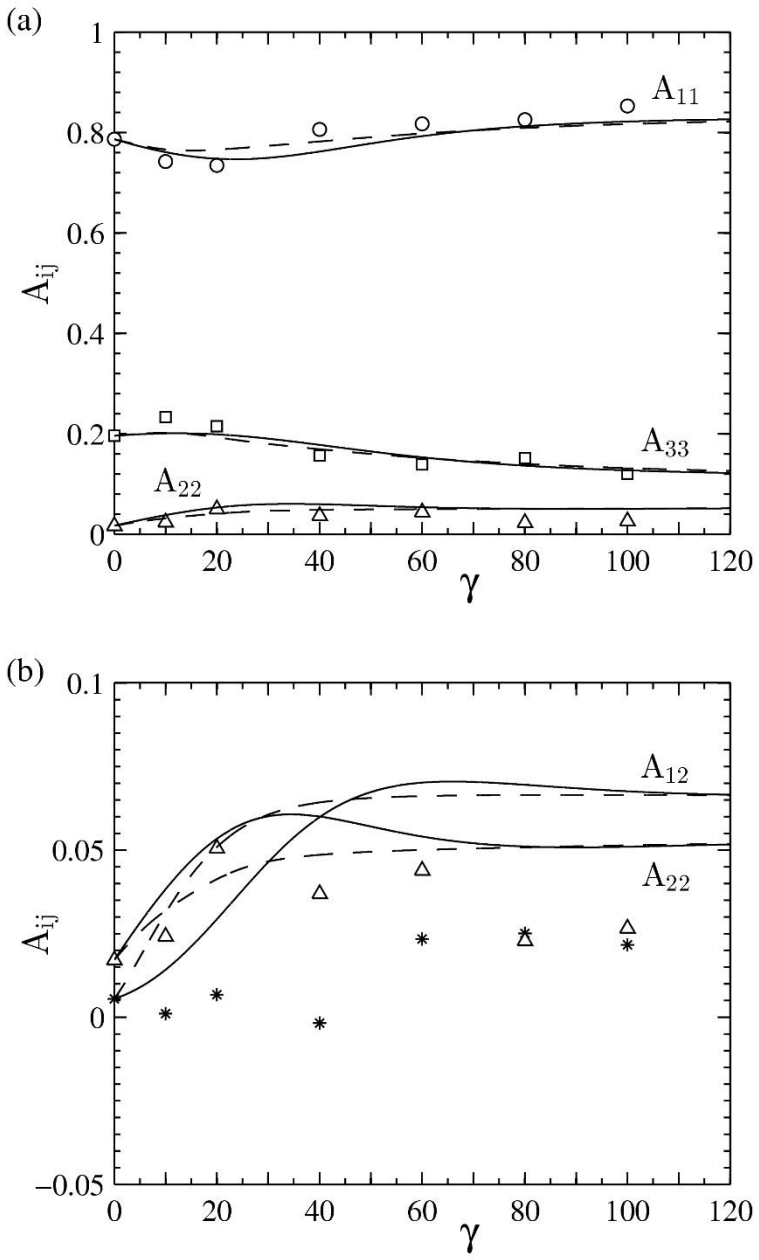

Figure 6.9: Measured values of (○) A_{11}, (∗) A_{12}, (Δ) A_{22} and (□) A_{33} compared to predictions of fiber orientation evolution from the uniform initial orientation using the (solid line) SRF and (dashed line) RSC with parameters (α = 0.25, κ = 0.2, C_I = 0.005) fit to the non-uniform experimental orientation evolution data.

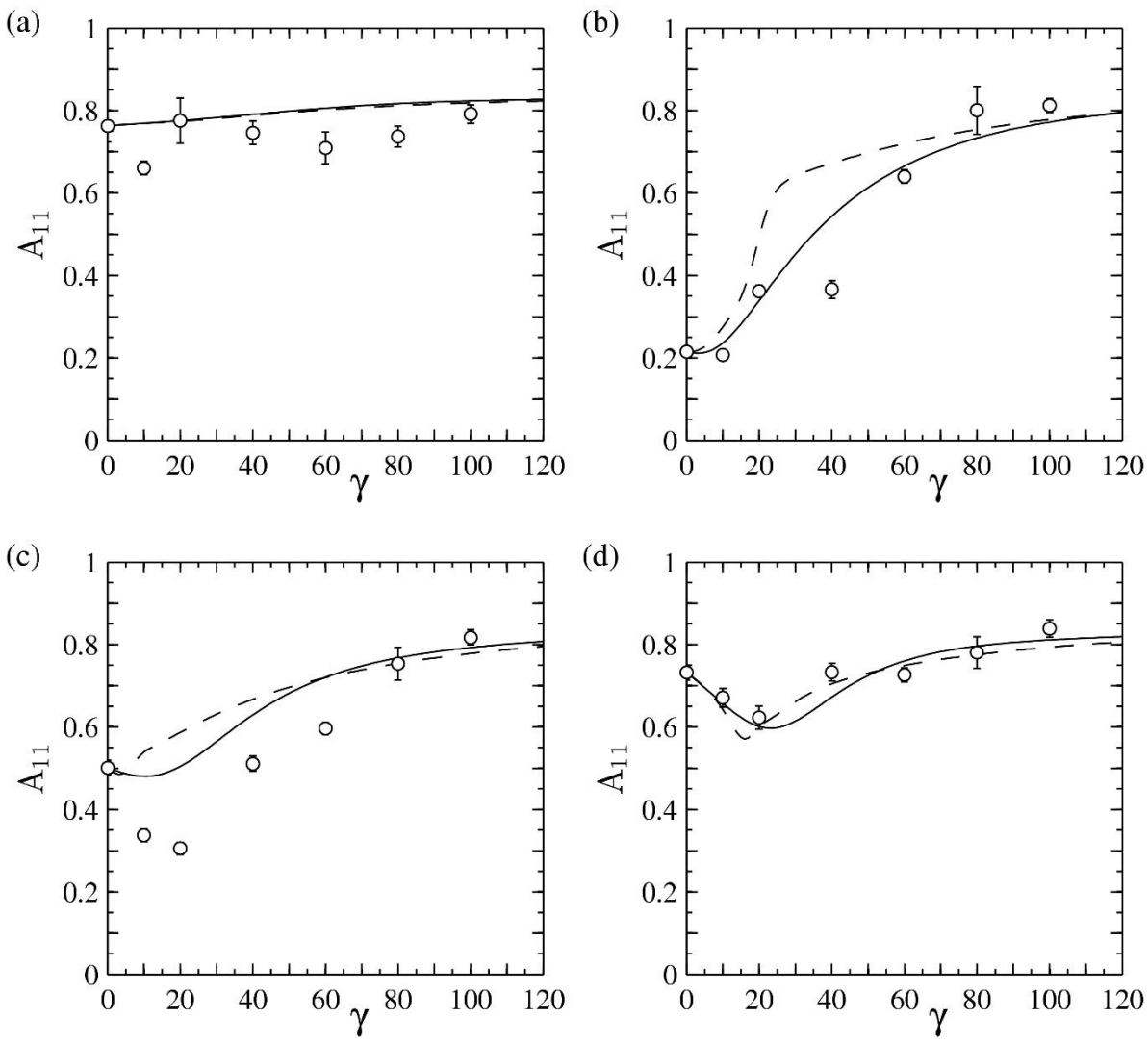

Figure 6.10: Simulations of the A_{11} component of orientation using the SRF (solid line) and RSC (dashed line) fiber orientation models with from the non-uniform initial orientation divided in to 15 layers through the sample thickness compared to the experimental data at values for x_2/H of (a) 0.1, (b) 0.43, (c) 0.56 and (d) 0.83.

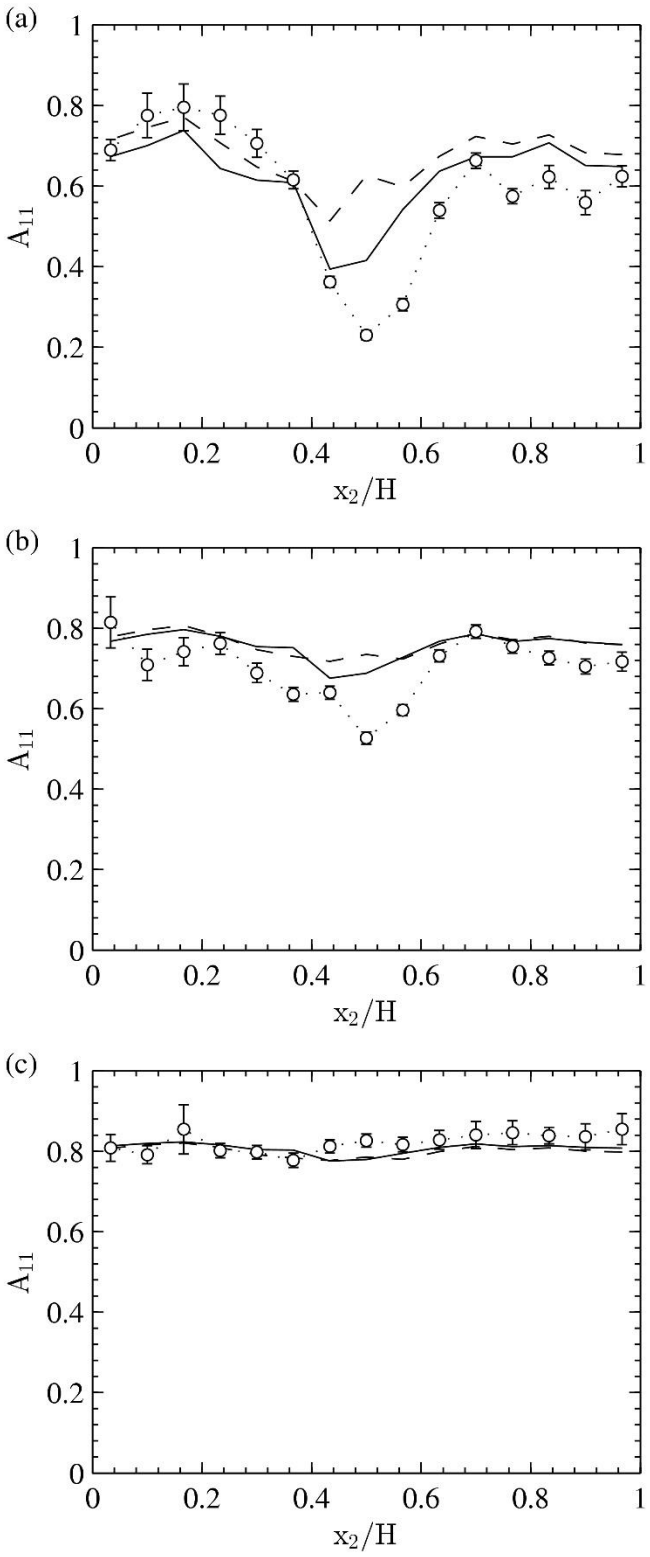

Figure 6.11: Predictions of the A_{11} component of fiber orientation through the sample thickness using the SRF (solid line) and RSC (dashed line) orientation models at shear strain units of (a) 20, (b) 60 and (c) 100 beginning from the non-uniform initial orientation.

Chapter 7 Conclusions and Recommendations

Chapter 7 Conclusions and Recommendations

7.1 Conclusions

The following conclusions stem from work pertaining to the research objectives described in Chapter 1:

1. The sliding plate rheometer with a shear stress transducer provided repeatable measurements of the transient shear stress response for glass and carbon fiber suspensions with concentrations up to 40 and 15.3 wt%, respectively, and number average fiber aspect ratios up to about 100. Increases in the aspect ratio or concentration of the fiber suspension was evident in the shear stress by an increased stress magnitude and an increased strain required to reach a steady state. Poor repeatability of the shear stress response during the startup of flow occurred for carbon fiber suspensions greater than 15.3 wt%. Furthermore, poor repeatability in glass fiber suspensions was observed with fiber aspect ratios significantly greater than 100 which was attributed to poor fiber dispersion (i.e. fiber bundles). Improved fiber dispersion resulted in a reduction of fiber length.

2. Fiber orientation measurements obtained as a function of shear strain provide necessary insight to the relationship between stress and fiber orientation. Fiber orientation data obtained at high shear strains was not always a constant value for high aspect ratio fibers, while a steady state was observed in the shear stress response, indicating that shear stress may be insensitive to small changes in fiber orientation. Direct measurements of fiber orientation obtained at multiple locations in a compression molded sample confirmed that the initial fiber orientation was not homogeneous nor repeatable, requiring alternative sample preparation methods to be pursued.

3. Generating samples with repeatable initial fiber orientation is critical for determining the relationship between orientation evolution and the measured stress response. Applying flow reversal to samples after they reached a steady state in the startup of flow improved the repeatability of the initial orientation, but measured values of the trace components of orientation did not change significantly under flow reversal. Additionally, a small overshoot that was within experimental error was measured during flow reversal for glass fibers with a number average length up to 0.7 mm. An injection molding sample preparation procedure provided improved repeatability in the initial orientation and the shear stress response during the startup of flow. A steady state in shear stress and fiber orientation were in excellent agreement using two different initial fiber orientations from the injection molded part.

4. Repeatable fiber evolution data allowed for stress and orientation models to be assessed independently. Based on measured orientation data, the available stress theories could not capture the transient response of a shear stress overshoot during the startup of simple shear flow. Fiber orientation model predictions can be sensitive to the initial fiber orientation, yielding different transient responses. Having repeatable orientation data allows for the fiber orientation models to be accurately assessed. Fiber orientation model parameters fit to fiber orientation evolution data from samples with a repeatable initial fiber orientation provided good agreement between model predictions and evolution data with different initial orientations in most cases. Parameters that provide reasonable agreement with different sets of orientation data in simple shear flow should allow for a better assessment of the orientation models in complex flow simulations.

7.2 Recommendations for Future Work

The following recommendations are presented based on the conclusions related to the proposed research objectives:

1. Some improvements to the sliding plate rheometer are recommended to increase measurement repeatability or to provide additional stress information. The first recommendation involves increasing the contact area of the shear stress transducer with the fluid. The current design of the shear stress transducer has a 10 mm diameter contact area. Local variations in fiber orientation or fiber bundles can result in a large, unrepeatable shear stress response. Increasing the contact area then determines the shear stress by averaging the force over a larger area. This improvement would likely allow for fibers with greater fiber lengths to be studied, which could not be reliably reported with the current design due to poor dispersion and fiber bundles. The second suggestion addresses the undesired sample deformation in the neutral direction for long fibers under flow reversal. To suppress sample deformation in the neutral direction, Teflon® rails could be added to the movable plate, as employed by Xu et al. [1] to mitigate a secondary flow. A third improvement would be to adapt the sliding plate rheometer to incorporate a normal stress transducer based on designs already available in the literature [1, 2]. Normal stresses provide an additional perspective into fiber orientation evolution. Measured fiber orientation data (see Figure 5.14) suggests that normal stresses will change to a greater extent than shear stresses under flow reversal. The normal stress transducers in the literature also do no interrupt the no slip boundary condition at the transducer location, which is not the case for shear stress transducers. Lastly, the flow in the sliding plate could be modified to provide an additional assessment of orientation and stress models under well-defined conditions. Specifically, an exponential shear flow (considered a strong shearing flow) [3] or converging shear flow (a well-defined, complex flow) [4] could be easily employed in the current sliding plate rheometer.

2. An extensional flow should be explored to provide comparison to the stress and orientation data obtained from simple shear flow. The fiber orientation components predicted to contribute to shear stress and normal stresses are small and any experimental variation in these orientation components is relatively large. An extensional flow would probe the stress equation with orientation components that would likely be greater in magnitude than the orientation components associated with the shear flow material functions. The extensional flow should dictate a preferential direction of fiber orientation, such as in uniaxial extension or planar elongation.

3. Additional approaches need to be considered to address fiber flexibility during flow. The concern that increasing the fiber length will potentially result in fibers bending during flow is difficult to assess in the sliding plate rheometer. From experimental measurements of fiber orientation, significant fiber curvature was not observed. Perhaps more curvature may be observed with materials that have a smaller tensile modulus, for example polymeric fibers. Once bent fibers are observed, experimental methods must be developed to quantify the degree of bending of the fibers to compare with model predictions.

4. Improvements to the stress equation are required in order to extract orientation information using the measured stresses obtained from a rheometer. Stress equations based on the fourth order orientation tensor were unable to predict a shear stress overshoot based on measured values of fiber orientation. Available stress equations that include fiber-fiber interactions in semi-dilute suspensions (see Appendix C) do not appear to predict a significantly different transient response compared to stress theories based only on the fourth order orientation tensor. Additional approaches to include fiber-fiber interactions must be considered to represent the dynamics of a concentrated long fiber system.

7.3 References

[1] Xu J, Costeux S, Dealy JM, Decker MN. Use of a sliding plate rheometer to measure the first normal stress difference at high shear rates. Rheol Acta. 2007;46:815-24.

[2] Oakley JG, Giacomin AJ. A sliding plate normal thrust rheometer for molten plastics. Polym Eng Sci. 1994;34:580-4.

[3] Doshi SR, Dealy JM. Exponential shear: a strong flow. J Rheol. 1987;31:563-82.

[4] Baek HM, Mix AW, Giacomin AJ. Converging shear rheometer. Korea-Aust Rheol J. 2014;26:127-39.

Appendix A Accounting for Fiber Flexibility

This section is devoted to the Bead-Rod orientation model used to predict the orientation of long, semi-flexible fibers. The orientation model is briefly presented from Chapter 2 for reference. The impact of the value describing the fiber flexibility on other empirical model parameters is addressed in simple shear flow. An approach is then provided to obtain an experimental approximation for fiber bending data that is intended to be used to compare with model predictions.

A.1 The Bead-Rod Orientation Model

The Bead-Rod orientation model represents a semi-flexible fiber by two adjoined vectors. The evolution equation for semi-flexible fibers was derived by Strautins and Latz [1], and later extended by Ortman et al. [2] to concentrated fiber suspensions:

$$\frac{D\mathbf{A}}{Dt} = \alpha\Big[\mathbf{W}\cdot\mathbf{A} - \mathbf{A}\cdot\mathbf{W} + (\mathbf{D}\cdot\mathbf{A} + \mathbf{A}\cdot\mathbf{D} - 2\mathbf{D}:\mathbf{A_4}) + 2C_I\dot{\gamma}(\mathbf{I} - 3\mathbf{A}) + \frac{l_B}{2}[\mathbf{Cm} + \mathbf{mC} - 2(\mathbf{m}\cdot\mathbf{C})\mathbf{A}] + 2k\big(\mathbf{B} - \mathbf{A}tr(\mathbf{B})\big)\Big] \tag{A.1}$$

$$\frac{D\mathbf{B}}{Dt} = \alpha\Big[\mathbf{W}\cdot\mathbf{B} - \mathbf{B}\cdot\mathbf{W} + (\mathbf{D}\cdot\mathbf{B} + \mathbf{B}\cdot\mathbf{D} - 2(\mathbf{D}:\mathbf{A})\mathbf{B}) - 4C_I\dot{\gamma}\mathbf{B} + \frac{l_B}{2}[\mathbf{Cm} + \mathbf{mC} - 2(\mathbf{m}\cdot\mathbf{C})\mathbf{B}] + 2k\big(\mathbf{A} - \mathbf{B}tr(\mathbf{B})\big)\Big] \tag{A.2}$$

$$\frac{D\mathbf{C}}{Dt} = \alpha\Big[\nabla\mathbf{v}^t\cdot\mathbf{C} - (\mathbf{A}:\nabla\mathbf{v}^t)\mathbf{C} - 2C_I\dot{\gamma}\mathbf{C} + \frac{l_B}{2}[\mathbf{m} - \mathbf{C}(\mathbf{m}\cdot\mathbf{C})] - k\mathbf{C}\big(1 - tr(\mathbf{B})\big)\Big] \tag{A.3}$$

$$\mathbf{m} = \sum_{i=1}^{3}\sum_{j=1}^{3}\sum_{k=1}^{3} \frac{\partial^2 \mathrm{v}_i}{\partial \mathrm{x}_j \partial \mathrm{x}_k} \mathrm{A}_{jk} \boldsymbol{\delta}_i \tag{A.4}$$

for the moments of fiber orientation defined as:

$$\mathbf{A} = \int\int \mathbf{pp}\psi(\mathbf{p},\mathbf{q},t)d\mathbf{p}d\mathbf{q} \tag{A.5}$$

$$\mathbf{B} = \int\int \mathbf{pq}\psi(\mathbf{p},\mathbf{q},t)d\mathbf{p}d\mathbf{q} \tag{A.6}$$

$$\mathbf{C} = \int\int \mathbf{p}\psi(\mathbf{p},\mathbf{q},t)d\mathbf{p}d\mathbf{q} \tag{A.7}$$

where $\mathbf{p}$ and $\mathbf{q}$ are adjoined vectors describing the orientation of a semi-flexible fiber. In the model, $\mathbf{W} = \frac{1}{2}(\nabla\mathbf{v}^t - \nabla\mathbf{v})$ is the vorticity tensor, $\mathbf{D} = \frac{1}{2}(\nabla\mathbf{v}^t + \nabla\mathbf{v})$ is the rate of deformation tensor, $\mathbf{I}$ is the identity tensor, $\boldsymbol{\delta}_i$ is a basis vector, l_B is half the fiber length, α is an empirical parameter to slow the orientation kinetics having a value from 0 to 1, C_I is the isotropic rotary diffusion coefficient and k describes the fiber flexibility. The average orientation of a bent fiber can be described by an end-to-end vector which can be written in terms of the orientation moments, $\mathbf{A}$ and $\mathbf{B}$:

$$\mathbf{R} = \frac{\mathbf{A} - \mathbf{B}}{1 - tr\mathbf{B}}. \tag{A.8}$$

The mechanism for bending in the semi-flexible fiber model is based on changes in the velocity gradient along the length of a fiber. In simple shear flow, the velocity gradient is constant and no bending is induced from the flow field (i.e. $\mathbf{m} = [0,0,0]$). Experimentally, little bending has been observed in the sliding plate rheometer. Figure A.1 shows a cross-section in the x_1x_2-midplane where there are two fibers greater than 1.2 mm in length that appear to be straight.

Slight bending is predicted in the model as a result of isotropic rotary diffusion, but this bending is small and would be difficult to compare with experimental measurements of bending. Rotary diffusion is a way to account for fiber interactions which may induce fiber bending. In a small number of samples, bent fibers have been observed in the polished cross section, but they are too infrequent to gather any insight on the average bending of fibers in the suspension. An example of the extent of bent fibers in a sample from the sliding plate rheometer is shown in Figure A.2. A more complex flow field containing a second derivative in velocity needs to be used to assess the ability of the Bead-Rod model to reflect the bending of long, semi-flexible fibers.

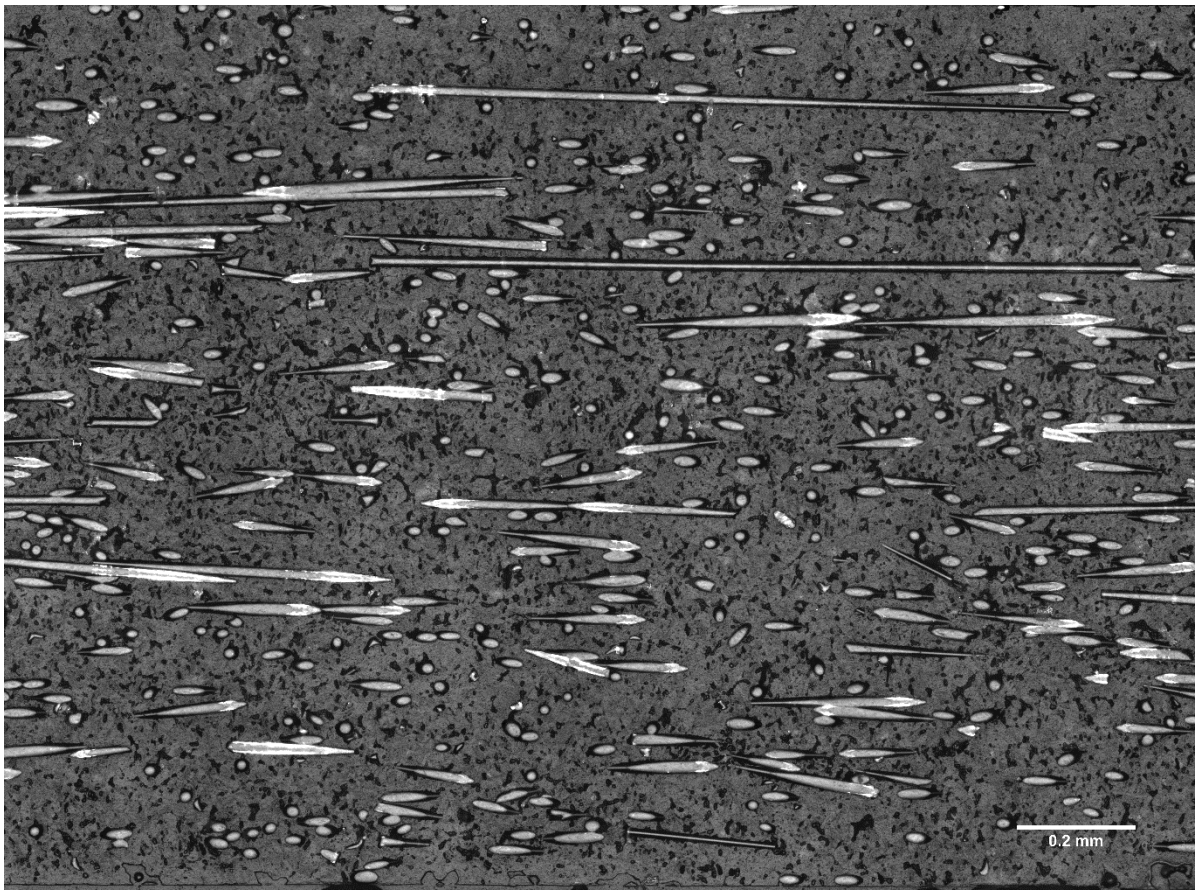

Figure A.1: Example of a sample from the sliding plate rheometer in the x_1x_2-midplane. Sample was tested at a shear rate of 1.0 s^{-1} for 80 strain units and has a number average fiber length of 0.9 mm. The top of the image coincides to the stationary plate while the bottom corresponds to the movable plate, traveling from left to right.

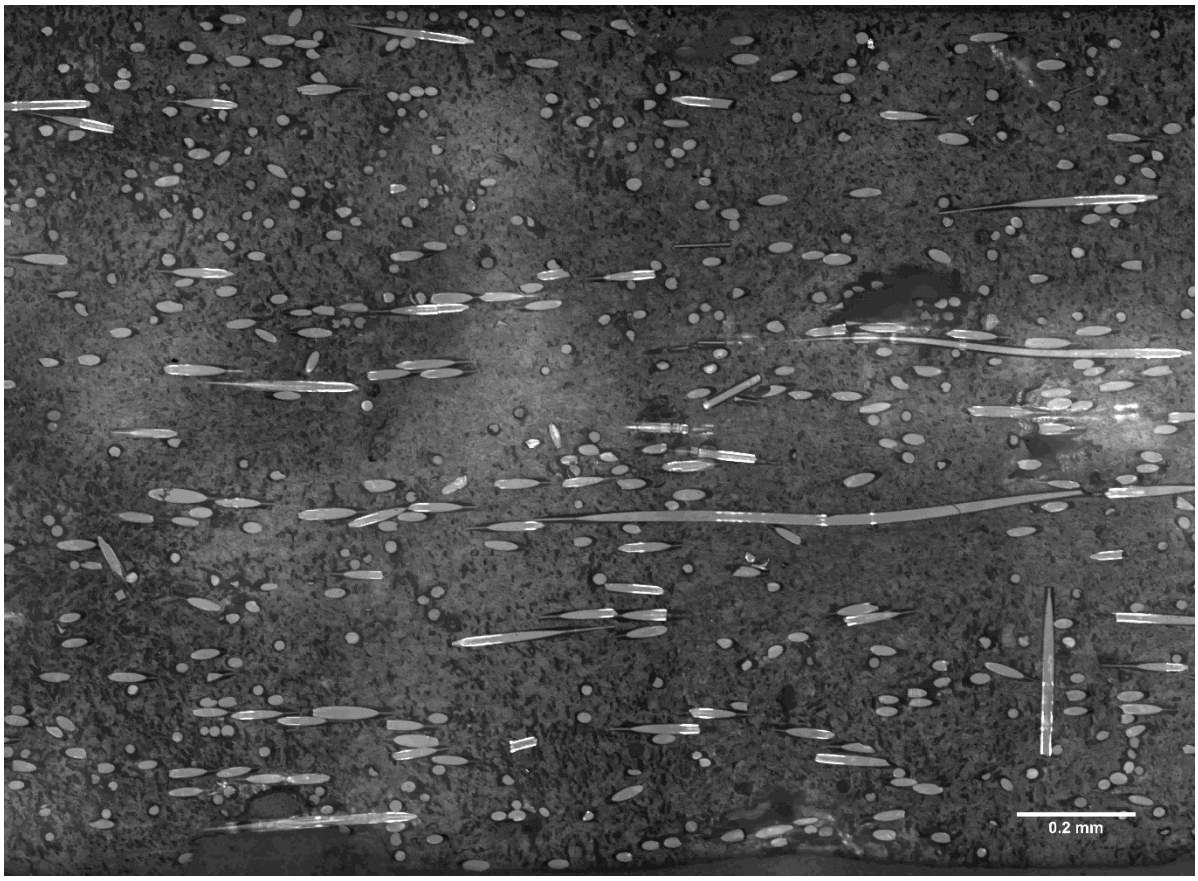

Figure A.2: Example of a sample from the sliding plate rheometer with some fiber curvature viewed in the x_1x_2-midplane. Sample was tested at a shear rate of 1.0 s^{-1} for 40 strain units and has a number average fiber length of 0.9 mm. The top of the image coincides to the stationary plate while the bottom corresponds to the movable plate, traveling from left to right.

A.2 Approximations for Fiber Bending

In the original model developed by Strautins and Latz [1], the parameter, k, that determines the fibers' flexibility is intended to be a fitting parameter. Ortman et al. [2] estimated this parameter by equating the bending potential of the bead-rod system with a beam under small deflection from a point load:

$$k = \frac{E_y}{8\eta_m}\frac{d^3}{L^3} \tag{A.9}$$

where E_y is the Young's modulus of the fiber, d the fiber diameter and η_m the matrix viscosity. This equation is dependent on the fiber aspect ratio, but in a typical system a broad range of fiber lengths exist. The approach from Ortman et al. [2] was to calculate a number average value for k based on the fiber length distribution:

$$k_n = \frac{\sum_i n_i k_i}{\sum_i n_i} \tag{A.10}$$

where n_i is the number of fibers length L_i and corresponding k_i. Encouraging predictions of fiber orientation were obtained from this method by Ortman et. al. [3], Mazahir [4] and Meyer et al. [5], but the sensitivity of this value has yet to be investigated. Instead of using Eq. (A.10), a weight average for k could be calculated which would give more preference to the shorter fibers:

$$k_w = \frac{\sum_i n_i k_i^2}{\sum_i n_i k_i}. \tag{A.11}$$

Other averages could be obtained by using the number average or weight average fiber lengths in Eq. (A.8):

$$k_{L_n} = \frac{E_y}{8\eta_m}\frac{d^3}{L_n^3} \tag{A.12}$$

$$k_{L_w} = \frac{E_y}{8\eta_m}\frac{d^3}{L_w^3}. \tag{A.13}$$

These four different averages for k were calculated based on three fiber length distributions that were generated from the experimental procedures in Chapters 3 and 5. Each fiber length distribution exhibits the typical log-normal profile. The average values for k are shown in Table

A.1. The four averaging techniques cause k to vary by orders of magnitude and it is unclear which value is a correct representation of the distribution of fiber lengths. Experimental measurements of fiber curvature could provide the additional constraint to define flexibility in the semi-flexible fiber orientation model.

Table A.1: Approximation of k for three fiber length distributions

	#1	#2	#3	Units
L_n	0.54	0.90	1.25	mm
L_w	0.72	1.81	2.28	mm
k_n	2655	2050	760	s^{-1}
k_w	19500	21079	11337	s^{-1}
k_{L_n}	602	133	49	s^{-1}
k_{L_w}	263	16	8	s^{-1}

A.3 Varying k in Simple Shear Flow

The Bead-Rod fiber orientation model imparts fiber bending through two mechanisms: velocity gradient changes along the length of the fiber and phenomenological fiber-fiber interactions governed by the parameter, C_I. In the sliding plate rheometer, simple shear flow is imposed on the suspension. As a result, the model only predicts bending to occur from rotary diffusion. This type of bending is small, but can still influence orientation behavior. To observe the model sensitivity to different values of k in simple shear flow, the predicted value of R_{11} in the model are fit to the measured A_{11} component of orientation by varying the values of α and C_I for a chosen value of k at a shear rate of 1.0 s^{-1} (Figure A.3)

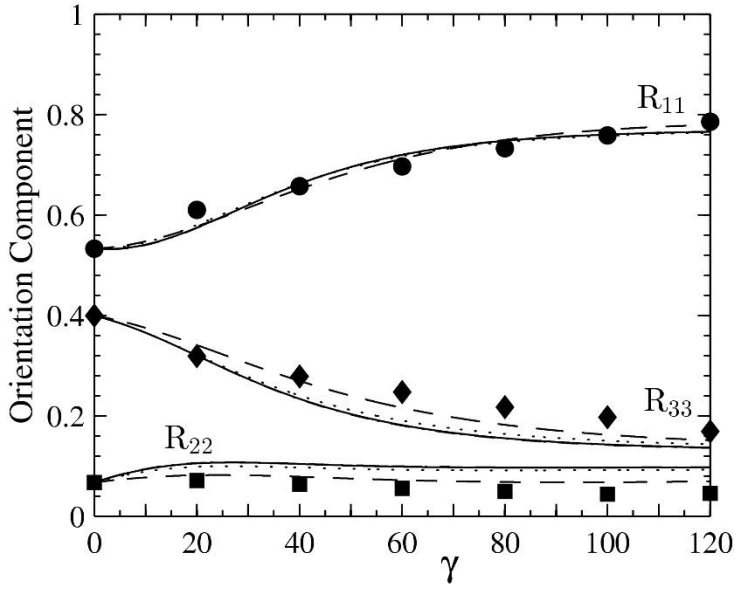

Figure A.3: Comparison between orientation evolution predictions from the semi-flexible fiber model for values of k = 0.02 (dashed line), 0.1 (dotted line), 1 (solid line) and 10 (dot-dashed line) s to measured A_{11} (●), A_{22} (■) and A_{33} (♦) orientation evolution data at a shear rate of 1.0 s^{-1}.

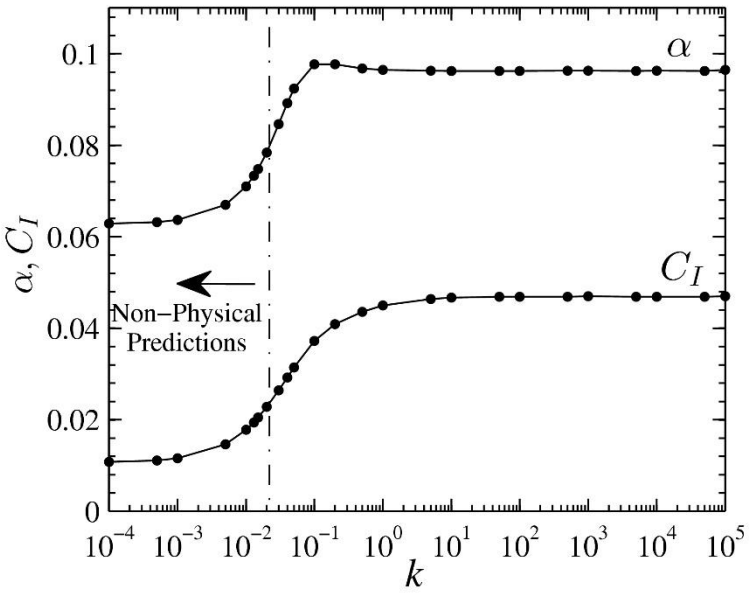

Figure A.4: Dependence of α and C_I on the choice of k at a number average fiber length of L_n = 1.25 mm fit to experimental orientation data at a shear rate of 1.0 s^{-1}. Values for k less than about 2 x 10^{-2} produced non-physical orientation predictions.

The parameters α and C_I used to fit R_{11} are plotted in Figure A.4 over range of k values spanning from 10^{-4} to 10^{5}. At low values for k, non-physical results were obtained. This is likely a result of a high degree of flexibility imparted in the model which may violate the assumption that these fibers are only semi-flexible. The non-phisicality was observed in the trace of **B** predictions which would drop below -1. It is unclear if this is a result of the closure approximate used for A_4 (IBOF), integration technique (Matlab ode45) or a fundamental limitation in the model. At high values of k, the parameters appear to be constant. This is likely a result of considering the fibers as nearly rigid. The parameters do show some dependency on k at values between about 0.02 to 10. However, it is unclear the accuracy of these results due to fact that the end-to-end tensor component was fit to experimental data obtained using the method of ellipses where fiber bending must be considered negligible. In the case where k is small, there is some significant discrepancy between the **A** and **R** orientation tensors in the semi-flexible fiber model. For this exercise, the prediction of R_{11} was compared to experimentally obtained values of A_{11}. When the model predicts significant bending (for example k = 0.02 to 1 in this case), both **R** and **A** tensors should be considered when comparing model predictions to experimental values of fiber orientation when the experimental curvature is unknown.

A.4 Bending in a Well-Defined Flow

Information on fiber evolution in the sliding plate rheometer could be combined with a more complex flow to validate bending described by the semi-flexible fiber orientation model. The parameters, α and C_I, in the model could be extracted from repeatable experimental orientation data from the sliding plate rheometer without much knowledge of the flexibility of the fiber suspension, because significant bending does not appear to occur in simple shear flow. The value prescribing the fiber flexibility, k, would then be addressed in a more complex flow that contains a second derivative in the velocity profile.

Well-defined flows encompassing a second derivative in velocity can be obtained from a tube or slit geometry. In addition to the second derivative in velocity, experimental measurements of fiber orientation should be able to quantify the degree of fiber bending to compare with model predictions. This section briefly documents attempts to produce samples of 30 wt% glass fiber in polypropylene in a simplified flow to observe bent fibers that could be characterized to compare with predictions from the Bead-Rod model.

A 9.5 mm diameter tube that was 230 mm in length was attached to the end of a 25 mm (20L/d) extruder (Killion KLB-100) in an attempt to provide a relatively simple, pressure driven flow. However, once the tube was cooled to preserve the fiber orientation, the sample was difficult to remove and it could not be guaranteed that the fiber orientation was undisturbed from the pressure required to push out the sample. From a polished cross section, it appeared that the fibers were not well dispersed exiting the extruder and maintain a fiber network that continued the rotation of the screw out to the end of the die.

A sample from a slit die was easy to extract because the die could be separated in half. The slit die had dimensions of (LxWxH) 107 mm x 12.6 mm x 1.23 mm. The slit die was attached to the end of the extruder and operated at 200 °C. The flow was stopped and the die was allowed to cool room temperature to preserve fiber orientation. The sample was removed and polished cross sections did not show a significant amount of fiber bending. It is thought that the fibers were either short and do not bend or that the fibers are spring-like and straightened upon the cessation of flow.

To avoid fiber straightening upon the cessation of flow, injection molded slits were created using the same die mentioned above. The mold was at room temperature and attached to an injection molder (Argburg Allrounder model 221-25-250). The cool mold temperature would minimize the amount of fiber straightening at the cessation of flow. The temperature gradient does complicate the problem to some extent, but this is intended to provide a first look at measuring bent fibers in a simple geometry. A polished cross section in the x_1x_3-midplane is shown in Figure A.5, such

that x_1 corresponds to the flow direct, x_2 is slit height and x_3 is the slit width. Near the top of the image, fibers are highly aligned in the flow direction. Fiber orientation is less aligned close to the die wall. Toward the center of the flow, there is less fiber alignment and some fiber curvature. However, this curvature does not appear to follow a clear pattern from x_1x_2-midplane out to the wall. Repeatable trends in fiber curvature must first be observed before they can be quantified and compared to model predictions.

A.5 Measurements of Fiber Curvature

According to Bay and Tucker [6] the standard method of ellipses for rigid fibers can be used when $L/2r_c \ll 1$, where r_c is the radius of curvature and L is the fiber length. However, it is clear from Figure 5 that the rigid rod assumption cannot be applied to many of the fibers exhibiting curvature. The approach of Hofmann [7] was to superimpose **p** and **q** vectors upon the curved objects visible in the imaging plane. This method does not account for the out-of-plane curvature. In addition, the fiber ends are not exposed so there is no way of determining the orientation of the fiber using this method. Without a full tracing of a fiber, a distinction between the **A** and **R** orientation tensors cannot be made.

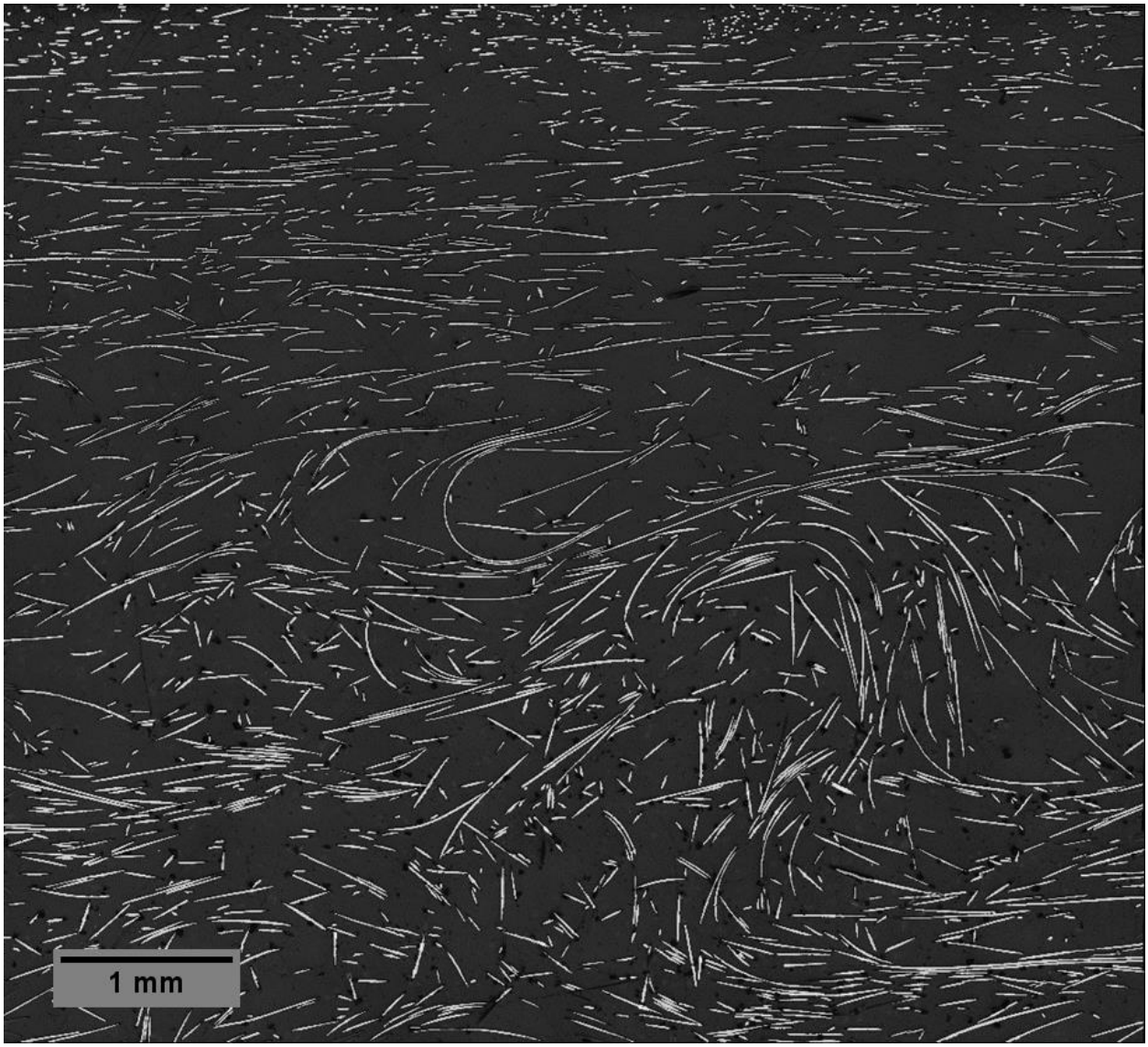

Figure A.5: Polished cross section in the x_1x_3-midplane from the slit die where the top of the image is at the wall and bottom is at the x_1x_2 symmetry plane. Pressure driven flow is from left to right. Image size is 6.3 mm height by 6.6 mm width.

Using polished cross sections, only a section of a fiber's orientation can be observed. The three-bead system of the Bead-Rod model can imply that a fiber will have a constant radius of curvature. The following analysis will relate a constant radius of curvature to the relative position of unit vectors **p** and **q**. The trace of **B** is the metric of fiber curvature in the semi-flexible fiber orientation model. Recalling the following relationship:

$$tr(\mathbf{B}) = \mathbf{p} \cdot \mathbf{q} = \cos(\theta_{\mathbf{pq}}) \tag{A.14}$$

where $\theta_{\mathbf{pq}}$ is the angle between unit vectors **p** and **q**.

A generic curved fiber is shown in Figure A.6. Three points from the fiber will exactly fit on a circle. The goal of the following analysis relates the curvature of this circle to the semi-flexible fiber orientation model.

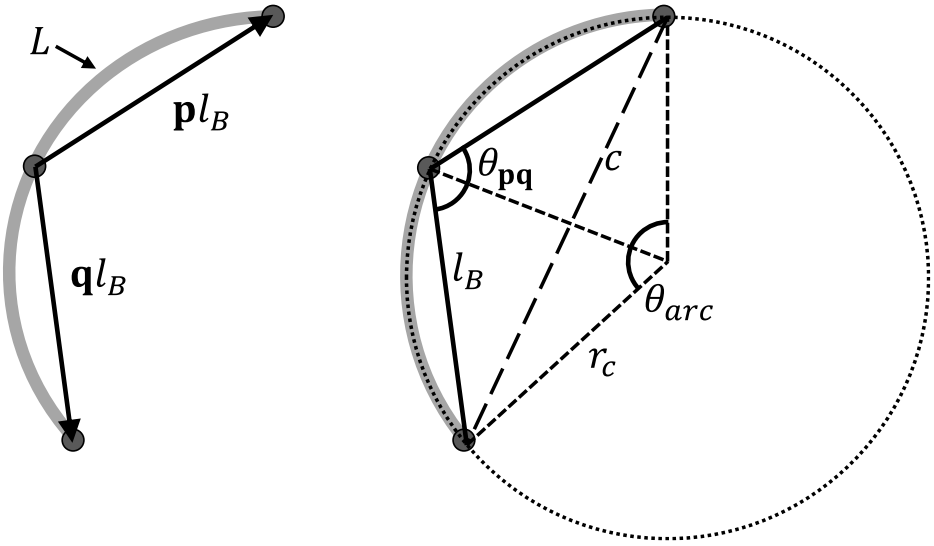

Figure A.6: A generic curved fiber of length L with a constant radius of curvature (left) represented by three beads and two rods and the fiber superimposed on a circle (right) with additional geometric relations.

Important quantities required for this analysis are the length of the fiber, L, and radius of curvature, r_c. From these two quantities, θ_{arc} can be determined:

$$\theta_{arc} = \frac{L}{r_c}. \tag{A.15}$$

Using the law of cosines, the following three relationships are made from triangles formed from l_B, r_c and chord c:

$$c^2 = 2r_c^2(1 - \cos(\theta_{arc})) \tag{A.16}$$

$$c^2 = 2l_B^2\left(1 - \cos\left(\theta_{\mathbf{pq}}\right)\right) \tag{A.17}$$

$$l_B^2 = 2r_c^2\left(1 - \cos\left(\frac{\theta_{arc}}{2}\right)\right). \tag{A.18}$$

These equations can be combined to find the trace of **B** for a single fiber length *L*:

$$tr(\mathbf{B}) = 1 - \frac{1}{2}\left(\frac{1 - \cos(\theta_{arc})}{1 - \cos\left(\frac{\theta_{arc}}{2}\right)}\right). \tag{A.19}$$

In the limit of $\theta_{arc} \to 0$, $tr(\mathbf{B}) = -1$. This equation will allow for comparison between model predictions and experimental measurements for the radius of curvature of a fiber. The intent is to use this equation in place of creating a full three dimensional trace of curved fibers through more involved experimental methods. However, more involved methods (for example, measuring curvature from perpendicular planes at the same location or creating a full fiber trace from μ-CT scans) must be used to verify that this relationship can be used to relate curved fibers to the $tr(\mathbf{B})$ in the bead-rod model.

This approximation has some significant limitations. First, this analysis is likely applicable for fibers that bend mostly in the plane parallel to the imaging plane. In order to measure the curvature perpendicular to the inspection plane, additional measurements would need to be made on parallel inspection planes separated by less than the fiber diameter. Secondly, the curvature predictions are based on the fact that the length of the fiber is known. The fiber length is unknown when measuring fiber orientation from a polished cross section. When considering a population of fibers, a weighting function is used to correct for sampling bias, but the weighting function must be modified to account for fiber curvature perpendicular to the inspection plane (see Bay and Tucker [6]). Lastly, long fibers may not be well represented by a single radius of curvature. In

Figure A.7, fibers are observed to have a S-shaped or U-shaped conformation. Large amount of curvature may not be well described by two adjoined rods, as in the Bead-Rod orientation model.

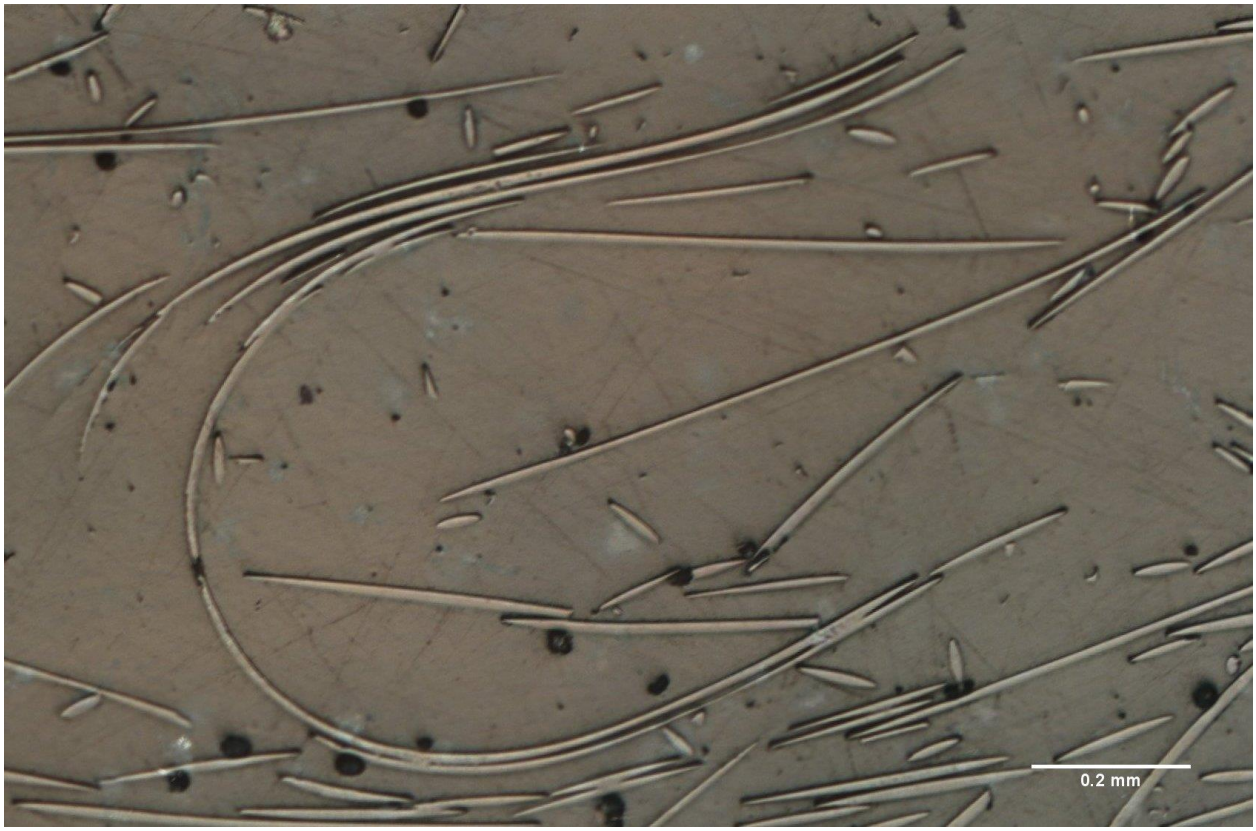

Figure A.7: An example of fiber curvature from Figure A.5 where the fibers cannot be described by a constant radius of curvature.

A.6 References

[1] Strautins U, Latz A. Flow-driven orientation dynamics of semiflexible fiber systems. Rheol Acta. 2007;46:1057-64.

[2] Ortman K, Baird D, Wapperom P, Whittington A. Using startup of steady shear flow in a sliding plate rheometer to determine material parameters for the purpose of predicting long fiber orientation. J Rheol. 2012;56:955-81.

[3] Ortman K, Baird D, Wapperom P, Aning A. Prediction of fiber orientation in the injection molding of long fiber suspensions. Polym Compos. 2012;33:1360-7.

[4] Mazahir S. Improvement in Orientation Predictions of High-Aspect Ratio Particles in Injection Mold Filling Simulations. PhD Thesis: Virginia Polytechnic Institute and State University; 2013.

[5] Meyer KJ, Hofmann JT, Baird DG. Initial conditions for simulating glass fiber orientation in the filling of center-gated disks. Composites Part A. 2013;49:192-202.

[6] Bay RS, Tucker CL. Stereological measurement and error estimates for three-dimensional fiber orientation. Polym Eng Sci. 1992;32:240-53.
[7] Hofmann JT. Extension of the Method of Ellipses to Determining the Orientation of Long, Semi-Flexible Fibers in Model 2- and 3-Dimensional Geometries. PhD Thesis: Virginia Polytechnic Institute and State University; 2013.

Appendix B Measurement Error Estimates

This section is devoted to extending the measurement error estimates of Bay and Tucker [1] to rectangular objects in the imaging plane. The measurement error is reported for the second order orientation tensors and components of the fourth order orientation tensor responsible for shear and normal stresses in simple shear flow. The image analysis region used for simple shear flow permits the measurement error to be larger than the sampling error. The relevant equations are reprinted from Bay and Tucker to estimate the measurement error. The analysis includes the additional approach of replacing the weighting function, F_k, with $F_k B_k$ to account for the fraction of an object when the analysis region is divided into bins through the sample thickness [2].

B.1 Estimation of Measurement Error

Four points are measured on the ellipse in the inspection plane (Figure B.1) in order to calculate the major, M, and minor, m, axes of the ellipse and the in plane orientation angle:

$$m = \sqrt{\left(x_1^{(3)} - x_1^{(4)}\right)^2 + \left(x_2^{(3)} - x_2^{(4)}\right)^2} \tag{B.1}$$

Bay and Tucker define additional variables, X and Y:

$$X = x_1^{(2)} - x_1^{(1)} \qquad Y = x_2^{(2)} - x_2^{(1)} \tag{B.2}$$

and the major axis is defined as:

$$M = \sqrt{X^2 - Y^2} \tag{B.3}$$

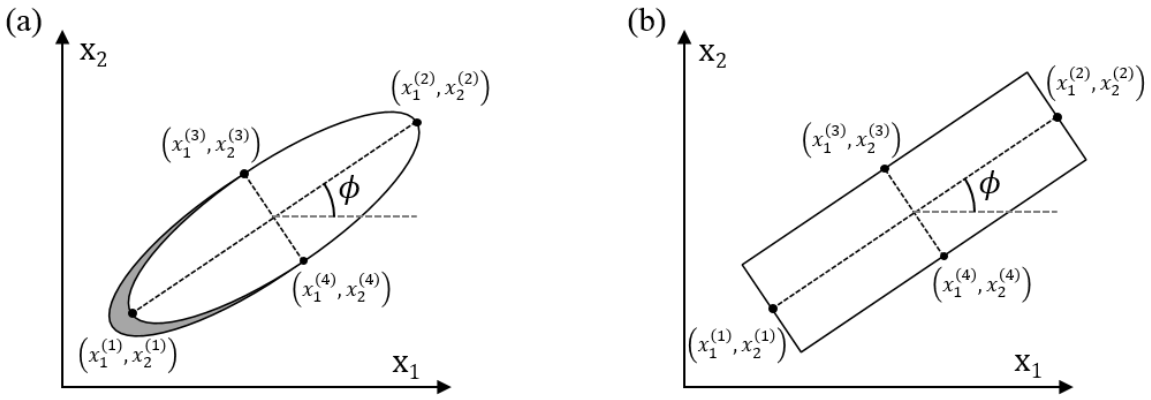

Figure B.1: Four points measured for (a) elliptical objects and (b) rectangular objects used to determine fiber orientation and measurement error

From these definitions the components of the second order orientation tensor are summarized in Table B.1 for elliptical and rectangular objects. Rectangular objects are assumed to have orientation only in the imaging plane.

Table B.1: Components of the second order tensor for a single fiber

Orientation Component	Elliptical Object	Rectangular Object
$(\mathrm{A}_{11})_k$	$X^2\left(\frac{1}{M^2}-\frac{m^2}{M^4}\right)$	$\frac{X^2}{M^2}$
$(\mathrm{A}_{12})_k = (\mathrm{A}_{21})_k$	$XY\left(\frac{1}{M^2}-\frac{m^2}{M^4}\right)$	$\frac{XY}{M^2}$
$(\mathrm{A}_{13})_k = (\mathrm{A}_{31})_k$	$X\sqrt{\frac{m^2}{M^4}-\frac{m^4}{M^6}}$	0
$(\mathrm{A}_{22})_k$	$Y^2\left(\frac{1}{M^2}-\frac{m^2}{M^4}\right)$	$\frac{Y^2}{M^2}$
$(\mathrm{A}_{23})_k = (\mathrm{A}_{32})_k$	$Y\sqrt{\frac{m^2}{M^4}-\frac{m^4}{M^6}}$	0
$(\mathrm{A}_{33})_k$	$\frac{m^2}{M^2}$	0

In obtaining an average fiber orientation using a polished cross section using the method of ellipses, a weighting function must be included to correct from sampling basis imposed from

using an imaging plate to obtain a three dimensional fiber orientation. The weighting function proposed by Bay and Tucker is specific to ellipses that are greater than half an ellipse and rectangular objects. The weighting function presented in Eq. (2.15) is recast as:

$$F_k = \begin{cases} \dfrac{M_k}{L_k m_k} & for \ \dfrac{m_k}{M_k} \leq \dfrac{d}{L_k} \\ \dfrac{1}{d} & for \ \dfrac{m_k}{M_k} > \dfrac{d}{L_k} \end{cases} \tag{B.4}$$

for the k-th fiber, where d is the diameter. A cut-off angle, $\theta_c = \arccos(d/L_k)$, is defined where the objects transition from elliptical to rectangular in shape. The weighted average fiber orientation can be constructed for a population of fibers as:

$$\mathrm{A}_{ij} = \frac{\sum_k \left(\mathrm{A}_{ij}\right)_k L_k F_k B_k}{\sum_k L_k F_k B_k} \tag{B.5}$$

where B_k is the fractional weighting function used when the sample is divided in bins through a part thickness [2]. The length of the fiber is assumed to be the number average fiber length, L_n, because the method of ellipse is a destructive process meaning that each fiber length cannot be determined.

For measurement error estimates, Eq. (B.5) is recast as:

$$\mathrm{A}_{ij} = \frac{G}{H} \tag{B.6}$$

where

$$G = \sum_{k=1}^{N} \left(\mathrm{A}_{ij}\right)_k F_k B_k \qquad H = \sum_{k=1}^{N} F_k B_k \tag{B.7}$$

The squared error is then defined as:

$$S_{\mathrm{A}_{ij}}^2 = \mathrm{A}_{ij}^2 \left(\frac{S_G^2}{G^2} + \frac{S_H^2}{H^2} + \frac{2\sqrt{S_H^2}}{H} \sqrt{\frac{S_G^2}{G^2}} \right) \tag{B.8}$$

with

$$S_G^2 = \sum_{k=1}^{N} S_{A_{ij_k} F_k}^2 B_k^2 \tag{B.9}$$

$$S_H^2 = \sum_{k=1}^{N} S_{F_k}^2 B_k^2 \tag{B.10}$$

The $S_{(\dots)_k}^2$ quantity in Eqs. (B.9) and (B.10) can found from Eq. (B.11), which has been extended to include variation in the fiber diameter measurements:

$$S_{(\dots)_k}^2 = \left(\frac{\partial (\dots)_k}{\partial X} \right)^2 \sigma_X^2 + \left(\frac{\partial (\dots)_k}{\partial Y} \right)^2 \sigma_Y^2 + \left(\frac{\partial (\dots)_k}{\partial m} \right)^2 \sigma_m^2 + \left(\frac{\partial (\dots)_k}{\partial L} \right)^2 \sigma_L^2 + \left(\frac{\partial (\dots)_k}{\partial d} \right)^2 \sigma_d^2 \tag{B.11}$$

where σ^2 is the fundamental measurement error for each measured quantity. The characteristic errors, σ_x , σ_y , σ_m , σ_L , and σ_d are determined based on the expected error of the instrument used to measure fiber orientation, length or diameter. In most cases, this is related to the imaging resolution of the microscope. For example, the measurement error reported in Chapters 5 and 6 were obtained at an image resolution of 0.24 μm/pixel and the error was assumed to be 5 pixels.

The large analysis region used to measure fiber orientation from samples obtained from the sliding plate rheometer allowed for the 95 % confidence interval of the mean value to be calculated:

$$\mathrm{A}_{ij} - 2\sqrt{S_{\mathrm{A}_{ij}}^2} \leq \mathrm{A}_{ij} \leq \mathrm{A}_{ij} + 2\sqrt{S_{\mathrm{A}_{ij}}^2}. \tag{B.12}$$

A similar expression can be developed for the confidence interval of the fourth order orientation tensor.

B.2 Calculations of Squared Error

Using the weighting function in Eq. (B.4), there are three cases that arise when an average fiber length is used (Table B.2). When an average fiber length is used to calculate the cut-off angle in the weighting function, it is possible to have ellipses with a major axis greater than the average fiber length. The cut-off angle is defined using the number average fiber length, L_n, in Table B.2. Bay and Tucker provide the first case for ellipses when the out-of-plane angle is less than the cut-off angle. In a 1-dimensional flow within the sliding plate rheometer, enough highly elongated objects and rectangles are observed to influence the average fiber orientation. To check the accuracy of the reported orientation averages, the measurement error is also calculated.

Table B.2: Weighting functions for three types of objects of measured objects

	Ellipses ≤ cut-off angle	Ellipses > cut-off angle	Rectangles
Definition	$\frac{m_k}{M_k} \leq \frac{d}{L_n}$	$\frac{m_k}{M_k} > \frac{d}{L_n}$	Fiber ends are observed
Weighting function, F_k	$\frac{M_k}{L_k m_k}$	$\frac{1}{d}$	$\frac{1}{d}$

The following definitions from Bay and Tucker are used for the for the k-th fiber to compactly present the squared error:

$$A = \frac{1}{m^2 M} + \frac{1}{M^3} \quad B = \frac{1}{mM} - \frac{m}{M^3} \quad C = \frac{3m}{M^4} - \frac{1}{mM^2} \quad D = \sqrt{\frac{1}{M^2} - \frac{m^2}{M^4}} \quad E = \frac{2m^2}{M^5} - \frac{1}{M^3} \tag{B.13}$$

The subscript, k, has been removed from the subsequent tables calculating the squared error.

B.2.1 Ellipses Less than the Cut-Off Angle

The squared error for each component in the second order orientation tensor is given in Table B.3(reprinted from Bay and Tucker [1]). The error for error for the orientation components contributing to shear and normal stresses is given in Table B.4.

Table B.3: Squared measurement error of **A** for elliptical objects below the cut-off angle

$$S^2_{\mathrm{A}_{11_k}F_k} = \left(\mathrm{A}_{11_k}F_k\right)^2\left(\frac{\sigma_L}{L}\right)^2 + \left(\frac{X^2}{L}A\right)^2\sigma_m^2 + \left(\frac{2X}{L}B + \frac{X^3}{ML}C\right)^2\sigma_X^2 + \left(\frac{YX^2}{ML}C\right)^2\sigma_Y^2$$

$$S^2_{\mathrm{A}_{12_k}F_k} = \left(\mathrm{A}_{12_k}F_k\right)^2\left(\frac{\sigma_L}{L}\right)^2 + \left(\frac{XY}{L}A\right)^2\sigma_m^2 + \left(\frac{Y}{L}B + \frac{YX^2}{ML}C\right)^2\sigma_X^2 + \left(\frac{X}{L}B + \frac{XY^2}{ML}C\right)^2\sigma_Y^2$$

$$S^2_{\mathrm{A}_{13_k}F_k} = \left(\mathrm{A}_{13_k}F_k\right)^2\left(\frac{\sigma_L}{L}\right)^2 + \left(\frac{mX}{LM^4}\frac{1}{D}\right)^2\sigma_m^2 + \left(\frac{1}{L}D + \frac{X^2}{ML}\frac{E}{D}\right)^2\sigma_X^2 + \left(\frac{XY}{ML}\frac{E}{D}\right)^2\sigma_Y^2$$

$$S^2_{\mathrm{A}_{22_k}F_k} = \left(\mathrm{A}_{22_k}F_k\right)^2\left(\frac{\sigma_L}{L}\right)^2 + \left(\frac{Y^2}{L}A\right)^2\sigma_m^2 + \left(\frac{Y^2X}{ML}C\right)^2\sigma_X^2 + \left(\frac{2Y}{L}B + \frac{Y^3}{ML}C\right)^2\sigma_Y^2$$

$$S^2_{\mathrm{A}_{23_k}F_k} = \left(\mathrm{A}_{23_k}F_k\right)^2\left(\frac{\sigma_L}{L}\right)^2 + \left(\frac{mY}{LM^4}\frac{1}{D}\right)^2\sigma_m^2 + \left(\frac{XY}{ML}\frac{E}{D}\right)^2\sigma_X^2 + \left(\frac{1}{L}D + \frac{Y^2}{ML}\frac{E}{D}\right)^2\sigma_Y^2$$

$$S^2_{\mathrm{A}_{33_k}F_k} = \left(\mathrm{A}_{33_k}F_k\right)^2\left(\left(\frac{\sigma_L}{L}\right)^2 + \left(\frac{\sigma_m}{m}\right)^2 + \frac{X^2\sigma_X^2 + Y^2\sigma_Y^2}{M^4}\right)$$

$$S^2_{F_k} = F_k^2\left(\left(\frac{\sigma_m}{m}\right)^2 + \left(\frac{\sigma_L}{L}\right)^2 + \frac{X^2\sigma_X^2 + Y^2\sigma_Y^2}{M^4}\right)$$

Table B.4: Squared measurement error for components of $\mathbf{A}_4$ contributing to shear and normal stresses in simple shear flow for ellipses less than the cut-off angle.

$$S^2_{\mathrm{A}_{1211_k F_k}} = \left(\mathrm{A}_{1211_k} F_k\right)^2 \left(\frac{\sigma_L}{L}\right)^2 + \left(\frac{3X^4YD^4}{LMm} - \frac{3X^2YD^4M}{Lm} - \frac{4X^4YmD^2}{LM^5}\right)^2 \sigma_x^2$$
$$+ \left(\frac{3X^3Y^2D^4}{LMm} - \frac{X^3MD^4}{Lm} - \frac{4X^3Y^2mD^2}{LM^5}\right)^2 \sigma_y^2 + \left(\frac{X^3YMD^4}{Lm^2} + \frac{4X^3YD^2}{LM^3}\right)^2 \sigma_m^2$$

$$S^2_{\mathrm{A}_{1212_k F_k}} = \left(\mathrm{A}_{1212_k} F_k\right)^2 \left(\frac{\sigma_L}{L}\right)^2 + \left(\frac{3X^3Y^2D^4}{LMm} - \frac{2XY^2D^4M}{Lm} - \frac{4X^3Y^2mD^2}{LM^5}\right)^2 \sigma_x^2$$
$$+ \left(\frac{3X^2Y^3D^4}{LMm} - \frac{2X^2YD^4M}{Lm} - \frac{4X^2Y^3mD^2}{LM^5}\right)^2 \sigma_y^2 + \left(\frac{X^2Y^2D^2}{L}\left(\frac{4}{M^3} + \frac{MD^2}{m^2}\right)\right)^2 \sigma_m^2$$

$$S^2_{\mathrm{A}_{1222_k F_k}} = \left(\mathrm{A}_{1222_k} F_k\right)^2 \left(\frac{\sigma_L}{L}\right)^2 + \left(\frac{3X^2Y^3D^4}{LMm} - \frac{Y^3MD^4}{Lm} - \frac{4X^2Y^3mD^2}{LM^5}\right)^2 \sigma_x^2$$
$$+ \left(\frac{3XY^4D^4}{LMm} - \frac{3XY^2D^4M}{Lm} - \frac{4XY^4mD^2}{LM^5}\right)^2 \sigma_y^2 + \left(\frac{XY^3MD^4}{Lm^2} + \frac{4XY^3D^2}{LM^3}\right)^2 \sigma_m^2$$

$$S^2_{\mathrm{A}_{1233_k F_k}} = \left(\mathrm{A}_{1233_k} F_k\right)^2 \left(\frac{\sigma_L}{L}\right)^2 + \left(\frac{2X^2Ym^3}{LM^7} + \frac{YmD^2}{LM} - \frac{3X^2YmD^2}{LM^3}\right)^2 \sigma_x^2$$
$$+ \left(\frac{2XY^2m^3}{LM^7} + \frac{XmD^2}{LM} - \frac{3XY^2mD^2}{LM^3}\right)^2 \sigma_y^2 + \left(\frac{2XYm^2}{LM^5} - \frac{XYD^2}{LM}\right)^2 \sigma_m^2$$

B.2.2 Ellipses greater than the cut-off angle

With the calculation of the cut-off angle based on an average fiber length, it is possible to have ellipses with a major axis greater than the average fiber length. The squared error for the components of orientation of interest in the second and fourth order orientation tensors are given in Table B.5and Table B.6, respectively. The case where the major axis was greater than the number average fiber length was seldom observed in the data in Chapter 5.

Table B.5: Squared measurement error of **A** for elliptical objects above the cut-off angle

$$S^2_{\mathrm{A}_{11_k}F_k} = F_k^2\left(\left(-\frac{2X^3}{M}E - 2XD^2\right)^2\sigma_X^2 + \left(\frac{2X^2Y}{M}E\right)^2\sigma_Y^2 + \left(\frac{2X^2m}{M^4}\right)^2\sigma_m^2\right) + \left(\mathrm{A}_{11_k}F_k\right)^2\left(\frac{\sigma_d}{d}\right)^2$$

$$S^2_{\mathrm{A}_{12_k}F_k} = F_k^2\left(\left(YD^2 + \frac{2X^2Y}{M}E\right)^2\sigma_X^2 + \left(XD^2 + \frac{2XY^2}{M}E\right)^2\sigma_Y^2 + \left(\frac{2XYm}{M^4}\right)^2\sigma_m^2\right) + \left(\mathrm{A}_{12_k}F_k\right)^2\left(\frac{\sigma_d}{d}\right)^2$$

$$S^2_{\mathrm{A}_{13_k}F_k} = F_k^2\left(\left(\frac{m}{M}D - \frac{X^2m}{DM^5}\left(2 - \frac{3m^2}{M^2}\right)\right)^2\sigma_X^2 + \left(\frac{XYm}{M^5D}\left(2 - \frac{3m^2}{M^2}\right)\right)^2\sigma_Y^2 + \left(\frac{X}{M^3D}\left(\frac{2m^2}{M^2} - 1\right)\right)^2\sigma_m^2\right) + \left(\mathrm{A}_{13_k}F_k\right)^2\left(\frac{\sigma_d}{d}\right)^2$$

$$S^2_{\mathrm{A}_{22_k}F_k} = F_k^2\left(\left(\frac{2XY^2}{M}E\right)^2\sigma_X^2 + \left(-\frac{2Y^3}{M}E - 2YD^2\right)^2\sigma_Y^2 + \left(\frac{2Y^2m}{M^4}\right)^2\sigma_X^2\right) + \left(\mathrm{A}_{22_k}F_k\right)^2\left(\frac{\sigma_d}{d}\right)^2$$

$$S^2_{\mathrm{A}_{23_k}F_k} = F_k^2\left(\left(\frac{XYm}{M^5D}\left(2 - \frac{3m^2}{M^2}\right)\right)^2\sigma_X^2 + \left(\frac{m}{M}D - \frac{Y^2m}{DM^5}\left(2 - \frac{3m^2}{M^2}\right)\right)^2\sigma_Y^2 + \left(\frac{Y}{M^3D}\left(\frac{2m^2}{M^2} - 1\right)\right)^2\sigma_m^2\right) + \left(\mathrm{A}_{23_k}F_k\right)^2\left(\frac{\sigma_d}{d}\right)^2$$

$$S^2_{\mathrm{A}_{33_k}F_k} = \left(\frac{2mF_k}{M^2}\right)^2\left(\sigma_m^2 + \frac{m^2(X^2\sigma_X^2 + Y^2\sigma_Y^2)}{M^4}\right) + \left(\mathrm{A}_{33_k}F_k\right)^2\left(\frac{\sigma_d}{d}\right)^2$$

$$S^2_{F_n} = \frac{\sigma_d^2}{d^4}$$

Table B.6: Squared measurement error for components of $\mathbf{A}_4$ contributing to shear and normal stresses in simple shear flow for ellipses less than the cut-off angle.

$$S^2_{\mathrm{A}_{1211_k}F_k} = \left(\frac{4X^3YmD^2}{dM^4}\right)^2 \sigma_m^2 + \left(\frac{4X^4YD^4}{dM^2} - \frac{3X^2YD^4}{d} - \frac{4X^4Ym^2D^2}{dM^6}\right)^2 \sigma_x^2 + \left(\frac{4X^3Y^2D^4}{dM^2} - \frac{X^3D^4}{d} - \frac{4X^3Y^2m^2D^2}{dM^6}\right)^2 \sigma_y^2 + \left(\mathrm{A}_{1211_k}F_k\right)^2 \left(\frac{\sigma_d}{d}\right)^2$$

$$S^2_{\mathrm{A}_{1212_k}F_k} = \left(\frac{2XYD}{M^2}\right)^4 \frac{m^2}{d^2} \sigma_m^2 + \left(\frac{4X^3Y^2D^4}{dM^2} - \frac{2XY^2D^4}{d} - \frac{4X^3Y^2m^2D^2}{dM^6}\right)^2 \sigma_x^2 + \left(\frac{4X^2Y^3D^4}{dM^2} - \frac{2X^2YD^4}{d} - \frac{4X^2Y^3m^2D^2}{dM^6}\right)^2 \sigma_y^2 + \left(\mathrm{A}_{1212_k}F_k\right)^2 \left(\frac{\sigma_d}{d}\right)^2$$

$$S^2_{\mathrm{A}_{1222_k}F_k} = \left(\frac{4XY^3mD^2}{dM^4}\right)^2 \sigma_m^2 + \left(\frac{4X^2Y^3D^4}{dM^2} - \frac{Y^3D^4}{d} - \frac{4X^2Y^3m^2D^2}{dM^6}\right)^2 \sigma_x^2 + \left(\frac{4XY^4D^4}{dM^2} - \frac{3XY^2D^4}{d} - \frac{4XY^4m^2D^2}{dM^6}\right)^2 \sigma_y^2 + \left(\mathrm{A}_{1222_k}F_k\right)^2 \left(\frac{\sigma_d}{d}\right)^2$$

$$S^2_{\mathrm{A}_{1233_k}F_k} = \left(\frac{2XYm^3}{dM^6} - \frac{2XYmD^2}{dM^2}\right)^2 \sigma_m^2 + \left(\frac{2X^2Ym^4}{dM^8} + \frac{Ym^2D^2}{dM^2} - \frac{4X^2Ym^2D^2}{dM^4}\right)^2 \sigma_x^2 + \left(\frac{2XY^2m^4}{dM^8} + \frac{Xm^2D^2}{dM^2} - \frac{4XY^2m^2D^2}{dM^4}\right)^2 \sigma_y^2 + \left(\mathrm{A}_{1233_k}F_k\right)^2 \left(\frac{\sigma_d}{d}\right)^2$$

B.2.3 Rectangular Objects

As shown by Table B.1, orientation measurements for rectangular objects assume that the fibers are exactly parallel to the imaging plane. However, this is likely not the case, but it is difficult to determine from the micrograph the extent a rectangular object is out-of-plane. Measurement error calculations based on Table B.1 would result in no error in the out-of-plane components. The conservative estimate for the measurement error is to assume the maximum out-of-plane component while still retaining a rectangular object. This occurs when the out-of-plane angle, $\theta_k = \mathrm{acos}(d/L_k)$. The measured quantity on the micrograph is M_k which is nearly equivalent to L_k [i.e. $M_k = L_k \mathrm{cos}(d/L_k)$]. For the error analysis of rectangular objects, the orientation equations in Table B.7 are used assuming $M_k \approx L_k$. The squared error for the second and fourth order tensor components of interest are provided in Tables B.8 and B.9, respectively.

Table B.7: Orientation equations for error calculations of rectangular objects to include maximum out-of-plane component

Orientation Component	Out-of-plane Maximum
$(\mathrm{A}_{11})_k$	$\frac{X^2}{M^2}\left(1-\frac{d^2}{L_k^2}\right)$
$(\mathrm{A}_{12})_k = (\mathrm{A}_{21})_k$	$\frac{XY}{M^2}\left(1-\frac{d^2}{L_k^2}\right)$
$(\mathrm{A}_{13})_k = (\mathrm{A}_{31})_k$	$\frac{Xd}{ML_k}\sqrt{1-\frac{d^2}{L_k^2}}$
$(\mathrm{A}_{22})_k$	$\frac{Y^2}{M^2}\left(1-\frac{d^2}{L_k^2}\right)$
$(\mathrm{A}_{23})_k = (\mathrm{A}_{32})_k$	$\frac{Yd}{ML_k}\sqrt{1-\frac{d^2}{L_k^2}}$
$(\mathrm{A}_{33})_k$	$\frac{d^2}{L_k^2}$

Table B.8: Squared measurement error of **A** for rectangular objects

$$S^2_{\mathrm{A}_{11_k}F_k} = \frac{4X^2(M^4 - M^2X^2 - M^2d^2 + 2X^2d^2)^2}{M^{12}d^2}\sigma_x^2 + \frac{4X^4Y^2(M^2-2d^2)^2}{M^{12}d^2}\sigma_y^2 + \frac{X^4(M^2+d^2)^2}{M^8d^4}\sigma_d^2$$

$$S^2_{\mathrm{A}_{12_k}F_k} = \frac{Y^2(M^4 - 2M^2X^2 - M^2d^2 + 4X^2d^2)^2}{M^{12}d^2}\sigma_X^2 + \frac{X^2(M^4 - 2M^2Y^2 - M^2d^2 + 4Y^2d^2)^2}{M^{12}d^2}\sigma_Y^2 + \frac{X^2Y^2(M^2+d^2)^2}{M^8d^4}\sigma_d^2$$

$$S^2_{\mathrm{A}_{13_k}F_k} = \frac{(M^4 - 2M^2X^2 - M^2d^2 + 3X^2d^2)^2}{M^{10}(M^2-d^2)}\sigma_x^2 + \frac{X^2Y^2(2M^2-3d^2)^2}{M^{10}(M^2-d^2)}\sigma_y^2 + \frac{X^2d^2}{M^6(M^2-d^2)}\sigma_d^2$$

$$S^2_{\mathrm{A}_{22_k}F_k} = \frac{4X^2Y^4(M^2-2d^2)^2}{M^{12}d^2}\sigma_x^2 + \frac{4Y^2(M^4 - M^2Y^2 - M^2d^2 + 2Y^2d^2)^2}{M^{12}d^2}\sigma_y^2 + \frac{Y^4(M^2+d^2)^2}{M^8d^4}\sigma_d^2$$

$$S^2_{\mathrm{A}_{23_k}F_k} = \frac{X^2Y^2(2M^2-3d^2)^2}{M^{10}(M^2-d^2)}\sigma_x^2 + \frac{(M^4 - 2M^2Y^2 - M^2d^2 + 3Y^2d^2)^2}{M^{10}(M^2-d^2)}\sigma_y^2 + \frac{X^2d^2}{M^6(M^2-d^2)}\sigma_d^2$$

$$S^2_{\mathrm{A}_{33_k}F_k} = \frac{4d^2}{M^8}\left(X^2\sigma_x^2 + Y^2\sigma_y^2\right) + \frac{1}{M^4}\sigma_d^2$$

$$S^2_{F_n} = \frac{\sigma_d^2}{d^4}$$

Table B.9: Squared measurement error for components of $\mathbf{A}_4$ contributing to shear and normal stresses in simple shear flow for rectangular objects

$$S^2_{\mathrm{A}_{1211_k}F_k} = \left(\frac{X^2Y(d^2-M^2)(3M^4-4M^2X^2-3M^2d^2+8X^2d^2)}{M^{10}d}\right)^2\sigma_x^2$$
$$+\left(\frac{X^3(d^2-M^2)(M^4-4M^2Y^2-M^2d^2+8Y^2d^2)}{M^{10}d}\right)^2\sigma_y^2+\left(\frac{X^3Y(M^2+3d^2)(M^2-d^2)}{M^8d^2}\right)^2\sigma_d^2$$

$$S^2_{\mathrm{A}_{1212_k}F_k} = \left(\frac{2XY^2(d^2-M^2)(M^4-2M^2X^2-M^2d^2+4X^2d^2)}{M^{10}d}\right)^2\sigma_x^2$$
$$+\left(\frac{2X^2Y(d^2-M^2)(M^4-2M^2Y^2-M^2d^2+4Y^2d^2)}{M^{10}d}\right)^2\sigma_y^2+\left(\frac{X^2Y^2(M^2+3d^2)(d^2-M^2)}{M^8d^2}\right)^2\sigma_d^2$$

$$S^2_{\mathrm{A}_{1222_k}F_k} = \left(\frac{Y^3(d^2-M^2)(M^4-4M^2X^2-M^2d^2+8X^2d^2)}{M^{10}d}\right)^2\sigma_x^2$$
$$+\left(\frac{XY^2(d^2-M^2)(3M^4-4M^2Y^2-3M^2d^2+8Y^2d^2)}{M^{10}d}\right)^2\sigma_y^2+\left(\frac{XY^3(M^2+3d^2)(M^2-d^2)}{M^8d^2}\right)^2\sigma_d^2$$

$$S^2_{\mathrm{A}_{1233_k}F_k} = \left(\frac{Yd(M^4-4M^2X^2-M^2d^2+6X^2d^2)}{M^8}\right)^2\sigma_x^2$$
$$+\left(\frac{Xd(M^4-4M^2Y^2-M^2d^2+6Y^2d^2)}{M^8}\right)^2\sigma_y^2+\left(\frac{XY(3d^2-M^2)}{M^6}\right)^2\sigma_d^2$$

B.3 References

[1] Bay RS, Tucker CL. Stereological measurement and error estimates for three-dimensional fiber orientation. Polym Eng Sci. 1992;32:240-53.

[2] Vélez-García GM, Wapperom P, Baird DG, Aning AO, Kunc V. Unambiguous orientation in short fiber composites over small sampling area in a center-gated disk. Composites Part A. 2012;43:104-13.

Appendix C Assessing a Stress Equation Including Fiber-Fiber Interactions

This section provides an assessment of a stress equation that includes fiber-fiber interactions. First, the stress theory and the additional fiber orientation dependent term is presented. Then, the stress equation is evaluated based on fiber orientation evolution data obtained during the startup of simple shear flow for samples generated by injection molding. The reader is referred to Chapter 5 for further details on the methods used to generate the initial fiber orientation. A brief conclusion discusses the performance of the available stress theory that includes fiber-fiber interactions.

C.1 Fiber-Fiber Interaction Stress Theory

The stress equation that was evaluated in Chapter 5 using experimental orientation data was based only on the fourth order orientation tensor, $\mathbf{A}_4$. An additional fiber-fiber interaction term was added by Djalili-Moghaddam and Toll [1] and Férec et al. [2] to provide better predictions of semi-dilute ($a_r^{-2} \leq \phi < a_r^{-1}$) fiber suspensions:

$$\boldsymbol{\sigma} = -P\mathbf{I} + 2\eta_m\mathbf{D} + 2\eta_m\phi_v\mu_2\mathbf{D} : \mathbf{A}_4 + \frac{4\eta_m k_{ff} a_r^2 \phi_v^2}{3\pi^2}\langle \mathbf{pppp}|\mathbf{p}\times\mathbf{p}'|\rangle : \mathbf{D} \qquad \text{(C.1)}$$

where P is the isotropic pressure, η_m is the matrix viscosity, $\mathbf{D} = \frac{1}{2}(\nabla\mathbf{v}^t + \nabla\mathbf{v})$ is the rate-of-deformation tensor, $\mathbf{W} = \frac{1}{2}(\nabla\mathbf{v}^t - \nabla\mathbf{v})$ is the vorticity tensor, ϕ_v is the fiber volume fraction, a_r is the fiber aspect ratio (length/diameter), $\mathbf{p}$ and $\mathbf{p}'$ are separate fiber orientation vectors, k_{ff} is an empirical parameter used to fit the model and μ_2 can be represented by theory up to semi-dilute concentrations or used as an additional fitting parameter. Djalili-Moghaddam and Toll [1] used the theory of Shaqfeh and Fredrickson [3] for μ_2 whereas Férec et al. [2] used μ_2 as a fitting parameter. Férec et al. [2, 4] introduced fiber interaction tensors and closures to compactly represent the additional fiber orientation dependent term:

$$\mathbf{b}_4 = \int_{\mathbf{p}} \int_{\mathbf{p}'} \mathbf{pppp} |\mathbf{p} \times \mathbf{p}'| \psi(\mathbf{p}') \psi(\mathbf{p}) \, d\mathbf{p}' d\mathbf{p} \tag{C.2}$$

where ψ is the orientation distribution function.

The shear viscosity and first normal stress difference in simple shear flow are predicted from Eqs. (C.3) and (C.4), respectively:

$$\eta = \eta_m [1 + \phi_v \mu_2 \mathrm{A}_{1212} + \mu_3 \mathrm{b}_{1212}] \tag{C.3}$$

$$N_1 = \sigma_{11} - \sigma_{22} = \eta_m \dot{\gamma} [\phi_v \mu_2 (\mathrm{A}_{1211} - \mathrm{A}_{1222}) + \mu_3 (\mathrm{b}_{1211} - \mathrm{b}_{1222})] \tag{C.4}$$

where $\dot{\gamma} = dv_1/dx_2$ and $\mu_3 = 4k_{ff} a_r^2 \phi_v^2 / 3\pi^2$. The fiber-fiber interaction term is removed from the equations when $k_{ff} = 0$. An assessment of the fiber-fiber interaction term in the stress equation has only been completed by using a fiber orientation model which induces additional approximations, such as the initial fiber orientation and closures approximations for the higher order terms.

The number of contacts per fiber is also of interest when considering the additional stress contributions from fiber-fiber interactions. Toll [5] describes the number of lubricated contacts per fiber as:

$$N_c = \frac{8}{\pi} a_r \phi f + 4\phi(g + 1) \tag{C.5}$$

$$f = \int_{\mathbf{p}} \int_{\mathbf{p}'} |\mathbf{p} \times \mathbf{p}'| \psi(\mathbf{p}') \psi(\mathbf{p}) \, d\mathbf{p}' d\mathbf{p} \tag{C.6}$$

$$g = \int_{\mathbf{p}} \int_{\mathbf{p}'} \mathbf{p} \cdot \mathbf{p}' \psi(\mathbf{p}') \psi(\mathbf{p}) \, d\mathbf{p}' d\mathbf{p}. \tag{C.7}$$

For high aspect ratio fibers, Eq. (C.5) can be approximated by first term on the right side of the equation. The values of f and g range from 0 to 1. Example values of f and g are given in Table C.1 for different orientation states.

Table C.1: Values of f and g for different fiber orientation states.

Orientation	f	g
Completely Aligned	0	1
2D random	$2/\pi$	$2/\pi$
3D random	$2/3$	$1/3$

Fiber orientation was obtained in samples using the method of ellipses. An orientation vector, **p**, is associated with each measured fiber. The fourth order fiber orientation tensor is calculated from the experimental data as:

$$\mathbf{A}_4 = \frac{\sum_k \ (\mathbf{pppp})_k L_k F_k B_k}{\sum_k \ L_k F_k B_k} \tag{C.8}$$

where L_k is the length of the k-th fiber, F_k is the weighting function accounting for imaging bias provided by Bay and Tucker [6], B_k accounts for the fraction of a fiber that is included in the average when the sample is divided into bins through the thickness [7]. Average values for the fourth order interaction tensor, $\mathbf{b}_4$, and scalars, f and g, can be calculated similarly:

$$\mathbf{b}_4 = \frac{\sum_k \sum_l \ (\mathbf{pppp})_k |\mathbf{p}_k \times \mathbf{p}_l| \ L_k L_l F_k F_l B_k B_l}{\sum_k \sum_l \ L_k L_l F_k F_l B_k B_l} \tag{C.9}$$

$$f = \frac{\sum_k \sum_l \ |\mathbf{p}_k \times \mathbf{p}_l| \ L_k L_l F_k F_l B_k B_l}{\sum_k \sum_l \ L_k L_l F_k F_l B_k B_l} \tag{C.10}$$

$$g = \frac{\sum_k \sum_l \ (\mathbf{p}_k \cdot \mathbf{p}_l) \ L_k L_l F_k F_l B_k B_l}{\sum_k \sum_l \ L_k L_l F_k F_l B_k B_l}. \tag{C.11}$$

The method ellipses does not allow for the fiber length of each fiber to be known. The orientation averages are then calculated by assuming each fiber has a length equal to the number average fiber length. The orientation data presented in this work came from injection molded plaques with a number average length of 0.7 mm [8].

C.2 Preliminary Results and Discussion

The stress equation can take many forms depending on if the material constants are taken from theory or empirically fit to data. This section will focus on the fiber orientation dependent tensors, $\mathbf{A}_4$ and $\mathbf{b}_4$. The values of orientation are calculated based on experimental fiber orientation data from samples prepared by injection molding and were given the general designation of non-uniform and uniform initial fiber orientation based on the orientation through the sample thickness. Further discussion of the initial fiber orientation is provided in Chapter 5. Using experimental orientation values allows for an assessment of the stress theory that is independent of the fiber orientation evolution equations or closure approximations.

The values of A_{1212} and b_{1212} are provided in Figure C.1 as a function of shear strain for samples prepared through injection molding during the startup of flow. For both the non-uniform and uniform initial orientations, the trend of the A_{1212} component of orientation and the b_{1212} component of the interaction tensor are similar in their evolution with strain, varying only in magnitude. Shear stress predictions using the additional fiber interaction term would not differ significantly from predictions that are only based on A_{1212}. For the uniform initial orientation, the value of A_{1212} gradually increases, but has some variability at higher strains. Both the A_{1212} and b_{1212} orientation components do not produce a clear overshoot profile as a function of strain that would reflect experimental data. Based on these experimental values of orientation, the predicted shear stress will not have an overshoot.

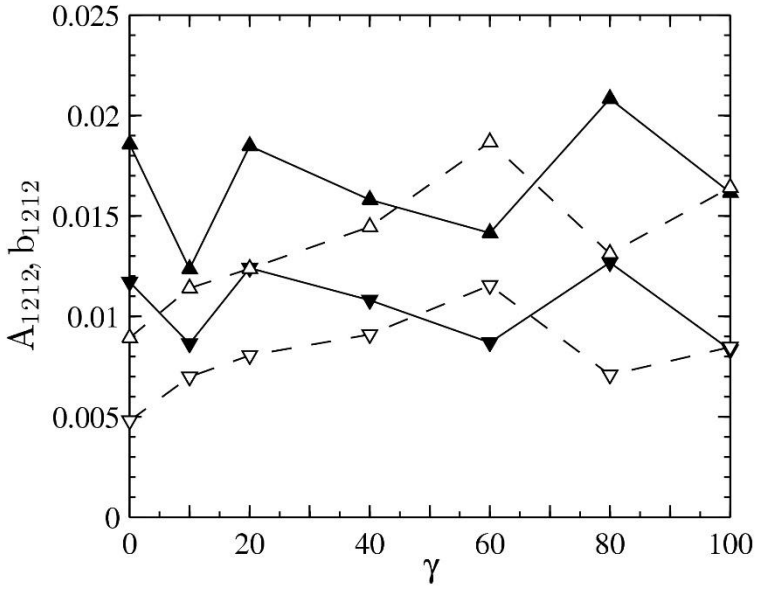

Figure C.1: Experimental values of A_{1212} (▲) and b_{1212} (▼) expected to contribute to shear stress for samples with the uniform (open symbols) and non-uniform (closed symbols) initial orientation.

The A_{1211} and b_{1211} components of orientation are provided in Figure C.2. The first normal stress difference is expected to be dependent on A_{1211}, A_{1222}, b_{1211} and b_{1222}, but the magnitudes of A_{1222} and b_{1222} are relatively small in comparison to A_{1211} and b_{1211}, respectively. As observed in Figure C.1, the components of the **A** and **b** orientation tensors show a similar transient evolution. The values of A_{1211} and b_{1211} increase rapidly from a negative value to a positive value for the non-uniform initial orientation and result in a steady value at high strains. The uniform initial orientation has a much more complex transient behavior that was observed in both of the two samples used to make orientation measurements. Above 60 strain units, there is excellent agreement between the non-uniform and uniform initial orientations. Experimental normal stress data could not be obtained in the sliding plate rheometer experiments, but an overshoot profile is expected based on the data available for short fiber suspensions [9, 10]. The values of A_{1211} and b_{1211} do not reflect an expected overshoot profile.

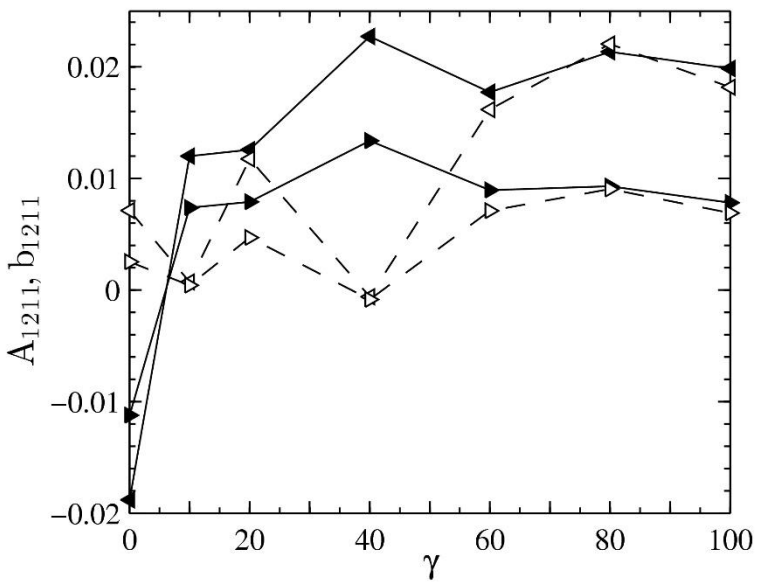

Figure C.2: Experimental values of A_{1211} (◀) and b_{1211} (▶) expected to contribute to shear stress for samples with the uniform (open symbols) and non-uniform (closed symbols) initial condition.

The fiber orientation dependent terms used to calculate the number of contacts per fiber are shown in Figure C.3. For both uniform and non-uniform initial orientations the evolution of g mirrors the evolution profile of f. In the non-uniform case, the initial value of f is 0.63 which is the same as the value for random in-plane orientation listed in Table C.1. The value of f remains does not change significantly until 40 strain units where the value decreases with strain indicating more fiber alignment and fewer fiber interactions. For the uniform initial orientation, the value of f increases at 20 strain units and reduces to a steady value near 0.46. This predicts that the number of fiber interactions slightly increase before decreasing to a constant value. The slight increase of f at 20 strain units does not appear to be large enough to result in a large change in the evolution of b_{1212} or b_{1211} when compared to A_{1212} or A_{1211}, respectively.

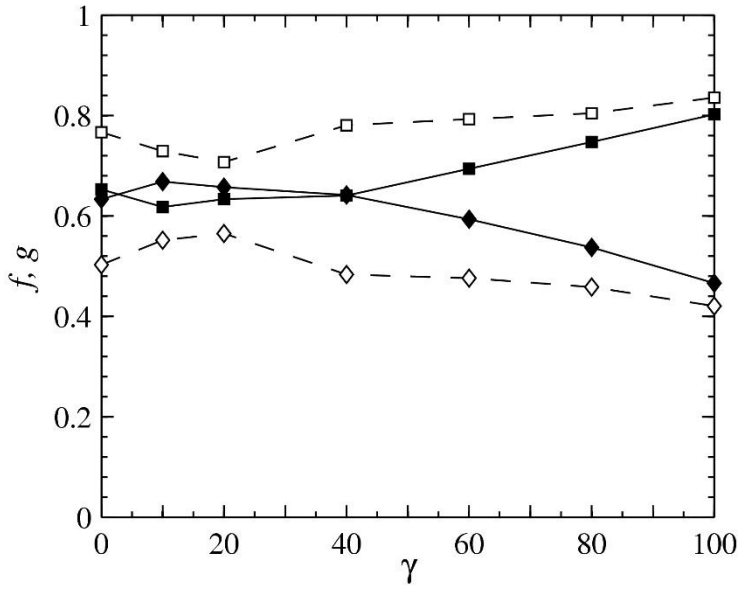

Figure C.3: Experimental values for f (♦) and g (■) used to predict the number of contacts per fiber for samples beginning with the uniform (open symbols) and non-uniform (closed symbols) initial fiber orientation.

C.3 Preliminary Conclusions

The extension of the semi-dilute stress theory to include fiber-fiber interactions does not predict an overshoot in the shear stress or the first normal stress difference using the experimental fiber orientation data. The dynamics of the fourth order fiber interaction tensor does not appear to produce a different evolution behavior as the fourth order orientation tensor. Further assessment of the stress tensor incorporating fiber-fiber interactions should be performed using different flows, like an extensional flow. From the analysis in simple shear flow, additional approaches must be developed to represent concentrated fiber suspensions to better reflect the stress overshoots observed in experimental data.

C.4 References

[1] Djalili-Moghaddam M, Toll S. A model for short-range interactions in fibre suspensions. J Non-Newton Fluid Mech. 2005;132:73-83.

[2] Férec J, Ausias G, Heuzey MC, Carreau PJ. Modeling fiber interactions in semiconcentrated fiber suspensions. J Rheol. 2009;53:49-72.
[3] Shaqfeh ESG, Fredrickson GH. The hydrodynamic stress in a suspension of rods. Phys Fluids A. 1990;2:7-24.
[4] Férec J, Abisset-Chavanne E, Ausias G, Chinesta F. On the use of interaction tensors to describe and predict rod interactions in rod suspensions. Rheol Acta. 2014;53:445-56.
[5] Toll S. Packing mechanics of fiber reinforcements. Polym Eng Sci. 1998;38:1337-50.
[6] Bay RS, Tucker CL. Stereological measurement and error estimates for three-dimensional fiber orientation. Polym Eng Sci. 1992;32:240-53.
[7] Vélez-García GM, Wapperom P, Baird DG, Aning AO, Kunc V. Unambiguous orientation in short fiber composites over small sampling area in a center-gated disk. Composites Part A. 2012;43:104-13.
[8] Cieslinski MJ, Wapperom P, Baird DG. Obtaining repeatable initial fiber orientation for the transient rheology of fiber suspensions in simple shear flow. (submitted to the Journal of Rheology). 2015.
[9] Eberle APR, Baird DG, Wapperom P, Vélez-García GM. Obtaining reliable transient rheological data on concentrated short fiber suspensions using a rotational rheometer. J Rheol. 2009;53:1049-68.
[10] Sepehr M, Ausias G, Carreau PJ. Rheological properties of short fiber filled polypropylene in transient shear flow. J Non-Newton Fluid Mech. 2004;123:19-32.

Appendix D Transient Rheological Data

Sample Preparation Method: Compression Molding
Concentration: 10 wt% Glass Fiber
Fiber Length: L_n = 1.40 mm, L_w = 3.59 mm
Temperature: 200 °C
Shear Rates: 0.4, 1.0 and 4.0 s^{-1}

γ	0.4, s^{-1} η^+, Pa s	1.0, s^{-1} η^+, Pa s	0.4, s^{-1} η^+, Pa s
0	0.0	0.0	0.0
2	645.5	592.8	452.8
4	688.0	610.2	471.8
6	701.1	622.5	483.1
8	700.9	634.3	484.6
10	702.7	641.3	484.7
12	701.0	645.6	484.9
14	696.2	643.9	485.3
16	691.1	631.6	481.6
18	680.6	624.9	478.8
20	665.1	617.4	474.6
22	656.0	607.5	467.6
24	647.5	597.0	461.5
26	639.5	588.9	455.4
28	626.2	583.2	446.8
30	613.8	577.7	442.3
32	604.0	570.1	441.8
34	597.1	561.1	439.0
36	592.9	556.4	437.2
38	590.9	549.5	434.6
40	590.9	543.6	433.1
42	590.6	537.9	431.8
44	591.4	532.6	430.4
46	591.9	526.4	429.2
48	592.2	521.5	428.0
50	592.2	516.6	425.8
52	591.8	513.4	422.8
54	591.1	509.4	420.3
56	590.0	507.2	417.7
58	588.2	505.5	413.4
60	582.1	505.4	411.8
62	579.7	504.6	408.9
64	577.4	504.0	406.8
66	575.4	502.4	405.4
68	573.6	500.7	404.8
70	571.9	498.1	403.0
72	570.5	495.6	401.0
74	569.4	493.1	399.4
76	568.7	491.1	398.0
78	568.3	489.5	397.0
80	567.9	488.3	396.5
82	567.6	487.4	396.0
84	567.1	486.7	396.0
86	566.5	486.4	396.0
88	565.7	486.3	395.8
90	564.9	486.6	395.4
92	564.0	487.0	395.0
94	563.1	487.6	394.4
96	562.2	488.3	394.3
98	561.2	489.1	393.7
100	560.1	489.9	393.1
102	558.9	490.7	392.4
104	557.7	491.4	391.9
106	556.4	492.1	391.4
108	555.3	492.6	391.4
110	554.3	493.1	391.4
112	553.7	493.5	391.4
114	553.3	493.8	391.4
116	553.3	493.9	391.4
118	553.3	494.0	391.4
120	553.3	494.1	391.4

Sample Preparation Method: Compression Molding
Concentration: 20 wt% Glass Fiber
Fiber Length: L_n = 1.28 mm, L_w = 2.59 mm
Temperature: 200 °C
Shear Rates: 0.4, 1.0 and 4.0 s^{-1}

γ	0.4, s^{-1} η^+, Pa s	1.0, s^{-1} η^+, Pa s	0.4, s^{-1} η^+, Pa s	γ	0.4, s^{-1} η^+, Pa s	1.0, s^{-1} η^+, Pa s	0.4, s^{-1} η^+, Pa s
0	0.0	0.0	0.0	62	1140.5	968.0	684.1
2	1157.7	1186.5	807.5	64	1138.1	967.4	681.5
4	1239.1	1280.3	827.1	66	1134.3	966.5	677.9
6	1339.8	1332.2	855.6	68	1132.1	965.1	675.8
8	1430.5	1341.3	870.2	70	1119.8	963.5	674.5
10	1511.9	1360.4	872.9	72	1126.2	962.4	670.1
12	1576.7	1357.9	880.7	74	1117.3	961.1	666.9
14	1642.0	1360.1	886.3	76	1109.8	959.5	663.9
16	1663.5	1350.6	887.8	78	1107.8	959.7	661.8
18	1676.8	1343.1	887.6	80	1111.2	960.5	662.0
20	1676.9	1323.7	880.5	82	1113.0	961.4	661.5
22	1669.4	1311.2	869.6	84	1111.9	961.1	659.5
24	1653.1	1277.1	853.8	86	1115.9	961.9	658.4
26	1639.0	1247.4	840.7	88	1110.2	962.9	657.1
28	1621.4	1209.6	829.1	90	1106.4	964.3	657.0
30	1597.4	1185.2	818.0	92	1107.7	965.9	655.8
32	1561.7	1158.8	812.3	94	1107.4	967.9	654.2
34	1532.7	1125.7	807.9	96	1100.0	970.0	653.0
36	1496.7	1093.7	799.8	98	1100.0	971.2	650.9
38	1472.2	1064.5	790.4	100	1107.4	972.0	649.7
40	1438.0	1043.8	779.9	102	1108.4	972.2	648.8
42	1401.6	1030.3	767.2	104	1102.5	972.2	647.6
44	1364.6	1016.8	754.6	106	1098.2	972.5	645.8
46	1328.9	1008.9	746.0	108	1091.6	972.8	644.4
48	1289.8	1000.7	737.1	110	1090.2	972.9	642.3
50	1263.9	996.2	730.0	112	1085.3	972.8	639.4
52	1240.2	991.4	718.0	114	1078.4	972.8	636.0
54	1213.1	987.7	709.4	116	1069.5	972.8	632.3
56	1193.5	981.9	701.8	118	1069.5	972.8	632.3
58	1178.3	974.9	694.1	120	1069.5	972.8	632.3
60	1161.9	969.4	686.0				

Sample Preparation Method: Compression Molding
Concentration: 30 wt% Glass Fiber
Fiber Length: L_n = 1.25 mm, L_w = 2.28 mm
Temperature: 200 °C
Shear Rates: 0.4, 1.0 and 4.0 s^{-1}

γ	0.4, s^{-1} η^+, Pa s	1.0, s^{-1} η^+, Pa s	0.4, s^{-1} η^+, Pa s	γ	0.4, s^{-1} η^+, Pa s	1.0, s^{-1} η^+, Pa s	0.4, s^{-1} η^+, Pa s
0	0.0	0.0	0.0	62	2752.3	2075.5	1404.8
2	2436.6	2208.5	1489.5	64	2721.1	2069.2	1396.9
4	2816.7	2547.6	1666.8	66	2668.6	2081.2	1382.4
6	3273.0	2781.9	1707.2	68	2597.2	2095.5	1375.3
8	3444.6	2942.7	1740.4	70	2529.3	2105.9	1368.4
10	3567.0	3034.0	1764.4	72	2472.3	2115.4	1361.7
12	3677.9	3083.9	1771.6	74	2427.7	2128.4	1353.8
14	3733.4	3097.7	1768.3	76	2388.5	2138.1	1346.5
16	3769.6	3109.5	1757.4	78	2382.1	2138.6	1342.1
18	3796.2	3088.4	1759.2	80	2374.5	2111.5	1339.3
20	3787.3	3021.8	1752.4	82	2353.3	2091.3	1339.6
22	3792.0	2918.5	1741.4	84	2346.5	2074.5	1338.9
24	3762.8	2812.3	1720.6	86	2347.8	2062.2	1336.9
26	3740.2	2713.2	1707.5	88	2352.6	2038.3	1335.5
28	3692.1	2643.5	1692.9	90	2348.2	2015.1	1333.9
30	3679.4	2577.1	1693.6	92	2349.6	2008.6	1330.6
32	3647.1	2506.7	1681.3	94	2357.1	1997.2	1327.1
34	3593.5	2446.1	1659.4	96	2362.4	1988.3	1323.8
36	3521.0	2355.8	1624.4	98	2361.8	1978.3	1320.6
38	3442.3	2282.6	1602.8	100	2357.4	1967.1	1316.4
40	3357.0	2236.8	1591.7	102	2355.0	1954.3	1311.6
42	3287.8	2180.4	1580.3	104	2353.0	1942.1	1305.8
44	3205.9	2122.1	1557.6	106	2346.1	1933.9	1300.5
46	3140.1	2095.7	1551.4	108	2337.2	1924.9	1294.6
48	3075.7	2083.0	1541.5	110	2326.8	1913.0	1287.9
50	3035.5	2075.3	1515.0	112	2312.0	1902.2	1280.3
52	3026.7	2077.1	1492.9	114	2296.5	1893.4	1270.9
54	2980.1	2075.0	1467.5	116	2281.2	1893.4	1261.0
56	2930.8	2082.4	1443.1	118	2281.2	1893.4	1261.0
58	2884.7	2091.9	1424.4	120	2281.2	1893.4	1261.0
60	582.1	505.4	411.8				

Sample Preparation Method: Compression Molding
Concentration: 40 wt% Glass Fiber
Fiber Length: L_n = 1.06 mm, L_w = 1.96 mm
Temperature: 200 °C
Shear Rates: 0.4, 1.0 and 4.0 s^{-1}

γ	0.4, s^{-1} η^+, Pa s	1.0, s^{-1} η^+, Pa s	0.4, s^{-1} η^+, Pa s	γ	0.4, s^{-1} η^+, Pa s	1.0, s^{-1} η^+, Pa s	0.4, s^{-1} η^+, Pa s
0	0.0	0.1	0.1	62	5597.6	3451.0	1923.7
2	2804.9	2346.5	1567.1	64	5574.3	3451.2	1903.4
4	3599.2	2833.2	1817.9	66	5514.3	3479.0	1881.0
6	4036.4	3282.8	1951.7	68	5433.2	3466.9	1853.1
8	4536.5	3649.5	2102.6	70	5340.0	3457.7	1833.1
10	4766.6	3963.5	2209.3	72	5259.2	3441.5	1817.5
12	5062.6	4168.7	2305.3	74	5187.9	3443.0	1811.7
14	5304.4	4357.8	2368.2	76	5112.7	3450.2	1805.9
16	5572.2	4409.9	2425.3	78	5039.9	3451.7	1806.7
18	5777.3	4406.7	2470.4	80	4984.7	3447.8	1808.5
20	5947.3	4388.3	2533.7	82	4968.2	3440.4	1808.4
22	6056.0	4347.6	2535.4	84	4972.5	3420.8	1802.1
24	6071.0	4266.7	2535.1	86	4985.4	3397.4	1790.9
26	6088.6	4222.7	2528.7	88	4994.7	3371.4	1785.1
28	6116.7	4188.4	2527.4	90	5017.0	3350.0	1776.3
30	6137.3	4143.2	2498.4	92	5029.0	3330.1	1759.2
32	6145.4	4112.8	2460.3	94	5030.3	3321.8	1751.4
34	6156.1	4062.1	2408.7	96	5011.9	3307.6	1745.9
36	6137.6	4006.6	2341.8	98	4983.8	3306.8	1738.7
38	6134.1	3942.4	2257.8	100	4957.6	3312.9	1733.9
40	6108.7	3854.6	2187.4	102	4932.3	3310.0	1730.4
42	6091.8	3802.7	2156.2	104	4908.7	3300.0	1727.7
44	6056.0	3760.2	2133.5	106	4891.9	3296.4	1722.9
46	5998.7	3704.8	2090.5	108	4889.1	3291.9	1717.5
48	5930.8	3650.5	2010.8	110	4898.4	3292.7	1710.2
50	5857.4	3615.7	1984.9	112	4901.9	3296.2	1699.4
52	5773.3	3573.0	1954.5	114	4900.7	3298.5	1689.5
54	5711.2	3541.2	1935.0	116	4896.8	3302.2	1698.7
56	5665.1	3488.4	1925.6	118	4897.1	3315.6	1684.3
58	5642.9	3453.5	1931.5	120	4895.8	3318.8	1676.5
60	5622.2	3446.9	1931.3				

Sample Preparation Method: Compression Molding
Concentration: 30 wt% Glass Fiber
Fiber Length: L_n = 0.54 mm, L_w = 0.70 mm
Temperature: 200 °C
Shear Rates: 0.4, 1.0 and 4.0 s^{-1}

γ	0.4, s^{-1} η^+, Pa s	1.0, s^{-1} η^+, Pa s	0.4, s^{-1} η^+, Pa s	γ	0.4, s^{-1} η^+, Pa s	1.0, s^{-1} η^+, Pa s	0.4, s^{-1} η^+, Pa s
0	0.0	0.0	0.0	62	708.4	653.1	429.4
2	819.6	981.7	514.9	64	709.0	654.3	426.8
4	1014.2	1018.4	600.8	66	714.3	654.6	428.8
6	1070.7	1039.1	608.1	68	720.8	653.3	427.1
8	1087.4	1039.1	618.2	70	728.9	652.5	427.8
10	1109.0	1026.7	621.7	72	732.9	650.2	425.1
12	1124.1	1003.6	616.3	74	737.0	646.6	426.9
14	1126.4	959.3	598.3	76	739.1	641.4	426.5
16	1106.0	923.5	581.5	78	742.1	639.0	428.6
18	1059.1	875.4	567.5	80	740.2	636.9	426.8
20	1031.0	840.5	555.3	82	738.0	632.3	426.1
22	977.6	804.5	543.2	84	734.2	630.0	420.1
24	938.3	780.5	530.8	86	734.8	625.5	413.4
26	894.6	757.7	517.9	88	735.3	617.3	412.9
28	883.8	744.9	502.4	90	735.7	616.4	414.0
30	886.2	729.4	492.9	92	732.2	613.8	415.9
32	877.8	721.2	483.1	94	727.6	605.2	413.0
34	853.9	717.8	476.4	96	721.3	598.1	409.5
36	842.1	710.0	466.9	98	715.4	594.1	403.4
38	827.3	704.9	461.3	100	707.2	584.9	394.0
40	804.4	695.3	461.7	102	698.8	572.7	386.1
42	789.0	688.0	457.9	104	691.8	568.0	377.1
44	774.1	672.5	454.5	106	689.0	556.8	369.4
46	760.2	663.5	444.4	108	689.1	547.3	358.3
48	747.3	657.9	438.0	110	688.9	542.8	348.8
50	737.6	654.9	429.1	112	686.8	531.5	335.8
52	728.6	650.2	427.9	114	684.3	525.8	320.2
54	720.3	650.1	426.3	116	683.1	515.0	302.1
56	714.0	652.0	431.1	118	682.9	518.3	285.8
58	710.8	651.8	430.2	120	680.4	517.4	277.6
60	709.2	652.9	430.0				

Sample Preparation Method: Compression Molding
Concentration: 30 wt% Glass Fiber
Fiber Length: L_n = 0.9 mm, L_w = 1.5 mm
Temperature: 200 °C
Shear Rates: 0.4, 1.0 and 4.0 s^{-1}

γ	0.4, s^{-1} η^+, Pa s	1.0, s^{-1} η^+, Pa s	0.4, s^{-1} η^+, Pa s
0	0.0	0.0	0.0
2	825.2	717.6	593.3
4	989.1	908.2	682.4
6	1204.2	1029.4	800.8
8	1419.5	1226.5	863.3
10	1547.8	1272.1	901.5
12	1619.7	1314.8	905.8
14	1724.0	1345.2	898.4
16	1801.5	1343.4	893.5
18	1876.3	1309.2	886.2
20	1903.6	1272.8	868.3
22	1923.2	1242.4	845.4
24	1934.7	1207.2	832.8
26	1942.0	1132.5	816.1
28	1954.6	1089.5	787.8
30	1926.3	1036.3	756.3
32	1831.6	982.6	738.5
34	1713.4	956.8	727.8
36	1638.3	926.9	718.1
38	1574.4	907.6	701.4
40	1524.9	873.4	686.8
42	1521.3	854.9	673.1
44	1498.1	837.5	666.9
46	1468.5	821.5	665.1
48	1455.7	812.8	654.8
50	1402.5	782.9	647.5
52	1330.1	749.9	639.1
54	1278.6	738.5	632.9
56	1273.2	729.4	630.7
58	1260.1	717.2	622.9
60	1258.2	708.4	626.6
62	1250.3	707.4	622.8
64	1234.8	705.8	623.9
66	1217.7	705.2	615.7
68	1200.2	708.8	602.9
70	1169.4	711.9	592.7
72	1148.0	712.4	589.1
74	1131.5	713.2	591.5
76	1126.6	713.0	586.2
78	1121.9	714.1	580.7
80	1119.4	719.5	579.3
82	1117.6	726.9	578.8
84	1127.9	731.1	575.8
86	1131.7	735.6	574.7
88	1134.2	739.7	575.7
90	1133.5	744.3	576.2
92	1133.5	746.9	576.2
94	1132.2	749.4	577.6
96	1133.6	750.2	578.4
98	1135.4	750.8	579.0
100	1136.4	751.3	578.6
102	1133.0	750.6	578.4
104	1138.5	749.4	578.2
106	1142.1	745.9	576.8
108	1145.1	740.9	573.7
110	1149.4	735.6	570.5
112	1152.8	730.1	566.6
114	1156.7	730.1	561.8
116	1162.7	730.1	557.5
118	1162.7	730.1	553.7
120	1162.7	730.1	553.7

Sample Preparation Method: Compression Molding
Concentration: 9.2 wt% Carbon Fiber
Fiber Length: L_n = 0.74 mm, L_w = 1.39 mm
Temperature: 200 °C
Shear Rates: 0.4, 1.0 and 4.0 s^{-1}

γ	0.4, s^{-1} η^+, Pa s	1.0, s^{-1} η^+, Pa s	0.4, s^{-1} η^+, Pa s	γ	0.4, s^{-1} η^+, Pa s	1.0, s^{-1} η^+, Pa s	0.4, s^{-1} η^+, Pa s
0	0.0	0.0	0.0	62	630.4	558.2	505.3
2	540.3	576.6	522.7	64	629.2	556.9	501.1
4	689.1	618.3	549.0	66	626.0	556.1	498.5
6	770.5	650.5	583.2	68	624.3	555.3	498.0
8	843.4	676.4	591.0	70	623.3	554.0	497.3
10	855.3	689.6	594.2	72	622.7	551.3	494.5
12	881.3	687.1	597.5	74	621.7	548.6	495.8
14	880.4	682.0	598.6	76	621.8	546.2	494.9
16	872.7	674.1	593.6	78	622.2	544.1	494.2
18	860.5	666.1	595.4	80	622.8	542.1	494.3
20	844.2	660.2	592.7	82	623.7	540.5	493.8
22	827.5	658.0	591.0	84	625.6	539.4	493.0
24	811.4	655.7	591.3	86	627.4	538.8	494.3
26	795.4	652.6	590.4	88	629.3	538.2	495.6
28	778.2	646.9	586.5	90	631.3	538.1	496.0
30	758.1	640.5	577.9	92	631.3	538.8	495.6
32	741.7	631.9	572.6	94	631.2	539.8	497.2
34	726.1	622.5	568.2	96	631.0	540.9	496.2
36	707.3	611.8	563.2	98	630.7	542.0	496.3
38	688.6	598.0	557.4	100	630.1	543.1	496.2
40	675.6	590.7	551.7	102	629.7	544.3	496.2
42	664.0	583.4	545.1	104	629.7	545.6	494.7
44	653.4	576.5	539.0	106	629.2	546.9	491.0
46	646.8	570.5	532.6	108	629.2	548.2	488.3
48	644.3	565.7	528.2	110	629.2	549.5	487.9
50	640.0	563.2	524.6	112	628.9	550.3	486.5
52	635.1	561.8	522.0	114	628.6	550.7	484.7
54	632.2	561.2	518.7	116	629.0	551.0	481.9
56	632.3	561.0	515.6	118	629.0	551.3	480.4
58	631.0	560.7	512.2	120	629.0	551.8	478.2
60	630.5	559.6	508.2				

Sample Preparation Method: Compression Molding
Concentration: 15.3 wt% Carbon Fiber
Fiber Length: L_n = 0.68 mm, L_w = 0.96 mm
Temperature: 200 °C
Shear Rates: 0.4, 1.0 and 4.0 s^{-1}

γ	0.4, s^{-1} η^+, Pa s	1.0, s^{-1} η^+, Pa s	0.4, s^{-1} η^+, Pa s	γ	0.4, s^{-1} η^+, Pa s	1.0, s^{-1} η^+, Pa s	0.4, s^{-1} η^+, Pa s
0	0.0	0.0	0.0	62	1295.9	914.8	738.1
2	1188.3	935.5	878.5	64	1297.1	920.4	740.4
4	1299.3	1104.0	914.8	66	1284.7	922.9	739.5
6	1480.4	1201.7	928.4	68	1273.1	923.7	736.6
8	1675.7	1296.6	924.8	70	1260.8	923.8	730.4
10	1882.2	1326.4	917.1	72	1249.3	921.5	726.6
12	1939.9	1340.8	923.3	74	1236.3	916.8	726.6
14	2001.7	1338.8	928.9	76	1226.3	909.5	728.2
16	2041.1	1326.0	940.9	78	1228.6	904.7	731.7
18	2017.2	1309.5	938.7	80	1225.9	900.1	735.0
20	1987.9	1282.9	927.1	82	1228.7	894.8	736.1
22	1974.3	1261.1	903.5	84	1232.5	894.2	736.4
24	1957.6	1230.1	878.7	86	1232.2	891.0	738.4
26	1925.9	1198.6	855.3	88	1236.4	888.2	741.2
28	1892.3	1173.8	835.4	90	1240.5	887.7	741.3
30	1842.8	1154.5	822.1	92	1244.1	888.2	741.1
32	1805.5	1128.3	807.7	94	1245.6	888.1	739.0
34	1745.8	1089.7	793.4	96	1249.1	887.7	737.7
36	1676.6	1057.0	779.3	98	1252.5	885.5	735.3
38	1611.9	1024.7	764.1	100	1252.4	882.5	733.0
40	1550.0	997.8	755.0	102	1251.9	880.3	729.7
42	1505.3	975.5	753.1	104	1252.4	878.9	726.2
44	1491.4	959.5	749.5	106	1252.1	877.4	723.1
46	1469.7	941.3	748.0	108	1252.4	872.8	721.8
48	1456.0	926.2	743.3	110	1252.6	872.0	719.4
50	1434.6	915.9	738.3	112	1252.0	870.6	717.0
52	1409.1	912.8	737.2	114	1252.5	871.4	715.5
54	1393.9	913.8	740.7	116	1252.4	871.2	715.6
56	1370.0	913.2	740.9	118	1252.6	870.9	716.0
58	1342.1	912.2	739.7	120	1252.4	871.1	715.6
60	1315.4	913.8	736.9				

Sample Preparation Method:
Compression Molding then Flow Reversal
Concentration: 30 wt% Glass fiber
Fiber Length: L_n = 0.54 mm, L_w = 0.70 mm
Temperature: 200 °C
Shear Rate: 1.0 s^{-1}

γ_{REV}	η^+, Pa s	γ	η^+, Pa s
0	0.0	62	562.3
2	328.2	64	558.8
4	336.7	66	559.6
6	379.8	68	558.1
8	406.2	70	558.3
10	451.3	72	561.8
12	476.8	74	566.0
14	508.7	76	566.8
16	540.1	78	565.7
18	556.8	80	564.5
20	574.3	82	562.0
22	581.4	84	560.0
24	586.1	86	558.8
26	590.9	88	559.7
28	603.3	90	552.5
30	625.9	92	549.4
32	648.1	94	547.5
34	659.0	96	551.1
36	658.7	98	555.8
38	666.3	100	565.5
40	669.6	102	572.6
42	670.3	104	580.6
44	656.0	106	582.4
46	644.9	108	582.3
48	630.0	110	579.5
50	612.0	112	576.4
52	590.1	114	568.8
54	575.0	116	559.8
56	568.8	118	554.3
58	564.0	120	552.6
60	565.0		

Sample Preparation Method:
Compression Molding then Flow Reversal
Concentration: 30 wt% Glass Fiber
Fiber Length: L_n = 0.90 mm, L_w = 1.50 mm
Temperature: 200 °C
Shear Rate: 1.0 s^{-1}

γ_{REV}	η^+, Pa s	γ	η^+, Pa s
0	0.0	62	1586.7
2	693.4	64	1639.8
4	748.4	66	1680.2
6	745.7	68	1696.5
8	769.1	70	1679.2
10	779.8	72	1697.1
12	801.3	74	1655.4
14	836.6	76	1624.2
16	883.8	78	1612.5
18	947.4	80	1606.4
20	999.1	82	1586.2
22	1087.5	84	1585.0
24	1159.3	86	1590.0
26	1242.3	88	1570.0
28	1305.5	90	1567.4
30	1326.5	92	1584.1
32	1340.5	94	1590.5
34	1334.9	96	1531.4
36	1380.4	98	1452.4
38	1407.7	100	1363.5
40	1433.0	102	1310.0
42	1448.2	104	1249.8
44	1474.6	106	1187.6
46	1473.8	108	1140.7
48	1494.2	110	1098.4
50	1487.0	112	1090.3
52	1513.1	114	1065.0
54	1512.1	116	1049.0
56	1537.3	118	1006.1
58	1547.9	120	982.6
60	1574.2		

Sample Preparation Method:
Injection Molding (non-uniform)
Concentration: 30 wt% Glass fiber
Fiber Length: L_n = 0.70 mm, L_w = 0.89 mm
Temperature: 200 °C
Shear Rate: 1.0 s^{-1}

γ	η^+, Pa s	γ	η^+, Pa s
0	0.0	52	930.8
2	750.7	54	913.3
4	870.8	56	893.9
6	974.4	58	869.2
8	1055.1	60	850.6
10	1076.3	62	841.8
12	1098.9	64	837.4
14	1102.4	66	835.5
16	1097.0	68	828.3
18	1082.2	70	818.9
20	1068.9	72	808.9
22	1064.4	74	796.2
24	1050.5	76	780.4
26	1049.2	78	777.0
28	1042.1	80	778.3
30	1029.5	82	782.5
32	1011.0	84	786.9
34	996.0	86	794.4
36	990.1	88	794.1
38	977.1	90	786.3
40	965.3	92	778.0
42	957.9	94	771.7
44	950.7	96	764.8
46	947.2	98	746.6
48	950.4	100	718.6
50	946.4		

Sample Preparation Method:
Injection Molding (uniform)
Concentration: 30 wt% Glass Fiber
Fiber Length: L_n = 0.70 mm, L_w = 0.89 mm
Temperature: 200 °C
Shear Rate: 1.0 s^{-1}

γ	η^+, Pa s	γ	η^+, Pa s
0	0.0	52	800.5
2	870.0	54	801.1
4	992.6	56	804.2
6	1126.3	58	784.1
8	1194.3	60	780.0
10	1210.9	62	773.0
12	1217.2	64	771.2
14	1202.1	66	769.7
16	1219.5	68	763.1
18	1179.7	70	757.0
20	1185.0	72	751.3
22	1210.4	74	743.6
24	1173.0	76	736.1
26	1159.8	78	728.9
28	1162.4	80	728.4
30	1151.4	82	726.1
32	1133.1	84	724.7
34	1095.0	86	724.5
36	1048.0	88	722.7
38	979.6	90	705.8
40	944.2	92	683.0
42	907.2	94	598.1
44	893.0	96	526.9
46	870.1	98	505.7
48	850.9	100	484.6
50	821.9		

Sample Preparation Method:
Injection Molding (non-uniform) then Flow Reversal
Concentration: 30 wt% Glass fiber
Fiber Length: L_n = 0.70 mm, L_w = 0.89 mm
Temperature: 200 °C
Shear Rate: 1.0 s^{-1}

γ_{REV}	η^+, Pa s	γ	η^+, Pa s
0	0.0	52	917.8
2	619.0	54	913.3
4	659.7	56	909.2
6	699.8	58	905.5
8	749.6	60	901.7
10	767.2	62	897.6
12	795.9	64	892.5
14	857.9	66	887.1
16	889.5	68	879.2
18	920.0	70	871.3
20	933.3	72	862.2
22	956.7	74	853.3
24	975.3	76	844.7
26	984.9	78	836.6
28	990.3	80	829.0
30	993.3	82	821.4
32	993.7	84	813.7
34	989.4	86	806.3
36	980.7	88	798.9
38	971.3	90	792.1
40	958.3	92	788.7
42	947.9	94	786.0
44	937.0	96	783.0
46	929.8	98	780.6
48	925.2	100	777.5
50	922.0		

Sample Preparation Method:
Injection Molding (uniform) then Flow Reversal
Concentration: 30 wt% Glass Fiber
Fiber Length: L_n = 0.70 mm, L_w = 0.89 mm
Temperature: 200 °C
Shear Rate: 1.0 s^{-1}

γ_{REV}	η^+, Pa s	γ	η^+, Pa s
0	0.0	62	879.6
2	588.1	64	866.7
4	615.2	66	860.7
6	638.2	68	848.3
8	670.0	70	837.0
10	706.4	72	834.5
12	794.5	74	822.7
14	832.0	76	811.6
16	853.8	78	807.2
18	875.5	80	802.1
20	899.0	82	797.8
22	914.3	84	796.8
24	914.7	86	799.8
26	915.0	88	800.3
28	909.7	90	798.9
30	918.9	92	794.2
32	925.0	94	789.3
34	912.7	96	785.0
36	893.4	98	779.3
38	893.1	100	776.2
40	885.6		

Appendix E Fiber Orientation Data

Sample Preparation Method: Compression Molding
Concentration: 10 wt% Glass Fiber
Fiber Length: L_n = 1.40 mm, L_w = 3.59 mm
Temperature: 200 °C
Shear Rates: 0.4, 1.0 and 4.0 s^{-1}

Shear Rate = 0.4 s^{-1}

γ	A_{11}	A_{12}	A_{22}	A_{33}	A_{1211}	A_{1212}	A_{1222}	A_{1233}
0	0.5329	0.0198	0.0676	0.3995	0.0145	0.0117	0.0016	0.0037
20	0.6357	0.0083	0.0405	0.3239	0.0062	0.0115	0.0006	0.0015
40	0.6924	0.0152	0.0472	0.2604	0.0115	0.0104	0.0010	0.0027
60	0.7197	0.0224	0.0502	0.23	0.0165	0.0151	0.0018	0.0041
80	0.7062	0.0178	0.0354	0.2584	0.0127	0.0103	0.0011	0.0040
100	0.7426	0.0224	0.0372	0.2201	0.0185	0.0114	0.0023	0.0016
120	0.7807	0.0106	0.034	0.1853	0.0038	0.0112	0.0047	0.0021

Shear Rate = 1.0 s^{-1}

γ	A_{11}	A_{12}	A_{22}	A_{33}	A_{1211}	A_{1212}	A_{1222}	A_{1233}
0	0.5329	0.0198	0.0676	0.3995	0.0145	0.0117	0.0016	0.0037
20	0.6265	-0.0087	0.0778	0.2957	-0.0101	0.0140	0.0043	-0.0029
40	0.6534	0.0176	0.0618	0.2848	0.0102	0.0113	0.0036	0.0038
60	0.6961	0.0167	0.0543	0.2496	0.0123	0.0113	0.0001	0.0043
80	0.7415	0.0032	0.0525	0.206	0.0008	0.0112	0.0004	0.002
100	0.7526	0.0017	0.0397	0.2077	0.0002	0.0109	0.0009	0.0006
120	0.7853	0.0115	0.0456	0.1691	0.0071	0.0128	0.0035	0.0009

Shear Rate = 4.0 s^{-1}

γ	A_{11}	A_{12}	A_{22}	A_{33}	A_{1211}	A_{1212}	A_{1222}	A_{1233}
0	0.5329	0.0198	0.0676	0.3995	0.0145	0.0117	0.0016	0.0037
20	0.6249	-0.0003	0.067	0.3081	-0.0002	0.0158	0.0000	-0.0001
40	0.6761	0.0046	0.0525	0.2715	0.0035	0.0107	0.0007	0.0004
60	0.7345	-0.0115	0.0562	0.2093	-0.0081	0.0116	-0.0027	-0.0007
80	0.7483	0.0022	0.0425	0.2092	0.0007	0.0101	0.0012	0.0003
100	0.7516	0.0025	0.0547	0.1937	0.0015	0.0120	0.0002	0.0008
120	0.7670	0.0084	0.0509	0.182	0.0050	0.0131	0.0028	0.0006

Sample Preparation Method: Compression Molding
Concentration: 20 wt% Glass Fiber
Fiber Length: L_n = 1.28 mm, L_w = 2.59 mm
Temperature: 200 °C
Shear Rates: 0.4, 1.0 and 4.0 s^{-1}

Shear Rate = 0.4 s^{-1}

γ	A_{11}	A_{12}	A_{22}	A_{33}	A_{1211}	A_{1212}	A_{1222}	A_{1233}
0	0.5363	-0.0405	0.0837	0.3799	-0.0272	0.0202	-0.0019	-0.0114
20	0.5958	-0.0141	0.0719	0.3323	-0.0061	0.0147	-0.0037	-0.0043
40	0.6395	-0.0176	0.0782	0.2823	-0.0111	0.0168	0.0008	-0.0073
60	0.7070	0.0086	0.0674	0.2257	0.0078	0.0155	-0.0012	0.0020
80	0.7385	0.0031	0.0660	0.1954	0.0006	0.0154	0.0007	0.0018
100	0.7331	0.0089	0.0599	0.2070	0.0060	0.0144	0.0004	0.0025
120	0.7283	0.0070	0.0571	0.2146	0.0017	0.0142	0.0036	0.0017

Shear Rate = 1.0 s^{-1}

γ	A_{11}	A_{12}	A_{22}	A_{33}	A_{1211}	A_{1212}	A_{1222}	A_{1233}
0	0.5363	-0.0405	0.0837	0.3799	-0.0272	0.0202	-0.0019	-0.0114
20	0.5605	0.0068	0.0936	0.3460	0.0052	0.0173	0.0011	0.0005
40	0.6438	0.0059	0.0771	0.2791	0.0078	0.0157	-0.0027	0.0008
60	0.7269	-0.0070	0.0606	0.2125	-0.0051	0.0135	-0.0005	-0.0014
80	0.7237	0.0038	0.0611	0.2152	0.0032	0.0138	0.0002	0.0004
100	0.7432	0.0094	0.0638	0.1929	0.0073	0.0135	0.0011	0.0010
120	0.7935	0.0097	0.0394	0.1672	0.0067	0.0123	0.0008	0.0022

Shear Rate = 4.0 s^{-1}

γ	A_{11}	A_{12}	A_{22}	A_{33}	A_{1211}	A_{1212}	A_{1222}	A_{1233}
0	0.5363	-0.0405	0.0837	0.3799	-0.0272	0.0202	-0.0019	-0.0114
20	0.5555	0.0010	0.0788	0.3658	0.0063	0.0145	-0.0071	0.0018
40	0.6695	0.0021	0.0604	0.2701	0.0230	0.0141	-0.0245	0.0036
60	0.7118	-0.0017	0.0510	0.2372	-0.0029	0.0127	0.0014	-0.0002
80	0.7442	0.0050	0.0512	0.2046	0.0054	0.0140	-0.0008	0.0004
100	0.7653	0.0144	0.0480	0.1867	0.0130	0.0144	0.0002	0.0012
120	0.7755	0.0073	0.0397	0.1848	0.0049	0.0124	0.0002	0.0022

Sample Preparation Method: Compression Molding
Concentration: 30 wt% Glass Fiber
Fiber Length: L_n = 1.25 mm, L_w = 2.28 mm
Temperature: 200 °C
Shear Rates: 0.4, 1.0 and 4.0 s^{-1}

Shear Rate = 0.4 s^{-1}

γ	A_{11}	A_{12}	A_{22}	A_{33}	A_{1211}	A_{1212}	A_{1222}	A_{1233}
0	0.5407	0.0199	0.0846	0.3747	0.0101	0.0163	0.0018	0.0080
10	0.5516	0.0277	0.0143	0.4340	0.0221	0.0204	0.0020	0.0036
20	0.5818	0.0154	0.0608	0.3574	0.0025	0.0143	0.0096	0.0033
30	0.6344	0.0051	0.0404	0.3252	0.0052	0.0198	-0.0042	0.0041
40	0.6513	0.0092	0.0510	0.2977	0.0030	0.0126	0.0059	0.0003
60	0.7300	0.0052	0.0450	0.2249	0.0052	0.0135	-0.0011	0.0011
80	0.7509	0.0047	0.0428	0.2063	0.0028	0.0129	0.0014	0.0005
100	0.7439	0.0073	0.0410	0.2152	0.0066	0.0153	-0.0009	0.0016
120	0.7818	0.0024	0.0292	0.1890	0.0006	0.0153	0.0012	0.0006

Shear Rate = 1.0 s^{-1}

γ	A_{11}	A_{12}	A_{22}	A_{33}	A_{1211}	A_{1212}	A_{1222}	A_{1233}
0	0.5407	0.0199	0.0846	0.3747	0.0101	0.0163	0.0018	0.0080
10	0.5341	0.0381	0.0382	0.4276	0.0172	0.0115	0.0185	0.0024
20	0.5696	0.0227	0.0587	0.3716	0.0189	0.0128	-0.0035	0.0073
30	0.6160	0.0222	0.0442	0.3398	0.0140	0.0153	0.0078	0.0004
40	0.6428	0.0246	0.0458	0.3114	0.0197	0.0122	0.0012	0.0037
60	0.7107	0.0211	0.0391	0.2502	0.0245	0.0119	-0.0073	0.0039
80	0.7497	0.0130	0.0360	0.2143	0.0057	0.0099	0.0073	0.0000
100	0.7668	0.0110	0.0364	0.1969	0.0117	0.0117	-0.0017	0.0010
120	0.7755	0.0117	0.0362	0.1883	0.0078	0.0131	0.0029	0.0010

Shear Rate = 4.0 s^{-1}

γ	A_{11}	A_{12}	A_{22}	A_{33}	A_{1211}	A_{1212}	A_{1222}	A_{1233}
0	0.5407	0.0199	0.0846	0.3747	0.0101	0.0163	0.0018	0.0080
10	0.5824	0.0116	0.0508	0.3668	0.0117	0.0135	-0.0043	0.0042
20	0.5785	0.0240	0.0546	0.3669	0.0181	0.0111	0.0005	0.0054
30	0.6315	0.0277	0.0401	0.3284	0.0130	0.0106	0.0135	0.0012
40	0.6523	0.0251	0.0395	0.3081	0.0225	0.0103	-0.0021	0.0047
60	0.7156	0.0232	0.0370	0.2475	0.0164	0.0112	0.0040	0.0028
80	0.7409	0.0202	0.0383	0.2207	0.0149	0.0113	0.0030	0.0023
100	0.7571	0.0164	0.0392	0.2036	0.0128	0.0113	0.0008	0.0028
120	0.7760	0.0175	0.0409	0.1831	0.0078	0.0117	0.0054	0.0043

Sample Preparation Method: Compression Molding
Concentration: 40 wt% Glass Fiber
Fiber Length: L_n = 1.06 mm, L_w = 1.96 mm
Temperature: 200 °C
Shear Rates: 0.4, 1.0 and 4.0 s^{-1}

Shear Rate = 0.4 s^{-1}

γ	A_{11}	A_{12}	A_{22}	A_{33}	A_{1211}	A_{1212}	A_{1222}	A_{1233}
0	0.5267	0.0077	0.1021	0.3712	0.0057	0.0184	-0.0027	0.0047
20	0.5446	-0.0182	0.0728	0.3826	-0.0128	0.0191	-0.0005	-0.0049
40	0.6400	0.0091	0.0756	0.2844	0.0051	0.0190	0.0004	0.0036
60	0.7752	-0.0018	0.0471	0.1777	-0.0005	0.0139	-0.0013	0.0000
80	0.7389	0.0096	0.0582	0.2029	0.0030	0.0157	0.0066	0.0000
100	0.7722	0.0202	0.0520	0.1758	0.0199	0.0144	-0.0005	0.0008
120	0.7563	0.0088	0.0641	0.1797	0.0070	0.0178	0.0017	0.0001

Shear Rate = 1.0 s^{-1}

γ	A_{11}	A_{12}	A_{22}	A_{33}	A_{1211}	A_{1212}	A_{1222}	A_{1233}
0	0.5267	0.0077	0.1021	0.3712	0.0057	0.0184	-0.0027	0.0047
20	0.4992	0.0110	0.0879	0.4129	0.0104	0.0118	-0.0056	0.0062
40	0.6845	0.0162	0.0402	0.2752	0.0058	0.0109	0.0098	0.0006
60	0.7599	-0.0010	0.0339	0.2062	-0.0007	0.0116	-0.0002	-0.0001
80	0.7602	0.0096	0.0344	0.2053	0.0118	0.0118	-0.0030	0.0008
100	0.7660	0.0061	0.0343	0.1998	0.0009	0.0131	0.0051	0.0001
120	0.8087	0.0038	0.0316	0.1597	0.0041	0.0134	-0.0009	0.0006

Shear Rate = 4.0 s^{-1}

γ	A_{11}	A_{12}	A_{22}	A_{33}	A_{1211}	A_{1212}	A_{1222}	A_{1233}
0	0.5267	0.0077	0.1021	0.3712	0.0057	0.0184	-0.0027	0.0047
20	0.5490	-0.0011	0.0588	0.3922	-0.0107	0.0126	0.0140	-0.0044
40	0.6581	0.0001	0.0339	0.3080	0.0011	0.0116	-0.0039	0.0029
60	0.7652	0.0160	0.0335	0.2013	0.0007	0.0108	0.0129	0.0024
80	0.7732	0.0133	0.0352	0.1917	0.0102	0.0121	0.0009	0.0022
100	0.8139	0.0161	0.0317	0.1544	0.0125	0.0123	0.0020	0.0016
120	0.7861	0.0072	0.0361	0.1778	0.0012	0.0147	0.0058	0.0002

Sample Preparation Method: Compression Molding
Concentration: 30 wt% Glass Fiber
Fiber Length: L_n = 0.54 mm, L_w = 0.70 mm
Temperature: 200 °C
Shear Rates: 0.4, 1.0 and 4.0 s^{-1}

Shear Rate = 0.4 s^{-1}

γ	A_{11}	A_{12}	A_{22}	A_{33}	A_{1211}	A_{1212}	A_{1222}	A_{1233}
0	0.4807	0.0101	0.0605	0.4588	0.0083	0.0163	-0.0030	0.0048
10	0.5234	0.0175	0.0501	0.4265	0.0175	0.0187	-0.0004	0.0004
20	0.6657	0.0208	0.0402	0.2941	0.0261	0.0169	-0.0076	0.0023
30	0.7491	0.0508	0.0421	0.2088	0.0419	0.0208	0.0059	0.0030
40	0.7804	0.0174	0.0405	0.1791	0.0243	0.0180	-0.0083	0.0014
60	0.827	0.0023	0.0233	0.1496	0.0076	0.0126	-0.0059	0.0006
120	0.8352	0.0037	0.0391	0.1256	0.0060	0.0150	-0.0031	0.0008

Shear Rate = 1.0 s^{-1}

γ	A_{11}	A_{12}	A_{22}	A_{33}	A_{1211}	A_{1212}	A_{1222}	A_{1233}
0	0.4807	0.0101	0.0605	0.4588	0.0083	0.0163	-0.0030	0.0048
10	0.5723	0.0282	0.0536	0.3741	0.0083	0.0163	-0.0030	0.0048
20	0.7130	0.0296	0.035	0.2520	0.0173	0.0218	0.0031	0.0078
30	0.7582	0.0295	0.0307	0.2112	0.0238	0.0195	0.0016	0.0042
40	0.7859	0.0042	0.0235	0.1906	0.0256	0.0186	0.0001	0.0038
60	0.8030	0.0158	0.0348	0.1652	0.0041	0.0138	-0.0012	0.0013
120	0.8458	0.0175	0.0322	0.1220	0.0140	0.0175	0.0031	0.0003

Shear Rate = 4.0 s^{-1}

γ	A_{11}	A_{12}	A_{22}	A_{33}	A_{1211}	A_{1212}	A_{1222}	A_{1233}
0	0.4807	0.0101	0.0605	0.4588	0.0083	0.0163	-0.0030	0.0048
10	0.5466	0.0485	0.0594	0.3939	0.0296	0.0166	0.0141	0.0048
20	0.6486	0.0226	0.0405	0.3109	0.0253	0.0182	-0.0033	0.0006
30	0.7759	0.0048	0.0372	0.1869	0.0132	0.0151	-0.0088	0.0004
40	0.7665	0.015	0.0383	0.1951	0.0141	0.0170	0.0008	0.0001
60	0.8117	0.0125	0.0373	0.1511	0.0157	0.0230	-0.0035	0.0003
120	0.816	0.0132	0.0616	0.1224	0.0085	0.0274	0.0041	0.0006

Sample Preparation Method: Compression Molding
Concentration: 30 wt% Glass Fiber
Fiber Length: L_n = 0.9 mm, L_w = 1.5 mm
Temperature: 200 °C
Shear Rates: 0.4, 1.0 and 4.0 s^{-1}

Shear Rate = 0.4 s^{-1}

γ	A_{11}	A_{12}	A_{22}	A_{33}	A_{1211}	A_{1212}	A_{1222}	A_{1233}
0	0.4807	0.0103	0.0732	0.4461	0.0076	0.0104	0.0008	0.0019
10	0.5417	0.0185	0.0280	0.4303	0.0099	0.0087	0.0019	0.0067
20	0.6739	0.0000	0.0567	0.2694	-0.0075	0.0197	0.0092	-0.0017
30	0.7047	0.0040	0.0279	0.2674	0.0197	0.0130	-0.0183	0.0026
40	0.7429	0.0093	0.0451	0.2120	0.0077	0.0198	0.0014	0.0002
60	0.7916	0.0056	0.0426	0.1658	0.0092	0.0115	-0.0045	0.0009
80	0.7920	0.0049	0.0418	0.1662	0.0092	0.0152	-0.0046	0.0003
100	0.8065	0.0171	0.0409	0.1526	0.0176	0.0156	-0.0007	0.0002
120	0.7913	0.0129	0.0599	0.1488	0.0116	0.0228	0.0003	0.0010

Shear Rate = 1.0 s^{-1}

γ	A_{11}	A_{12}	A_{22}	A_{33}	A_{1211}	A_{1212}	A_{1222}	A_{1233}
0	0.4807	0.0103	0.0732	0.4461	0.0076	0.0104	0.0008	0.0019
10	0.5177	0.0258	0.0450	0.4373	0.0158	0.0154	0.0098	0.0002
20	0.5490	0.0136	0.0606	0.3904	0.0139	0.0174	-0.0006	0.0003
30	0.6223	0.0141	0.0319	0.3457	0.0178	0.0179	-0.0043	0.0006
40	0.7563	-0.0025	0.0257	0.2181	-0.0037	0.0136	0.0038	-0.0026
60	0.7974	0.0101	0.0345	0.1681	0.0131	0.0161	-0.0051	0.0021
80	0.8274	0.0120	0.0283	0.1443	0.0117	0.0161	-0.0005	0.0008
100	0.819	0.0114	0.0393	0.1417	0.0115	0.0171	-0.0016	0.0015
120	0.8336	0.0148	0.0223	0.1441	0.0140	0.0115	0.0014	-0.0006

Shear Rate = 4.0 s^{-1}

γ	A_{11}	A_{12}	A_{22}	A_{33}	A_{1211}	A_{1212}	A_{1222}	A_{1233}
0	0.4807	0.0103	0.0732	0.4461	0.0076	0.0104	0.0008	0.0019
10	0.4954	0.0043	0.0250	0.4796	0.0040	0.0073	-0.0001	0.0004
20	0.6357	-0.0028	0.0514	0.3129	-0.0041	0.0156	0.0044	-0.0031
30	0.6679	0.0122	0.0219	0.3103	0.0095	0.0077	0.0023	0.0004
40	0.7111	0.0124	0.0347	0.2542	0.0130	0.0119	-0.0027	0.0021
60	0.7876	0.0023	0.0407	0.1717	0.0052	0.0191	-0.0047	0.0018
80	0.7741	0.0063	0.0441	0.1818	0.0022	0.0214	0.0029	0.0012
100	0.8173	0.0139	0.0397	0.1430	0.0126	0.0196	0.0006	0.0007
120	0.8084	0.0041	0.0692	0.1224	0.0008	0.0205	0.0031	0.0002

Sample Preparation Method: Compression Molding
Concentration: 9.2 wt% Carbon Fiber
Fiber Length: L_n = 0.74 mm, L_w = 1.39 mm
Temperature: 200 °C
Shear Rates: 1.0 s^{-1}

γ	A_{11}	A_{12}	A_{22}	A_{33}	A_{1211}	A_{1212}	A_{1222}	A_{1233}
0	0.5437	0.0591	0.0514	0.4049	0.0054	0.0194	0.0362	0.0175
20	0.6216	0.0231	0.0395	0.3390	0.0057	0.0179	0.0010	0.0164
40	0.6587	0.0606	0.0798	0.2616	0.0044	0.0245	0.0528	0.0034
60	0.6982	0.0155	0.0278	0.2739	0.0175	0.0331	-0.0122	0.0102
80	0.7184	0.0129	0.0273	0.2544	0.0267	0.0351	-0.0211	0.0073
100	0.7130	0.0009	0.0384	0.2487	0.0243	0.0105	-0.0318	0.0084
120	0.7450	0.0300	0.0416	0.2135	0.0046	0.0129	0.0229	0.0025

Sample Preparation Method: Compression Molding
Concentration: 15.3 wt% Carbon Fiber
Fiber Length: L_n = 0.68 mm, L_w = 0.96 mm
Temperature: 200 °C
Shear Rates: 1.0 s^{-1}

γ	A_{11}	A_{12}	A_{22}	A_{33}	A_{1211}	A_{1212}	A_{1222}	A_{1233}
0	0.5827	0.0315	0.0724	0.3449	0.0127	0.0244	0.0036	0.0152
20	0.5548	0.0296	0.0542	0.3910	0.0061	0.0162	0.0106	0.0129
40	0.6100	0.0120	0.0680	0.3220	0.0367	0.0349	-0.0384	0.0137
60	0.6891	0.0318	0.0753	0.2356	0.0088	0.0118	0.0169	0.0061
80	0.7381	0.0375	0.0727	0.1892	0.0004	0.0097	0.0265	0.0106
100	0.7849	0.0350	0.0238	0.1913	0.0052	0.0168	0.0259	0.0039
120	0.7797	0.0080	0.0253	0.1950	0.0178	0.0191	-0.0156	0.0058

Sample Preparation Method: Compression Molding then Flow Reversal
Concentration: 30 wt% Glass fiber
Fiber Length: L_n = 0.54 mm, L_w = 0.70 mm
Temperature: 200 °C
Shear Rate: 1.0 s^{-1}

γ_{REV}	A_{11}	A_{12}	A_{22}	A_{33}	A_{13}	A_{23}	A_{1211}	A_{1212}	A_{1222}	A_{1233}
0	0.8458	0.0175	0.0322	0.1220	0.0054	-0.0046	0.0140	0.0175	0.0031	0.0003
20	0.8526	-0.0022	0.0247	0.1227	-0.0136	-0.0015	-0.0031	0.0124	-0.0001	0.0010
40	0.8492	-0.0120	0.0290	0.1218	0.0077	-0.0003	-0.0089	0.0176	-0.0030	-0.0001
60	0.8646	-0.0121	0.0223	0.1131	-0.0031	0.0036	-0.0106	0.0135	-0.0011	-0.0004
80	0.8530	-0.0089	0.0224	0.1246	-0.0050	0.0015	-0.0094	0.0133	-0.0007	0.0012
100	0.8677	-0.0084	0.0298	0.1025	-0.0090	-0.0007	-0.0077	0.0168	-0.0009	0.0002
120	0.8561	-0.0103	0.0282	0.1157	-0.0148	-0.0019	-0.0089	0.0171	-0.0022	0.0008

Sample Preparation Method: Compression Molding then Flow Reversal
Concentration: 30 wt% Glass Fiber
Fiber Length: L_n = 0.90 mm, L_w = 1.50 mm
Temperature: 200 °C
Shear Rate: 1.0 s^{-1}

γ_{REV}	A_{11}	A_{12}	A_{22}	A_{33}	A_{13}	A_{23}	A_{1211}	A_{1212}	A_{1222}	A_{1233}
0	0.8336	0.0148	0.0223	0.1441	-0.0107	-0.0040	0.0140	0.0115	0.0014	-0.0006
10	0.8059	0.0146	0.0317	0.1624	0.0180	0.0059	0.0113	0.0173	0.0023	0.0010
20	0.8046	0.0000	0.0242	0.1712	0.0081	0.0027	-0.0017	0.0122	0.0003	0.0014
40	0.7821	-0.0017	0.0361	0.1818	0.0028	0.0082	-0.0011	0.0188	0.0001	-0.0007
60	0.7436	-0.0152	0.0296	0.2268	0.0356	0.0084	-0.0124	0.0150	-0.0012	-0.0017
80	0.7468	-0.0127	0.0391	0.2141	-0.0136	0.0028	-0.0155	0.0154	0.0044	-0.0016
100	0.7349	-0.0154	0.0408	0.2243	-0.0123	0.0014	-0.0159	0.0191	0.0000	0.0005
120	0.7256	-0.0123	0.0351	0.2393	0.0317	0.0061	-0.0120	0.0163	0.0002	-0.0005

Sample Preparation Method: Injection Molding (non-uniform)
Concentration: 30 wt% Glass fiber
Fiber Length: L_n = 0.70 mm, L_w = 0.89 mm
Temperature: 200 °C
Shear Rate: 1.0 s^{-1}

Average orientation through the sample thickness

γ	A_{11}	A_{12}	A_{22}	A_{33}	A_{13}	A_{23}	A_{1211}	A_{1212}	A_{1222}	A_{1233}
0	0.6011	-0.0021	0.0282	0.3707	-0.0068	-0.0023	-0.0061	0.0131	-0.0025	0.0066
10	0.5452	0.0158	0.0424	0.4124	-0.0084	0.0436	0.0120	0.0124	0.0008	0.0030
20	0.5912	0.0181	0.0416	0.3672	-0.0117	0.0347	0.0126	0.0185	0.0023	0.0033
40	0.6261	0.0290	0.0523	0.3216	-0.0202	0.0306	0.0227	0.0158	0.0003	0.0060
60	0.6976	0.0228	0.0303	0.2721	0.0040	0.0189	0.0177	0.0141	0.0004	0.0047
80	0.7655	0.0232	0.0375	0.1969	0.0058	0.0179	0.0213	0.0208	-0.0017	0.0035
100	0.8232	0.0212	0.0307	0.1461	-0.0176	0.0249	0.0198	0.0162	0.0011	0.0002

Injection molded orientation (non-uniform) through the sample thickness at $\gamma = 0$

x_2/H	A_{11}	A_{12}	A_{22}	A_{33}	A_{13}	A_{23}	A_{1211}	A_{1212}	A_{1222}	A_{1233}
0.033	0.7370	0.0208	0.0196	0.2434	-0.0247	0.0049	-0.0221	0.0139	-0.0020	0.0030
0.100	0.7628	0.0553	0.0295	0.2078	-0.0404	-0.0068	-0.0228	0.0196	-0.0036	0.0037
0.167	0.7887	0.0554	0.0304	0.1809	-0.0139	-0.0011	-0.0055	0.0225	-0.0060	0.0029
0.233	0.6976	0.0117	0.0417	0.2606	0.0366	0.0023	-0.0305	0.0294	-0.0095	0.0045
0.300	0.5884	-0.0165	0.0278	0.3838	0.0544	-0.0067	-0.0002	0.0124	-0.0012	0.0101
0.367	0.5360	0.0015	0.0290	0.4350	-0.0067	-0.0099	0.0174	0.0087	-0.0019	0.0130
0.433	0.2149	-0.0139	0.0268	0.7582	-0.0013	0.0059	0.0032	0.0031	0.0012	0.0171
0.500	0.2499	-0.0043	0.0305	0.7196	-0.0092	0.0151	-0.0038	0.0050	0.0013	0.0176
0.567	0.5010	-0.0160	0.0201	0.4789	-0.0602	-0.0035	0.0005	0.0076	0.0000	0.0049
0.633	0.6227	-0.0098	0.0379	0.3394	-0.0377	-0.0123	-0.0072	0.0158	-0.0038	0.0083
0.700	0.7135	-0.0217	0.0431	0.2434	0.0021	-0.0053	-0.0168	0.0176	-0.0093	0.0023
0.767	0.7028	-0.0265	0.0209	0.2763	0.0166	-0.0065	-0.0037	0.0130	-0.0012	0.0013
0.833	0.7321	-0.0574	0.0169	0.2510	-0.0182	-0.0035	0.0088	0.0089	0.0001	0.0005
0.900	0.6605	-0.0602	0.0266	0.3129	-0.0095	-0.0132	0.0002	0.0081	-0.0025	0.0005
0.967	0.6535	-0.0223	0.0214	0.3251	0.0472	-0.0105	0.0033	0.0093	0.0000	0.0025

Injection molded orientation (non-uniform) through the sample thickness at $\gamma = 10$

x_2/H	A_{11}	A_{12}	A_{22}	A_{33}	A_{13}	A_{23}	A_{1211}	A_{1212}	A_{1222}	A_{1233}
0.033	0.7182	0.0262	0.0199	0.2619	0.0354	0.0343	0.0227	0.0116	0.0020	0.0015
0.100	0.6604	0.0227	0.0311	0.3085	0.0351	0.0258	0.0181	0.0119	0.0009	0.0038
0.167	0.6672	0.0070	0.0387	0.2941	0.0687	0.0256	0.0076	0.0137	-0.0026	0.0020
0.233	0.6463	0.0211	0.0318	0.3219	-0.0035	0.0328	0.0156	0.0129	0.0031	0.0024
0.300	0.5904	0.0221	0.0543	0.3553	0.0522	0.0565	0.0146	0.0134	-0.0005	0.0081
0.367	0.5266	0.0156	0.0396	0.4338	-0.0340	0.0693	0.0080	0.0107	0.0016	0.0060
0.433	0.2073	0.0038	0.0524	0.7403	-0.0684	0.1010	0.0004	0.0050	0.0008	0.0026
0.500	0.3162	0.0100	0.0471	0.6367	-0.0777	0.0417	0.0114	0.0060	0.0004	-0.0018
0.567	0.3370	0.0103	0.0540	0.6090	-0.0601	0.0714	0.0013	0.0104	0.0024	0.0066
0.633	0.5262	0.0091	0.0350	0.4388	-0.1122	0.0387	0.0053	0.0107	0.0019	0.0019
0.700	0.7397	0.0197	0.0381	0.2221	0.0065	0.0329	0.0210	0.0203	-0.0004	-0.0009
0.767	0.6944	0.0052	0.0365	0.2691	0.0574	0.0300	0.0024	0.0180	-0.0009	0.0036
0.833	0.6708	0.0173	0.0378	0.2913	0.0102	0.0248	0.0102	0.0194	0.0014	0.0057
0.900	0.5850	0.0283	0.0657	0.3492	0.0694	0.0250	0.0257	0.0149	0.0008	0.0018
0.967	0.6055	0.0352	0.0486	0.3458	-0.0281	0.0214	0.0242	0.0136	0.0018	0.0093

Injection molded orientation (non-uniform) through the sample thickness at $\gamma = 20$

x_2/H	A_{11}	A_{12}	A_{22}	A_{33}	A_{13}	A_{23}	A_{1211}	A_{1212}	A_{1222}	A_{1233}
0.033	0.6895	0.0208	0.0205	0.2899	0.1260	0.0185	0.0115	0.0101	0.0019	0.0074
0.100	0.7754	0.0553	0.0325	0.1921	0.0051	0.0186	0.0461	0.0231	0.0060	0.0032
0.167	0.7954	0.0554	0.0290	0.1756	-0.0163	0.0182	0.0524	0.0199	0.0038	-0.0007
0.233	0.7759	-0.0117	0.0353	0.1889	0.0043	0.0237	-0.0101	0.0225	-0.0033	0.0017
0.300	0.7060	-0.0165	0.0350	0.2590	0.0262	0.0239	-0.0171	0.0206	-0.0028	0.0034
0.367	0.6153	-0.0015	0.0361	0.3486	0.0378	0.0461	-0.0026	0.0126	-0.0015	0.0027
0.433	0.3619	0.0139	0.0473	0.5908	-0.0731	0.0672	0.0041	0.0113	0.0030	0.0068
0.500	0.2299	0.0043	0.0576	0.7125	-0.0782	0.0536	0.0001	0.0088	-0.0004	0.0045
0.567	0.3054	-0.0160	0.0500	0.6446	-0.0660	0.0659	-0.0111	0.0099	-0.0021	-0.0028
0.633	0.5396	-0.0098	0.0279	0.4325	-0.0068	0.0460	-0.0098	0.0092	0.0000	0.0000
0.700	0.6634	-0.0217	0.0342	0.3024	-0.0238	0.0396	-0.0182	0.0169	-0.0016	-0.0019
0.767	0.5746	0.0265	0.0590	0.3663	0.0135	0.0558	0.0120	0.0227	0.0055	0.0090
0.833	0.6228	0.0574	0.0561	0.3211	-0.0351	0.0294	0.0397	0.0334	0.0130	0.0047
0.900	0.5590	0.0602	0.0647	0.3763	-0.0149	-0.0009	0.0453	0.0344	0.0085	0.0065
0.967	0.6242	0.0223	0.0349	0.3409	-0.0277	0.0174	0.0120	0.0198	0.0054	0.0049

Injection molded orientation (non-uniform) through the sample thickness at $\gamma = 40$

x_2/H	A_{11}	A_{12}	A_{22}	A_{33}	A_{13}	A_{23}	A_{1211}	A_{1212}	A_{1222}	A_{1233}
0.033	0.8320	0.0250	0.0140	0.1540	-0.0077	0.0191	0.0222	0.0074	0.0007	0.0021
0.100	0.7456	0.0185	0.0225	0.2319	0.0105	0.0249	0.0188	0.0108	-0.0003	0.0000
0.167	0.7014	0.0248	0.0225	0.2761	-0.0287	0.0352	0.0205	0.0095	0.0012	0.0031
0.233	0.6770	0.1203	0.0969	0.2261	0.0477	0.0241	0.0840	0.0579	0.0337	0.0026
0.300	0.6455	0.0192	0.0344	0.3201	-0.0797	0.0189	0.0153	0.0152	-0.0006	0.0046
0.367	0.4598	0.0245	0.0283	0.5118	-0.0773	0.0554	0.0135	0.0087	0.0016	0.0094
0.433	0.2844	0.0028	0.2172	0.4984	-0.0475	0.0429	0.0162	0.0171	-0.0330	0.0195
0.500	0.3962	0.0385	0.0587	0.5452	-0.0145	0.0561	0.0207	0.0129	0.0017	0.0161
0.567	0.5108	0.0408	0.0479	0.4413	-0.0217	0.0544	0.0287	0.0148	0.0015	0.0106
0.633	0.5648	0.0364	0.0329	0.4023	-0.0006	0.0289	0.0244	0.0127	0.0030	0.0090
0.700	0.7268	0.0040	0.0311	0.2421	0.0015	0.0227	0.0045	0.0130	-0.0004	-0.0001
0.767	0.7320	0.0111	0.0348	0.2332	-0.0728	0.0236	0.0109	0.0118	-0.0023	0.0026
0.833	0.7327	0.0292	0.0258	0.2415	-0.0159	0.0038	0.0232	0.0124	0.0005	0.0055
0.900	0.7196	0.0049	0.0248	0.2556	-0.0168	0.0172	0.0042	0.0114	0.0001	0.0006
0.967	0.6584	0.0149	0.0293	0.3122	0.0015	0.0344	0.0132	0.0145	-0.0003	0.0020

Injection molded orientation (non-uniform) through the sample thickness at $\gamma = 60$

x_2/H	A_{11}	A_{12}	A_{22}	A_{33}	A_{13}	A_{23}	A_{1211}	A_{1212}	A_{1222}	A_{1233}
0.033	0.8145	0.0173	0.0107	0.1748	-0.0105	0.0173	0.0173	0.0054	0.0000	-0.0001
0.100	0.7091	0.0404	0.0346	0.2563	0.0221	0.0298	0.0372	0.0186	0.0018	0.0013
0.167	0.7418	0.0243	0.0348	0.2234	-0.0365	0.0169	0.0268	0.0211	0.0004	-0.0028
0.233	0.7622	0.0378	0.0327	0.2051	0.0113	0.0084	0.0351	0.0194	-0.0017	0.0044
0.300	0.6890	0.0177	0.0299	0.2812	0.0072	0.0197	0.0141	0.0152	-0.0007	0.0044
0.367	0.6356	0.0168	0.0324	0.3319	-0.0109	0.0170	0.0096	0.0146	0.0015	0.0057
0.433	0.6398	0.0220	0.0288	0.3314	0.0317	0.0165	0.0140	0.0141	-0.0015	0.0096
0.500	0.5271	0.0349	0.0310	0.4419	0.0473	0.0303	0.0178	0.0099	0.0014	0.0158
0.567	0.5963	0.0236	0.0374	0.3663	0.0170	0.0254	0.0157	0.0120	-0.0010	0.0090
0.633	0.7316	0.0005	0.0335	0.2349	0.0024	0.0275	0.0003	0.0134	-0.0015	0.0017
0.700	0.7918	0.0178	0.0230	0.1852	0.0397	0.0101	0.0135	0.0125	0.0025	0.0019
0.767	0.7548	0.0205	0.0285	0.2167	-0.0172	0.0100	0.0132	0.0146	0.0028	0.0044
0.833	0.7262	0.0137	0.0334	0.2404	-0.0527	0.0136	0.0085	0.0144	0.0003	0.0048
0.900	0.7049	0.0218	0.0281	0.2670	-0.0195	0.0174	0.0173	0.0123	0.0014	0.0031
0.967	0.7169	0.0410	0.0293	0.2538	0.0099	0.0223	0.0355	0.0126	0.0017	0.0038

Injection molded orientation (non-uniform) through the sample thickness at $\gamma = 80$

x_2/H	A_{11}	A_{12}	A_{22}	A_{33}	A_{13}	A_{23}	A_{1211}	A_{1212}	A_{1222}	A_{1233}
0.033	0.7525	0.0208	0.0273	0.2202	-0.0309	0.0260	0.0200	0.0116	0.0007	0.0001
0.100	0.7368	0.0206	0.0237	0.2395	-0.0059	0.0251	0.0156	0.0104	0.0018	0.0032
0.167	0.7943	0.0158	0.0128	0.1930	0.0305	0.0167	0.0106	0.0079	0.0004	0.0048
0.233	0.7287	0.0358	0.0187	0.2526	-0.0549	0.0259	0.0270	0.0098	0.0007	0.0081
0.300	0.6519	0.0416	0.0389	0.3092	-0.0021	0.0288	0.0327	0.0163	0.0010	0.0078
0.367	0.7658	0.0555	0.0194	0.2147	0.0743	0.0150	0.0473	0.0098	0.0010	0.0072
0.433	0.8006	-0.0280	0.0428	0.1566	0.0249	0.0135	-0.0191	0.0251	-0.0122	0.0033
0.500	0.7541	-0.0430	0.0719	0.1741	-0.0132	0.0253	-0.0196	0.0360	-0.0270	0.0036
0.567	0.7535	-0.0182	0.0803	0.1662	-0.0531	0.0126	-0.0098	0.0422	-0.0123	0.0039
0.633	0.7871	0.0846	0.0475	0.1654	0.0354	0.0081	0.0666	0.0335	0.0121	0.0059
0.700	0.8047	0.0091	0.0182	0.1771	0.0110	0.0110	0.0069	0.0108	-0.0007	0.0029
0.767	0.7679	0.0244	0.0193	0.2128	0.0243	0.0120	0.0230	0.0087	0.0001	0.0013
0.833	0.7805	0.0707	0.0447	0.1748	0.0356	0.0133	0.0628	0.0285	0.0080	0.0000
0.900	0.7567	0.0528	0.0484	0.1949	-0.0378	0.0350	0.0482	0.0308	0.0068	-0.0023
0.967	0.8800	0.0142	0.0176	0.1024	0.0767	0.0000	0.0149	0.0104	-0.0015	0.0007

Injection molded orientation (non-uniform) through the sample thickness at $\gamma = 100$

x_2/H	A_{11}	A_{12}	A_{22}	A_{33}	A_{13}	A_{23}	A_{1211}	A_{1212}	A_{1222}	A_{1233}
0.033	0.8086	0.0134	0.0208	0.1705	-0.0045	0.0285	0.0120	0.0101	0.0005	0.0009
0.100	0.7914	-0.0102	0.0311	0.1775	0.0125	0.0402	-0.0054	0.0161	-0.0012	-0.0036
0.167	0.8546	-0.0252	0.0374	0.1080	-0.0036	0.0164	-0.0248	0.0193	-0.0012	0.0008
0.233	0.8019	-0.0098	0.0372	0.1610	-0.0103	0.0406	-0.0048	0.0206	-0.0038	-0.0012
0.300	0.7977	0.0169	0.0367	0.1656	-0.0329	0.0457	0.0179	0.0145	-0.0008	-0.0002
0.367	0.7776	0.0260	0.0295	0.1929	-0.0056	0.0382	0.0187	0.0143	0.0020	0.0053
0.433	0.8121	0.0136	0.0264	0.1614	-0.0475	0.0339	0.0139	0.0144	-0.0003	0.0000
0.500	0.8266	0.0214	0.0285	0.1449	-0.0579	0.0209	0.0202	0.0143	0.0020	-0.0009
0.567	0.8168	0.0250	0.0320	0.1512	0.0310	0.0252	0.0201	0.0153	0.0014	0.0035
0.633	0.8285	0.0201	0.0285	0.1430	-0.0039	0.0231	0.0172	0.0153	0.0003	0.0026
0.700	0.8405	0.0364	0.0289	0.1307	-0.0492	0.0166	0.0334	0.0180	0.0017	0.0012
0.767	0.8461	0.0424	0.0313	0.1226	-0.0072	0.0123	0.0419	0.0151	0.0014	-0.0008
0.833	0.8389	0.0231	0.0219	0.1392	-0.0529	0.0253	0.0262	0.0113	0.0005	-0.0036
0.900	0.8360	0.0645	0.0354	0.1287	-0.0054	0.0151	0.0561	0.0204	0.0067	0.0017
0.967	0.8548	0.0608	0.0341	0.1111	-0.0125	0.0051	0.0551	0.0224	0.0062	-0.0005

Sample Preparation Method: Injection Molding (uniform)
Concentration: 30 wt% Glass Fiber
Fiber Length: L_n = 0.70 mm, L_w = 0.89 mm
Temperature: 200 °C
Shear Rate: 1.0 s^{-1}

Average orientation through the sample thickness

γ	A_{11}	A_{12}	A_{22}	A_{33}	A_{13}	A_{23}	A_{1211}	A_{1212}	A_{1222}	A_{1233}
0	0.7866	0.0055	0.0171	0.1963	-0.0122	-0.0023	0.0071	0.0089	-0.0005	-0.0011
10	0.7420	0.0011	0.0242	0.2337	-0.0314	0.0000	0.0007	0.0114	-0.0006	0.0009
20	0.7342	0.0068	0.0505	0.2153	-0.0031	0.0019	0.0117	0.0124	-0.0066	0.0017
40	0.8061	-0.0017	0.0369	0.1570	0.0147	0.0040	-0.0006	0.0145	-0.0014	0.0003
60	0.8168	0.0234	0.0439	0.1393	-0.0048	0.0012	0.0162	0.0187	0.0069	0.0004
80	0.8255	0.0251	0.0228	0.1517	-0.0121	-0.0005	0.0220	0.0131	0.0020	0.0011
100	0.8527	0.0217	0.0266	0.1207	-0.0436	0.0017	0.0182	0.0164	0.0022	0.0014

Injection molded orientation (uniform) through the sample thickness at $\gamma = 0$

x_2/H	A_{11}	A_{12}	A_{22}	A_{33}	A_{13}	A_{23}	A_{1211}	A_{1212}	A_{1222}	A_{1233}
0.033	0.6994	0.0150	0.0168	0.2839	0.0288	0.0129	0.0150	0.0077	0.0004	-0.0004
0.100	0.8363	0.0024	0.0150	0.1486	0.0013	0.0040	0.0044	0.0101	-0.0007	-0.0013
0.167	0.8688	0.0065	0.0100	0.1211	-0.0048	0.0045	0.0059	0.0074	0.0004	0.0001
0.233	0.8630	0.0125	0.0154	0.1217	-0.0102	0.0036	0.0115	0.0088	0.0000	0.0010
0.300	0.8283	0.0063	0.0145	0.1572	0.0763	0.0056	0.0064	0.0093	0.0000	-0.0001
0.367	0.7125	0.0056	0.0132	0.2743	-0.0002	0.0082	0.0053	0.0061	-0.0011	0.0015
0.433	0.5541	-0.0089	0.0198	0.4262	-0.1490	0.0032	-0.0037	0.0060	-0.0007	-0.0045
0.500	0.7160	-0.0179	0.0223	0.2617	-0.1982	0.0077	-0.0095	0.0073	-0.0031	-0.0052
0.567	0.7393	-0.0100	0.0217	0.2390	-0.0193	-0.0173	-0.0041	0.0077	-0.0027	-0.0032
0.633	0.8020	0.0075	0.0125	0.1856	0.0349	-0.0096	0.0082	0.0069	0.0000	-0.0008
0.700	0.8721	0.0405	0.0185	0.1094	0.0435	-0.0055	0.0396	0.0147	0.0020	-0.0011
0.767	0.8379	0.0064	0.0126	0.1495	-0.0149	0.0015	0.0061	0.0071	-0.0002	0.0005
0.833	0.7435	0.0052	0.0219	0.2346	-0.0016	-0.0087	0.0067	0.0107	-0.0012	-0.0003
0.900	0.7605	0.0209	0.0304	0.2091	0.0111	-0.0298	0.0257	0.0138	-0.0010	-0.0037
0.967	0.8518	-0.0250	0.0134	0.1348	0.0040	-0.0155	-0.0241	0.0079	-0.0014	0.0004

Injection molded orientation (uniform) through the sample thickness at $\gamma = 10$

x_2/H	A_{11}	A_{12}	A_{22}	A_{33}	A_{13}	A_{23}	A_{1211}	A_{1212}	A_{1222}	A_{1233}
0.033	0.8470	0.0143	0.0196	0.1333	0.0449	0.0131	0.0102	0.0084	0.0026	0.0015
0.100	0.8562	0.0008	0.0110	0.1328	0.0014	0.0017	-0.0003	0.0083	0.0006	0.0005
0.167	0.8838	0.0074	0.0079	0.1083	0.0028	0.0043	0.0045	0.0064	0.0010	0.0019
0.233	0.8325	-0.0096	0.0156	0.1519	-0.0147	-0.0083	-0.0121	0.0054	0.0010	0.0014
0.300	0.8183	-0.0187	0.0171	0.1647	0.0214	-0.0113	-0.0177	0.0073	0.0008	-0.0018
0.367	0.7778	0.0245	0.0218	0.2005	-0.0013	-0.0150	0.0167	0.0118	0.0037	0.0041
0.433	0.6926	0.0376	0.0372	0.2703	0.0132	0.0406	0.0255	0.0204	0.0015	0.0106
0.500	0.6524	-0.0271	0.0256	0.3219	-0.2144	0.0351	-0.0149	0.0127	-0.0041	-0.0081
0.567	0.6627	-0.0119	0.0178	0.3195	-0.1331	0.0093	-0.0091	0.0083	-0.0008	-0.0021
0.633	0.7202	-0.0118	0.0100	0.2698	0.0218	0.0041	-0.0096	0.0052	-0.0003	-0.0019
0.700	0.6232	0.0024	0.0236	0.3533	-0.0741	0.0116	0.0044	0.0092	-0.0024	0.0005
0.767	0.6041	-0.0191	0.0591	0.3368	0.0058	-0.0349	-0.0071	0.0216	-0.0105	-0.0015
0.833	0.6989	0.0028	0.0461	0.2550	-0.0094	-0.0301	0.0016	0.0216	-0.0007	0.0019
0.900	0.6683	0.0452	0.0320	0.2997	-0.0733	-0.0252	0.0306	0.0145	0.0029	0.0117
0.967	0.7183	-0.0028	0.0314	0.2503	-0.0578	0.0052	0.0062	0.0141	-0.0068	-0.0022

Injection molded orientation (uniform) through the sample thickness at $\gamma = 20$

x_2/H	A_{11}	A_{12}	A_{22}	A_{33}	A_{13}	A_{23}	A_{1211}	A_{1212}	A_{1222}	A_{1233}
0.033	0.7015	0.0201	0.0085	0.2900	0.0415	-0.0046	0.0133	0.0041	0.0008	0.0060
0.100	0.7830	0.0109	0.0078	0.2092	0.0271	-0.0044	0.0093	0.0051	0.0000	0.0016
0.167	0.8307	0.0105	0.0121	0.1571	0.0623	-0.0014	0.0094	0.0076	-0.0008	0.0019
0.233	0.6931	-0.0010	0.1732	0.1337	0.0623	-0.0087	0.0074	0.0084	-0.0118	0.0034
0.300	0.7934	0.0040	0.0130	0.1936	0.0997	-0.0057	0.0049	0.0076	-0.0006	-0.0003
0.367	0.8176	0.0172	0.0199	0.1626	0.0309	0.0076	0.0184	0.0119	-0.0014	0.0002
0.433	0.7606	0.0081	0.0324	0.2070	-0.0261	0.0124	0.0122	0.0166	-0.0055	0.0015
0.500	0.6329	0.0051	0.0425	0.3246	-0.1455	0.0327	0.0089	0.0124	-0.0046	0.0008
0.567	0.5786	-0.0601	0.1769	0.2444	-0.1142	0.0170	-0.0052	0.0291	-0.0542	-0.0007
0.633	0.7770	0.0172	0.0238	0.1991	-0.0558	-0.0026	0.0157	0.0128	-0.0007	0.0021
0.700	0.8004	0.0309	0.0298	0.1698	0.0027	-0.0072	0.0294	0.0172	-0.0006	0.0020
0.767	0.7675	0.0277	0.0224	0.2102	0.0001	0.0013	0.0242	0.0134	0.0007	0.0028
0.833	0.7206	0.0070	0.0433	0.2362	0.0168	-0.0051	0.0114	0.0168	-0.0031	-0.0013
0.900	0.6546	0.0172	0.0232	0.3223	-0.0873	-0.0018	0.0128	0.0083	0.0007	0.0036
0.967	0.6320	0.0158	0.0214	0.3466	0.0587	-0.0131	0.0124	0.0102	0.0013	0.0022

Injection molded orientation (uniform) through the sample thickness at $\gamma = 40$

x_2/H	A_{11}	A_{12}	A_{22}	A_{33}	A_{13}	A_{23}	A_{1211}	A_{1212}	A_{1222}	A_{1233}
0.033	0.8215	-0.0277	0.0142	0.1642	0.0428	-0.0036	-0.0277	0.0092	-0.0005	0.0005
0.100	0.7847	-0.0111	0.0366	0.1787	0.0061	-0.0018	-0.0175	0.0163	0.0060	0.0004
0.167	0.7979	0.0497	0.0814	0.1207	0.0027	0.0038	0.0164	0.0269	0.0308	0.0025
0.233	0.8324	0.0137	0.0368	0.1308	0.0331	0.0033	0.0167	0.0113	-0.0043	0.0014
0.300	0.6904	-0.0922	0.1512	0.1584	0.0545	-0.0019	-0.0370	0.0460	-0.0538	-0.0013
0.367	0.7767	0.0058	0.0193	0.2040	0.0449	0.0015	0.0033	0.0098	0.0007	0.0017
0.433	0.7720	0.0185	0.0205	0.2075	-0.0054	0.0115	0.0182	0.0134	-0.0003	0.0006
0.500	0.8427	0.0163	0.0196	0.1378	-0.0381	0.0166	0.0149	0.0110	0.0022	-0.0008
0.567	0.8369	-0.0053	0.0190	0.1441	-0.0194	0.0134	-0.0004	0.0111	-0.0013	-0.0036
0.633	0.8575	0.0008	0.0137	0.1287	0.0002	-0.0013	0.0005	0.0085	0.0000	0.0003
0.700	0.8113	-0.0009	0.0161	0.1726	-0.0020	0.0028	-0.0003	0.0085	0.0001	-0.0007
0.767	0.8258	0.0191	0.0133	0.1609	0.0098	0.0083	0.0140	0.0072	0.0014	0.0037
0.833	0.7917	-0.0033	0.0306	0.1778	0.0143	0.0013	-0.0047	0.0072	0.0013	0.0002
0.900	0.8144	-0.0020	0.0238	0.1618	0.0387	0.0064	-0.0022	0.0111	0.0019	-0.0017
0.967	0.8740	0.0130	0.0109	0.1152	0.0344	0.0027	0.0116	0.0064	-0.0001	0.0014

Injection molded orientation (uniform) through the sample thickness at $\gamma = 60$

x_2/H	A_{11}	A_{12}	A_{22}	A_{33}	A_{13}	A_{23}	A_{1211}	A_{1212}	A_{1222}	A_{1233}
0.033	0.8523	0.0262	0.0308	0.1169	0.0050	-0.0002	0.0165	0.0141	0.0090	0.0008
0.100	0.7852	0.0701	0.0925	0.1223	-0.0079	0.0056	0.0327	0.0375	0.0359	0.0015
0.167	0.8111	0.0200	0.0264	0.1624	-0.0395	0.0104	0.0186	0.0098	0.0002	0.0013
0.233	0.8226	0.0161	0.0340	0.1434	-0.0388	0.0002	0.0175	0.0094	-0.0016	0.0001
0.300	0.8057	0.0110	0.0258	0.1685	-0.0273	-0.0057	0.0113	0.0104	-0.0008	0.0005
0.367	0.8232	0.0257	0.0143	0.1625	-0.0403	0.0014	0.0204	0.0089	0.0017	0.0036
0.433	0.8175	0.0203	0.0249	0.1576	-0.0927	0.0057	0.0195	0.0146	0.0001	0.0007
0.500	0.8048	0.0082	0.0305	0.1646	-0.0121	-0.0057	0.0136	0.0191	-0.0050	-0.0004
0.567	0.7089	0.0676	0.1562	0.1348	-0.0374	0.0134	0.0243	0.0350	0.0439	-0.0005
0.633	0.8047	-0.0008	0.0405	0.1548	0.0428	-0.0039	0.0105	0.0181	-0.0094	-0.0019
0.700	0.8331	-0.0077	0.0303	0.1366	0.0286	0.0015	-0.0084	0.0177	-0.0023	0.0029
0.767	0.8554	0.0054	0.0306	0.1140	0.0346	-0.0023	0.0023	0.0159	0.0014	0.0017
0.833	0.8258	0.0603	0.0678	0.1064	0.0404	-0.0025	0.0441	0.0425	0.0195	-0.0032
0.900	0.8287	0.0042	0.0183	0.1530	0.0174	0.0011	0.0050	0.0112	0.0000	-0.0008
0.967	0.8969	0.0062	0.0057	0.0974	0.0444	-0.0040	0.0071	0.0036	-0.0003	-0.0006

Injection molded orientation (uniform) through the sample thickness at $\gamma = 80$

x_2/H	A_{11}	A_{12}	A_{22}	A_{33}	A_{13}	A_{23}	A_{1211}	A_{1212}	A_{1222}	A_{1233}
0.033	0.8543	0.0366	0.0126	0.1331	-0.0409	0.0055	0.0332	0.0104	0.0017	0.0017
0.100	0.8309	0.0199	0.0108	0.1583	-0.0437	0.0021	0.0193	0.0068	0.0005	0.0001
0.167	0.8597	0.0278	0.0216	0.1187	-0.0418	0.0009	0.0227	0.0125	0.0019	0.0032
0.233	0.8555	0.0346	0.0166	0.1279	-0.0406	0.0014	0.0295	0.0119	0.0026	0.0025
0.300	0.8604	0.0271	0.0162	0.1235	0.0265	-0.0025	0.0267	0.0091	0.0008	-0.0005
0.367	0.8519	0.0729	0.0420	0.1062	-0.0036	-0.0019	0.0555	0.0293	0.0155	0.0020
0.433	0.8073	0.0115	0.0257	0.1669	-0.0075	-0.0038	0.0096	0.0129	0.0016	0.0004
0.500	0.8244	-0.0046	0.0168	0.1588	-0.0266	-0.0001	-0.0013	0.0101	0.0002	-0.0036
0.567	0.9437	0.0452	0.0026	0.0537	-0.2129	-0.0102	0.0428	0.0023	0.0001	0.0023
0.633	0.8447	0.0298	0.0186	0.1367	-0.0167	0.0010	0.0253	0.0103	0.0011	0.0033
0.700	0.8476	0.0238	0.0269	0.1255	-0.0089	0.0020	0.0215	0.0158	0.0022	0.0001
0.767	0.7947	0.0306	0.0378	0.1675	0.0621	-0.0091	0.0323	0.0196	-0.0016	-0.0001
0.833	0.9676	-0.0621	0.0058	0.0266	0.1169	-0.0081	-0.0607	0.0049	-0.0004	-0.0010
0.900	0.7342	0.0142	0.0379	0.2279	-0.0104	-0.0070	0.0121	0.0144	-0.0001	0.0021
0.967	0.6731	0.0072	0.0259	0.3010	0.0423	-0.0074	0.0024	0.0099	0.0007	0.0041

Injection molded orientation (uniform) through the sample thickness at $\gamma = 100$

x_2/H	A_{11}	A_{12}	A_{22}	A_{33}	A_{13}	A_{23}	A_{1211}	A_{1212}	A_{1222}	A_{1233}
0.033	0.0204	0.0132	0.1244	-0.0599	0.0007	0.0165	0.0101	0.0027	0.0013	0.0204
0.100	0.0160	0.0280	0.1669	-0.0448	0.0037	0.0102	0.0149	0.0022	0.0036	0.0160
0.167	0.0191	0.0404	0.1086	-0.0466	0.0038	0.0106	0.0267	0.0077	0.0007	0.0191
0.233	0.0505	0.0424	0.0861	-0.0598	0.0094	0.0388	0.0257	0.0101	0.0016	0.0505
0.300	0.0545	0.0321	0.0894	-0.0515	0.0006	0.0416	0.0227	0.0107	0.0022	0.0545
0.367	0.0177	0.0119	0.0693	-0.0665	-0.0008	0.0166	0.0084	0.0013	-0.0002	0.0177
0.433	0.0268	0.0149	0.0922	-0.0673	-0.0098	0.0233	0.0094	0.0021	0.0015	0.0268
0.500	0.0311	0.0276	0.1372	-0.0706	0.0088	0.0266	0.0099	0.0022	0.0023	0.0311
0.567	0.0097	0.0160	0.1751	-0.0279	-0.0018	0.0078	0.0089	0.0005	0.0014	0.0097
0.633	0.0172	0.0197	0.1105	-0.0024	-0.0047	0.0128	0.0126	0.0022	0.0023	0.0172
0.700	0.0089	0.0216	0.1167	-0.0478	-0.0015	0.0101	0.0152	-0.0018	0.0006	0.0089
0.767	0.0146	0.0336	0.1262	-0.0508	0.0023	0.0159	0.0201	-0.0027	0.0014	0.0146
0.833	0.0105	0.0289	0.1439	-0.0240	0.0043	0.0112	0.0170	-0.0018	0.0010	0.0105
0.900	0.0204	0.0346	0.1546	-0.0180	0.0097	0.0206	0.0228	-0.0014	0.0013	0.0204
0.967	-0.0003	0.0257	0.1193	-0.0016	0.0026	0.0030	0.0159	-0.0036	0.0003	-0.0003